

University of Nottingham
UK | CHINA | MALAYSIA

Development of a Conceptual Model for the Ultra-Fine Particulate Matter Processes in Gasoline Direct Injection Engines Using Integrated CFD-Chemical Kinetic Modelling

Jing Yang Tan, B.Eng. (Hons)

Thesis Submitted to the University of Nottingham Malaysia for the Degree of Doctor of Philosophy

August 2019

ABSTRACT

Despite the improvement in fuel economy and engine performance, gasoline direct injection (GDI) engines have been relatively recently identified as a prominent source of ultra-fine particulate matter (PM) which mainly consists of soot. Adverse health impacts of these airborne particles call for stringent legislations to monitor both the number and mass emissions. Set against this background, an integrated computational fluid dynamics (CFD)-chemical kinetic modelling approach is developed in order to acquire an in-depth understanding of PM processes within GDI engine configurations.

Given the nature of spark-ignited engines, GDI combustion is characterised by flame propagation under high-temperature conditions. To represent gasoline fuels, reduced mechanisms of toluene reference fuel (TRF), coupled with the chemistry of polycyclic aromatic hydrocarbon, are evaluated using ignition delay (ID) time, laminar flame speed and speciation data as validation targets. The optimal TRF mechanism predicts the ID times of stoichiometric gasoline-air mixture at 55 bar with the highest deviation of 13% throughout 900–1160 K. The effect of high pressures at 20 bar and 25 bar on the flame speeds of a binary surrogate is also captured accurately (< 14% difference). In addition, the concentrations of PAH from flame burners and reactors are computed within the same order of magnitude as the experimental measurements. The selected TRF mechanism is subsequently incorporated to CFD modelling of the GDI engine.

A complete set of CFD sub-models is formulated to describe the whole panoply of in-cylinder events numerically, covering turbulence, spray, fuel impingement, liquid fuel film, ignition, combustion, flame propagation and emissions. The dynamic multi-zone partitioning method is introduced within the Detailed Chemistry model to expedite the calculations. Along with the sectional method for soot modelling, the resulting computational time only increases by 13% as compared to the modelling approach that relies on tabulated chemistry. Based on the reference case at 2300 rpm and 90 N m, in-cylinder pressures are replicated with the peak value predicted within a 1% margin. Computed number density of soot differs from the tailpipe measurement by 8% while its mass density is under-predicted by a factor of two. The modelled particle size distribution function captures the decreasing trend in particle number as the size becomes larger within the range of 10–100 nm. The integrated approach is extended across different speed-load points whereby engine speed is varied from 1600 rpm to

3000 rpm while engine load is changed by altering the torque from 60 N m to 120 N m. The effects of speed and load are manifested in terms of in-cylinder flow conditions and mixing time, thus affecting the mixture distribution at spark ignition timing.

A conceptual model describing the ultra-fine PM processes in the wall-guided GDI engine under the homogeneous stoichiometric mode is developed. The dominant PM formation mechanisms are the presence of fuel-rich regions and remaining liquid fuel droplets at the onset of spark event. The mixture inhomogeneity is attributed to film stripping and evaporation from the liquid film deposited due to spray impingement. Piston wetting is the most severe, accounting for up to 76% of the maximum film mass. Pyrene and acetylene contribute towards the increase in soot particle number and mass, respectively while post-flame oxidation becomes effective at high-temperature regions with large concentrations of hydroxyl radicals. Based on the reference case, three engine operating parameters are varied in isolation to examine their effects on PM emissions. In the order of decreasing sensitivity, they are ranked as fuel injection timing, spark ignition timing and rate of exhaust gas recirculation. Overall, the detailed fundamental understanding of PM processes obtained from this study is beneficial in strategy optimisation for PM mitigation in GDI engines.

ACKNOWLEDGEMENTS

First and foremost, I would like to express my sincere gratitude to my supervisors, Prof. Hoon Kiat Ng, Prof. Suyin Gan and Dr. Fabrizio Bonatesta for their continuous guidance and support over the course of my study. The insightful feedback provided has positively contributed to improving the quality of research works. The University of Nottingham Malaysia and the Ministry of Higher Education are deeply thanked for providing the scholarship and funding the project as a whole.

I would also like to thank Oxford Brookes University for providing the necessary experimental data from the engine test bed with a special mention to Edward Hopkins. Technical assistance on the simulation software given by Dr. Rickard Solsjö and Jose Tijiboy at Siemens PLM Software is highly appreciated. Special thanks go to my then seniors, Dr. Xinwei Cheng, Dr. Hiew Mun Poon and Dr. Jiun Cai Ong for their valuable advice and suggestions in overcoming the research roadblocks.

I am greatly appreciative of my fellow peers and colleagues who always encourage me to never give up and cheer me up in times of distress. In particular, I am thankful for Lillian Olule and Ricardo Parra in making pacts and setting goals to keep each other motivated and believing in me during the tough moments. To all my friends who have helped me and stood by me throughout the journey, I would like to extend my wholehearted thanks.

Last but not least, I would like to convey my profound gratitude to my father, Chuai Heng Tan, my mother, Khar Lin Lee and my siblings. I would not have achieved what I did without their unconditional love and unrelenting support at all times. It is the patience, understanding and company from my family that empowered me to strive to complete the project successfully.

TABLE OF CONTENTS

ABSTRACT i

ACKNOWLEDGEMENTS iii

ABBREVIATIONS viii

NOMENCLATURE x

LIST OF FIGURES xvi

LIST OF TABLES xxiv

CHAPTER 1 INTRODUCTION 1

1.1 Background 1

1.1.1 Association of GDI Engines with Ultra-Fine Particulate Matter 2

1.1.2 Current Understanding of PM Formation within GDI Engines 4

1.2 Aim and Objectives 5

1.3 Thesis Outline 9

CHAPTER 2 LITERATURE REVIEW 10

2.1 Introductory Remarks 10

2.2 Chemical Kinetic Modelling of Gasoline Fuels 11

2.2.1 Development of Reaction Mechanisms as Gasoline Surrogates 12

2.2.2 TRF Reaction Mechanisms 16

2.2.3 Applicability of Reaction Mechanisms in GDI Engines 18

2.3 CFD Modelling of In-Cylinder Processes in GDI Engines 19

2.3.1 Spray, Mixture Formation and Combustion Modelling of GDI Engines 24

2.3.2 PM Processes and Mechanisms in GDI Engines 32

2.4 Concluding Remarks 44

CHAPTER 3 MATHEMATICAL MODELS AND GOVERNING EQUATIONS 46

3.1 Introductory Remarks 46

3.2 Composition of TRF Surrogates 46

3.3 Chemical Kinetics 47

3.3.1 Homogenous Reactor Models 51
3.3.2 Premixed Laminar Flame Models 53
3.3.3 Sensitivity Analysis and ROP Analysis 54
3.4 CFD Modelling 56
3.4.1 Basic Conservation Equations 56
3.4.2 Thermophysical Properties 57
3.4.3 Turbulence Model 60
3.4.4 Fuel Spray and Atomisation Models 61
3.4.5 Liquid Films 66
3.4.6 Combustion Model 68
3.4.7 Soot Model 70
3.5 Concluding Remarks 73
CHAPTER 4 EVALUATIVE STUDY OF TRF MECHANISMS 75
4.1 Introductory Remarks 75
4.2 Reduced Mechanisms of TRF 75
4.3 Validation Criteria Based on GDI Engine-Like Operating Conditions 77
4.4 ID Time 79
4.4.1 Gasoline Fuels and TRF Surrogates 80
4.4.2 PRF Surrogates 85
4.5 Flame Speed 86
4.5.1 Gasoline Fuels and TRF Surrogates 87
4.5.2 PRF Surrogates 89
4.6 Speciation Profile 91
4.6.1 Flame Burners 91
4.6.2 JSR 94
4.7 Chemical Kinetic Analyses 95
4.7.1 Temperature Sensitivity for ID Time 96

4.7.2 Mass Flow Rate Sensitivity for Flame Speed 98
4.7.3 ROP of A1 for Speciation Profile of PAH 100
4.8 Selection of the Optimal TRF Mechanism 102
4.9 Concluding Remarks 104
CHAPTER 5 DEVELOPMENT OF INTEGRATED CFD-CHEMICAL KINETIC MODELLING FOR GDI ENGINES 105
5.1 Introductory Remarks 105
5.2 Experimental Setup of GDI Engine Test Bed 105
5.2.1 Fuel Specifications 105
5.2.2 Engine Specifications and Data Acquisition 106
5.2.3 Experimental Operating Conditions 108
5.3 Numerical Formulation of GDI Engine Modelling with Integrated CFD-Chemical Kinetics 111
5.3.1 General Numerical Setting 111
5.3.2 CFD Sub-models for In-Cylinder Processes 113
5.3.3 Validation of Integrated CFD-Chemical Kinetic Modelling 119
5.4 Concluding Remarks 137
CHAPTER 6 INVESTIGATION OF PM FORMATION MECHANISMS UNDER DIFFERENT SPEED-LOAD POINTS 139
6.1 Introductory Remarks 139
6.2 Effect of Engine Speed on PM Formation Mechanisms 139
6.2.1 Spray Development and Mixture Formation 140
6.2.2 Combustion Progress 148
6.2.3 PM Formation and Emissions 152
6.3 Effect of Engine Load on PM Formation Mechanisms 158
6.3.1 Spray Development and Mixture Formation 159
6.3.2 Combustion Progress 167
6.3.3 PM Formation and Emissions 172

6.4 Concluding Remarks 179

CHAPTER 7 NUMERICAL STUDY ON EFFECTS OF ENGINE OPERATING PARAMETERS ON PM EMISSIONS 181

7.1 Introductory Remarks 181

7.2 Conceptual Model for Ultra-Fine PM Processes in GDI Engines 182

7.3 Effect of SOI Timing on PM Emissions 201

7.4 Effect of SI Timing on PM Emissions 207

7.5 Effect of EGR Rate on PM Emissions 212

7.6 Concluding Remarks 218

CHAPTER 8 CONCLUSIONS AND FUTURE WORK 221

8.1 Conclusions 221

8.1.1 Evaluation of TRF Mechanisms for Application in GDI Engines 221

8.1.2 Integrated CFD-Chemical Kinetic Modelling of GDI Engines 222

8.1.3 Conceptual Model for Ultra-Fine PM Processes in GDI Engines 224

8.1.4 Numerical Study on PM Emissions from GDI Engines 225

8.2 Future Work 226

REFERENCES 227

APPENDICES 243

Appendix A Chemical Kinetic Validation Results for Neat Hydrocarbons 243

Appendix B Chemical Reactions under An-TRF 250

Appendix C Computational Mesh of the GDI Engine 257

ABBREVIATIONS

0D	Zero-dimensional
1D	One-dimensional
3D	Three-dimensional
ABDC	After bottom dead centre
AFR	Air-fuel ratio
ATDC	After top dead centre
BBDC	Before bottom dead centre
BDC	Bottom dead centre
BMEP	Brake mean effective pressure
BML	Bray-Moss-Libby
BTDC	Before top dead centre
CAD	Crank angle degree
CFD	Computational fluid dynamics
CFM	Coherent flame model
CMC	Continuous multi-component
CTC	Characteristic-time combustion
DDM	Discrete droplet model
DMZ	Dynamic multi-zone
DPF	Diesel particulate filter
DPIK	Discrete particle ignition kernel
ECFM	Extended coherent flame model
EDM	Eddy-dissipation model
EGR	Exhaust gas recirculation
EOI	End of injection
EVC	Exhaust valve closing
EVO	Exhaust valve opening
FSC	Flame speed closure
GDI	Gasoline direct injection
H/C	Hydrogen/carbon
HAB	Height above burner
HACA	Hydrogen-abstraction-C_2H_2-addition
HACARC	HACA ring closure
HCCI	Homogenous charge compression ignition
ICE	Internal combustion engine

ID	Ignition delay
IMEP	Indicated mean effective pressure
IVC	Intake valve closing
IVO	Intake valve opening
KH	Kelvin-Helmholtz
KH-RT	Kelvin-Helmholtz and Rayleigh-Taylor
MON	Motor octane number
NTC	Negative temperature coefficient
ON	Octane number
OPPDIF	Opposed-flow diffusion flame
PAH	Polycyclic aromatic hydrocarbon
PDF	Probability density function
PFI	Port fuel injection
PM	Particulate matter
PREMIX	Premixed flame
PRF	Primary reference fuel
PSDF	Particle size distribution function
PSR	Perfectly stirred reactor
RANS	Reynolds-averaged Navier-Stokes
RCM	Rapid compression machine
RNG	Re-normalisation group
RON	Research octane number
ROP	Rate of production
RT	Rayleigh-Taylor
SI	Spark ignition
SMD	Sauter mean diameter
SOI	Start of injection
SparkCIMM	Spark channel ignition monitoring model
ST	Shock tube
TAB	Taylor analogy breakup
TDC	Top dead centre
TRF	Toluene reference fuel
UHC	Unburnt hydrocarbon
UNIFAC	UNIQUAC Functional-group Activity Coefficients
VPFR	Variable pressure flow reactor

NOMENCLATURE

Chemical Formulas

A1	Benzene
A1-	Phenyl radical
A2	Naphthalene
A2R5	Acenaphthene
A3	Phenanthrene
A4	Pyrene
A7	Coronene
C^*_{soot}	Radical of soot particle with an ‘armchair’ site
C_2H_2	Acetylene
C_2H_4	Ethylene
C_3H_3	Propargyl radical
C_4H_5	Butadienyl radical
$C_6H_5CH_2$	Benzyl radical
$C_6H_5CH_2O$	Alkoxy benzyl radical
$C_6H_5CH_3$	Toluene
C_7H_{16}	n-Heptane
C_8H_{17}	Octyl radical
C_8H_{18}	Isooctane
CH_3	Methyl radical
CH_4	Methane
CO	Carbon monoxide
CO_2	Carbon dioxide
$C_{soot}H$	Soot particle with an ‘armchair’ site
H	Hydrogen atom
H_2O	Water molecule
H_2O_2	Hydrogen peroxide
HO_2	Hydroperoxyl radical
NO	Nitric oxide
O	Oxygen atom
O_2	Oxygen
OH	Hydroxyl

Latin Symbols

a	Polynomial coefficient [-]
A	Area [m^2]; Pre-exponential factor [Varies]
A_s	Surface area [m^2]
AVGD	Average soot diameter [m]
B	Spalding transfer number [-]
B	Model constant [-]
Bo_l	Liquid film Bond number [-]
c_p	Constant-pressure specific heat capacity [J kg^{-1} K^{-1}]
C	Model constant [-]; ROP [mol m^{-3} s^{-1}]; Scale factor [-]
$\overline{C}^d$ ($\overline{C}^p$)	Normalised ROP for species destruction (production) [-]
D	Droplet diameter [m]; Soot diameter [m]
D_l	Mass diffusion coefficient [m^2/s]
D_m	Molecular diffusivity [m^2/s]
D^T	Thermal diffusion coefficient [kg m^{-1} s^{-1}]
E_a	Activation energy [cal/mol]
f	Distribution [-]; Function [-]
F	Residual vector [Varies]
$\mathbf{F}_{am}$	'Virtual mass' force vector [N]
$\mathbf{F}_b$	General body force vector [N]
$\mathbf{F}_{dr}$	Drag force vector [N]
F_h	Diffusional energy flux [J m^{-2} s^{-1}]
F_m	Diffusional flux component [kg m^{-2} s^{-1}]
$\mathbf{F}_p$	Pressure force vector [N]
FR	Force ratio [-]
FV	Total soot volume fraction [-]
g_i ($\mathbf{g}$)	Gravitational acceleration (vector) [m/s^2]
h	Film thickness [m]; Specific enthalpy [J/kg]
h_{fg}	Latent heat of phase change [J/kg]
H	Heat of formation [J/kg]; Molar enthalpy [J/mol]
j	Diffusive mass flux [J/kg]
k	Thermal conductivity [J m^{-1} s^{-1} K^{-1}]; Turbulence kinetic energy [m^2/s^2]; Rate constant [Varies]
k_{RT}	Wave number [1/m]
K	Critical number [-]; Dimensionless parameter [-]; Equilibrium constant [Varies];

K_g	Mass transfer coefficient [-]
L_b	Breakup length [m]
$\dot{m}$	Mass flow rate [kg/s]
$\dot{m}_{con}$	Condensation/evaporation rate [kg/s]
$\dot{m}_{imp}$	Mass source/sink per unit area [kg m^{-2} s^{-1}]
MSOOT	Total mass density [kg/m^3]
n	Temperature exponent [-]
n	Vector normal to film surface [-]
n_r	Number of rotations of crankshaft [-]
N_R (N_S)	Number of reactions (species) [-]
Oh	Ohnesorge number [-]
p	Pressure [Pa]
p_v	Partial pressure [Pa]
P	Molar production [mol m^{-3} s^{-1}]
q	Empirical parameter [-]; Energy flux [J m^2 s^{-1}]; Rate of progress [Varies]
Q	Heat energy [J/s]; Mass fraction [-]
$\dot{Q}_{imp}$	Enthalpy source [J m^{-2} s^{-1}]
$\dot{Q}_{rad}$	Radiative heat loss [J/s]
R	Universal gas constant [J mol^{-1} K^{-1}]
Re	Reynolds number [-]
$R_{r,k}$	Fraction of outflow [-]
Sc	Schmidt number [-]
s	Source component [Varies]
s_{ij} (S_{ij})	Rate of strain tensor [1/s] (Mean strain [-])
s_L	Laminar flame speed [m/s]
$\dot{s}$	Molar surface production rate [mol m^{-2} s^{-1}]
S	Source term [Varies]; Molar entropy [J mol^{-1} K^{-1}]
t	Time [s]
T	Temperature [K]; Torque [N m]
T^*	Dimensionless temperature [-]
T_0 (T_c) (T_W)	Reference (Critical) (Wall) temperature [K]
T_L	Leidenfrost temperature [K]
T_N	Nukiyama temperature [K]
TOTN	Total number density of soot [1/m^3]
u (**u**)	Velocity (vector) [m/s]

$\mathbf{U}$	Local average velocity vector [m/s]
U_{sys}	Total internal energy [J]
v	Specific molar volume [m^3 kg^{-1} mol^{-1}]
$\mathbf{v}$	Velocity vector [m/s]
V	Volume [m^3]
V_c (V_j) ($V_{o,j}$)	Correction (Diffusion) (Ordinary diffusion) velocity [m/s]
$w_{j,i}$	First-order sensitivity coefficient matrix [-]
We	Weber number [-]
W	Molecular weight [kg/mol]; Thermal diffusion velocity [m/s]
x	Cartesian coordinate [m]; Empirical parameter [-]
X	Mole fraction [-]
[X]	Molar concentration [mol/m^3]
Y	Mass fraction [-]

Greek Symbols

α	Model parameter [Varies]
β	Model coefficient [-]
Γ	Gamma function [-]
γ	Model coefficient [-]
δ_{ij}	'Kronecker delta' [-]
$\hat{\delta}$	Unit tensor [-]
Δ	Change [-]
$\Delta\mathbf{U}^2$	Gas/film relative velocity [m^2/s^2]
δ	Dirac delta function [-]
ε	Turbulence dissipation rate [m^2/s^3]
η_0	Model coefficient [-]
θ	Corner angle [rad]
Θ_j	Thermal diffusion ratio [-]
κ	Bulk viscosity [Pa s]
λ_r	Resonance wavelength [m]
Λ_{KH} (Λ_{RT})	Wavelength associated with KH (RT) [m]
μ (μ_t)	Dynamic (Turbulent) viscosity [Pa s]
ξ	Local coordinate normal to the wall [m]
ρ	Density [kg/m^3]
σ	Surface tension [N/m]; Turbulent Prandtl number [-]

τ	Momentum flux [kg m^{-1} s^{-2}]; Residence time [s]; Stress tensor [N/m^2]
τ_{KH} (τ_{RT})	Characteristic KH (RT) breakup timescale [s]
υ	Stoichiometric coefficient [-]
ϕ	Equivalence ratio [-]
ϕ_m	Viscosity [Pa s]; Thermal conductivity [J m^{-1} s^{-1} K^{-1}]; Molecular diffusivity [m^2/s]
φ	Vector of temperature [K] or mass fraction [-]
ω	Reaction rate [1/s]
ω_{RT} (Ω_{KH})	Maximum growth rate of RT (KH) [1/s]
$\dot{\omega}$	ROP [mol m^{-3} s^{-1}]
Ω	Source term [1/s]

Other Symbols

$\nabla \mathbf{v}$	Dyadic product [Varies]
$(\nabla \mathbf{v})^T$	Transpose of dyadic product [Varies]
$\emptyset$	Solution vector [Varies]
$\bar{}$	Ensemble-averaged [Varies]

Subscripts and Superscripts

’	Fluctuation; Forward
”	Reverse
∞	Surroundings
atm	Atmospheric
bg	Background
coag	Coagulation
cond	PAH condensation
d	Droplet; Engine displacement
f	Forward
g	Gas state; Group
h	Energy
i	Component; Direction; Inlet; Order; Reaction; Section; Species
int	Interface
j	Cell; Component; Dependent variable; Direction; Species

k	Direction; Reactor
l	Liquid film; Liquid state
m	Component; Mass; Material; Mean
max	Maximum
min	Minimum
n	Order; Time-step
o	Saturation; Standard state
ox	Oxidation
pi	Particle inception
r	Reactor; Reverse
s	Surface
sg	Surface growth
t	Thermal

LIST OF FIGURES

Figure 1-1 Classification of GDI combustion systems [4]. 2
Figure 1-2 Operating modes of GDI engines within the speed-load domain [5]. 2
Figure 1-3 Number and mass emissions of PM from light-duty passenger vehicles measured over the New European Driving Cycle [7]. 3
Figure 1-4 Schematic representation of main phases of the present work with research objectives. 8
Figure 2-1 Flowchart illustrating the influence of chemical kinetic mechanisms of gasoline fuel on CFD modelling in GDI engines particularly soot processes. 10
Figure 2-2 (a) Homogeneous and (b) stratified charge formation in GDI engines [134]. 26
Figure 2-3 Steps in soot formation process from gas phase to solid particles [151]. 33
Figure 3-1 KHRT breakup process schematic. 63
Figure 3-2 Transition criteria of the Bai-ONERA model for a (a) dry wall and a (b) wetted wall [199]. 66
Figure 3-3 Sequential steps of the DMZ method within the Detailed Chemistry model. 69
Figure 3-4 Schematic of soot diameter distribution within 20 sections. 71
Figure 4-1 TRF mechanisms represented in terms of numbers of species and reactions. 76
Figure 4-2 Validation criteria established based on the GDI engine combustion mode and operating conditions. 79
Figure 4-3 Measured [205] and computed ID times of RD387 at pressures of (a) 20 bar and (b) 55 bar with equivalence ratios of (i) 0.5, (ii) 1 and (iii) 2. 82
Figure 4-4 Measured [205] and computed ID times of Surrogate A at pressures of (a) 20 bar and (b) 55 bar with equivalence ratios of (i) 0.5, (ii) 1 and (iii) 2. 84
Figure 4-5 Measured [205] and computed ID times of Surrogate B at pressures of (a) 20 bar and (b) 55 bar with the equivalence ratio of 1. 85
Figure 4-6 Computed ID times of RD387 at pressures of 20 bar and 55 bar with the equivalence ratio of 1 for temperatures ranging from 650 K to 1350 K. 85
Figure 4-7 Measured [206] and computed ID times of (a) PRF 80 and (b) PRF 90 at the pressure of 40 bar with the equivalence ratio of 1. 86

Figure 4-8 Measured [213] and computed flame speeds of CR-87 at the pressure of 1 bar and initial temperatures of (a) 353 K and (b) 500 K. 88
Figure 4-9 Measured [214] and computed flame speeds of TAE7000 and its surrogate at the pressure of 1 bar and initial temperature of 358 K. 89
Figure 4-10 Measured [215] and computed flame speeds of different PRF under the stoichiometric condition with the pressure of 1 bar and initial temperature of 298 K. 90
Figure 4-11 Measured [216] and computed flame speeds of PRF 87 at the initial temperature of 373 K and pressures of (a) 10 bar, (b) 15 bar, (c) 20 bar and (d) 25 bar. 90
Figure 4-12 Measured [219] and computed speciation profiles in the rich premixed flame of isooctane at atmospheric pressure and equivalence ratio of 1.9. 92
Figure 4-13 Measured [219] and computed speciation profiles in the rich premixed flame of n-heptane at atmospheric pressure and equivalence ratio of 1.9.....92
Figure 4-14 Measured [220] and computed speciation profiles in the rich premixed flame of n-heptane at atmospheric pressure and equivalence ratio of 2.1.....93
Figure 4-15 Measured [222] and computed speciation profiles of stoichiometric PRF 90 in the JSR at the pressure of 10 bar and mean residence time of 1 s.....95
Figure 4-16 Normalised sensitivity coefficients for the ID time of RD387 at the pressure of 55 bar, temperature of 1000 K and equivalence ratio of 1 for (a) Jiao-TRF, (b) Wang-TRF and (c) An-TRF. 97
Figure 4-17 Normalised sensitivity coefficients for the laminar flame speed of CR-87 at atmospheric pressure, initial temperatures of 353 K and 500 K and equivalence ratio of 1 for (a) Jiao-TRF, (b) Wang-TRF and (c) An-TRF. 99
Figure 4-18 ROP of A1 for the rich premixed flame of n-heptane as a function of HAB at atmospheric pressure and equivalence ratio of 2.1 for (a) Jiao-TRF, (b) Wang-TRF and (c) An-TRF. 101
Figure 5-1 Schematic diagram of the engine test rig [228]. 107
Figure 5-2 Classic grid of equally-spaced speed-load points studied experimentally. 108
Figure 5-3 Valve timing diagrams including the injection and ignition events for the five part-load operating conditions examined experimentally. 110
Figure 5-4 Modelled fuel injection profiles for all the operating conditions studied. 114

Figure 5-5 Illustration of CFD sub-models adopted along with the geometrical parts of the GDI engine. 115
Figure 5-6 General framework in validating combustion and emission modelling. 120
Figure 5-7 Measured and computed spray tip penetration length as a function of time after SOI at the injection pressure of 120 bar over the period of 0.32 ms. 122
Figure 5-8 Computed in-cylinder (a) pressure, (b) temperature and (c) fuel mass as a function of CAD when the fuel is represented as isooctane and TRF surrogate. 123
Figure 5-9 Computed (a) mass of fuel evaporated and (b) mass of liquid film as a function of CAD when the fuel is represented as isooctane and TRF surrogate. 124
Figure 5-10 Computed number density and mass density of soot at EVO when the fuel is represented as isooctane and TRF surrogate. 124
Figure 5-11 Computed in-cylinder (a) pressure, (b) rate of change of pressure, (c) temperature and (d) mass of fuel species as a function of CAD when the Detailed Chemistry model is activated at SOI and at the onset of SI. 126
Figure 5-12 Computed in-cylinder (a) pressure, (b) temperature and (c) change in fuel mass for different ways of group construction in the DMZ partitioning method. 130
Figure 5-13 Computed (a) number density and (b) mass density of soot at different CAD ATDC for different ways of group construction in the DMZ partitioning method. 131
Figure 5-14 Measured and computed in-cylinder (a) pressure and (b) rate of change of pressure for the reference case. 133
Figure 5-15 Computed (a) number density and (b) mass density of soot for the reference case along with the experimental data compared at EVO. 135
Figure 5-16 Measured and computed number-weighted PSDF normalised with total number density of soot for the reference case. 137
Figure 6-1 In-cylinder flow velocity at (a) maximum lift of intake valve and (b) SOI for engine speeds of (i) 1600 rpm, (ii) 2300 rpm and (iii) 3000 rpm. 141
Figure 6-2 (a) Tumble velocity and (b) turbulence kinetic energy as a function of CAD for different engine speeds. 142
Figure 6-3 (a) SMD of fuel droplets and (b) ratio of fuel evaporated to fuel injected as a function of CAD for different engine speeds. 143
Figure 6-4 In-cylinder distributions of equivalence ratio at (a) 10 CAD and (b) 20 CAD after SOI for engine speeds of (i) 1600 rpm, (ii) 2300 rpm and (iii) 3000 rpm. 144

Figure 6-5 Total mass of liquid fuel film formed within the cylinder as a function of CAD for different engine speeds. 145
Figure 6-6 Proportions of total film mass formed on combustion dome, piston crown and cylinder wall as a function of CAD after the respective SOI of different engine speeds. 146
Figure 6-7 In-cylinder (a) flow velocity and (b) distribution of equivalence ratio at 90 CAD BTDC during the compression stroke for engine speeds of (i) 1600 rpm, (ii) 2300 rpm and (iii) 3000 rpm. 148
Figure 6-8 Measured and computed in-cylinder pressures for different engine speeds. 149
Figure 6-9 In-cylinder distributions of equivalence ratio at SI timing for engine speeds of (a) 1600 rpm, (b) 2300 rpm and (c) 3000 rpm. 150
Figure 6-10 Computed in-cylinder temperatures for different engine speeds. 151
Figure 6-11 In-cylinder temperature contours for engine speeds of (a) 1600 rpm, (b) 2300 rpm and (c) 3000 rpm at (i) 40 CAD, (ii) 60 CAD and (iii) 80 CAD after SI. 152
Figure 6-12 Measured and computed (a) number density and (b) mass density of soot and their normalised values based on the reference case for different engine speeds. 153
Figure 6-13 Measured and computed number-weighted PSDF normalised with total number density of soot at engine speeds of (a) 1600 rpm and (b) 3000 rpm. 154
Figure 6-14 In-cylinder distributions of number density of soot for engine speeds of (a) 1600 rpm, (b) 2300 rpm and (c) 3000 rpm at (i) 40 CAD, (ii) 60 CAD and (iii) 80 CAD after SI. 156
Figure 6-15 In-cylinder distributions of mass density of soot for engine speeds of (a) 1600 rpm, (b) 2300 rpm and (c) 3000 rpm at (i) 40 CAD, (ii) 60 CAD and (iii) 80 CAD after SI. 157
Figure 6-16 Computed in-cylinder (a) number of soot particles and (b) soot mass as a function of CAD up to EVO for different engine speeds. 158
Figure 6-17 In-cylinder flow velocity at (a) SOI and (b) 90 CAD BTDC for engine loads of (i) 60 N m, (ii) 90 N m and (iii) 120 N m. 160
Figure 6-18 In-cylinder pressure at intake manifold, SOI and 50–200 CAD after SOI for different engine loads. 161

Figure 6-19 (a) Swirl ratio and (b) turbulence kinetic energy as a function of CAD for different engine loads. 161
Figure 6-20 (a) SMD of fuel droplets and (b) mass of fuel evaporated as a function of CAD for different engine loads. 162
Figure 6-21 In-cylinder distributions of equivalence ratio at (a) 10 CAD and (b) 20 CAD after SOI for engine loads of (i) 60 N m, (ii) 90 N m and (iii) 120 N m. 164
Figure 6-22 Total mass of liquid fuel film formed within the cylinder as a function of CAD for different engine loads. 165
Figure 6-23 Proportions of total film mass formed on combustion dome, piston crown and cylinder wall as a function of CAD after the respective SOI of different engine loads. 166
Figure 6-24 In-cylinder distributions of liquid film expressed in film thickness at the respective maximum film mass for engine loads of (a) 60 N m, (b) 90 N m and (c) 120 N m. 166
Figure 6-25 Proportions of total film mass formed on combustion dome, piston crown and cylinder wall at the respective maximum film mass for different engine loads. 167
Figure 6-26 Measured and computed in-cylinder pressures for different engine loads. 168
Figure 6-27 In-cylinder distributions of equivalence ratio at SI timing for engine loads of (a) 60 N m, (b) 90 N m and (c) 120 N m. 169
Figure 6-28 Fuel droplets coloured by their diameters at SI timing for engine loads of (a) 60 N m, (b) 90 N m and (c) 120 N m. 170
Figure 6-29 Computed in-cylinder temperatures for different engine loads. 171
Figure 6-30 In-cylinder temperature contours for engine loads of (a) 60 N m, (b) 90 N m and (c) 120 N m at (i) 40 CAD, (ii) 60 CAD and (iii) 80 CAD after SI. 172
Figure 6-31 Measured and computed (a) number density and (b) mass density of soot and their normalised values based on the reference case for different engine loads. 173
Figure 6-32 Measured and computed number-weighted PSDF normalised with total number density of soot at engine loads of (a) 60 N m and (b) 120 N m. 174
Figure 6-33 In-cylinder distributions of number density of soot for engine loads of (a) 60 N m, (b) 90 N m and (c) 120 N m at (i) 40 CAD, (ii) 60 CAD and (iii) 80 CAD after SI. 176

Figure 6-34 In-cylinder distributions of mass density of soot for engine loads of (a) 60 N m, (b) 90 N m and (c) 120 N m at (i) 40 CAD, (ii) 60 CAD and (iii) 80 CAD after SI. 177
Figure 6-35 Computed in-cylinder (a) number of soot particles and (b) soot mass as a function of CAD up to EVO for different engine loads. 178
Figure 7-1 Computed number density of soot plotted against mass density for all part-load operating points varying in engine speeds and loads..... 181
Figure 7-2 In-cylinder flow velocity at (a) maximum lift of intake valve and (b) IVC. 182
Figure 7-3 (a) Turbulence kinetic energy, (b) tumble ratio and swirl ratio as a function of CAD with IVO, SOI, EOI and SI timings indicated. 183
Figure 7-4 In-cylinder (a) flow velocity and (b) distribution of equivalence ratio superimposed with fuel droplets injected at (i) SOI, (ii) 10 CAD after SOI and (c) EOI. 185
Figure 7-5 Total mass of liquid fuel film formed and the respective proportions on combustion dome, piston crown and cylinder wall as a function of CAD with SOI and EOI timings indicated. 186
Figure 7-6 In-cylinder distributions of equivalence ratio superimposed with fuel droplets injected at (a) 30 CAD, (b) 40 CAD, (c) 50 CAD, (d) 60 CAD, (e) 80 CAD and (f) 100 CAD after SOI. 187
Figure 7-7 (a) Laser-induced fluorescence of liquid and gaseous phases of fuel and (b) simulated fuel mass fraction at (i) 40 CAD, (ii) 70 CAD, (iii) 160 CAD and (iv) 210 CAD after their respective SOI timings. 188
Figure 7-8 Fuel droplets coloured by their diameters at SI timing. 189
Figure 7-9 In-cylinder distributions of equivalence ratio across three cross-sectional planes at SI timing. 190
Figure 7-10 In-cylinder distributions of (a) temperature, mass fractions of (b) OH radicals, (c) C_2H_2, (d) C_2H_4, (e) A1, (f) A2, (g) A3 and (h) A4 at 5 CAD after SI. 191
Figure 7-11 In-cylinder distributions of (a) temperature, mass fractions of (b) OH radicals, (c) C_2H_2 and (d) A4, (e) number density and (f) mass density of soot at 19 CAD after SI. 193
Figure 7-12 In-cylinder (a) mass of C_2H_2 and A4 and (b) number of soot particles and soot mass as a function of CAD. 194

Figure 7-13 In-cylinder distributions of (a) temperature, mass fractions of (b) OH radicals, (c) C_2H_2 and (d) A4, (e) number density and (f) mass density of soot at 40 CAD after SI. 196
Figure 7-14 In-cylinder distributions of (a) temperature, mass fractions of (b) OH radicals, (c) C_2H_2 and (d) A4, (e) number density and (f) mass density of soot at 60 CAD after SI. 197
Figure 7-15 In-cylinder distributions of (a) temperature, mass fractions of (b) OH radicals, (c) C_2H_2 and (d) A4, (e) number density and (f) mass density of soot at 80 CAD after SI. 198
Figure 7-16 Conceptual model describing the ultra-fine PM processes in the wall-guided GDI engine. 199
Figure 7-17 In-cylinder distributions of fuel droplets injected for SOI timings at (a) 39 CAD, (b) 59 CAD and (c) 79 CAD ATDC at (i) 10 CAD, (ii) 20 CAD and (iii) 30 CAD after SOI. 202
Figure 7-18 Proportions of total film mass formed on combustion dome, piston crown and cylinder wall as a function of CAD after SOI for different SOI timings..... 203
Figure 7-19 Total mass of liquid fuel film formed within the cylinder as a function of CAD for different SOI timings. 203
Figure 7-20 In-cylinder distributions of (a) equivalence ratio and (b) fuel droplets coloured by their diameters at SI timing for SOI timings at (i) 39 CAD, (ii) 59 CAD and (iii) 79 CAD ATDC. 204
Figure 7-21 In-cylinder pressures and temperatures for different SOI timings. 205
Figure 7-22 In-cylinder mass of C_2H_2 and A4 as a function of CAD for different SOI timings. 205
Figure 7-23 (a) Number density and mass density of soot at EVO timing and (b) their normalised values based on the reference case for different SOI timings..... 206
Figure 7-24 In-cylinder distributions of (a) equivalence ratio and (b) fuel droplets coloured by their diameters at SI timings at (i) 35 CAD, (ii) 25 CAD and (iii) 15 CAD BTDC. 209
Figure 7-25 In-cylinder pressures and temperatures for different SI timings. 209
Figure 7-26 In-cylinder mass of C_2H_2 and A4 as a function of CAD for different SI timings. 210
Figure 7-27 (a) Number density and mass density of soot at EVO timing and (b) their normalised values based on the reference case for different SI timings. 211

Figure 7-28 In-cylinder mass of fuel and oxygen as a function of CAD for different EGR rates.....213
Figure 7-29 Total mass of liquid fuel film formed within the cylinder as a function of CAD for different EGR rates.....214
Figure 7-30 In-cylinder distributions of (a) equivalence ratio and (b) fuel droplets coloured by their diameters at SI timing for EGR rates at (i) 0%, (ii) 5% and (iii) 10%. 215
Figure 7-31 In-cylinder pressures and temperatures for different EGR rates. 215
Figure 7-32 In-cylinder mass of C_2H_2 and A4 as a function of CAD for different EGR rates.....216
Figure 7-33 (a) Number density and mass density of soot at EVO timing and (b) their normalised values based on the reference case for different EGR rates. 217
Figure 7-34 Effects of operating parameters on number density and mass density of soot segregated into four zones based on an increase or a decrease.....220

LIST OF TABLES

Table 2-1 Approximate ranges of hydrocarbons found in commercial gasoline [26]. 11
Table 2-2 Advantages and disadvantages of PRF and TRF reaction mechanisms. ..13
Table 2-3 Bibliographic compilation of the available TRF mechanisms for gasoline. 15
Table 2-4 Multi-dimensional CFD combustion modelling of GDI engines with optical and/or experimental validations.....21
Table 2-5 Relevant combustion models applied within GDI engine configurations.28
Table 2-6 Concise description of soot models adapted for soot modelling studies in GDI engines. 38
Table 3-1 Required chemical data in a reaction mechanism to run kinetic simulations in Chemkin-Pro. 48
Table 3-2 Descriptions of reactor models in Chemkin-Pro used to evaluate the chemical kinetics of reaction mechanisms. 51
Table 3-3 Coefficients of RNG k-ε model derived numerically and empirically. 61
Table 3-4 0D and 1D models in Chemkin-Pro used for chemical kinetic simulations. 73
Table 3-5 CFD sub-models in STAR-CD adopted for 3D engine simulations. 74
Table 4-1 Potential reduced TRF mechanisms identified. 76
Table 4-2 Adapted rate coefficients for two reactions of isooctane under An-TRF. 77
Table 4-3 Experimental specifications of ST studies of fuel components and mixtures relevant to gasoline fuels used as validation conditions. 80
Table 4-4 Compositions of TRF surrogates for RD387, Surrogate A and Surrogate B. 81
Table 4-5 Experimental specifications of flame speed studies of fuel components and mixtures relevant to gasoline fuels used as validation conditions. 87
Table 4-6 Experimental specifications of laminar premixed flames of fuel components relevant to gasoline fuels used as validation conditions. 91
Table 4-7 Experimental specifications of JSR experiments of fuel components and mixtures relevant to gasoline fuels used as validation conditions. 94
Table 4-8 Selected engine-like operating conditions for chemical kinetic analyses. 96

Table 4-9 Summary of chemical kinetic validations on the three TRF mechanisms at important operating conditions. 103
Table 5-1 Fuel properties of 95 RON reference gasoline. 106
Table 5-2 Technical specifications of the GDI test engine. 106
Table 5-3 Detailed information on fuel injection and SI events from the experiment. 109
Table 5-4 Intake and exhaust valve timings from the experiment. 109
Table 5-5 Average pressures and temperatures during intake and exhaust phases from the experiment. 111
Table 5-6 Time-step sizes employed for different in-cylinder engine events. 112
Table 5-7 Boundary conditions in terms of designated temperatures for different regions of the cylinder, ports and valves. 113
Table 5-8 Comparisons of the 3-zone ECFM and the Detailed Chemistry model as combustion models. 116
Table 5-9 Comparisons between computing facilities and the associated costs for 3D engine modelling. 121
Table 5-10 Predicted SMD in the present work compared to reported experimental values of SMD. 122
Table 5-11 Computed peak pressure and temperature when Detailed Chemistry model is activated at SOI and at the onset of SI with the computational time required. 127
Table 5-12 Flow variables proposed as criteria for group construction in the DMZ partitioning method. 128
Table 5-13 Setting of group construction for the DMZ partitioning method. 129
Table 5-14 Computed peak pressure, temperature and their locations as well as number density and mass density of soot at EVO for different ways of group construction in the DMZ partitioning method. 131
Table 6-1 Measured and computed peak pressures and their locations in CAD for different engine speeds. 149
Table 6-2 BMEP at different engine loads with the fixed engine speed of 2300 rpm. 159
Table 6-3 Measured and computed peak pressures and their locations in CAD for different engine loads. 168
Table 6-4 Main changes in operating parameters, in-cylinder conditions and engine phenomena as a result of varying engine speed and load from the reference case. 179

Table 7-1 Parametric sweep of SOI timing at engine speed of 2300 rpm and engine load of 90 N m. 201
Table 7-2 Parametric sweep of SI timing at engine speed of 2300 rpm and engine load of 90 N m. 208
Table 7-3 Parametric sweep of EGR rate at engine speed of 2300 rpm and engine load of 90 N m. 213
Table 7-4 Summary of key changes in in-cylinder conditions contributing to PM emissions with respect to the variations in operating parameters. 220

CHAPTER 1
INTRODUCTION

1.1 Background

Extensive research and development efforts have been carried out in the past decades to enhance performance of internal combustion engines (ICE) of automobile vehicles globally. Among the technological advances accomplished, gasoline direct injection (GDI) engines hold practical potential to achieve a substantial improvement between 5% and 15% in fuel economy within the short term [1]. In a GDI engine, the fuel is pressurised and injected via a common rail fuel line system into the combustion chamber of each cylinder directly as opposed to the conventional multi-point port fuel injection (PFI) [2]. The incorporation of direct injection strategy of fuel into a spark ignition (SI) engine offers minimised pumping loss, higher compression ratio, reduced knock tendency and improved transient response. The benefits over PFI engines are mainly attained through removal of throttling mechanism and precise control of air-fuel ratio [3].

GDI combustion systems are classified into spray-guided, wall-guided and air-guided based on the manners by which an ignitable mixture is formed near spark plug during part load operations [4] as distinguished in Figure 1-1. Typically, fuel stratification is achieved by combinations of the three approaches with varying relative contributions [3]. From Figure 1-2, GDI engines operate in stratified, homogeneous lean and homogeneous stoichiometric modes depending on the speed-load points [5]. In the stratified lean operation, late injection of fuel during compression stroke maximises the fuel economy due to reduced throttling loss and lower heat loss [3]. Nonetheless, homogeneous operation which requires early injection strategy during intake stroke covers the majority of the engine operating map, particularly at high-speed and high-load conditions.

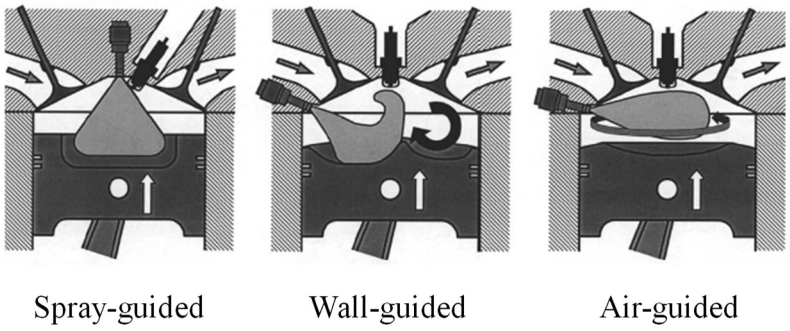


Figure 1-1 Classification of GDI combustion systems [4].

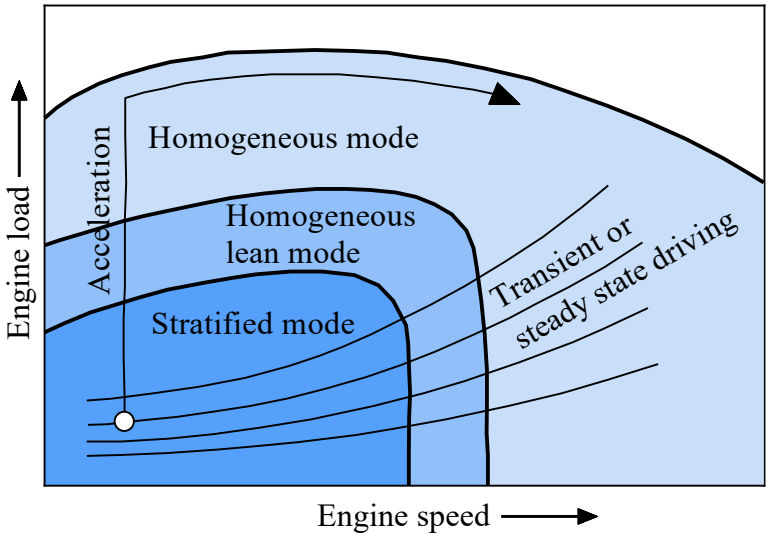


Figure 1-2 Operating modes of GDI engines within the speed-load domain [5].

1.1.1 Association of GDI Engines with Ultra-Fine Particulate Matter

Despite the sound advantages of GDI technology, continuing research works have, relatively recently, identified GDI engines as a prominent source of anthropogenic ultra-fine particulate matter (PM) in the atmosphere. Under the Particle Measurement Programme, it was demonstrated that both number and mass emissions of PM from GDI engines are higher than those of conventional PFI engines and diesel engines fitted with diesel particulate filters (DPF) [6]. Similar trends in PM emissions from light-duty passenger vehicles were also reported by Braisher et al. [7] over the New European Driving Cycle as displayed in Figure 1-3. It is noted that the difference in number emission of PM between the GDI engine and its PFI counterpart is as much as one order of magnitude.

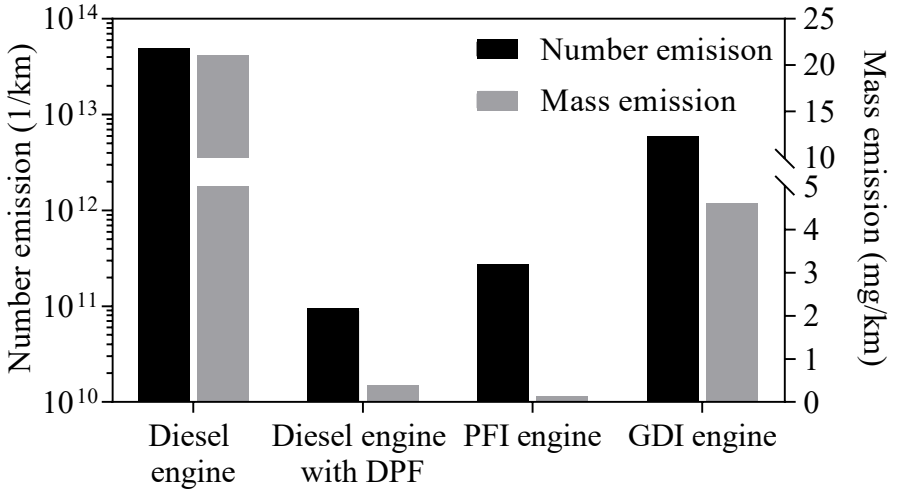


Figure 1-3 Number and mass emissions of PM from light-duty passenger vehicles measured over the New European Driving Cycle [7].

PM emissions are essentially a complex mixture of volatile species including nitrates, sulphates and organic elements and non-volatile solid components with carbonaceous fractions and ash [8]. Analysis of exhaust emissions from light-duty GDI vehicles reveals that the composition of PM is dominated by elemental carbon [9] (up to 92% of total carbon content on average [10]) which is more commonly known as soot. Characterised by diameters less than 100 nm, the airborne ultra-fine particles pose elevated health risks to the public. Upon inhalation, particle deposition along the respiratory tracts leads to potential development of asthma, pulmonary inflammation and adverse cardiovascular and neurodegenerative effects as evidenced in numerous medical studies [11–13].

Consequently, it comes as no surprise that progressively more stringent legislations are being implemented to monitor the engine-out exhausts. In Europe, the 5 mg/km limit of PM was imposed on GDI engines in 2009 under the Euro 5 emission standard. Recognising the weight of GDI vehicles in emitting PM, the newer Euro 6 standard tightens the mass limit to 4.5 mg/km and restricts the number emission to 6×10^{11}/km whereby the limits are expected to take full effect by 2020 [14]. It remains unclear whether additional internal engine improvements will suffice to comply with the anticipated emission requirements under real world driving operations. To facilitate the quest for strategy optimisation in PM mitigation, fundamental knowledge on PM processes within the GDI engine configurations is both imperative and timely.

1.1.2 Current Understanding of PM Formation within GDI Engines

Advanced optical techniques such as high-speed imaging, two-colour pyrometry [15], laser-induced fluorescence [16] and laser-induced incandescence [17] are employed to visualise the combustion and PM processes in GDI engines. Concurrently, sampling and measurement systems are continually upgraded to provide detailed information on particle size distribution function (PSDF) and chemical composition of exhaust emissions. Many experimental studies [18–20] highlighted that the vast majority of soot particles (> 80%) falls in the diameter range of 10–100 nm whereas above 50% is emitted in nucleation mode with diameter below 50 nm. However, quantification of PM data downstream at the tailpipe lacks informative insights on in-cylinder events contributing to the formation mechanisms at the rudimental level.

To this end, numerical modelling through computational fluid dynamics (CFD) serves as a robust and cost-effective predictive tool to complement the experimental findings. Within the context, significant works in calibrating and developing CFD models have been performed to properly characterise spray formation, mixture preparation and combustion for GDI engines. In particular, current combustion models widely adopted for the GDI system (elaborated in Section 2.3.1) typically rely on pre-generated library tables from reaction kinetics of transportation fuels in lieu of direct computation of fuel chemistry. Thus, computational expedition provided by this approach comes at the expense of accuracy of the chemistry effects.

Contrariwise, modelling studies on PM emissions from GDI engines are scarce as compared to those conducted on diesel engines as a result of the relatively recently discovered association of the former to PM. Furthermore, adaptation of the existing knowledge from diesel combustion to understand PM formation in GDI engines is not straightforward. This is because of the inherent differences between diesel and GDI soot in terms of nanostructure [21], particle diameter [20] and number concentration [22] as pinpointed through transmission electron microscopy on the exhaust particles. Hence, there is a pressing need to expand the understanding of PM processes in GDI engines, specifically from a joint viewpoint of CFD and chemical kinetics, in order to formulate optimised operating strategies for PM abatement.

1.2 Aim and Objectives

The present work seeks to acquire in-depth insights on the formation mechanisms of ultra-fine PM in GDI engines through an integrated modelling approach which bridges the gap between CFD and chemical kinetics. In that regard, the four key research objectives to be accomplished are to:

i. *evaluate and validate reduced reaction mechanisms to emulate real gasoline fuels under GDI engine-like operating conditions*

   Accurate numerical modelling of engine combustion systems requires precise descriptions of chemical kinetics of fuels. For gasoline fuels, simple binary mixtures of primary reference fuel (PRF) comprising isooctane and n-heptane are commonly utilised to characterise their octane ratings. To take into account fuel sensitivity, toluene is included to form toluene reference fuel (TRF) as a representative for aromatics. The expanding knowledge base of fuel kinetics results in a large pool of TRF mechanisms, each with varying degrees of detail and intended applications.

   However, it is noted that most, if not all, of the reduced mechanisms of TRF are developed for the application of homogenous charge compression ignition (HCCI) engines. Thus, incorporating such mechanisms in GDI engines entails further evaluation and re-validation under the relevant operating conditions. Additionally, chemistry of polycyclic aromatic hydrocarbons (PAH) is crucial for soot formation. As GDI system is spark ignited, three reduced mechanisms (about 100 species) identified are primarily compared in terms of their high-temperature chemistry. Validation targets of ignition delay (ID) time, laminar flame speed and speciation profiles against experimental measurements of real fuels and multi-component surrogates are prioritised whenever available.

ii. *integrate chemical kinetics to CFD modelling of homogeneous stoichiometric combustion within a GDI engine and validate the approach across different speed-load points*

   Unlike the combustion models which depend on pre-tabulated chemistry, the optimal TRF mechanism selected is used to compute the chemistry effects on

the fly during CFD modelling of the engine cycle. Here, a complete set of CFD models is formulated to describe fuel injection and spray, flow and turbulence, fuel impingement, liquid film formation, ignition, combustion and emission under the homogeneous stoichiometric mode. Simulated results are validated against measured in-cylinder pressure, number density and mass density of PM emitted at the tailpipe of the GDI engine.

In particular, the sectional method which is more commonly applied in modelling simple flame configurations [23,24] and diesel combustion [25] is adopted to describe soot processes and capture the experimentally measured PSDF for the GDI engine. General versatility of the modelling approach is also verified across different speed-load points to explicate their effects on PM emissions. The range of engine speed is 1600–3000 rpm while engine load is varied by changing the corresponding torque from 60 N m to 120 N m.

iii. develop a fundamental conceptual model detailing the ultra-fine PM processes within a GDI engine operating in the homogeneous stoichiometric mode

Fundamental understanding in PM formation mechanisms in GDI engines is valuable in drafting control strategies for PM minimisation. Hence, to identify the dominant mechanisms with assigned relative significances, a conceptual model is proposed under the homogeneous stoichiometric operation. Starting at fuel injection, the sequence of in-cylinder events leading to the eventual emission stage is highlighted. The roles of engine phenomena are elucidated through changes in flow intensity, temporal developments of pressure and temperature and spatial distributions of critical chemical species and soot.

iv. study effects and sensitivities of engine operating parameters on PM emissions from a GDI engine operating in the homogeneous stoichiometric mode

Deriving thorough information on underlying effects of engine operating parameters on PM emissions based solely on engine-out measurements is difficult. Thus, numerical study on PM formation and emissions with respect to variations in engine operating parameters of the GDI engine is carried out. Three operating parameters examined are injection timing of fuel, ignition timing and exhaust gas recirculation (EGR) level. Correlations between in-

cylinder conditions and quantitative changes in number density and mass density of soot are established for each operating parameter. Results from the numerical simulations are corroborated through qualitative comparisons with relevant experimental findings.

Figure 1-4 summarises main phases of the present work schematically in line with the interconnected research objectives. The first phase aims to evaluate chemical kinetics of the TRF mechanisms under GDI engine-like operating conditions to identify the optimal one. Next, the mechanism is coupled with a complete set of CFD models to simulate homogeneous stoichiometric combustion in the GDI engine over the speed-load domain. Based on the computed results and data analyses, the conceptual model on PM processes is developed for the GDI engine. Such knowledge extracted is then applied to correlate in-cylinder conditions to PM emissions due to variations in the engine operating parameters.

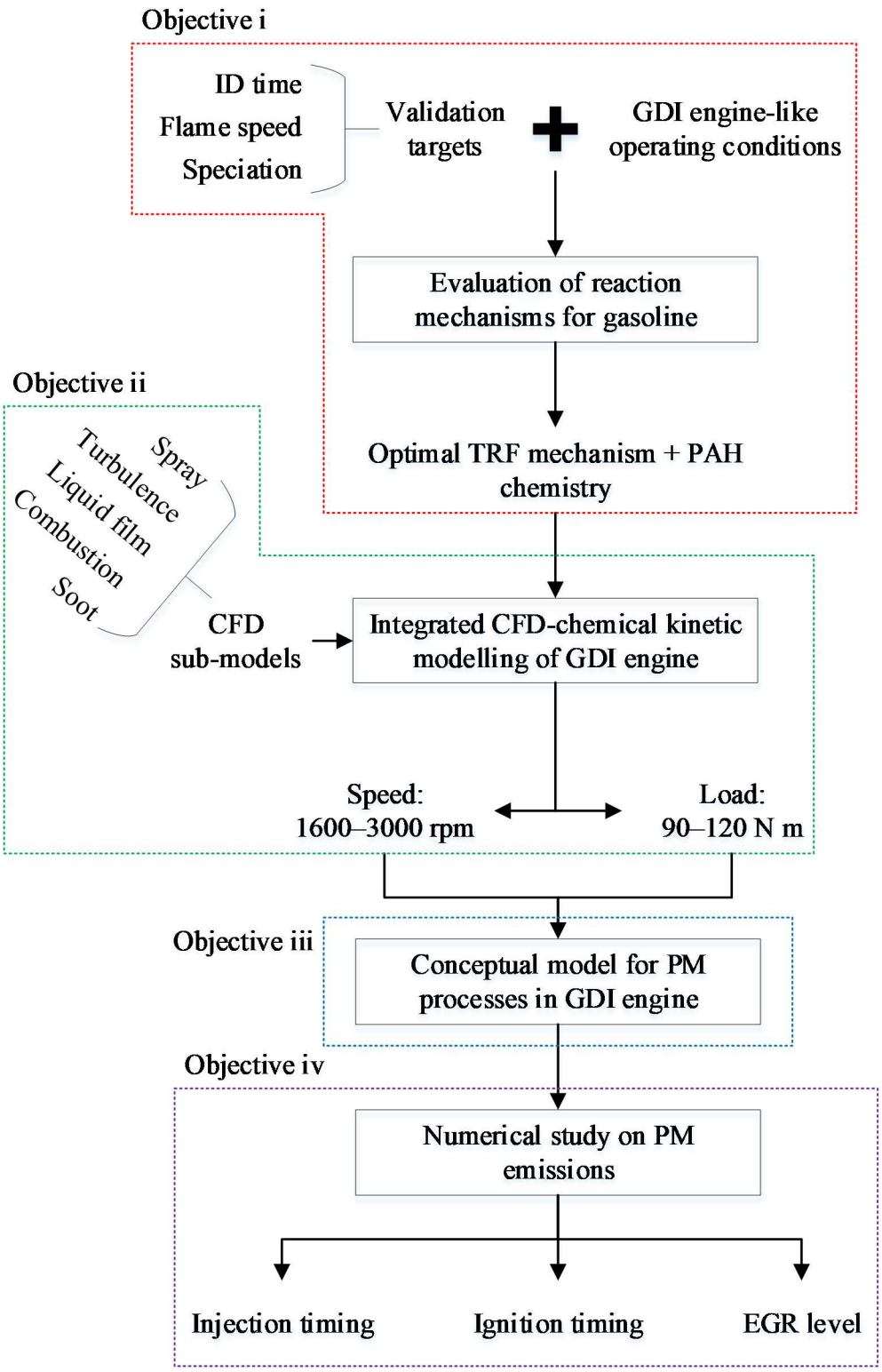


Figure 1-4 Schematic representation of main phases of the present work with research objectives.

1.3 Thesis Outline

The current chapter, Chapter 1 introduces the overview of GDI technology and reports the relatively recently identified connection to ultra-fine PM that motivates the present research work. The overall scope and specific objectives are also established. Set against this background, a comprehensive literature review is presented in Chapter 2 on development in chemical kinetic modelling of gasoline fuels and recent CFD modelling of GDI engines. Detailed and reduced reaction mechanisms of TRF are reviewed in terms of range of validity and applicability. Emphasis of engine modelling is placed on existing combustion and soot models with their limitations pinpointed.

Chapter 3 records the mathematical formulations and governing equations involved for chemical kinetics and CFD computations. Detailed specifications for sub-models of spray, turbulence, liquid film, combustion and soot are included. Chemistry of the identified TRF mechanisms is evaluated under a broad range of operating conditions pertinent to GDI engine operations in Chapter 4. Moreover, discrepancies in model predictions of validation targets are explained through chemical kinetic analyses. Numerical integration of the optimal TRF mechanism to CFD modelling of the GDI engine is discussed at length in Chapter 5, together with the validations against experimental data. Particularly, capability of the sectional method to estimate soot emitted and capture the associated PSDF is highlighted.

Subsequently, application of the integrated modelling approach at different engine speeds and loads is elaborated in Chapter 6. Upon validation, levels of PM emissions are attributed to engine phenomena induced by the changes in speed and load. Chapter 7 describes development of the conceptual model of PM processes within the GDI engine under the homogenous stoichiometric mode at the critical speed-load point. This is followed by an exhaustive numerical study on effects of the engine operating parameters on PM emissions. Correlations of PM formation based on the in-cylinder conditions are drawn for each operating parameter. Lastly, Chapter 8 summarises key findings and major conclusions from the research work undertaken with potential recommendations for future work suggested.

CHAPTER 2
LITERATURE REVIEW

2.1 Introductory Remarks

The present chapter reports on the recent developments in chemical kinetic modelling of gasoline fuels and CFD numerical studies for GDI engines, with emphasis on the combustion and emission stages. Regarding fuel kinetics, the use of PRF and TRF mechanisms as gasoline surrogates is discussed in Section 2.2. As detailed in Section 2.3, CFD modelling of GDI engines typically covers the simulations of spray, mixture formation, combustion and emission processes. The dependency of CFD simulations of in-cylinder events, especially soot modelling, on fuel chemical kinetics is illustrated in Figure 2-1. Progress in combustion modelling for both homogeneous and stratified charge modes is elaborated thoroughly. Still in its infancy, soot modelling studies for GDI engines are reviewed in which several soot models adapted from earlier studies on diesel combustion systems and flame configurations are appraised.

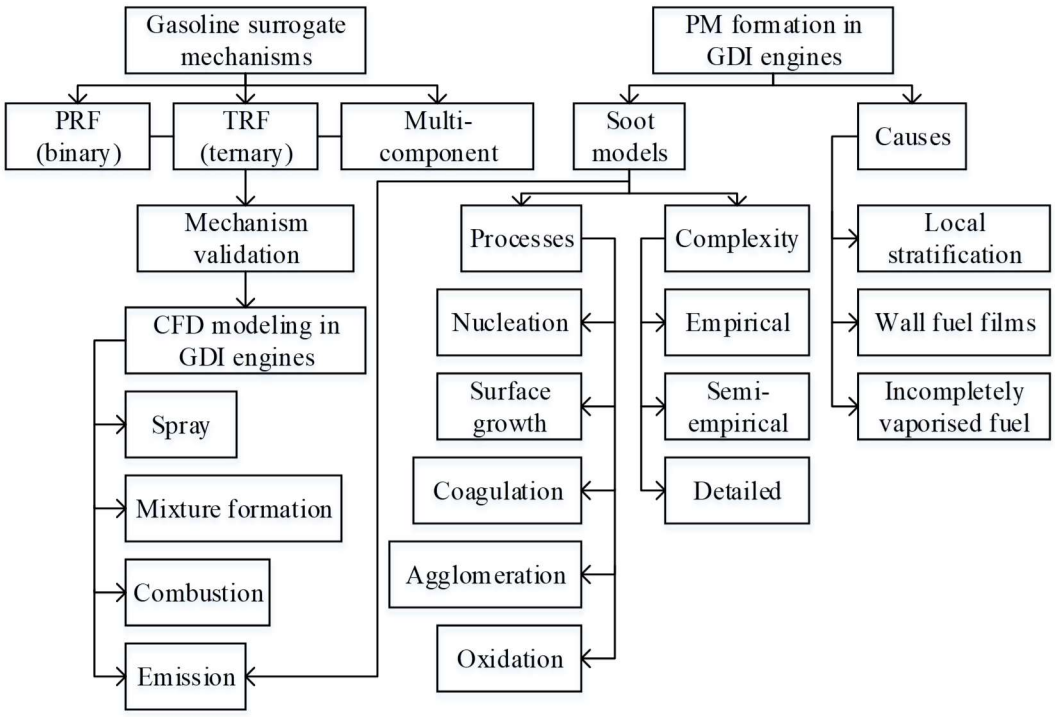


Figure 2-1 Flowchart illustrating the influence of chemical kinetic mechanisms of gasoline fuel on CFD modelling in GDI engines particularly soot processes.

2.2 Chemical Kinetic Modelling of Gasoline Fuels

Gasoline fuel is a complex mixture which consists of various hydrocarbon classes, ranging from linear and branched chain aliphatic compounds to aromatics. The boiling range components comprise paraffins, naphthenes (cycloparaffins) and aromatics mainly. Additional processing and upgrading are necessary to enable its utilisation in ICE. Typically, olefins are produced at the refinery and blended into the finished fuel in order to increase the octane rating [26]. A large variation in gasoline composition is observed across the market fuels, as illustrated in Table 2-1, which can be attributed to differences in crude sources as well as the relevant refinery, blending and finishing processes involved.

Table 2-1 Approximate ranges of hydrocarbons found in commercial gasoline [26].

Hydrocarbon class	Volume percentage (%)
Paraffins	32–80
Naphthenes	2–10
Olefins	2–18
Aromatics	10–44

The combustion behaviour of gasoline in engine applications can be observed through the integration of CFD tools and chemical kinetic models. However, due to the lack of understanding in the reaction kinetics of all gasoline components as well as their chemical interactions, it is not possible to model full blend gasoline in detailed kinetic studies currently. Also, the associated computational efforts and cost in modelling full gasoline is impractical [27]. Thus, it is common practice to develop surrogate mixtures which are capable of mimicking the actual behaviour of real fuels through simplified representations with a limited number of components. The surrogates are formulated in such a way that the physical properties and combustion behavioural targets such as composition, bulk burn duration and emissions can be reproduced with reasonable accuracy [26]. In fact, a reaction mechanism for these surrogate mixtures should retain its high-fidelity to model individual fuel components apart from being capable to emulate the combustion characteristics of practical fuels appropriately [28].

In developing the fuel surrogates, the approach utilised widely involves identifying an individual species for each class of hydrocarbon present, with the assumption that its kinetic behaviour resembles others having similar chemical structure. The selection of representative species and its respective proportion depends primarily on the targets or properties required to be predicted successfully over a range of operating conditions for a particular fuel. On the other hand, the decision on the suitable set of targets relies on the specific type of engine application such as PFI, HCCI and GDI engines [26]. For instance, replicating the fuel reactivity under a certain set of operating conditions is a common way in surrogate formulation. Apart from ignition properties, matching other aspects like distillation curve, flame development and propagation as well as sooting tendency is important to ensure the effectiveness of surrogate mixtures [29].

2.2.1 Development of Reaction Mechanisms as Gasoline Surrogates

For gasoline, the simplest fuel models contain only a single component of isooctane which are applied in flame propagation studies [30]. Due to the simplification it brings, this approximation is also commonly accepted in CFD simulations of GDI engines [31,32] and has produced reasonable results. However, several modelling studies [28] questioned the reliability of using isooctane alone as gasoline surrogate. This is attributed to the obvious fact that the octane number (ON) of isooctane is 100 [33] which is relatively higher than that of typical gasoline [34]. The more widespread approach in formulating gasoline surrogates is based on the binary blends of isooctane and n-heptane which was first proposed by Edgar [35] to measure knock properties of commercial gasoline. The two paraffinic hydrocarbons form the PRF and establish the scale of octane rating for gasoline. By definition, ON is the percentage by volume of isooctane in a PRF mixture which just causes engine knock in standardised tests as the real fuel does under identical operating conditions [36]. So, PRF mixtures are applied to represent gasoline fuels with different ON by varying the proportions of the binary blends.

The two octane scales characterising the knock behaviour of gasoline are research octane number (RON) and motor octane number (MON) which are determined from the standardised research method [37] and motor method [38] tests, respectively using the cooperative fuel research engine. While PRF mixtures continue to be a popular surrogate option to model real gasoline fuels, their associated deficiencies begin to

surface during applications involving more complex engine phenomena found in SI and HCCI engines. Unlike PRF, practical gasoline possesses a quasi-continuous spectrum of hydrocarbon constituents with dissimilar RON and MON values. The difference between RON and MON is termed fuel sensitivity which is zero for a PRF fuel. Conversely, actual fuels for SI engines normally have fuel sensitivity ranging from 7 to 12 [34]. Additionally, typical engine operating parameters such as pressure and temperature deviate from those employed in the standardised tests [39], causing RON and MON to be incomplete indicators for real-life knock resistance and, more generally, engine performance.

The limitations of PRF mixtures have driven researchers in the combustion community to look into the development of complex reaction mechanisms with more fuel components so as to better replicate the exact composition and actual combustion characteristics of real fuels. As a result, the inclusion of a fuel component to account for the aromatic content is becoming increasingly important. Being the most abundant aromatic in gasoline (up to 35%), toluene is typically selected as the representative fuel species [26]. Furthermore, the chemistry of aromatics is crucial for examining the formation of soot in ICE as demonstrated in several studies [40–42] which correlated sooting tendency to the amount of aromatic rings present. The addition of toluene into the PRF mixtures leads to the establishment of TRF models. Since toluene has a RON of 120 and a MON of 109 [36], ternary blends of TRF are surrogate mixtures with intended fuel sensitivities. In fact, the application of TRF as surrogates is in line with the recommendations given by Pitz et al. [26] for short-term development on chemical kinetic modelling of gasoline. Hence, the current trend observes a shift of focus from PRF to TRF models. The advantages and disadvantages of PRF and TRF mechanisms are summarised in Table 2-2.

Table 2-2 Advantages and disadvantages of PRF and TRF reaction mechanisms.

Model	Advantage	Disadvantage
PRF	• Simpler binary fuel models • Direct representation of octane rating • Well-established chemical reaction mechanisms	• Match RON or MON but not both • Represent linear and branched paraffins only

Model	Advantage	Disadvantage
	• Extensive experimental data for validation	• Inappropriate for complex engine phenomena deviated from standardised tests
TRF	• Varied RON and MON to account for fuel sensitivity • Include representation of aromatics in real fuels • Emulate physical properties of fuels	• Larger ternary fuel models • Lack of understanding in toluene mechanism • Limited experimental data for a wide range of operating conditions

More recently, with detailed insights gained on the chemistry for other hydrocarbons, chemical modellers have extended the complexity of kinetic models by merging those representative of naphthenes, olefins and oxygenates. Thus, numerous quaternary, quinary and multi-component mechanisms are extensively constructed. Nonetheless, incorporating these large-sized mechanisms in three-dimensional (3D) modelling is hindered by the aforementioned limitations in current computing power because the computational cost scales cubically with the number of species [43]. Within this context, TRF mechanisms remain as the suitable candidate to represent gasoline fuels. Table 2-3 presents a bibliographic compilation of the available TRF mechanisms, to the author's best knowledge, which are applied as gasoline surrogates. The validation criteria and relevant test conditions involving ternary mixtures and real fuels are tabulated. For brevity, the validations based on neat hydrocarbons and binary blends are not reported in Table 2-3 whenever applicable. It is observed that most, if not all, of the surrogate models are generally validated against experimental data of pure and binary mixtures of isooctane, n-heptane and/or toluene. Such validation studies ensure the robustness of mechanisms across varying compositions and retain their predictive capability for each individual component making up the tri-component models [28].

Substantial developmental works in chemical kinetic modelling of gasoline has resulted in the wide availability of reaction mechanisms. Each of them differs in terms of complexity and accuracy. The predictive capability relies on validations against important targets including ID time, laminar flame speed (s_L) and speciation profiles from experimental devices such as shock tube (ST), rapid compression machine (RCM), perfectly stirred reactor (PSR), variable pressure flow reactor (VPFR), jet-stirred reactor (JSR), premixed flame (PREMIX), opposed-flow diffusion flame

(OPPDIF) and HCCI engine setup over a range of operating pressures, temperatures and equivalence ratios as summarised in Table 2-3. As mentioned previously, multi-dimensional CFD simulations can only afford reduced reaction mechanism with small and compact sizes. Hence, there is a variety of mechanism reduction techniques and schemes including rate analysis for flame modelling [44], directed relation graph [45], generic algorithm [46] and simulation error minimisation [47], among others which are tailored for intended applications.

Table 2-3 Bibliographic compilation of the available TRF mechanisms for gasoline.

Author(s)	N_S*	N_R*	Validation conditions			
			Criterion	T* (K)	p* (bar)	ϕ*
Nakano et al. [48]	782	3631	HCCI[a]	490[b]	-	0.39
Ogink and Golovitchev [49]	109	506	HCCI[a, c]	469, 471, 482[b]	1.9, 2.4, 3.8[b]	0.64, 0.82, 1.01
Andrae et al. [50]	1083	4635	ST[d]	850–1280	55	1
Chaos et al. [51]	469	1221	s_L[e]	400, 550	1	0.6–1.4
			VPFR[f]	550–950	12.5	1
			ST[d]	850–1280	20, 55	0.5, 1, 2
Andrae et al. [52]	137	633	ST[d]	850–1280	30.4, 50.7	1
			RCM[d]	318	1	0.4
			s_L[e]	353, 500	1	0.7–1.3
			HCCI[a]	353, 523[b]	1, 2[b]	0.25
Anderlohr et al. [53]	536	3000	RCM[g]	318	10	0.4
			ST[d]	850–1100	12–25, 45–60	1
Cancino et al. [54]	1053	4277	ST[d]	850–1280	25, 55	1
Sakai et al. [55]	783	2883	ST[d]	850–1280	25, 50	1
			VPFR[f]	550–950	12.5	1
Machrafi et al. [56]	49	62	ST[d]	850–1280	20, 55	0.5, 1
			HCCI[a]	343[b]	-	0.462
Lee et al. [57]	48	67	ST[d]	850–1280	18, 50	0.5, 1, 2
			RCM[g]	293, 323	0.48	1
Zhang et al. [58]	70	196	ST[d]	850–1200	30.4	1
			HCCI[a]	435, 489[b]	1.5, 3.3[b]	0.25
Raj et al. [59]	226	2121	PREMIX[f]	-	1	1.8–3.06
			OPPDIF[f]	-	-	-
Liu et al. [60]	56	168	ST[d]	850–1280	15–25, 45–60	0.5, 1, 2
			s_L[e]	353, 373, 500	1, 10–25	0.7, 1.3
			HCCI[a]	523[b]	1[b]	0.2857
Ranzi et al. [61]	156	3370	ST[d]	850–1280	15, 50	1
			s_L[e]	298, 358	1	0.7–1.3
Niemeyer and Sung [62]	386[h]/ 276[i]	1591[h] /936[i]	Auto-ignition[j]	700–1600	1-20	0.5–1.5
			PSR[k]	300	1, 20	0.5–1.5
			s_L[l]	450	1, 20	0.6–1.4
			HCCI[m]	421–489	1.5–3.3	0.5, 0.75

Author(s)	N_S*	N_R*	Validation conditions			
			Criterion	T* (K)	p* (bar)	ϕ*
Niemeyer and Sung [62]	199[h]/ 173[i]	1011[h] /689[i]	Auto-ignition[j]	1000–1600	1–20	0.5–1.5
			PSR[k]	300	1, 20	0.5–1.5
			s_L[l]	450	1, 20	0.6–1.4
Jiao and Reitz [63]	89	506	PREMIX[f]	-	0.04, 0.053, 1	1, 1.59, 3.06
Zheng and Lv [64]	80	184	ST[d]	850–1250	30.4, 50.7	1
Wang et al. [65]	109	543	ST[d]	850–1280	20, 50	1
An et al. [66]	219	1229	ST[d]	850–1280	15–25, 45–60	0.5, 1, 2
			s_L[e]	338, 358	1	0.8–1.3
			PREMIX[f]	-	1	1.9, 1.97
			OPPDIF[f]	-	-	-
An et al. [67]	85	232	ST[d]	850–1280	15–25, 45–60	0.5, 1, 2
			s_L[e]	338, 358	1	0.7–1.3
			PREMIX[f]	-	1	1.9, 1.97

* N_S and N_R represent number of species and number of reactions, respectively.
* T, p and ϕ represent temperature, pressure and equivalence ratio, respectively.
[a] Validation by comparing pressure profiles and/or heat release rate against experimental data.
[b] Temperatures and pressures at initial/intake conditions of HCCI engines.
[c] Validation by comparing emissions against experimental data.
[d] Validation by comparing ID times against experimental data.
[e] Validation by comparing laminar flame speeds against experimental data.
[f] Validation by comparing species profiles against experimental data.
[g] Validation by comparing pressure changes against experimental data.
[h] 10% error limit.
[i] 30% error limit.
[j] Validation by comparing ID times against detailed mechanisms.
[k] Validation by comparing temperature response curves against detailed mechanisms.
[l] Validation by comparing laminar flame speeds against detailed mechanisms.
[m] Validation by comparing species profiles against detailed mechanisms.

2.2.2 TRF Reaction Mechanisms

Recognising the significance of TRF reaction mechanisms for near-term development in kinetic modelling of gasoline, many fuel models have been proposed and validated under engine-like operating conditions. For instance, the TRF model developed by Andrae et al. [50] comprised 1083 species within 4635 reactions by incorporating the toluene mechanism of Sivaramakrishnan et al. [68] into the PRF model by Lawrence Livermore National Laboratory [69]. This highly detailed mechanism was extensively utilised in successive studies on chemical kinetics of gasoline [54,57,60]. In their model, Andrae et al. [50] included cross reactions between different fuel components, despite their trivial effects on the ID in ST experiments, arguing that their importance might dominate under auto-ignition in an ICE. Later, Andrae et al. [52] integrated the skeletal mechanisms of PRF into a detailed model of toluene in order to formulate a

semi-detailed TRF model with 137 species and 633 reactions, a significantly smaller size as compared to the previous detailed model [50]. Particularly, introducing cross reactions between benzylperoxy radicals and n-heptane enhanced model performance for a binary blend of n-heptane and toluene at temperatures below 800 K.

The incorporation of toluene induces differences in chemical structures within the fuel models, thus signalling the potential importance of cross reactions. The works by Andrae et al. [50,52] highlighted the need to consider cross reactions among different fuel components. In contrast, Chaos et al. [51] refuted the significance of cross reactions by pointing out that the coupling between toluene and PRF involved only a small radical pool without participation of large radical species. They associated the discrepancies in Andrae et al.'s model [50] with the insufficiency of the toluene sub-mechanism at high pressures which could not be compensated by inclusion of cross reactions. Likewise, the detailed TRF mechanism assembled by Cancino et al. [54] did not consider the cross reactions proposed by Andrae et al. [50]; they claimed that the reactions were insignificant in predicting ID times in ST at 25 bar and 55 bar. Nevertheless, Sakai et al. [55] discovered the acceleration effect in ID with toluene addition to isooctane at high temperatures in an earlier ST study [70] and increase in ID of n-heptane by adding toluene. Suggesting that cross reactions between alkenes and aromatics were responsible for such observations, they performed reaction path and sensitivity analyses which revealed that cross reactions between allene and benzyl radicals and those between alkenes and aromatic radicals were dominant [55].

Recently, the imperative need to attain feasible computational modelling of gasoline combustion within complex engine phenomena motivated the expansive development of relatively reduced TRF mechanisms [56–58,60–65,67]. Generally, the validations are extensive and thorough in which crucial targets such as ID times, flame speeds and speciation profiles were reproduced with reasonable accuracy. Furthermore, most of the reduced mechanisms [56–58,60,64] were formulated with the goal to model gasoline combustion in HCCI mode as the auto-ignition characteristics are dependent primarily on chemical kinetics of fuel [49]. As an example, Niemeyer and Sung [62] performed skeletal mechanism reductions on TRF for comprehensive (700–1600 K) and high-temperature (1000–1600 K) ranges, respectively at two levels of accuracy (10% and 30% error limits). Their work recommended reduction through multi-component fuel mechanism altogether over combination of reduced mechanisms of

individual neat fuel components. This is because the latter led to a larger reaction mechanism with the loss of important cross reactions.

The understanding of soot processes within ICE has always been at the centre of attention in the combustion community. PAH are inferred to be the presumed soot precursors whereby the incipient of a soot particle occurs by the collision of two PAH molecules [71]. Detailed information on PAH formation and their sequential growth to soot was discussed by Richter and Howard [72]. Realising the contribution of PAH chemistry, Raj et al. [59] incorporated PAH sub-mechanisms up to coronene (A7) to formulate a reaction mechanism for gasoline surrogates possessing 226 species and 2121 reactions. The mechanism was capable of capturing the experimentally observed synergistic effect on PAH formation for fuel mixtures of n-heptane/toluene and isooctane/toluene, an improvement over the previous associated reaction mechanisms [73,74]. Low-temperature chemistry and validations of ID times and flame speeds were, however, left out in the study. In order to overcome these limitations, An et al. [66] updated Raj et al.'s work [59] to cover additional validations of ID in ST and flame speeds for gasoline fuels. For the similar purpose of soot predictions, reduced TRF mechanisms coupled with PAH chemistry were further developed by Jiao and Reitz [63], Wang et al. [65] and An et al. [67] to allow feasible 3D engine simulations.

2.2.3 Applicability of Reaction Mechanisms in GDI Engines

It is evident that many reaction mechanisms for gasoline fuels have been constructed owing to the continuing development of kinetic studies in hydrocarbon classes and advancement in mechanism generation as well as reduction techniques. The models are usually targeted to match important validation parameters under a particular range of engine-like operating conditions. More species and reactions are consistently introduced while their reaction rates are updated from time to time to enhance the overall model predictions. Generally, most, if not all, of the mechanisms are validated under HCCI engine operating conditions, as shown in Table 2-3. This, however, does not guarantee good performance for GDI engine applications due to the fundamental differences in the combustion mode, starting with the inclusion of SI. While fuel kinetics mainly governs the combustion in HCCI engines [49], it is uncertain whether the chemical processes occurring behind the turbulent flame front in GDI engines (or SI engines in general) are predominantly controlled by turbulence mixing or chemical

kinetics. This contentious issue needs to be resolved with further experimental studies and/or advanced numerical simulations [75].

The incorporation of reaction mechanisms in simulating GDI combustion systems is rather limited. In fact, mostly simplified mono- and bi-component of isooctane and PRF, respectively, have been utilised in the associated numerical CFD studies. Although scarce, more complex mechanisms of TRF and multi-component nature are increasingly coupled to combustion and emission modelling in GDI engines as discussed in Section 2.3. Nevertheless, it is observed that these reaction mechanisms were pre-formulated with validations under HCCI engine conditions only. Pitz et al. [26] emphasised the need to consider validations under non-premixed flames for GDI engines as the fuel is directly injected into the cylinder. Advocating a similar opinion, Bieleveld et al. [76] experimented and modelled the combustion characteristics of gasoline surrogates and commercial fuels in non-premixed flows. Thus, it is important to identify the critical range of operating conditions pertinent to GDI systems and establish proper validation criteria to which the development of chemical kinetic models can be tailored to.

It is believed that CFD modelling in GDI engines would benefit from the ongoing developmental works in reaction mechanisms for gasoline. TRF is likely to remain as the appropriate fuel model because it provides a reasonably good representation of gasoline fuels while retaining the feasibility in complex engine simulations. More fuel constituents can be added, especially ethanol due to the increasing use of gasoline-ethanol blends in GDI engines [77]. Relevant to soot emissions, description of PAH chemistry needs to be incorporated into the fuel models simulating GDI combustion systems [28,66]. However, care should be taken to avoid intractable computational time induced by the overly large mechanisms. Apart from fuel chemical kinetics, the success of GDI engine modelling is also subject to the accuracy of CFD models developed to describe various in-cylinder processes.

2.3 CFD Modelling of In-Cylinder Processes in GDI Engines

The combustion in ICE essentially involves complex gas dynamics and flows, heat transfer and turbulence-chemistry interactions [78]. Within a single engine cycle, combustion regimes can change between premixed turbulent flame propagation,

mixing-controlled non-premixed combustion and chemical-kinetics-controlled burning [79]. Therefore, the role of combustion science, particularly in development of advanced gasoline engines is prevalent along with the concurrent applications of modern optical techniques, multi-dimensional CFD modelling and conventional combustion diagnostic tools [80] to understand the fundamental in-cylinder processes. Among all, numerical simulations serve to represent such physical and chemical processes partly or completely with their tailored mathematical models [78]. The flows induced within GDI engine configurations are compressible and transient [81]. Generally, the key physical processes cover intake air flow, fuel injection, spray and vaporisation, mixture preparation and formation, SI and early flame formation, turbulent flame propagation, and exhaust flow with engine-out emissions [80]. These stages have varying degrees of influence on the overall engine performance in which different parameters from each stage affect the output independently or collectively. Successful simulations of the in-cylinder processes rely on the modellers' judgment and knowledge in appropriate selection of CFD models and schemes in order to draw meaningful comparisons with ongoing experimental measurements in the field.

The emphasis of current modelling works in GDI engine development is placed on understanding spray, mixture preparation and combustion processes. While spray and mixture formation aspects can be examined in detail separately to optimise injector design and position as well as combustion chamber geometry, combustion modelling often depends on the accuracy of numerical studies for the former two preceding processes. The present review briefly summarises the most relevant information regarding in-depth studies of spray and mixture formation; the main focus is instead directed towards the growing trend of combustion modelling. 3D CFD combustion simulations performed under various GDI engine setups which have been validated against experimental and optical measurements are tabulated, to the author's best knowledge, in Table 2-4 along with the corresponding engine parameters used for comparisons. Modelling studies incorporating soot processes for GDI engines are not included here, but treated subsequently in Section 2.3.2.1.

Table 2-4 Multi-dimensional CFD combustion modelling of GDI engines with optical and/or experimental validations.

Author(s)	Code	CFD sub-models	Parameter comparison[a]	H/S[b]
Gill et al. [82]	KIVA-II	k-ϵ turbulence, spray, flamelet	In-cylinder pressure, species concentration	S
Kech et al. [83]	KIVA-3V	Hollow-cone fuel spray, flame area evolution	In-cylinder pressure	S
Duclos and Zolver [84]	KMB	k-ϵ turbulence, Kays and Crawford's heat transfer, hollow-cone fuel spray, Naber and Reitz's wall impingement, coherent flame model (CFM), Zeldovich et al.'s NO	In-cylinder pressure, NO and CO emissions	H, S
Tatschl and Riediger [85]	FIRE	k-ϵ turbulence, transported multi-scalar probability density function (PDF) combustion	Flame size probability distribution, flame front speed, heat release rate	H, S
Henriot et al. [86]	KMB	WAVE-FIPA, Naber and Reitz's wall impingement, extended CFM (ECFM)	In-cylinder pressure, NO and UHC emissions	H, S
Duclos et al. [87]	KMB	Spray, ECFM, Zeldovich et al.'s NO	In-cylinder pressure, NO emission	H, S
Fan et al. [88]	KIVA-3V	Hollow-cone fuel spray, Taylor analogy breakup (TAB), Naber and Reitz's wall impingement, characteristic-time combustion (CTC), Zeldovich et al.'s NO, spark plug protrusion, discrete particle ignition kernel (DPIK), RNG k-ϵ turbulence	In-cylinder pressure	H, S
Georjon et al. [89]	KIVA-II	k-ϵ turbulence, WAVE-FIPA, Naber and Reitz's wall impingement, ECFM, Zeldovich et al.'s NO	Spray shape, spray penetration, flame propagation, evaporated mass fraction, in-cylinder pressure, NO emission	S
Tatschl et al. [90]	FIRE	Hollow-cone spray, transported multi-scalar PDF combustion	Spray shape, penetration length, fuel distribution, reaction products distribution, fuel mass concentration	S
Hélie et al. [91]	KMB	k-ϵ turbulence, Angelberger et al.'s heat transfer, hollow-cone fuel spray, ECFM, eddy-dissipation model (EDM), Zeldovich et al.'s NO	In-cylinder pressure	S
Nomura et al. [92]	STAR-CD	k-ϵ turbulence, DDM, Naber and Reitz's wall impingement, CFM	Spray shape, fuel distribution, equivalence ratio field	S
Wallesten et al. [93]	FIRE	Lagrangian approach, Naber and Reitz's wall impingement, flame speed closure (FSC)	Flow field, equivalence ratio field, in-cylinder pressure, UHC emission	H, S

Author(s)	Code	CFD sub-models	Parameter comparison[a]	H/S[b]
Castagné et al. [94]	KMB	k-ϵ turbulence, Kays and Crawford's heat transfer, hollow-cone fuel spray, Naber and Reitz's wall impingement, combustion	Spray shape, fuel concentration at spark plug, in-cylinder pressure, indicated mean effective pressure (IMEP)	S
Colin et al. [95]	KMB	ECFM, arc and kernel tracking ignition model, knock, scalar fluctuation	In-cylinder pressure, equivalence ratio field	H, S
Wakisaka and Esumi [96]	GTT	Hollow-cone spray, CTC	Spray shape, Sauter mean diameter (SMD), fuel mass concentration, in-cylinder pressure	S
Tan et al. [97]	KIVA-3V	Linearized instability sheet atomisation, RNG k-ϵ turbulence, Han and Reitz's heat transfer, Naber and Reitz's wall impingement, Zeldovich et al.'s NO, DPIK, G-equation, CTC	In-cylinder pressure, NO emission	S
Vanzieleghem et al. [98]	KIVA-3V	Linearized instability sheet atomisation, TAB, Grover et al.'s wall impingement, ECFM	Spray vaporisation rate, in-cylinder pressure, equivalence ratio field	H, S
Drake et al. [99]	GMTEC	k-ϵ turbulence, Stanton and Rutland's spray-wall interaction, modified Bray-Moss-Libby (BML), EDM	Spray shape, combustion location and progression, in-cylinder pressure, mass burn rate	S
Gao et al. [100]	KIVA-3V	Liquid sheet atomisation, TAB, O'Rourke and Amsden's wall impingement, CTC	In-cylinder pressure	S
Olmo and Thornton [101]	STAR-CD	Lagrangian approach, Reitz-Diwakar's breakup, El Wakil's evaporation, Bai's wall impingement, ECFM, EBU, Zeldovich et al.'s NO	Spray shape, SMD, mean diameter, droplet size distribution, in-cylinder pressure, mass burn rate	H, S
Liu et al. [102]	ICFD-CN	Kelvin−Helmholtz (KH) and Rayleigh Taylor (RT) (KH-RT), TAB, Lefebvre fuel vaporisation, O'rourke and Bracco's droplet impingement and coalescence, Stanton's wall impingement, DPIK, single-step combustion, Zeldovich et al.'s NO	In-cylinder pressure, NO emission	S
Rotondi [103]	NCF-3D	k-ϵ turbulence, Nagaoka and Kawamura's primary atomisation, WAVE, TAB, DDB, CTC, spark plug	Penetration length, spray shape, in-cylinder pressure	H, S
Bohbot et al. [104]	IFP-C3D	WAVE-FIPA, 3-zone ECFM, RNG k-ϵ turbulence	Intake pressure, in-cylinder pressure, species concentration	H
Liang and Reitz [75]	KIVA-3V	DPIK, G-equation	In-cylinder pressure, NO emission	S
Kim et al. [105]	STAR-CD	Reitz-Diwakar's breakup, modified eddy-breakup model (EBM), k-ϵ turbulence	Spray shape, in-cylinder pressure	S

Author(s)	Code	CFD sub-models	Parameter comparison[a]	H/S[b]
Yang and Reitz [106]	KIVA-3V	Continuous multi-component (CMC), G-equation	In-cylinder pressure, heat release rate	S
Dahms et al. [107]	ACFluX	k-ϵ turbulence, spray, spark channel ignition monitoring model (SparkCIMM), G-equation	Spark and combustion luminosity, flame probability contours	S
Bai et al. [108]	FIRE	WAVE, Naber and Reitz's wall impingement, PDF combustion	Spray shape, penetration length, in-cylinder pressure	H, S
Dahms et al. [109]	ACFluX	DDM, Lagrangian approach, k-ϵ turbulence, CMC, Grover et al.'s wall impingement, SparkCIMM, G-equation	Flame probability contours, in-cylinder pressure, heat release rate, characteristic burn points, combustion efficiency	S
Yang et al. [110]	CONVERGE	RNG k-ϵ turbulence, Lagrangian approach, O'Rourke and Amsden's wall impingement, Arrhenius combustion, spark-energy deposition	Heat release rate	H
Givler et al. [111]	CONVERGE	RNG k-ϵ turbulence, KH-RT, multi-zone	In-cylinder pressure	H, S
Bonatesta et al. [32]	STAR-CD	Lagrangian approach, Reitz-Diwakar's breakup, RNG k-ϵ turbulence, Bai-ONERA wall impingement, 3-zone ECFM	Spray shape, penetration length, SMD, in-cylinder pressure, rate of pressure variation	H
Costa et al. [112]	FIRE	DDM, Mundo-Sommerfeld's wall impingement, 3-zone ECFM, Zeldovich et al.'s NO	Spray shape, in-cylinder pressure, flame surface density, flame duration, NO and UHC emissions	H
Costa et al. [113]	FIRE	Lagrangian approach, Huh-Gosman's breakup, O'Rouke's turbulent dispersion, Nordin's coalescence, Dukowicz's evaporation, Mundo-Sommerfeld's and Kunkhe's wall impingement, ECFM, Zeldovich et al.'s NO	Penetration length, spray impingement, in-cylinder pressure, spray shape, flame front	H, S
Kim et al. [114]	KIVA-3V	KH-RT, O'Rourke and Amsden's wall impingement, Lagrangian approach, RNG k-ϵ turbulence, DPIK, G-equation	Penetration length, spray shape, in-cylinder pressure, heat release rate, flame speed	H
Qian et al. [115,116]	ICEM-CFD	RNG k-ϵ turbulence, WAVE, Naber and Reitz's wall impingement, Dukowicz's evaporation, ECFM	Spray shape, in-cylinder pressure, in-cylinder temperature, heat release rate	H

[a] Validation by comparing engine parameters against optical and/or experimental measurements obtained from GDI test bed facilities.

[b] H/S represents homogeneous- or stratified-charge combustion modes, respectively.

In engine simulations, one of the most prominent aspects is turbulence modelling. Overall, the three distinct approaches in solving chemically reacting turbulent flow fields are the Reynolds-averaged Navier-Stokes (RANS) equations, the large eddy simulation and the direct numerical simulation. It is speculated that RANS will continue to be the leading mainstream CFD approach in development of engine modelling [80]. Among the RANS-based models, the two-equation models are widely employed due to their effectiveness and simplicity. In fact, the standard k-ϵ model [82,84,85,89,91,92,94,99,103,105,107] dominates the turbulence modelling for GDI engine combustion with a recent shift to its successor, re-normalisation group (RNG) k-ϵ model [32,88,97,104,110,111,114] as shown in Table 2-4. The latter was derived based on the RNG theory to resolve small-scale flows [117]. It was reported that to better capture the effects of compression, expansion and rapid strain on the turbulence scales, an additional term is introduced in the dissipation rate equation to account for the effect of mean flow distortion on turbulence [118].

2.3.1 Spray, Mixture Formation and Combustion Modelling of GDI Engines

Conceptually, spray combustion can be divided into liquid penetration, breakup, formation of droplets, transport of droplets during evaporation, collision, scattering, recombination and slow down, and gas-phase reactions [119]. CFD sub-models are developed to describe the spray-related processes which include atomisation, droplet breakup and deformation, droplet collision and coalescence, droplet vaporisation and spray-wall impingement at sub-grid scale. Based on current capabilities in CFD, spray modelling for GDI technology is still relatively poorly understood which is partly caused by difficulty in obtaining optical measurements in the near-nozzle region [80]. Early spray models simulated the transport of droplets with the assumption of an initial size distribution, velocity and even composition of droplets. The effects of other droplet dynamics such as collisions and coalescence were later included [119]. Currently, spray models are tuned and tailored to reproduce characteristic quantities such as penetration lengths, radial profiles of droplets size and velocity downstream of the nozzle, which are measured experimentally [80].

Within a spray regime, dense spray consists of the liquid core and the dispersed flow region. Across the dispersed flow, a multiphase mixing layer is formed, followed by a jet evolving into a dilute spray flow [120]. Three major approaches dealing with the

multiphase flow are identified [81] as the volume of fluid method [121], the Eulerian method [122] and the discrete droplet model (DDM) in a Lagrangian framework [123]. The application of DDM dominates the current spray modelling works because of its simplicity and steadiness [81]. The atomisation breakup of spray can be divided into primary and secondary breakups which are often modelled separately. Primary breakup refers to the formation of ligaments and irregular liquid elements along the liquid core surface [120], thus initiating atomisation, controlling the length of liquid core and establishing initial conditions for the dispersed flow region [124]. In secondary breakup, droplets detached from the core undergo further disintegration into even smaller fragments. Subject to the Weber number and time of deformation, the secondary breakup modes can be categorised into bag breakup, stripping breakup and catastrophic breakup [125].

Other physical processes involving the droplets formed include drag and deformation, collision, vaporisation and wall impingement which are modelled to varying levels in spray simulations. For example, collisions between the droplets were neglected in several modelling studies of GDI engines [31,32]. This is because droplet collision and coalescence are expected to be trivial in such engine simulations as mixing and vaporisation occur far from the nozzle where the spray is well-dispersed [31]. Droplet vaporisation links spray breakup to mixture preparation which determines combustion characteristics subsequently. The basic droplet vaporisation model, d^2-law model was proposed by Godsave [126] and Spalding [127]. The model holds that the square of droplet diameter decreases linearly with time for a pure fuel droplet under stagnant conditions. In terms of spray-wall impingements, common impingement regimes due to interactions between droplets and surfaces include stick, rebound, spread and splash [128]. Impingement models formulated describe transition regimes which cover two different regimes as evidenced from experimental studies [129].

Simple spray models such as the Reitz-Diwakar model are commonly applied in CFD simulations of GDI engines [32,101,105] owing to their simplicity with reasonable model predictions. The particular model works on the limiting assumption that all the injected droplets have the same initial diameter as the size of nozzle exit. The whole droplet disintegration is demanded to the subsequent secondary breakup [130,131]. To yield a more accurate description of the spray phenomenon, more complex spray models are utilised. One such model is the KH-RT model which has been increasingly

adapted for GDI engines [102,111,114]. Huang and Lipatnikov [132] compared liquid penetration and SMD of gasoline and ethanol sprays predicted by various spray models which were implemented in an open source code called OpenFOAM. They concluded that the KH-RT model displayed the best agreement particularly at high pressure conditions. Within the framework, the droplet breakup is caused by the growth of competing KH and RT instabilities [132]. The breakup due to KH instability is induced by relative velocity at the interface whereas RT instability is caused by the influence of liquid acceleration within the gas flow field [133]. Notably, KH and RT models are intrinsically inter-related, thus enhancing the numerical capture capability of primary and secondary breakup processes.

The quality of fuel-air mixing and mixture preparation directly determine the resulting combustion characteristics of fuels in the cylinder. Generically, based on the level of mixture homogeneity at the time of ignition, the combustion is distinguished between the two main modes of homogeneous charge or stratified charge in GDI engines [79] as illustrated in Figure 2-2. The former involves early fuel injection during the intake stroke to allow spatial homogeneity of the in-cylinder mixture [80]. The combustion is then characterised by a premixed turbulent flame propagation [79]. Conversely, the stratified system applies late fuel injection (normally during the compression stroke) to form a layered charge featuring a fuel-richer zone in the vicinity of the spark plug, while the charge remains globally lean [79]. The two-stage combustion is primarily initiated through premixed turbulent flame propagation near the spark plug, followed by a secondary diffusion-controlled combustion as unoxidised or partially oxidised fuel fragments in locally rich zones react with leftover oxygen (O_2) from fuel-lean regions [80].

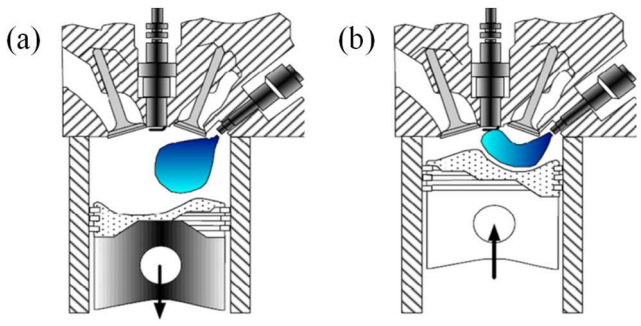


Figure 2-2 (a) Homogeneous and (b) stratified charge formation in GDI engines [134].

While knowledge regarding GDI engines operating in a homogeneous mode can be extracted partly from studies of conventional PFI engines due to similarities in the combustion processes, stratified combustion presents further complications as a result of its two-stage behaviour. Such behaviour is comparable to diesel engine combustion which typically consists of a rich premixed reaction zone and a mixing-controlled diffusion flame [135]. However, one important feature linked to GDI combustion is the turbulent flame front propagation from spark plug upon ignition whereas there is no definite flame front in diesel combustion which is compression-ignited. This is the reason why characterisation of flame surface and propagation speed is vital in GDI combustion modelling. Besides, gasoline has been reported to have higher volatility and longer ID time than diesel [136]. The variation in fuel properties facilitates fuel-air mixing in GDI engines with fewer resulting stratified regions formed as compared to the compression-ignition counterparts [137]. Therefore, care should be exercised in exploiting the profound knowledge on diesel combustion to understand fundamentals behind GDI combustion systems.

While a formal distinction between homogeneous and stratified operations remains essential, it is noted that, due to the inherent short time for fuel vaporisation and mixing, proper combustion chamber homogeneity is extremely difficult to achieve in a GDI engine. The permanence of sub-stoichiometric regions at the time of ignition leads to local stratification, which is identified as one of the most important triggers for soot formation [18,138]. The work of Bohbot et al. [104] also linked the inaccurate predictions in unburnt hydrocarbons (UHC) and nitric oxide (NO) emissions from a turbocharged GDI engine to the assumption of homogenous mixture used in the 3D calculations. Hence, significant modifications and improvements are performed on the current turbulent combustion models for their applications in GDI engines. Several relevant combustion models which are widely utilised include the EBU model, the CTC model, the BML model, the CFM and its variants, the G-equation model and the FSC model. Brief descriptions of the models are provided in Table 2-5 where detailed information can be found in the references cited [139–144].

Table 2-5 Relevant combustion models applied within GDI engine configurations.

Model	Brief description	Reference
EBU	Reaction rates are controlled by the rate of entrainment caused by turbulent mixing.	[139]
CTC	Species conversion time is a combination of both turbulent-mixing time and chemical-kinetics time.	[140]
BML	Thermochemical state of the mixture is expressed as a single scalar combustion progress variable, c based on the flamelet concept.	[141]
CFM	Mean chemical reaction rate is the product of reaction rate per unit area of flamelets and flame surface density.	[142]
G-equation	Flame surface is described by a smooth function, G with the assumption of negligible thickness in the level set approach.	[143]
FSC	Combustion is modelled as a single transport equation for the reaction progress variable, c.	[144]

Early combustion modelling in GDI engines was carried out by Gill et al. [82] who first modified the classical flamelet model by treating the turbulent diffusion flame during stratified combustion as an ensemble of laminar flamelets. Premixed burning mode was not taken into consideration. More importantly, the flamelet model coupled with a precompiled library from a detailed mechanism of n-octane exhibited closer agreement to measured pressures and species mass concentrations as compared to the simplified-chemistry model. Chemical kinetics and turbulence-chemistry interactions provided the direction for subsequent computational combustion studies in ICE. Kech et al. [83] modelled partially premixed combustion through the flame area evolution model which was able to replicate a triple flame configuration observed in stratified engines [145]. The abrupt rise in cylinder pressures predicted after ignition was attributed to the higher spray vaporisation simulated. Both homogeneous and stratified operations were simulated by Duclos and Zolver [84]. The combustion process was modelled with the CFM whereby the average cylinder pressures and NO levels (< 1000 ppm) were properly predicted. Prediction of CO, on the other hand, was less satisfactory due to uncertainties in fuel stratification and simplicity of the reaction

mechanism used. In a successive study by Duclos et al. [87], an extended version of the CFM, the ECFM was applied which relies on the thermo-chemical properties of unburnt and burnt gases. Similar agreement in pressure traces and NO emissions was achieved. The ECFM was also employed in the works of Henriot et al. [86], Georjon et al. [89], Hélie et al. [91] and Qian et al. [115,116] for modelling GDI combustion.

The approach to simulate turbulent reacting flows in stratified-charge combustion by Tatschl and Riediger [85] involved solving a PDF transport equation for scalars including mixture fraction, reaction progress variable and enthalpy. Predicted spatial and temporal characteristics of flame propagation resembled cycle-averaged shots of the burnt charge. In a later study, Tatschl et al. [90] integrated advanced meshing tools into the similar combustion modelling method at part load operating conditions. The modelling work of Fan et al. [88] focused on investigating effects of injection angle and tumble ratio for a GDI engine operating at part load. The combustion was described by the CTC model [140] which considered both turbulent-mixing time and kinetics time. The CFD models were first validated in a propane-fuelled SI engine in terms of in-cylinder pressures. It was demonstrated that injection orientation, piston deflection and gas tumble determined proper preparation of fuel stratification in the combustion chamber. The application of the CTC model for stratified combustion was also observed in the works by Wakisaka and Esumi [96], Gao et al. [100] and Rotondi [103]. Nomura et al. [92] performed 3D combustion simulations in a GDI engine with fan-shaped spray. The results recommended the use of thin thickness fan spray coupled with compact cavity to reduce UHC.

Wallesten et al. [93] incorporated a PRF mechanism containing 100 species among 475 reactions into combustion modelling using the FSC model. The complex effect of chemistry was taken into account through calculation of laminar flame speed. The computed in-cylinder pressures resembled the measured values (< 10%) under various engine speeds and loads. Castagné et al. [94] carried out 3D modelling studies which paralleled the experimental investigation on wall-guided and spray-guided engines. Overall, in-cylinder pressure traces and IMEP across varying injection timings and spark advances were effectively reproduced. To improve the effect of large-scale stratification on combustion, Colin et al. [95] adapted the ECFM for combustion of multi-component fuels. The combustion model involved defining a fictitious mean fuel locally to represent all the components of the real fuel. However, the computation

of laminar flame speed was simplified through a linear interpolation technique based on the local mean fuel composition. Coupled with a knock model, the in-cylinder pressures were well predicted. Also, the average equivalence ratio and its fluctuation at the spark location were accurately modelled. Meanwhile, Tan et al. [97] used the G-equation model to represent premixed flame propagation and the CTC model to describe the subsequent diffusion-controlled combustion. Based on the flamelet concept, the G-equation allows the calculations of chemical reaction and turbulent hydrodynamics to be decoupled. Effects of SI timing, EGR rate and engine speed on in-cylinder pressures and NO concentrations were captured. The study was extended by Liang and Reitz [75] who included reaction mechanisms into the G-equation model. The fuel used in a two-stroke marine GDI engine was represented by a kinetic model of isooctane with 21 species and 42 reactions. The calculated pressure curves and NO emissions matched the experimental measurements for various SI timings.

Vanzieleghem et al. [98] studied full-cycle combustion modelling in a single-cylinder GDI engine with different swirl intensities at speeds of 600–2000 rpm. Furthermore, the CFM was extended to examine the effect of EGR on flame propagation. The formulation enabled quantification of EGR in each computational cell instead of homogeneous distribution assumption, thus allowing accurate flame speeds to be calculated. The results showed that a fairly small increase in EGR level caused large reduction in laminar flame speed. The two-stage stratified combustion behaviour in a spray-guided engine was modelled by Drake et al. [99] in which premixed combustion was described using the modified BML flamelet model while the EDM was applied to model diffusion-controlled burning. The CFD results highlighted that higher fuel burn rate was detected in the premixed combustion as compared to the diffusion mode. Similar observation was presented in Koch et al.'s work [146] whereby the first phase of heat release was dominated by premixed combustion. Liu et al. [102] optimised combustion chamber shape design through CFD modelling. In the combustion model, burning rate was governed by chemical reaction rate initially, followed by turbulence dissipation rate. The model was calibrated based on the measured pressures with a 5% error tolerance.

Kim et al. [105] selected the modified EBM to study the influence of tumble flow on combustion and the effects of injection timing and compression ratio on mixture formation in a spray-guided engine. Yang and Reitz [106] improved the G-equation

model by incorporating the effects of multi-component fuel through the CMC approach. A reduced PRF mechanism consisting of 41 species and 130 reactions was also used to model the chemistry processes in burnt and unburnt regions. Under lean stratified-charge conditions, the simulated pressures and heat release rates agreed well with the experimental data at different manifold pressures, injection timings and SI timings. Dahms et al. [107] integrated the SparkCIMM ignition model with the G-equation model and validated the results against experimental findings in terms of flame probability contours. In a later study [109], a deeper investigation was carried out at different engine speeds, loads, EGR rates, injection timings and SI timings. Excellent agreement was achieved between computed and measured peak pressures (< 1%) and combustion efficiencies (2–4%). The modelling work by Bai et al. [108] showed that slower flame propagation and lower peak pressure were observed for stratified-charge combustion as compared to the homogenous mode. Yang et al. [110] applied an Arrhenius combustion model with a simplified mechanism of isooctane. It was argued that the combustion in spray-guided engines occurred in a thickened flame regime where the chemical reactions dominate. The effect of turbulent fluctuations was, however neglected. A PRF mechanism was employed by Givler et al. [111] to model combustion in GDI and PFI engines through the multi-zone approach. The importance of selecting a mechanism which was reduced under similar operating conditions to engine cases was specifically emphasised to ensure accurate predictions.

A recent theoretically-homogeneous and stoichiometric combustion modelling in a wall-guided engine was performed by Bonatesta et al. [32] using the 3-zone ECFM model. Spray modelling was initially verified based on spray morphology and tip penetration. For both mid and high engine speeds, the computed average pressures and rates of pressure variation exhibited good agreement with the experimental data. Costa et al. [112] applied simultaneous numerical and experimental techniques to study combustion in a wall-guided engine under various injection strategies and SI timings. Likewise, the spray sub-models were properly assessed. The 3-zone ECFM was calibrated in terms of initial flame surface density and flame stretch factor to capture the pressure traces. Spatial evolution of the flame during early combustion was reproduced while effects of injection timing on NO and UHC were replicated qualitatively. In a further study, Costa et al. [113] detected the possible occurrence of knocking in GDI engine through pre-validated CFD models. The primary interest of

Kim et al.'s work [114] was to examine the feasibility of a double injection strategy in GDI engines using the G-equation model. It was shown that a first injection mid-way through the intake stroke, followed by an early second injection in the compression stroke improved turbulence intensity, while maintaining the in-cylinder mixture homogeneity globally. However, higher emissions were anticipated with such injection strategy due to the presence of overly-rich local zone at the intake port side.

Similar to SI engines, combustion modelling of GDI systems aims to characterise the initiation of early flame kernel and flame propagation across the combustion domain. Conceptualising the flame front with numerical formulations is the common trait shared by combustion models utilised in GDI engine simulations depicted in Table 2-5. For example, in the popular flamelet approach, the tracking of flame front interface for GDI combustion is based on a progress variable, c or a non-reacting scalar, G while the mixture fraction, Z is applied to account for effects of turbulent mixing on non-premixed combustion in diesel engines [147]. Specifically, the ECFM and G-equation models as well as their variants have demonstrated significant success in recent trend of GDI combustion modelling. However, the role of fuel chemistry is fairly restricted to the mechanisms of neat isooctane [75,110,114] and binary blends of PRF [93,106,109]. Even so, their applications focus on generating precompiled libraries and look-up tables under simplified configurations to describe the effects of chemistry such as auto-ignition and laminar flame speed. Turbulent flame propagation in GDI engines has been found to rely on fuel properties during the main combustion phase as well as towards the end approaching lean flammability limit and extinction [109]. Thus, integrating accurate fuel kinetics in GDI engine simulations is inevitably essential, particularly when modelling pollutant emissions comes into play.

2.3.2 PM Processes and Mechanisms in GDI Engines

GDI engines produce a substantial amount of PM as compared to conventional PFI engines and diesel engines mounted with DPF [148,149], even exceeding 10 mg/km for some first generation vehicles [150]. Since soot constituents a large proportion of the ultra-fine PM, the understanding of soot formation and oxidation in GDI engines is of paramount importance. Soot is generated as an undesirable solid by-product of hydrocarbon combustion in many practical combustion devices. With no clear definition, it consists of roughly eight parts carbon and one part hydrogen in which

the hydrogen content decreases as soot matures. Its formation is linked to the nucleation of carbonaceous fuel from the vapour phase to a solid phase under fuel-rich conditions at elevated temperatures [151]. The structure of soot aggregates is fractal in nature and the typical chain-like structures are made up of primary quasi-spherical particles [21,152]. The size of spherules usually ranges from 15 nm to 50 nm in diameter [153].

There is a consensus agreed by most scientists engaged in soot research that the basic physical and chemical processes during soot formation are similar regardless of the types of fuels and flames [154]. In other words, same formation mechanisms and growth constraints are applicable for soot originating from various combustion sources [155]. Hence, knowledge derived from soot studies in simple laboratory flame configurations can be applied to extract information regarding complex combustion phenomena in ICE. The six commonly identified processes include fuel pyrolysis, nucleation, coalescence, surface growth, agglomeration and oxidation. It is noted that coagulation is used interchangeably with coalescence. Figure 2-3 depicts the first five steps of soot formation, while soot oxidation takes place at any point during the entire process. Fuel pyrolysis involves alteration in molecular structure of fuels under high temperature without significant oxidation despite the presence of oxygen. Essentially, pyrolysis of all fuels generates the same species including unsaturated hydrocarbons, polyacetylenes, PAH and particularly acetylene (C_2H_2). Some of the species act as soot precursors which are the building blocks of soot particles [151].

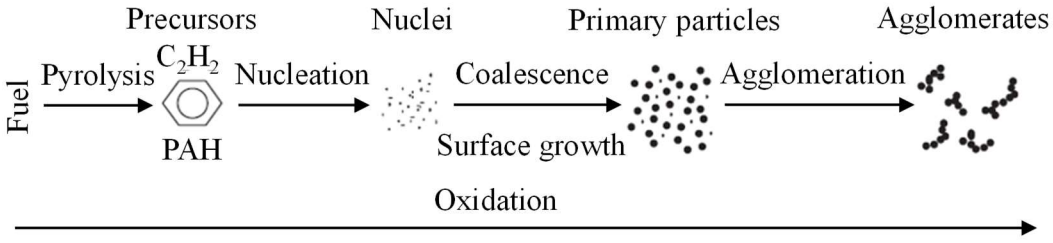


Figure 2-3 Steps in soot formation process from gas phase to solid particles [151].

Nucleation refers to the inception of solid particles from gas-phase species in which its exact mechanism remains poorly understood [156]. Glassman [157] postulated the existence of a fuel-independent soot formation mechanism possessing alternative routes to intermediate species. The propensity to soot would then be controlled by the initial rate of formation of the first and second ring structures. It is likely that the first

ring is formed from two propynyl radicals and the aromatic ring transforms into a PAH structure with the addition of alkyl groups. At present, the majority of soot models rely on the assumption of PAH as the soot precursors [158,159]. Then, the nascent soot particles undergo surface growth which causes an increase in mass due to the addition of gas-phase species especially C_2H_2 to the reactive surface of particles [151]. In this context, Frenklach and Wang [160] treated the surface growth of soot analogously to the planar growth of PAH through the hydrogen-abstraction-C_2H_2-addition (HACA) mechanism. It is observed that increasing particle growth decreases the tendency of soot particles to experience further surface growth [156] as a result of reduction in the availability of radical sites [161].

Coalescence is the physical process in which relatively small particles collide and merge into a larger spheroid, thus reducing the number of particles while maintaining the same total combined mass [151]. The rate of coalescence is hence governed by the frequency of particle collisions. Agglomeration takes place when existing particles stick together to form large groups of soot aggregates with fractal-like structures typically [151]. It is noteworthy that not all collisions will lead to coalescence or agglomeration [162]. Oxidation converts carbon or more volatile hydrocarbons in the external particle layers into combustion products. In fact, partial oxidation of carbon to carbon monoxide (CO) ceases the evolution of carbon into a soot particle even in a fuel-rich zone [151]. Particle oxidation is said to begin when the temperature exceeds 1300 K [157]. The two-stage process involves chemical attachment of oxygen to the surface and subsequent desorption of oxygen with fuel components from the surface. Oxidation under fuel-rich and stoichiometric conditions is most likely dominated by hydroxyl (OH) radicals whereas both OH radicals and oxygen oxidise soot under fuel-lean conditions [161]. Other oxygenated species including oxygen atom (O), water molecule (H_2O) and carbon dioxide (CO_2) are crucial under certain conditions [163].

For GDI engine operations, soot is speculated to be generated mainly from three sources: (1) imperfect mixture preparation including stratified-charge combustion with fuel-rich regions locally [18,31], (2) piston and wall wetting due to liquid spray impingement as well as the resulting pool fires [17,63,164] and (3) diffusive burning of the remaining incompletely volatilised liquid fuel droplets [18]. Some studies have suggested that soot formation from pool fires may be the most prominent source as the particles produced survive until late in the cycle when the conditions for further

soot oxidation are unfavourable (low temperature and absence of OH radicals) [165]. Nonetheless, the relative importance of these PM formation mechanisms remains difficult to be determined and quantified due to variations in combustion chamber and injection system designs as well as engine operating conditions [32].

The inherently short time available for the fuel to vaporise and mix with air properly in GDI engines is responsible for the charge inhomogeneity and wall wetting in the cylinder [18,31]. As a consequence of the inhomogeneous mixture with locally fuel-rich regions, the PM number emissions in stratified charge operation were observed by Maricq et al. [18] to increase by 10–40 times that of the homogeneous mode. Meanwhile, extensive fuel impingement during injection leads to the formation of liquid films within the cylinder. When the films persist until after combustion of the premixed charge has initiated, they ignite and burn with a diffusion flame event [164]. This phenomenon termed pool fire contributes to soot formation in both homogenous and stratified modes [17] as well as to increased engine-out UHC and smoke in GDI engines [166]. Stevens and Steeper [164] demonstrated the production of PM from the pool fires induced by the fuel films through visualisation with a laser-induced fluorescence imaging technique and laser elastic scattering of soot.

On a closer look, when a flame approaches a liquid film on the piston top, the regions swept by flame surface become burnt regions at high temperature. Although film vaporisation is subsequently enhanced to form locally fuel-rich zones, fuel oxidation in the gas phase is somehow limited due to the lack of oxygen in the burnt regions. Through fuel pyrolysis, soot particles grow in high-temperature and fuel-rich regions and then undergo oxidation in the OH-rich combustion zone in the lean side of the flame, particularly diffusion flame in GDI engines. As a result, high amount of soot is more likely to be produced in the rich areas near the wall films [63]. Furthermore, Fujimoto et al. [167] pointed out that spray impingement and wall wetting might additionally lead to lubricant oil dilution which eventually became another potential source of soot formation in GDI engines. Apart from that, rich combustion arising from the charring of remaining liquid droplets which are not volatilised before the event of SI is theorised to contribute to engine-out PM for late injection timings [18].

2.3.2.1 Soot Modelling of GDI Engines

While advanced optical techniques allow the visualisation of in-cylinder processes, the major drawback is that only limited geometric specifications and operating conditions can be studied due to costly maintenance and problems caused by thermal evolution and blow-by [31]. Therefore, the application of CFD emerges as a powerful alternative to acquire deeper understanding of engine performance across a wide range of operating parameters and designs. Soot modelling in ICE is relatively challenging due to the complex structure, composition and chemical interactions of soot particles in formation and oxidation mechanisms [78]. Generally, soot models are categorised into purely empirical correlations, semi-empirical approaches and detailed models, in order of growing complexity [151,163].

Empirical models typically predict trends in soot loadings using direct correlation to experimental measurements collected under premixed and diffusion flames. The general validity of such models is however uncertain as the modelling constants are adjusted against a set of specified baseline measurements to provide good agreement [163]. The simplest models utilise one rate expression for soot formation and another one for soot oxidation [151]. Semi-empirical models incorporate rate equations for reactions involving soot precursors and particles with input from experimental data. They tend to include dominant physicochemical phenomena and rely on simplified chemistry to compute the rate equations. Similarly, the application of ad-hoc models is restricted inherently to specific conditions under which the rates are obtained [163]. Detailed models solve the rate equations for elementary reactions contributing to soot by treating the entire panoply of phenomena during net soot formation. Often, detailed descriptions of kinetics for PAH and soot particles are required [163]. For example, the works by Frenklach et al. [160,168] covered comprehensive soot modelling from fuel pyrolysis to oxidation in detail. Despite the broad applicability and generality of detailed models, the associated high computational cost restricts their implementation into CFD simulations with complex geometric configurations [151].

Overall, the inherent superiority and efficacy of various soot models proposed are difficult to be evaluated as most models are calibrated against specific experimental measurements. Kennedy [163] suggested the establishment of universally acceptable experimental data sets to which the development of soot models can be based upon.

To model soot processes in ICE configurations, the trade-off between computational cost and prediction accuracy justifies the common selection of semi-empirical models. Nonetheless, the boundary distinguishing between semi-empirical and detailed approaches is not clearly defined with many models shifting to the detailed type as progress is continuously made to incorporate fuel chemistry. Apart from soot kinetics, soot particle dynamics need to be addressed in the modelling works through the PSDF. Generally, three approaches are utilised to extract information on the population of particles [169]. The first one is the Monte Carlo method whereby the soot particles are represented by a stochastic particle system [170]. Secondly, the soot particles are discretised into bins where the evolution equations are solved in the sectional method [23,171]. In the third approach known as the method of moments, evolution equations are computed for moments of the PSDF which are expressed as mean quantities [172]. The various soot models adapted for numerical simulations of soot processes in GDI engines are summarised and appraised in Table 2-6. Additional information including precursor species and variables solved is also tabulated.

Table 2-6 Concise description of soot models adapted for soot modelling studies in GDI engines.

Author(s); Soot model	Precursor	Description	Variable solved	Limitation
Wallesten et al. [173]; Kennedy-Hiroyasu-Magnussen soot model	Fuel vapour	• The three-stage model includes nucleation, surface growth and oxidation. • The model is corrected based on the two-step empirical soot model proposed by Hiroyasu.	Mass fraction	• Particle coagulation is not considered. • Exaggerated trends in soot mass fraction are obtained for different injection timings.
Etheridge et al. [174]; Detailed population balance soot model	A4	• The model includes nucleation, condensation, surface growth, coagulation and oxidation. • The population of soot aggregates is represented by an ensemble of stochastic soot particles. • The equations are solved using Monte Carlo methods.	Mass, number density, volume fraction, surface area, composition	• The engine model is spatially zero-dimensional (0D). • It is computationally intractable with sectional or moment methods.
Kwon et al. [175]; Phenomenological soot model	Fuel radicals	• The model includes pyrolysis, nucleation, surface growth, coagulation and oxidation. • Soot processes are described through global rate expressions. • The collision frequency factors of radical and acetylene formation processes are tuned.	Number density, species concentration, volume fraction	• It is assumed that oxidation does not affect the number density of particles. • The model is commonly suited for non-premixed combustion. • Average particle diameter is estimated based on the monodisperse assumption.
Kim et al. [176]; Phenomenological soot model	C_2H_2	• The model consists of four steps including nucleation, surface growth, coagulation and oxidation. • The rate constant of particle coagulation is revised.	Mass fraction, number density, average size	• The results of soot emission predicted by the model are not shown.
Naik et al. [177]; Pseudo-gas soot model	A4	• The model contains seven steps which describe nucleation, surface growth and oxidation. • The rate constants of reactions are altered. • The model is included within the fuel mechanism.	Mass	• Particle coagulation is not considered. • Number density and PSDF of soot particles cannot be determined.
Liang et al. [178]; Detailed soot model	A4	• The model includes nucleation, surface growth, coagulation and oxidation. • The surface processes are modelled through a surface chemistry mechanism. • The evolution of soot particles is solved through the method of moments.	Number density, volume fraction, surface area, average size	• Only mean properties of the population of soot particles are obtainable. • The results of soot emission lack validations for engine configurations.

Author(s); Soot model	Precursor	Description	Variable solved	Limitation
Jiao and Reitz [63]; Semi-detailed soot model	A4	• The model includes nucleation, surface growth, coagulation and oxidation. • Transport equations are solved including the effects of thermophoretic diffusion.	Mass, number density	• The effect of soot radiation is not considered. • The results of soot emission lack validations for engine configurations.
Wang et al. [137]; Detailed population balance soot model	A7	• The model includes nucleation, condensation, surface growth, coagulation and oxidation. • The equations are solved using Monte Carlo methods. • The engine model is extended to include spray impingement and wall film evaporation.	Mass, number density, volume fraction, surface area, composition	• The engine model is spatially 0D. • It is computationally intractable with sectional or moment methods. • The size of particles in the main mode and total mass are under-predicted.
An et al.[179]; Detailed soot model	A4	• The model includes nucleation, condensation, surface growth, coagulation and oxidation. • The evolution of soot particles is solved through the method of moments.	Number density, mass, average size	• Only mean properties of the population of soot particles are obtainable. • The validation only covers mass density of soot.
Kim et al. [180]; Detailed soot model	A4–A7	• The model includes nucleation, surface growth, coagulation and oxidation. • The evolution of soot particles is solved through the method of moments	Number density, volume fraction, average size	• Only mean properties of the population of soot particles are obtainable. • Mass density and average size of soot particles are under-predicted.
Dong et al. [181]; Two-step soot model	Ethylene (C_2H_4)	• The two-step model accounts for soot formation and oxidation. • The model is improved by using C_2H_4 as the precursor as opposed to using fuel vapour concentration.	Mass	• The model is over-simplistic as surface growth and coagulation are omitted. • Number density and PSDF of soot particles cannot be determined.
Costa et al. [182]; PAH kinetic model	PAH	• Soot formation is accounted by a detailed PAH mechanism under premixed C_2H_4 and C_2H_2 flames.	Mass density	• Underestimation of mass density of soot is attributed to the inadequacy of the kinetic model.
Gong et al. [183]; Frolov Kinetic soot model	Fuel vapour	• The three-step model accounts for soot formation and oxidation by oxygen and H_2O. • The kinetic parameters are fitted across a range of operating conditions.	Mass fraction	• The model is over-simplistic as surface growth and coagulation are omitted. • Number density and PSDF of soot particles cannot be determined.

The early work by Wallesten et al. [173] examined combustion modelling in a GDI engine under both homogeneous and stratified charge conditions. With the FSC model coupled with a reaction mechanism for isooctane, combustion phasing for different operating conditions was reproduced by comparing the computed pressure curves to the measured ones. At the same time, the Kennedy-Hiroyasu-Magnussen model was applied to account for the soot formation processes. The trend of decreasing soot mass fractions with advancing fuel injection was captured qualitatively, but led to an over-prediction under stratified charge combustion. The substantial tuning effort required restricted the soot model to roughly indicate soot formation regions and general trends rather than as an effective predictive tool for soot emissions. It is not until recently that soot modelling of GDI engines has drawn significant attention to investigate the relevant mechanisms in depth.

Detailed soot modelling in a SI engine was first attempted by Etheridge et al. [174] with the application of the stochastic reactor model and a highly detailed soot model. The integrated models were initially calibrated based on a GDI engine with early injection strategy, before utilising them under stratified charge conditions. The soot model involved solving a detailed set of population balance equations through the Monte Carlo method to describe particle morphology and chemical composition of soot [159]. It was found that retarding the injection timing led to an increase in both number density and particle size which matched the experimental trends of exhaust measurements. The observation was because of higher charge stratification which in turn caused incomplete combustion in locally fuel-rich regions [174]. Most recently, Wang et al. [137] employed the same soot model and extended the engine model to include spray impingement and wall film evaporation. The chemistry calculations were performed using a detailed PRF mechanism consisting of 208 species among 1002 reactions. However, unlike the previous work which used C_2H_2 as the precursor [174], the nucleation of a soot particle was modelled by dimerization of A7. Although the simulated PSDF lay within the same order of magnitude as the measurements, particle size in the main mode of distribution was under-predicted by nearly a factor of two, causing lower total mass of soot computed. Hence, the results called for further model tuning and improvements. By tracing the evolution of particles in equivalence ratio-temperature diagrams, the study demonstrated that soot was mainly formed in the rich mixture near the wall caused by spray impingement [137].

Meanwhile, the adaptation of multi-step phenomenological models was seen in the works by Kwon et al. [175] and Kim et al. [176] who combined flamelet models for premixed and diffusion flames. Kwon et al. [175] induced a presumed shape of PDF approach to extend the flamelet model for partially premixed conditions along with pre-calculated laminar flame speeds from a TRF mechanism (120 species and 677 reactions). Furthermore, they modelled soot formation as a post-flame reaction with a phenomenological model proposed by Fusco et al. [184] for diesel engines. In the model, pyrolysis, inception, surface growth, coagulation and oxidation were described as global rate expressions with the rate constants fitted within the same range as those of elementary soot kinetic reactions. With collision frequency factors of radicals and C_2H_2 formation tuned, the computed number density (< a factor of 1.4) and volume fraction (< 33%) increased at higher intake pressure and agreed with the experimental results. Higher intake pressure was associated with higher in-cylinder temperature which favoured the formation of soot radicals and growth species [175]. Following a relatively similar approach, Kim et al. [176] integrated a flame kernel development model with the G-equation model to characterise the turbulent flame propagation. As the soot model of Fusco et al. [184] was suited for non-premixed combustion, a four-step phenomenological soot model based on the concepts of El-Asrag et al. [185] was applied for partially premixed combustion. The model included nucleation, surface growth via C_2H_2, coagulation and oxidation by oxygen and OH radicals. Nonetheless, the results on soot emissions were not presented.

Soot modelling in GDI engines was also carried out by the research group at Reaction Design using the FORTÉ software [177,178]. Full cycle simulations were performed by Naik et al. [177] to examine the combustion and emission behaviours. To account for the detailed chemistry effects, a seven-component surrogate was formulated with 230 species and 1740 reactions. The updated soot model treated soot as a pseudo-gas-phase species which only increased the size of fuel mechanism by two species, thus maintaining the computational efficiency. Soot nucleation, growth and oxidation were described in seven steps. Soot oxidation by nitrogen dioxide and sensitisation by steam were also included. The soot model was validated using species concentrations and soot mass fraction of premixed C_2H_4 flames. The computed results showed that retarding ignition timing caused an increase in soot volume fraction as observed experimentally. The results of soot volume fraction were, however, planar averaged

(two-dimensional) rather than cylinder-averaged. In a study by Liang et al. [178], a detailed soot model was coupled with the method of moments. The detailed soot model was developed by Puduppakkam et al. [186] and validated against soot particle size data in laboratory-scale flames of single-component fuels including n-heptane and toluene. The model was first applied for spray combustion of n-heptane and a jet fuel surrogate in a constant volume chamber to estimate lift-off lengths and soot volume fractions. Subsequently, the model simulated soot processes in a spray-guided GDI engine by illustrating the time evolution of soot cloud [178]. However, the engine results lacked validations from experimental measurements or optical diagnostics. Particularly, the study demonstrated that soot formation was mainly a post-flame phenomenon as also indicated in previous works [175,176]. Continuation of the work was reported recently by Puduppakkam et al. [187] to predict soot emissions from GDI engines. While the trend was correctly captured by the model, the magnitudes of average soot volume fraction were over-predicted by a factor of three as compared with the measurements obtained in a planar laser sheet.

Jiao and Reitz [63] investigated the significance of wall films as a soot source in GDI engines numerically. The gasoline fuel was represented by a TRF reaction mechanism comprising 89 species and 506 reactions. In the study, a semi-detailed soot model was adapted from the formulation by Vishwanathan and Reitz [188]. The improved model had been utilised successfully in a homogeneous charge SI engine to predict the PSDF of soot [189]. The model assumed that the smallest incipient particle size was 1.25 nm and experienced surface growth from both C_2H_2 and PAH. Particle coagulation was modelled through the normal square dependence. Soot oxidation was described to occur via oxygen and OH radicals. In spray combustion simulations of n-heptane, trends and magnitudes of peak soot volume fraction were estimated reasonably well with changes in ambient conditions. For GDI engine setups, the operating conditions included late injection and lean-burn stratified charge combustion. The results for spray, mixture distributions, combustion and emission were compared to those using the two-step soot model proposed by Hiroyasu [63]. Soot was formed and the mass increased continuously for the former while no soot mass was computed for the latter. The improved semi-detailed model was able to correlate soot formation to the vaporisation of wall films as observed in experiments. In a subsequent study [190], Jiao and Reitz examined the effects of engine operating parameters including fuel

composition, spray cone angle, injection timing and wall temperature on soot emissions. Particularly, the significance of using multi-component fuel surrogates was highlighted as the heavy components (low volatility) caused the formation of wall films which then contributed to soot emissions during combustion.

Coupled with a TRF mechanism of 85 species and 232 reactions, a soot particle model based on the method of moments was developed by An et al. [179] to simulate PAH and soot emissions from the GDI engine under 2000 rpm and 120 N m. Since a large amount of PAH adsorption was observed experimentally on the soot particle surface, PAH condensation of naphthalene (A2), acenaphthene (A2R5), phenanthrene (A3) and pyrene (A4) was included in the soot model. As the exhaust valve continuously opened, PAH and soot concentrations increased to gradually stabilised values which coincided with the measurements. They found that spatial distribution of soot number density was consistent with those of A4 and C_2H_2. Similarly, the method of moments was also adapted by Kim et al. [180], along with the G-equation model and laminar flamelet library generated from a reaction mechanism of PAH to numerically analyse the causes of soot reduction via increased injection pressure. The effect of injection pressure on soot emissions was however, over-predicted by 54–61% as compared to the experimental trends. Meanwhile, to reduce computational expenses, simple soot models were employed by Dong et al. [181] (two-step) and Gong et al. [183] (three-step) to predict soot mass. The models take into account soot formation and oxidation only, neglecting major phases of surface growth and coagulation. Thus, information on soot particle dynamics such as PSDF could not be extracted. Despite the agreement observed in volume fraction [181] and concentration [183] of soot, credibility of these simplistic models remains highly questionable. Moreover, the inadequacy of using a PAH reaction mechanism to account for soot formation in the work by Costa et al. [182] was manifested in the overall underestimation of PM mass density across both stoichiometric and stratified operations.

Soot modelling in GDI engines is still in its infancy hitherto with relatively limited works performed to investigate the soot formation mechanisms in detail. The focus of the modelling works is placed on stratified-charge combustion due to the associated higher PM emissions. It is apparent that most soot models adapted are based on the formulations previously applied to diesel engine combustion and/or derived from laboratory-scale flame configurations. Owing to the knowledge gained regarding the

importance of PAH as soot precursor, the recent soot models utilised for GDI engines consider nucleation of soot particles via A4 [63,177,178] and even A7 [137], as tabulated in Table 2-6. Moreover, the soot models are more comprehensive in nature in which the crucial phases of inception, surface growth, coagulation and oxidation are typically modelled as opposed to the conventional over-simplified empirical approaches. While the qualitative trends of soot emissions are often captured reasonably well, quantitative agreement of the numerical results with the experimental measurements is relatively poor. In addition, there is a lack of understanding in soot particle dynamics among the modelling works as the PSDF are not usually considered or accurately modelled. Hence, further enhancements in soot models at increasing details are needed to accurately describe soot processes in GDI engines, supported by consistent validations against optical images and engine-out measurements from test-bed facilities.

2.4 Concluding Remarks

Being a promising technology in the automotive industry, GDI engines hold great potential to substitute the conventional PFI engines. However, the emissions of ultra-fine PM by this type of engines represents one of the main challenges faced by major car manufacturers globally. While experimental and optical techniques are paving the way to significant advancements with detailed examination on in-cylinder events, numerical analysis through multi-dimensional CFD modelling plays an important role to facilitate the understanding of complex engine phenomena in a timely and cost-effective manner. Within this context, successful simulations of engine processes rely on accurate representation of practical fuels in terms of their chemical kinetics.

In order to acquire an in-depth understanding of PM processes within the GDI engine configurations through numerical modelling, the potential areas in the current field of study requiring close attention and improvements are identified as follows.

i. TRF mechanisms are likely to remain as a popular fuel model of gasoline for integration in CFD modelling in the foreseeable future. Despite the abundance of reaction mechanisms developed, most models are validated in HCCI engine conditions which deviate from those of GDI engines. At the same time, it has been well established that PAH chemistry is crucial in soot modelling. Hence,

the performance of TRF mechanisms, coupled with kinetic descriptions of PAH, should be investigated under GDI engine-like operating conditions.

ii. Current combustion modelling practices focus on characterising the turbulent flame propagation in GDI engines based on precompiled libraries and lookup tables for the chemistry effects. The libraries and tables are typically generated from the reaction mechanisms of a generalised fuel within a defined range of operating conditions under 0D and one-dimensional (1D) calculations. Thus, in order to better capture the effects of fuel chemistry in 3D engine modelling, pre-validated reduced reaction mechanisms can be incorporated directly into the CFD computations.

iii. Soot modelling studies for GDI engines are somehow limited with scant success achieved for accurate prediction of PM emissions. Although simple and multi-step phenomenological soot models have reproduced mass, volume fraction and number density of soot/PM measured from GDI engines, detailed information on the particle population represented by the PSDF is still lacking. Therefore, advanced computational approaches such as the method of moment and the sectional method need to be extended to the computation of major soot phases within GDI engines, along with the selection of large PAH as reliable precursor species.

CHAPTER 3
MATHEMATICAL MODELS AND GOVERNING EQUATIONS

3.1 Introductory Remarks

The chapter outlines the mathematical modelling employed in the present study, along with an in-depth description of the governing equations. The numerical framework to model gasoline fuels and GDI engine processes is elaborated thoroughly in terms of surrogate formulation, chemical kinetics and CFD computations. The methodology to propose the composition of a TRF surrogate that replicates the RON, MON and hydrogen/carbon (H/C) ratio of a real fuel is discussed in Section 3.2. Section 3.3 provides an overview of the relationships and formulations utilised in the chemical kinetic calculations in ANSYS Chemkin-Pro 17.2. The models include those of homogenous reactors and premixed laminar flame systems to calculate ID times, laminar flame speeds and speciation profiles. To facilitate further understanding of chemical reacting flows, sensitivity and rate-of-production (ROP) analyses adopted are also detailed. For multi-dimensional engine simulations in STAR-CD 4.30, the underlying conservation equations of fluid dynamics and basic construction of CFD sub-models are explained in Section 3.4, together with the evaluation of thermophysical properties of fluids. The important in-cylinder phenomena modelled cover turbulent mixing, spray and breakup of droplets, formation of liquid fuel film, film stripping, ignition and combustion as well as soot emissions.

3.2 Composition of TRF Surrogates

The degree of success of a TRF surrogate in emulating a complex gasoline fuel largely depends on the accuracy of its composition to resemble one or more target properties of the real fuel. To this end, several methodologies have been proposed to determine the optimised composition of the ternary mixture including linear and non-linear blending rules based on liquid volumes or mole fractions [191,192] and fitted correlations based on ID time measurements [193,194]. The simplistic linear-by-volume rule often introduces errors in estimating the associated properties of TRF,

particularly ON due to the synergistic and antagonistic effects arising from different fuel components. Hence, Morgan et al. [36] addressed the limitation by mapping the TRF compositions to the experimentally quantified RON and MON through a second order response surface model. Cai and Pitsch [28] further extended the correlations in the second order model by incorporating the H/C ratio to calculate the composition of a TRF surrogate given its RON and MON. In the present study, their work as shown in Equations (3-1)–(3-3) is utilised to determine the individual proportions of toluene ($C_6H_5CH_3$), n-heptane (C_7H_{16}) and isooctane (C_8H_{18}), respectively. The model coefficients were calibrated against the experimental data of a variety of ternary TRF mixtures.

$$C_6H_5CH_3 \text{ (in liquid volume \%)} = 1.9528 \times RON + 1.2987 \times MON - 5.3703 \times H/C - 0.0101 \times RON \times MON - 0.9047 \times RON \times H/C - 0.1244 \times MON \times H/C \quad (3\text{-}1)$$

$$C_7H_{16} \text{ (in liquid volume \%)} = -0.3592 \times RON + 1.9130 \times MON + 37.8896 \times H/C - 0.0097 \times RON \times MON + 0.2760 \times RON \times H/C - 0.9815 \times MON \times H/C \quad (3\text{-}2)$$

$$C_8H_{18} \text{ (in liquid volume \%)} = 100 - (C_6H_5CH_3 + C_7H_{16}) \quad (3\text{-}3)$$

3.3 Chemical Kinetics

Chemical kinetics encompasses the study of rates of chemical reactions with respect to the relevant parameters under varying operating conditions. Often, understanding chemical processes relies on thorough kinetic simulations of the underlying detailed chemistry for cost-effective design of systems with reduced environmental impacts. In this context, ANSYS Chemkin-Pro is a proprietary software tool for modelling the complex gas phase and surface chemistry reactions for the conceptual development of various combustion systems. The necessary chemical data required to run kinetic simulations in Chemkin-Pro are collectively grouped under a reaction mechanism as detailed in Table 3-1.

Table 3-1 Required chemical data in a reaction mechanism to run kinetic simulations in Chemkin-Pro.

File	Type	Description
chem.inp	Input	A description of the chemical reactions and their rate parameters occurring in the gas phase
therm.dat	Data	Thermochemical data of the chemical species
tran.dat	Data	Gas-phase transport data of the chemical species

In any chemically reacting-flow problem, state variables are used to define the thermodynamic and chemical states of the fluid mixture. In Chemkin-Pro, gas-phase state variables include pressure (p) in Pa, density (ρ) in kg/m^3, temperature (T) in K, mass fraction (Y_j), mole fraction (X_j) and molar concentration ($[X_j]$) in mol/m^3 of the j-th species. Pressure is a natural choice in situations where pressure is fixed while density is preferable in isochoric conditions. Temperature is always taken as a natural variable as it affects directly thermodynamic properties and chemical rate constants. Mass and mole fractions are useful in characterising the composition of a gas mixture. Molar concentration is also convenient due to the direct dependence of the rate of progress of reactions on the molar concentrations of reactants and products. The equation of state of an ideal multi-fluid gas is given by

$$p = \sum_{j=1}^{N_S} [X_j] RT \tag{3-4}$$

where N_S is the number of species and R is the universal gas constant in J mol^{-1} K^{-1}.

The standard-state thermodynamic properties of all species are expressed as functions of temperatures which are fitted with 14 NASA polynomial coefficients [195]. Seven of them are utilised for the low-temperature range (300–1000 K) and the other half is for the high-temperature range (1000–5000 K). At a given temperature, standard state molar constant-pressure heat capacity (C_p^o) in J mol^{-1} K^{-1}, enthalpy (H^o) in J/mol and entropy (S^o) in J mol^{-1} K^{-1} are calculated as follows:

$$C_p^o = a_1 + a_2 T + a_3 T^2 + a_4 T^3 + a_5 T^4 \tag{3-5}$$

$$\frac{H^o}{RT} = a_1 + \frac{a_2}{2}T + \frac{a_3}{3}T^2 + \frac{a_4}{4}T^3 + \frac{a_5}{5}T^4 + \frac{a_6}{T} \quad (3\text{-}6)$$

$$\frac{S^o}{R} = a_1 \ln T + a_2 T + \frac{a_3}{2}T^2 + \frac{a_4}{3}T^3 + \frac{a_5}{4}T^4 + a_7 \quad (3\text{-}7)$$

where a_n is the n-th NASA polynomial coefficient.

The interactions between gas-phase species are described by their chemical reactions. In theory, all thermal elementary reactions are reversible (i.e. the reaction products react with each other to reform the reactants). A reaction is termed irreversible if the backward reaction is neglected or the reversible reaction is represented by a pair of opposing irreversible reaction steps. The reaction rates typically change with temperature, pressure and species composition. The production rate of the j-th species ($\dot{\omega}_j$) in mol m^{-3} s^{-1} can be written as the sum of the rates of progress for all reactions involving the species as shown in Equation (3-8):

$$\dot{\omega}_j = \sum_{i=1}^{I} \upsilon_{j,i} q_i \quad (3\text{-}8)$$

where I is the total number of reactions involving the j-th species, $\upsilon_{j,i}$ and q_i are the difference between forward ($\upsilon'_{j,i}$) and reverse stoichiometric coefficients ($\upsilon''_{j,i}$) and the rate of progress, respectively for the i-th reaction. The rate of progress in mol m^{-3} s^{-1} is given by the difference between forward and reverse rates as

$$q_i = k_{f,i} \prod_{j=1}^{N_s} [X_j]^{\upsilon'_{j,i}} - k_{r,i} \prod_{j=1}^{N_s} [X_j]^{\upsilon''_{j,i}} \quad (3\text{-}9)$$

where $k_{f,i}$ and $k_{r,i}$ are the forward and reverse rate constants of the i-th reaction, respectively.

The forward rate constant of the i-th reaction is typically described by the modified Arrhenius equation:

$$k_{f,i} = AT^n \exp(-E_a/RT) \quad (3\text{-}10)$$

where A is the pre-exponential factor, n is the temperature exponent and E_a is the activation energy in cal/mol. Then, the reverse rate coefficient can be computed from

$$k_{r,i} = k_{f,i}/K_{c,i} \tag{3-11}$$

$$K_{c,i} = K_{p,i}\left(\frac{p_{atm}}{RT}\right)^{\sum_{j=1}^{N_s}\upsilon_{j,i}};\ K_{p,i} = \exp\left(\frac{\Delta S^o}{R} - \frac{\Delta H^o}{RT}\right) \tag{3-12}$$

where $K_{c,i}$ and $K_{p,i}$ are the equilibrium constants obtained from the thermodynamic properties of the species, p_{atm} is the atmospheric pressure in Pa and Δ refers to the change occurring in passing from reactants to products in the i-th reaction. For reactions involving third bodies, Equation (3-9) is modified as follows:

$$q_i = \left(\sum_{j=1}^{N_s}(a_{j,i})\,[X_j]\right)\left(k_{f,i}\prod_{j=1}^{N_s}[X_j]^{\upsilon'_{j,i}} - k_{r,i}\prod_{j=1}^{N_s}[X_j]^{\upsilon''_{j,i}}\right) \tag{3-13}$$

where $a_{j,i}$ is unity if all species in the mixture contribute equally as third bodies in the i-th reaction.

Gas-phase species transport properties become relevant where the transport of species and energy is rate limiting. Describing the molecular transport of species, momentum, and energy in a multi-component gaseous mixture requires the evaluation of diffusion coefficients, viscosities and thermal conductivities via mixture averaging rules or full multi-component approach. The momentum flux (τ) in kg m^{-1} s^{-2} is related to the gas mixture viscosity (μ) in kg m^{-1} s^{-1} and the velocities by

$$\tau = -\mu(\nabla\mathbf{v} + (\nabla\mathbf{v})^T) + \left(\frac{2}{3}\mu - \kappa\right)(\nabla\cdot\mathbf{v})\hat{\delta} \tag{3-14}$$

where $\mathbf{v}$ is the velocity vector in m/s, $\nabla\mathbf{v}$ is the dyadic product, $(\nabla\mathbf{v})^T$ is the transpose of the dyadic product , κ is the bulk viscosity in kg m^{-1} s^{-1} and $\hat{\delta}$ is the unit tensor. The energy flux (q) in J m^2 s^{-1} is expressed in terms of the thermal conductivity (k) in J m^{-1} s^{-1} K^{-1}as

$$q = \sum_{j=1}^{N_s} j_j h_j - k\nabla T - \sum_{j=1}^{N_s}\frac{RT}{W_j X_j}D_j^T d_j;\ d_j = \nabla X_j + (X_j - Y_j)\frac{1}{p}\nabla p \tag{3-15}$$

where j_j is the diffusive mass flux in J/kg, h_j is the specific enthalpy in J/kg, W_j is the molecular weight in kg/mol and D_j^T is the thermal diffusion coefficient in kg m^{-1} s^{-1} of the j-th species.

There is a wide array of reactor models available in Chemkin-Pro that addresses industry-specific reacting-flow conditions including open and closed homogenous systems, flow reactors and flame configurations. Detailed understanding of the effects of chemistry on the steady-state and transient solutions is achieved through sensitivity and ROP analyses. The list of reactor models employed in the current study to evaluate the chemical kinetics of reaction mechanisms based on the relevant experimental setups is described in Table 3-2.

Table 3-2 Descriptions of reactor models in Chemkin-Pro used to evaluate the chemical kinetics of reaction mechanisms.

Icon	Reactor model	Type	Description
	Closed Homogeneous Batch Reactor	0D	Transient, closed, homogeneous system or batch reactor
	PSR	0D	Transient or steady-state perfectly stirred reactor
	Premixed Laminar Flame-Speed Calculation	1D	Freely propagating flame for computing premixed laminar flame speeds
	Premixed Laminar Burner-Stabilised Flame	1D	Premixed, laminar flame stabilised on the burner

3.3.1 Homogenous Reactor Models

Closed Homogeneous Batch Reactor and PSR models are 0D homogenous systems whose behaviours are dominated by gas-phase chemical kinetics. The contents of the well-mixed or stirred reactor are assumed to be nearly spatially uniform due to high diffusion rates or forced turbulent mixing. In other words, the rate of conversion of reactants to products is controlled by chemical reaction rates and not by mixing process. Additionally, mass transport to the reactor walls is treated to be infinitely fast and the flow through the reactor must be characterised by a nominal residence time (τ) in s deduced from the flow rate and the reactor volume.

Conservations of mass, energy and species for the homogenous system include net generation of species within the volume and net loss of species and mass to surfaces

in the reactor. The global mass and species conservations are stated transiently in Equations (3-16) and (3-17), respectively.

$$\frac{d}{dt}(\rho V)^{(k)} = \sum_{i=1}^{N_{inlet}(k)} \dot{m}_i^{*(k)} + \sum_{r=1}^{N_{PSR}} \dot{m}^{(r)} R_{r,k} - \dot{m}^{(k)} + \sum_{m=1}^{M} A_m^{(k)} \sum_{j=1}^{N_s} \dot{s}_{j,m}^{(k)} W_j \tag{3-16}$$

$$(\rho V)^{(k)} \frac{dY_j^{(k)}}{dt} = \sum_{i=1}^{N_{inlet}(k)} \dot{m}_i^{*(k)} \left(Y_{j,i}^{*} - Y_j\right) + \sum_{r=1}^{N_{PSR}} \dot{m}^{(r)} R_{r,k} \left(Y_j^{(r)} - Y_j^{(k)}\right) \tag{3-17}$$

$$- Y_j^{(k)} \sum_{m=1}^{M} A_m^{(k)} \sum_{j=1}^{N_s} \dot{s}_{j,m}^{(k)} W_j + \left(\dot{\omega}_j V\right)^{(k)} W_j + \sum_{m=1}^{M} A_m^{(k)} \dot{s}_{j,m}^{(k)} W_j$$

t refers to the time in s, V is the reactor volume in m^3, k is the reactor number, i is the inlet number, N_{inlet} is the total number of inlets, N_{PSR} is the total number of reactor modules in the network, $\dot{m}^*$ is the inlet mass flow rate in kg/s, $\dot{m}$ is the outlet mass flow rate in kg/s, $R_{r,k}$ is the fraction of the outflow of the r-th reactor that is recycled into the k-th reactor, A_m is the surface area of the m-th material in m^2, M is the total number of materials, $\dot{s}_{j,m}$ is the molar surface production rate of the j-th species on the m-th material in mol m^{-2} s^{-1} and $Y_{j,i}^{*}$ is the mass fraction of the j-th species at the i-th inlet. For steady-state conditions, the nominal residence time is calculated as follows:

$$\tau = \frac{\rho V}{\left(\sum_{i=1}^{N_{inlet}(k)} \dot{m}_i^{*(k)} + \sum_{r=1}^{N_{PSR}} \dot{m}^{(r)} R_{r,k}\right)} \tag{3-18}$$

The energy balance is derived based on a control volume including the reactor, walls and any deposited material therein as shown in Equation (3-19).

$$\frac{dU_{sys}^{(k)}}{dt} = \sum_{i=1}^{N_{inlet}(k)} \dot{m}_i^{*(k)} \sum_{j=1}^{N_s} \left(Y_{j,i}^{*} h_{j,i}^{*}\right)^{(k)} + \sum_{r=1}^{N_{PSR}} \dot{m}^{(r)} R_{r,k} \sum_{j=1}^{N_s} \left(Y_j h_j\right)^{(r)} \tag{3-19}$$

$$- \left(\dot{m} \sum_{j=1}^{N_s} \left(Y_j h_j\right)\right)^{(k)} - Q_{loss}^{(k)} + Q_{source}^{(k)} - p^{(k)} \frac{dV^{(k)}}{dt}$$

U_{sys} is the total internal energy in J, $h_{j,i}^{*}$ is the specific enthalpy of the j-th species at the i-th inlet in J/kg, Q_{loss} is the net heat flux directed out of the reactor in J/s while Q_{source} is the energy deposited into the reactor in J/s.

3.3.2 Premixed Laminar Flame Models

For Premixed Laminar Flame-Speed Calculation and Premixed Laminar Burner-Stabilised Flame models, the flame propagation is treated as steady, isobaric and 1D. The former determines the characteristic flame speed of a gas mixture under specified pressure and inlet temperature while the latter is often used to analyse the speciation profiles in flame experiments. Both the models solve the set of differential equations describing the flame dynamics using implicit finite difference methods with combined time-dependent and steady-state methods. The solver algorithm automates coarse-to-fine grid refinement as a means to enhance the convergence properties of the steady-state approach and provide optimal mesh placement.

With the assumption of 1D flow and uniform inlet conditions, the conservation equations of continuity, energy and species are represented as

$$\dot{m} = \rho u A \tag{3-20}$$

$$\dot{m}\frac{dT}{dx} - \frac{1}{c_p}\frac{d}{dx}\left(kA\frac{dT}{dx}\right) + \frac{A}{c_p}\sum_{j=1}^{N_s}\rho Y_j V_j c_{p,j}\frac{dT}{dx} + \frac{A}{c_p}\sum_{j=1}^{N_s}\dot{\omega}_j h_j W_j + \frac{A}{c_p}\dot{Q}_{rad} = 0 \tag{3-21}$$

$$\dot{m}\frac{dY_j}{dx} + \frac{d}{dx}\left(\rho A Y_j V_j\right) - A\dot{\omega}_j W_j = 0 \tag{3-22}$$

where x denotes the spatial coordinate in m, $\dot{m}$ is the mass flow rate in kg/s, u is the velocity of the fluid mixture in m/s, c_p is the constant-pressure specific heat capacity in J kg^{-1} K^{-1}, V_j is the diffusion velocity of the j-th species in m/s, $\dot{Q}_{rad}$ is the heat loss due to gas and particle radiation in J/s and A is the cross-sectional area of the stream tube encompassing the flame normalised by the burner area in m^2. By adding time derivatives into Equations (3-21) and (3-22), the transient equations are obtained as

$$\rho A\frac{\partial T}{\partial t} + \dot{m}\frac{\partial T}{\partial x} - \frac{1}{c_p}\frac{\partial}{\partial x}\left(kA\frac{\partial T}{\partial x}\right) + \frac{A}{c_p}\sum_{j=1}^{N_s}\rho Y_j V_j c_{p,j}\frac{\partial T}{\partial x} + \frac{A}{c_p}\sum_{j=1}^{N_s}\dot{\omega}_j h_j W_j = 0 \tag{3-23}$$

$$\rho A\frac{\partial Y_j}{\partial t} + \dot{m}\frac{\partial Y_j}{\partial x} + \frac{\partial}{\partial x}\left(\rho A Y_j V_j\right) - A\dot{\omega}_j W_j = 0 \tag{3-24}$$

Using the mixture-averaged approach, the diffusion velocity which is composed of three parts is calculated as follows:

$$V_j = V_{o,j} + W_j + V_c \tag{3-25}$$

$$V_{o,j} = -D_{j,m}\frac{1}{X_j}\frac{dX_j}{dx} \tag{3-26}$$

$$W_j = \frac{D_{j,m}\Theta_j}{X_j}\frac{1}{T}\frac{dT}{dx} \tag{3-27}$$

where $V_{o,j}$ is the ordinary diffusion velocity in m/s, W_j is the thermal diffusion velocity in m/s of the j-th species, V_c is the correction velocity in m/s included to insure that the mass fractions always add up to unity, $D_{j,m}$ is the mixture-averaged diffusion coefficient in m^2/s and Θ_j is the thermal diffusion ratio.

3.3.3 Sensitivity Analysis and ROP Analysis

Sensitivity analysis of a problem solution enables quantitative understanding of how the solution depends on the available parameters within a model. To specify the sensitivity coefficients for steady-state calculations, the vector of governing equations is written as

$$F(\emptyset(\alpha); \alpha) = 0 \tag{3-28}$$

where the residual vector (F) depends on the solution vector ($\emptyset$) and a set of model parameters (α). By differentiating Equation (3-28) with respect to a parameter, α, a matrix equation for the sensitivity coefficients is obtained as

$$\frac{\partial F}{\partial \emptyset}\frac{\partial \emptyset}{\partial \alpha} + \frac{\partial F}{\partial \alpha} = 0 \tag{3-29}$$

The matrix $\partial F/\partial \emptyset$ is the Jacobian of the original system and $\partial F/\partial \alpha$ is the matrix of partial derivatives of F with respect to the parameters. The sensitivity coefficients matrix ($\partial \emptyset/\partial \alpha$) contains quantitative information on how each rate coefficient of reaction affects the temperatures and species mass fractions.

For transient problems, the system of ordinary differential equations is given in the general form

$$\frac{d\varphi}{dt} = F(\varphi, t; \alpha) \tag{3-30}$$

where φ is the vector of temperatures and species mass fractions. The first-order sensitivity coefficient matrix is defined as

$$w_{j,i} = \frac{\partial \varphi}{\partial \alpha_i} \tag{3-31}$$

where the subscripts j and i denote the dependent variables and reactions, respectively. To make the raw sensitivity coefficients more meaningful, the sensitivity coefficients are normalised in the form of logarithmic derivatives as

$$\left.\frac{\partial \ln Y_j}{\partial \ln \alpha_i}\right|_F = \left.\frac{\alpha_i}{Y_j}\frac{\partial Y_j}{\partial \alpha_i}\right|_F, \left.\frac{\partial \ln T}{\partial \ln \alpha_i}\right|_F = \left.\frac{\alpha_i}{T}\frac{\partial T}{\partial \alpha_i}\right|_F \tag{3-32}$$

where the subscript j denotes the j-th species.

ROP analysis determines the contribution of each reaction to the net production or destruction rates of a species, thus allowing the identification of dominant reaction paths in a reacting flow system. For a homogenous system, the molar production of species j (P_j) in mol m^{-3} s^{-1} is calculated by

$$P_j = \sum_{i=1}^{I} \upsilon_{j,i} q_i \tag{3-33}$$

where $\upsilon_{j,i}$ is the stoichiometric coefficient for the gas reaction while q_i is the rate of progress of the i-th reaction from I gas-phase reactions in mol m^{-3} s^{-1}.

Hence, the contribution to the ROP of species j from gas-phase reaction i ($C_{j,i}$) in mol m^{-3} s^{-1} is given by

$$C_{j,i} = \upsilon_{j,i} q_i \tag{3-34}$$

Furthermore, the normalised values of the reaction contributions to species production ($\overline{C}_{j,i}^{\,p}$) and destruction ($\overline{C}_{j,i}^{\,d}$) rates are determined using Equations (3-35) and (3-36), respectively.

$$\overline{C}_{j,i}^{\,p} = \frac{\max\left[\upsilon_{j,i}, 0\right] q_i}{\sum_{i=1}^{I} \max\left[\upsilon_{j,i}, 0\right] q_i} \tag{3-35}$$

$$\overline{C}_{j,i}^{\,d} = \frac{\min\left[\upsilon_{j,i}, 0\right] q_i}{\sum_{i=1}^{I} \min\left[\upsilon_{j,i}, 0\right] q_i} \tag{3-36}$$

3.4 CFD Modelling

CFD is a branch of fluid mechanics that produces quantitative predictions of fluid-flow phenomena based on the conservation laws governing fluid motion with the help of computers. Licensed by Siemens PLM Software, STAR-CD is a comprehensive CFD package for simulating the behaviour and improving the performance of ICE from intake to after-treatment. To complement the solver of STAR-CD, a pre- and post-processing environment called es-ice has been developed. The pre-processor enables the generation of computational meshes with accurate geometric details and the setup of operating conditions and modelling choices. The complex processes in ICE including turbulence, heat transfer, two-phase flow, evaporation and mixing, spray-wall impingement, film dynamics, chemistry and high-speed flow are accounted for by appropriate sub-models within STAR-CD.

3.4.1 Basic Conservation Equations

The Navier-Stokes equations solved by STAR-CD for general incompressible and compressible fluid flows in Cartesian tensor notation are

$$\frac{\partial \rho}{\partial t} + \frac{\partial}{\partial x_j}\left(\rho u_j\right) = s_m \tag{3-37}$$

$$\frac{\partial \rho u_i}{\partial t} + \frac{\partial}{\partial x_j}\left(\rho u_j u_i - \tau_{ij}\right) = -\frac{\partial p}{\partial x_i} + s_i \tag{3-38}$$

where x_i is the Cartesian coordinate (i = 1, 2, 3), u_i is the absolute velocity in m/s in direction x_i, τ_{ij} is the stress tensor components in N/m^2, s_m is the mass source in kg m^{-3} s^{-1}, s_i is the momentum source components in kg m^{-2} s^{-2} and the subscript j denotes summation (e.g. $\frac{\partial \rho u_j}{\partial x_j} = \frac{\partial \rho u_1}{\partial x_1} + \frac{\partial \rho u_2}{\partial x_2} + \frac{\partial \rho u_3}{\partial x_3}$). The constitutive relations connecting the components of the stress tensor to the velocity gradients for laminar and turbulent flows are provided in Equations (3-39) and (3-40), respectively.

$$\tau_{ij} = 2\mu s_{ij} - \frac{2}{3}\mu\frac{\partial u_k}{\partial x_k}\delta_{ij} \tag{3-39}$$

$$\tau_{ij} = 2\mu s_{ij} - \frac{2}{3}\mu\frac{\partial u_k}{\partial x_k}\delta_{ij} - \underbrace{\bar{\rho}\overline{u_i' u_j'}}_{\substack{\text{Turbulence-induced} \\ \text{Reynolds stresses}}} \tag{3-40}$$

The subscripts i, j and k refer to the directions x_i, x_j and x_k respectively, μ is the molecular dynamic viscosity in Pa s, s_{ij} is the rate of strain tensor in 1/s, δ_{ij}, the 'Kronecker delta', is unity when i equals to j or zero otherwise, u' is the fluctuation about the ensemble average velocity in m/s and the overbar indicates the ensemble averaging process.

Heat transfer is implemented through the general form of the chemico-thermal enthalpy conservation equation for a fluid mixture as

$$\frac{\partial \rho h}{\partial t} + \frac{\partial}{\partial x_j}\left(\rho h u_j + F_{h,j}\right) = \frac{\partial p}{\partial t} + u_j\frac{\partial p}{\partial x_j} + \tau_{ij}\frac{\partial u_i}{\partial x_j} + s_h \tag{3-41}$$

$$h = \bar{c_p}T - c_p{}^0 T_0 + \sum Y_m H_m = h_t + \underbrace{\sum Y_m H_m}_{\text{Chemical component}} \tag{3-42}$$

where h is the static enthalpy in J/kg, $F_{h,j}$ is the diffusional energy flux in direction x_j in J m^{-2} s^{-1}, s_h is the energy source in J m^{-3} s^{-1}, h_t is the thermal enthalpy in J/kg, $c_p{}^0$ is the reference constant-pressure specific heat capacity in J kg^{-1} K^{-1} at the reference temperature (T_0) in K and H_m is the heat of formation of constituent m in J/kg. The species conservation equation for each constituent m is given in the form of

$$\frac{\partial}{\partial t}(\rho Y_m) + \frac{\partial}{\partial x_j}\left(\rho u_j Y_m + F_{m,j}\right) = s_m \tag{3-43}$$

where $F_{m,j}$ is the diffusional flux component in kg m^{-2} s^{-1} and s_m is the rate of mass production or consumption in kg m^{-3} s^{-1}.

3.4.2 Thermophysical Properties

In the modelling framework of STAR-CD, thermophysical properties of fluids, namely density, viscosity, thermal conductivity, species diffusivities and specific heats are expressed as functions of pressure, temperature, mass fraction and other relevant parameters. Equations of state in describing the density vary based on the

type, compressibility and composition of fluids as well as the conditions they are subjected to.

3.4.2.1 Gaseous Mixture Properties

For a gaseous mixture consisting of multiple constituents in a 'background' fluid (bg), the constant-pressure specific heat capacity is computed as a mass-weighted average of its component values as follows:

$$c_p = \sum_{m \neq bg} Y_m c_{p,m} + \left(1 - \sum_{m \neq bg} Y_m\right) c_{p,bg} \tag{3-44}$$

The Wilke formula is used to calculate the mixture viscosity as

$$\mu = \sum_{i=1}^{N} \left(X_i \mu_i\right) \Bigg/ \left(\sum_{j=1}^{N} X_j \Phi_{ij}\right) \tag{3-45}$$

$$\Phi_{ij} = \frac{1}{\sqrt{8}} \left(1 + \frac{W_i}{W_j}\right)^{-1/2} \left(1 + \left(\frac{\mu_i}{\mu_j}\right)^{\frac{1}{2}} \left(\frac{W_j}{W_i}\right)^{\frac{1}{4}}\right)^2 \tag{3-46}$$

where i and j refer to components i and j, respectively while N is the total number of components in the mixture, including the 'background' fluid. To determine thermal conductivity of the gas mixture, the Mathur formula is utilised as follows:

$$k = \frac{1}{2}\left(\sum_{i=1}^{N} X_i k_i + 1 \Bigg/ \left(\sum_{i=1}^{N} \frac{X_i}{k_i}\right)\right) \tag{3-47}$$

The molecular diffusivity of component m in the gas mixture (D_m) in m^2/s is computed as

$$D_m = \left(\sum_{i=1,\, i \neq m}^{N} X_i W_i\right) \Bigg/ \left(\bar{W} \sum_{i=1,\, i \neq m}^{N} \frac{X_i}{D_{im}}\right) \tag{3-48}$$

where D_{im} is the binary diffusivity of components i and m in m^2/s.

The property values of the 'background' fluid and individual constituents can be calculated from polynomial relationships as functions of temperature. Thus, the specific heat of the constituent m can be determined from

$$\left(\frac{c_p}{R}\right)_m = \sum_i^n (a_m)_i \, T^{i-1} \tag{3-49}$$

where i and n are orders of the polynomial while a_m is a polynomial coefficient. For molecular viscosity, thermal conductivity and diffusivity, three optional relationships as shown in Equations (3-50)–(3-52) can be adopted.

$$\phi_m = \sum_i^n (\alpha_m)_i \, T^{i-1} \tag{3-50}$$

$$\ln(\phi_m) = \sum_i^n (\beta_m)_i \, (\ln T)^{i-1} \tag{3-51}$$

$$\ln(\phi_m) = \sum_i^n (\gamma_m)_i / (\ln T)^{i-1} \tag{3-52}$$

ϕ_m is μ, k or D_m while α_m, β_m and γ_m are polynomial coefficients.

3.4.2.2 Liquid Mixture Properties

For both Lagrangian two-phase flows and liquid film simulations, the properties of liquid mixtures are calculated as follows:

$$\rho = \left(\sum_i \frac{Y_{l,i}}{\rho_{l,i}}\right)^{-1} \tag{3-53}$$

$$c_p = \sum_i Y_{l,i} c_{p_{l,i}} \tag{3-54}$$

$$\ln \mu = \sum_i X_{l,i} \ln \mu_{l,i} \tag{3-55}$$

$$k = \sum_i \sum_j \varphi_i \varphi_j k_{ij} \; ; \; \varphi_i = \frac{X_{l,i} v_i}{\sum X_{l,j} v_j} \; ; \; k_{ij} = 2\left(k_i^{-1} + k_j^{-1}\right)^{-1} \tag{3-56}$$

$$\sigma = \left(\rho \sum_i \frac{X_{l,i} \sigma_i^{\frac{1}{4}}}{\rho_{l,i}} \right)^4 \tag{3-57}$$

$$T_c = \sum \varphi_i T_{c,i} \; ; \; \varphi_i = \frac{X_{l,i} v_{c,i}}{\sum X_{l,i} v_{c,j}} \tag{3-58}$$

where the subscript l denotes the liquid state, v is the specific molar volume in m^3 kg^{-1} mol^{-1}, σ is the surface tension in N/m and T_c is the critical temperature in K.

3.4.3 Turbulence Model

In the concept of eddy viscosity, the Reynolds stresses and turbulent scalar fluxes are directly linked to the local gradients of the mean flow field through a turbulent viscosity (μ_t) in Pa s and diffusivity. The most widely used eddy-viscosity based turbulence model is the k-ε model that comprises transport equations for the turbulence kinetic energy (k) in m^2/s^2 and its dissipation rate (ε) in m^2/s^3. The RNG k-ε model [196] is a variant of the standard model which is applied in high Reynolds number (Re) form in conjunction with law-of-the-wall functions. Accounting for the effects of compressibility and buoyancy, the transport equations for turbulence kinetic energy and turbulence dissipation rate derived via the RNG theory are

$$\frac{\partial}{\partial t}(\rho k) + \frac{\partial}{\partial x_j}\left(\rho u_j k - \left(\mu + \frac{\mu_t}{\sigma_k} \right) \frac{\partial k}{\partial x_j} \right) = \mu_t (P + P_B) - \rho\varepsilon - \frac{2}{3}\left(\mu_t \frac{\partial u_i}{\partial x_i} + \rho k \right) \frac{\partial u_i}{\partial x_i} \tag{3-59}$$

$$\frac{\partial}{\partial t}(\rho\varepsilon) + \frac{\partial}{\partial x_j}\left(\rho u_j \varepsilon - \left(\mu + \frac{\mu_t}{\sigma_\varepsilon} \right) \frac{\partial \varepsilon}{\partial x_j} \right) = C_{\varepsilon 1} \frac{\varepsilon}{k}\left(\mu_t P - \frac{2}{3}\left(\mu_t \frac{\partial u_i}{\partial x_i} + \rho k \right) \frac{\partial u_i}{\partial x_i} \right) \tag{3-60}$$

$$+ C_{\varepsilon 3} \frac{\varepsilon}{k} \mu_t P_B - C_{\varepsilon 2} \rho \frac{\varepsilon^2}{k} + C_{\varepsilon 4} \rho\varepsilon \frac{\partial u_i}{\partial x_i} - \frac{C_\mu \eta^3 (1 - \eta/\eta_0)}{1 + \beta\eta^3} \frac{\rho\varepsilon^2}{k}$$

$$\mu_t = \frac{C_\mu \rho k^2}{\varepsilon} \tag{3-61}$$

$$P = S_{ij} \frac{\partial u_i}{\partial x_j} ; \; S_{ij} = \frac{\partial u_i}{\partial x_j} + \frac{\partial u_j}{\partial x_i} \tag{3-62}$$

$$P_B = -\frac{g_i}{\sigma_h} \frac{1}{\rho} \frac{\partial \rho}{\partial x_i} \tag{3-63}$$

$$\eta = S\frac{k}{\varepsilon};\ S = \sqrt{2S_{ij}S_{ij}} \tag{3-64}$$

where σ_k, σ_ε and σ_h are turbulent Prandtl numbers, S_{ij} is the mean strain, g_i is the gravitational acceleration in m/s^2 while C_μ, $C_{\varepsilon1}$, $C_{\varepsilon2}$, $C_{\varepsilon3}$, $C_{\varepsilon4}$, η_0 and β are model coefficients whose values are tabulated in Table 3-3.

Table 3-3 Coefficients of RNG k-ε model derived numerically and empirically.

C_μ	σ_k	σ_ε	σ_h	$C_{\varepsilon1}$	$C_{\varepsilon2}$	$C_{\varepsilon3}$*	$C_{\varepsilon4}$	η_0	β
0.085	0.719	0.719	0.9	1.42	1.68	0.0/1.42	–0.387	4.38	0.012

* $C_{\varepsilon3}$ = 1.42 for $P_B > 0$ and is zero otherwise.

3.4.4 Fuel Spray and Atomisation Models

Dispersed multi-phase flows in ICE consist of a continuous phase (gaseous or liquid) and one or more dispersed phases in the form of liquid droplets. Generally, the motion of the dispersed phase is affected by that of the continuous one and vice versa via displacement and interphase momentum, mass and heat transfer effects. The flow modelling framework is of the Lagrangian/Eulerian kind, in which the conservation equations of mass, momentum and energy for the dispersed phase are written for each individual element. The governing equations for the carrier phase are expressed in modified Eulerian form to take account of the presence of the dispersed phase. For immense number of droplets, a statistical approach is adopted whereby the total population is modelled by a finite number of computational parcels, each of which represents a cluster of elements with the same properties.

3.4.4.1 Conservation Equations

The instantaneous fluid and droplet velocity vectors in m/s are denoted by $\mathbf{u}$ and $\mathbf{u}_d$, respectively. The subscript d indicates the droplet/dispersed phase whereas non-subscripted quantities refer to the continuous phase. The conservation equations of momentum, mass and energy for droplets in the Lagrangian framework are listed in Equations (3-65)–(3-67), respectively.

$$m_d\frac{d\mathbf{u}_d}{dt} = \mathbf{F}_{dr} + \mathbf{F}_p + \mathbf{F}_{am} + \mathbf{F}_b \tag{3-65}$$

$$\frac{dm_d}{dt} = -A_s F_m;\ F_m = K_g p_t \ln\frac{\left(p_t - p_{v,\infty}\right)}{\left(p_t - p_{v,s}\right)} \tag{3-66}$$

$$m_d c_{p,d}\frac{dT_d}{dt} = -A_s\left(h(T_d - T)\right) + h_{fg}\frac{dm_d}{dt} \tag{3-67}$$

$\mathbf{F}_{dr}$ is the drag force in N, $\mathbf{F}_p$ is the pressure force in N, $\mathbf{F}_{am}$ is the 'virtual mass' force required to accelerate the carrier fluid entrained by the droplet in N, $\mathbf{F}_b$ is the general body force which represents the effects of gravity and accelerations present in a non-inertial coordinate frame in N, A_s is the droplet surface area in m^2, K_g is the mass transfer coefficient, p_t, $p_{v,\infty}$ and $p_{v,s}$ are the gas pressure in Pa and partial pressures of vapour in the droplet surroundings and at its surface in Pa, respectively while h_{fg} is the latent heat of phase change in J/kg.

For multi-component droplets of a miscible liquid, the evaporation of each component depends on the other components because its vapour pressure is a function of the concentrations of these components in the mixture. To calculate the vapour pressure, Raoult's law is altered using the UNIQUAC Functional-group Activity Coefficients (UNIFAC) method as

$$p_{v,s,i} = \gamma_i X_{i,l} p_{v,s,i}^{\,o}\ ;\ \ln(\gamma_i) = \ln\underbrace{\left(\gamma_i^{\,C}\right)}_{\substack{\text{Due to molecular}\\ \text{size differences}}} + \ln\underbrace{\left(\gamma_i^{\,R}\right)}_{\substack{\text{Due to molecular}\\ \text{interactions}}} \tag{3-68}$$

where $p_{v,s,i}$ is the partial pressure of component i at the liquid-vapour interface in Pa, γ_i is the activity coefficient of component i, $X_{i,l}$ is its mole fraction in the liquid and $p_{v,s,i}^{\,o}$ is the saturation pressure of the pure substance that constitutes component i in Pa. For improved accuracy, the Modified UNIFAC model is introduced in which parameters of the contribution due to molecular size differences take into account the temperature dependence.

3.4.4.2 Droplet Breakup Model

Under the action of the interfacial forces induced by the motion of droplets relative to the continuous phase, the droplets become unstable and undergo the breakup process. The KH-RT breakup model described by Patterson and Reitz [197] comprises two competing mechanisms in which KH aerodynamic instabilities growing on a droplet surface are simultaneously calculated with RT instabilities caused by the deceleration

of the injected droplets. In a KH breakup, small droplets are shed by the parent computational parcel to form a new parcel whereas all droplets break up completely into new droplets of different sizes in an RT breakup. Their number is then adjusted to conserve mass while retaining the original number of parcels at the same time. The overall process is illustrated schematically in Figure 3-1.

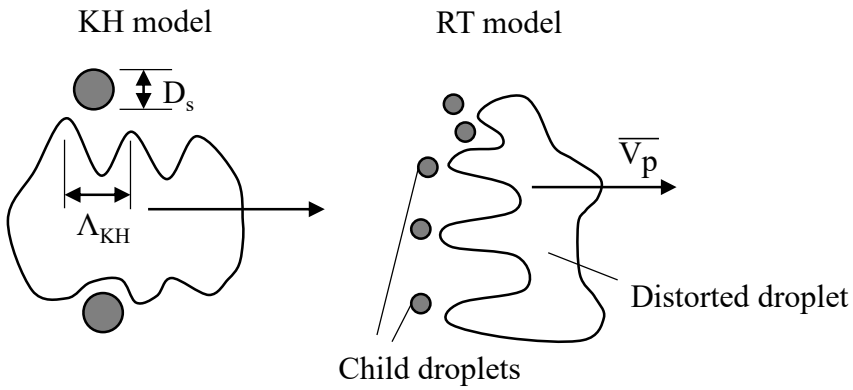


Figure 3-1 KHRT breakup process schematic.

In the KH model, a parent droplet with radius larger than the wavelength Λ_{KH} of the growing unstable surface wave in m will break into a new parent and child droplet pair. The diameter of the stable child droplet (D_s) in m is

$$D_s = 2B_0\Lambda_{KH} \tag{3-69}$$

where B_0 is a model constant of 0.61. Furthermore, the rate of change of the parent droplet diameter (D) in m is expressed as

$$\frac{dD}{dt} = -\frac{D - D_s}{\tau_{KH}};\ \tau_{KH} = \frac{3.726B_1\, D/2}{\Lambda_{KH}\Omega_{KH}} \tag{3-70}$$

where τ_{KH} is the characteristic KH breakup timescale in s, B_1 is a model constant of 40 and Ω_{KH} is the growth rate of the fastest growing wave in 1/s. If the difference between the original and new parcel masses is larger than a given threshold (3% of the original mass), the smaller droplets are shed off to form a new parcel.

To enable an RT breakup, the droplet diameter should be larger than the wavelength Λ_{RT} of the fastest growing wave in m, scaled by a constant C_3 of 0.1 so that

$$D > C_3\Lambda_{RT} \tag{3-71}$$

Additionally, sufficient time greater than the RT breakup timescale (τ_{RT}) in s must have elapsed since the last RT breakup. The breakup timescale is calculated as

$$\tau_{RT} = \frac{C_\tau}{\omega_{RT}};\ \omega_{RT} = \omega(k_{RT});\ k_{RT} = \frac{2\pi}{\Lambda_{RT}} \tag{3-72}$$

where C_τ is a model constant of unity and ω_{RT} is the maximum growth rate in 1/s expressed in terms of the associated wave number (k_{RT}) in 1/m. The approach assumes a viscid form of the RT mechanism as viscosity can have a significant effect on instability for the high decelerations typical of spray droplets.

3.4.4.3 Turbulent Dispersion

A droplet in a turbulent flow experiences a randomly-varying velocity field to which it responds according to its inertia. Using a stochastic approach, the model assumes that as a droplet traverses the turbulent flow field, it interacts with a sequence of turbulent eddies. It is also assumed that the fluctuating velocity within each eddy is isotropic and obeys a Gaussian PDF. Moreover, the interaction time is taken to be sufficiently short that the fluid velocity in a given eddy is effectively constant during the process. Thus, the droplet experiences an instantaneous fluid velocity in each eddy given by

$$\mathbf{u} = \mathbf{U} + \mathbf{u'} \tag{3-73}$$

where **U** is the local average velocity in m/s and **u'** is the random perturbation calculated from a Gaussian PDF in m/s.

3.4.4.4 Initial Droplet Size Distributions

The nozzle community have over the years gathered vast amount of test data regarding droplet size distributions for different types of nozzles. The data are correlated into numerous size distribution functions whose form and applicability are well known. The Rosin-Rammler distribution is defined as

$$Q = 1 - \exp\left(-\left(\frac{D}{X}\right)^q\right) \tag{3-74}$$

where Q is the mass fraction of droplets having diameter less than D while X and q are user-supplied empirical parameters. They are related to a characteristic diameter known as the Sauter mean diameter (SMD) in m as follows:

$$\mathrm{SMD} = \frac{\mathrm{X}}{\Gamma\left(1 - \frac{1}{\mathrm{q}}\right)} \tag{3-75}$$

where Γ is the gamma function whereas SMD is defined in terms of the number-based distribution (f_{number}) as

$$\mathrm{SMD} = \frac{\int_0^\infty \mathrm{D}^3 \mathrm{f}_{\mathrm{number}}(\mathrm{D})\,\mathrm{dD}}{\int_0^\infty \mathrm{D}^2 \mathrm{f}_{\mathrm{number}}(\mathrm{D})\,\mathrm{dD}} \tag{3-76}$$

3.4.4.5 Particle-Wall Interaction

The outcome of an impingement event depends on dynamic characteristics of the droplets, physical properties of the liquid and wall surface conditions. The Bai-ONERA model incorporates features of wall impingement models developed by Bai and Gosman [198] and by Rosa et al. [199] to determine the impingement regime transition criteria. Three possible outcomes of an impact include deposition/spread, rebound and splashing, depending on a dimensionless parameter K defined as

$$\mathrm{K} = \mathrm{WeOh}^{-0.4} = \left(\mathrm{We}^2\mathrm{Re}\right)^{0.4} \tag{3-77}$$

where We and Oh are the Weber and Ohnesorge numbers, respectively. The critical numbers characterising the transitions between deposition and splashing and between deposition and rebound are denoted as K_s and K_r, respectively. The transition criteria are plotted graphically in Figure 3-2 as logarithm of K against a dimensionless temperature, T^* that is defined as

$$\mathrm{T}^* = \frac{\mathrm{T_W} - \mathrm{T_N}}{\mathrm{T_W} - \mathrm{T_L}} \tag{3-78}$$

where T_W is the wall temperature in K, T_N is the Nukiyama temperature in K and T_L is the Leidenfrost temperature in K. The two dotted lines in Figure 3-2(a) indicate that the transition can occur within the area bounded based on the wall surface roughness.

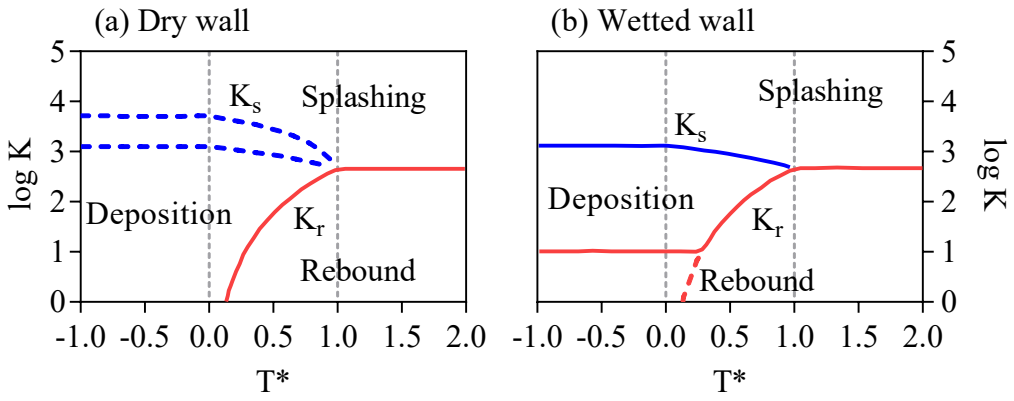


Figure 3-2 Transition criteria of the Bai-ONERA model for a (a) dry wall and a (b) wetted wall [199].

3.4.5 Liquid Films

The formation of liquid films is a common phenomenon in ICE when sprays from fuel injectors impinge and form a film on the walls of intake ports, valves and pistons. The film behaviour affects the subsequent mixture formation, combustion and emission processes strongly. The basic model to solve liquid film equations is of the Eulerian framework which accounts for convective transport of conserved quantities within the film and from/to the gas phase.

3.4.5.1 Conservation Equations

The mass conservation equation is provided as

$$\frac{\partial \rho_l}{\partial t} + \nabla \cdot (\rho_l \mathbf{u}_l) = \frac{\dot{m}_{imp}}{h} \tag{3-79}$$

where the subscript l represents the liquid film, h is the film thickness in m and $\dot{m}_{imp}$ is the mass source/sink per unit area in kg m^{-2} s^{-1} due to droplet wall impingement or film separation. The mass conservation equation of species i is given by

$$\frac{\partial}{\partial t}(\rho_l Y_{i,l}) + \nabla \cdot (\rho_l \mathbf{u}_l Y_{i,l}) = \nabla \cdot (\rho_l D_l \nabla Y_{i,l}) + \frac{\dot{m}_{i_{imp}}}{h} \tag{3-80}$$

where D_l is the mass diffusion coefficient in m^2/s.

The momentum conservation equation is described as

$$\frac{\partial}{\partial t}\left(\rho_l \mathbf{u}_l\right) + \nabla\cdot\left(\rho_l \mathbf{u}_l \mathbf{u}_l\right) = \nabla p_l + \rho_l \mathbf{g} + \nabla\cdot\tau_l + \mathbf{S}_{imp}\delta(\xi - h) \tag{3-81}$$

where $\mathbf{g}$ is the gravitational acceleration vector in m/s^2, τ_l is the stress tensor within the film in N/m^2, $\mathbf{S}_{imp}$ is the momentum source corresponding to the mass source in kg m^{-3} s^{-2}, δ denotes the Dirac delta function while ξ is the local coordinate normal to the wall in m.

The conservation equation for enthalpy is as follows:

$$\frac{\partial}{\partial t}\left(\rho_l h_l\right) + \nabla\cdot\left(\rho_l \mathbf{u}_l h_l\right) = \nabla\cdot(k_l \nabla T_l) + \frac{\dot{Q}_{imp}}{h} \tag{3-82}$$

where h_l and k_l are enthalpy in J/kg and thermal conductivity in J m^{-1} s^{-1} K^{-1} of the liquid film, respectively while $\dot{Q}_{imp}$ represents the enthalpy source corresponding to the mass source in J m^{-2} s^{-1}.

3.4.5.2 Condensation/Evaporation

The condensation/evaporation rate ($\dot{m}_{con}$) in kg/s at the film surface is computed as

$$\dot{m}_{con} = \frac{\sum_i \rho_{i,g_{int}} D_{i,g} \ln(1+B)\left(Y_{i,g_{cell}} - Y_{i,g_{int}}\right)}{B\left(1 - \sum_i Y_{i,g_{int}}\right)} \tag{3-83}$$

where the subscript g denotes the gas phase, the subscript cell denotes the cell centroid next to the film cell, the subscript int denotes the interface and B is the Spalding transfer number. The summations are taken over all species contained within the film.

3.4.5.3 Film Stripping

Subject to the physical processes and the wall geometry, the liquid film can become detached from the wall and form droplets. There are three ways of film stripping: (1) stripping due to wave instability, (2) stripping due to body-force induced instability and (3) breakup caused by flow over a sharp edge. For the first two mechanisms, waves develop at the liquid-gas interface. The growing waves then become unstable and form cylinders of liquid which are ejected into the surrounding gas. The cylinders further break up into spherical droplets. The model is closed by computing the wavelength for which surface breakup is most likely to occur. It is known as the resonance wavelength (λ_r) in m which is calculated using the dispersion equation as

$$\lambda_r = \frac{2\pi}{\rho_l \mathbf{g}\cdot\mathbf{n}}\left(\frac{1}{3}\rho_g \Delta\mathbf{U}^2 - \sqrt{\left(\frac{1}{3}\rho_g \Delta\mathbf{U}^2\right)^2 - \rho_l \mathbf{g}\cdot\mathbf{n}\sigma}\right) \tag{3-84}$$

where $\Delta\mathbf{U}^2$ is the gas/film relative velocity in m^2/s^2, **n** is the vector normal to the film surface and σ is the surface tension in N/m.

The model for the breakup of liquid films over a sharp edge is established based on the RT instability. The model is applied only for edges whose corner angle (θ) in rad is larger than a predefined minimum angle. The force ratio (FR) is defined as the ratio of film momentum flux to the surface tension and gravity force as follows:

$$FR = \frac{We_l}{\max\left[1 + \frac{1}{\sin\theta} + Bo_l \frac{L_b}{h_l \sin\theta},\ 10^{-20}\right]} \tag{3-85}$$

where the subscript l denotes the liquid film, Bo_l is the liquid film Bond number, L_b is the breakup length in m while h_l is the film thickness in m. The breakup is deemed to occur if FR is greater than unity.

3.4.6 Combustion Model

The Detailed Chemistry model in STAR-CD is designed to incorporate chemical kinetics in ICE simulations. The model efficiently solves transport equations for all chemical species using reaction mechanisms input in an identical manner as described in Table 3-1 for Chemkin-Pro. The transport equations for species mass fractions are

$$\frac{\partial}{\partial t}(\rho Y_i) + \frac{\partial}{\partial x_j}\left(\rho u_j Y_i - \underbrace{F_{i,j}}_{\substack{\text{Diffusion flux}\\ \text{component}}}\right) = S_i \tag{3-86}$$

$$F_{i,j} = \frac{\mu_t}{Sc_i}\frac{\partial Y_i}{\partial x_j} + \rho D_{im}\frac{\partial Y_i}{\partial x_j} + \frac{D_i^T}{T}\frac{\partial T}{\partial x_j} \tag{3-87}$$

where S_i is the source term due to chemical reactions and/or any user-defined sources in kg m^{-3} s^{-1}, Sc_i is the Schmidt number for species i, D_{im} is the molecular diffusivity of species i in the mixture in m^2/s while D_i^T is the thermal diffusion coefficient of species i in kg m^{-1} s^{-1}.

Due to the large differences in time scale between different reactions in a system, the set of transport equations is often very 'stiff'. Using the time-split numerical solution method, Equation (3-86) can be written as

$$\frac{\partial}{\partial t}(\rho Y_i) + \frac{\partial}{\partial x_j}\left(\rho u_j Y_i - F_{i,j}\right) = 0 \tag{3-88}$$

$$\frac{d}{dt}(\rho \mathbf{Y}) = \mathbf{S};\ \mathbf{Y} = (Y_1, Y_2, \ldots, Y_n);\ \mathbf{S} = (S_1, S_2, \ldots, S_n) \tag{3-89}$$

To expedite the computation, the dynamic multi-zone (DMZ) partitioning method is adopted to create groups of computational cells sharing a similar thermo-chemical state. With this approach, Equation (3-89) is solved for each group instead of for each cell to warrant a substantial saving in the associated computational time. The overview of the DMZ method within the Detailed Chemistry model is illustrated in Figure 3-3.

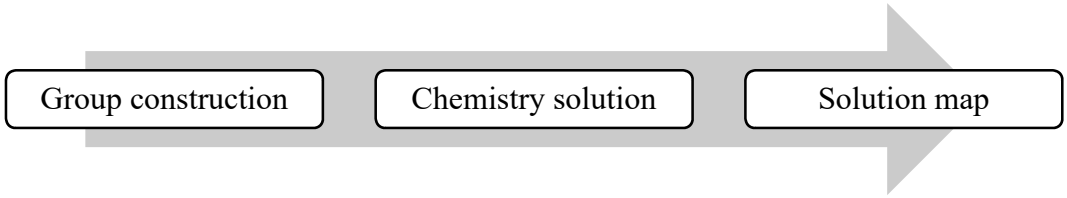


Figure 3-3 Sequential steps of the DMZ method within the Detailed Chemistry model.

Groups are constructed by clustering cells that are in similar thermal and chemical states described by certain characteristic quantities. These quantities can include temperature (representing the combustion progress), mixture fraction (representing the mixing process), enthalpy (representing the energy level) and mass fractions of species. Group mean quantities are determined by averaging the corresponding quantities for all cells in the group according to

$$Y_{i,g} = \frac{\sum Y_{i,j}\rho_{i,j}V_j}{\sum \rho_{i,j}V_j},\ \rho_{i,g} = \frac{\sum \rho_{i,j}V_j}{\sum V_j},\ T_g = \frac{\sum T_j V_j}{\sum V_j},\ p_g = \frac{\sum p_j V_j}{\sum V_j} \tag{3-90}$$

where the subscripts i, j and g denote species i, cell j and group g, respectively while V is the cell volume in m^3.

Subsequently, the calculated mean mass fractions of a group can be advanced in time by solving Equation (3-89) in the form

$$\rho_{i,g}\frac{\partial Y_{i,g}}{\partial t} = \omega_{i,g} \tag{3-91}$$

where $\omega_{i,g}$ is the reaction rate of species i in group g in 1/s, evaluated on the basis of group mean quantities. After the chemistry solution is obtained for each group, the mean reaction rate of all species in the group can be deduced. Through solution mapping, the mass fractions of all species in a cell at the (n + 1)-th time-step can be calculated as follows:

$$Y_i^{n+1} = Y_i^n + \delta t \cdot \overline{\omega_{i,g}};\ \overline{\omega_{i,g}} = \frac{Y_{i,g}^{\ n+1} - Y_{i,g}^{\ n}}{\delta t} \tag{3-92}$$

The mapping algorithm makes sure that the mass fractions of species are bounded and conservations of mass and atoms are maintained accordingly.

To simulate the SI process, a numerical ignition model is implemented in which the spark is initiated from a specified position for a defined period. The spark kernel size is 2 mm while the ignition temperature is given as 2500 K. The latter is used in the calculation of reaction rates inside the spark kernel.

3.4.7 Soot Model

In ICE, the formation of soot is mostly an unwanted by-product of incomplete combustion of hydrocarbons, often resulting in a loss in combustion efficiency. The challenges in accurate soot modelling are posed by the inherent complexity of the associated processes including fuel pyrolysis, formation of PAH, particle inception, surface growth, coagulation and oxidation of soot particles and intermediates. The sectional method solves a transport equation for mass fraction of soot in a predefined number of sections. The soot content in each computational cell is divided into the fixed number of sections based on the particle diameter. Solving for the mass fraction in each section generates the local mass fraction distribution, thus also providing the PSDF, number density, mass density and mean diameter of soot particles.

The model formulation involves a description of sections containing soot particles of equal volume, allowing a volume-based discretisation of particle sizes together with the conservations of number density and mass. The minimum ($V_{i,min}$), maximum ($V_{i,max}$) and mean ($V_{i,m}$) volumes of each section i in m^3 are given by

$$V_{i,min} = \frac{3V_{PAH}}{2} 2^{i-1} \tag{3-93}$$

$$V_{i,max} = 2V_{i,min} \tag{3-94}$$

$$V_{i,m} = \frac{V_{i,min} + V_{i,max}}{2} \tag{3-95}$$

where V_{PAH} is the volume of PAH in m^3. The default number of sections is 20 as depicted in Figure 3-4 with the respective soot diameter (D) in m shown. The sections correspond to soot particles with the diameter range of 1.05–106 nm.

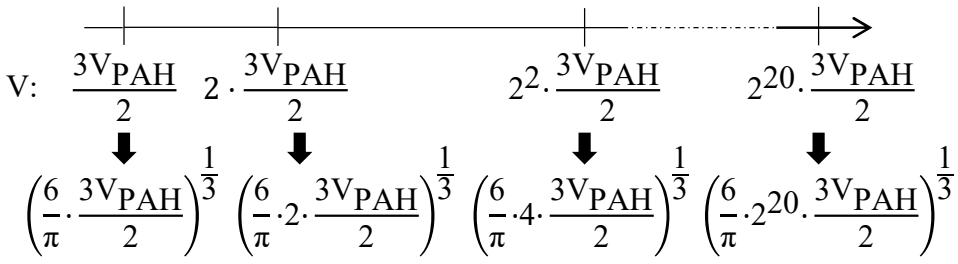


Figure 3-4 Schematic of soot diameter distribution within 20 sections.

In computing the soot mass in each section i, the formation and oxidation processes ranging from gas phase to solid interactions covered in the model are:

- Inception or nucleation, being the formation of first particles from the gas phase by collisions between two PAH molecules
- Condensation of PAH on the particle surfaces
- Coagulation characterising the inter-particle collisions to form bigger particles
- Surface growth and oxidation of particles based on the HACA mechanism.

The soot mass fraction per section i is then solved by the following set of transport equations:

$$\bar{\rho} \frac{\partial Y_{i,soot}}{\partial t} + \bar{\rho} u_j \frac{\partial Y_{i,soot}}{\partial x_j} = \frac{\partial}{\partial x_j} \left(\bar{\rho} \frac{\mu_t}{Sc_{soot}} \frac{\partial Y_{i,soot}}{\partial x_j} \right) + \rho_{soot} \Omega_{i,soot} \tag{3-96}$$

$$Y_{i,soot} = \frac{mass_{i,soot}}{mass_{cell}} \tag{3-97}$$

where Sc_{soot} is the Schmidt number, ρ_{soot} is the density of a soot particle in kg/m^3, $\Omega_{i,soot}$ is the source term in 1/s expressed in Equations (3-98)–(3-103), $mass_{i,soot}$ is the soot mass in section i of a cell in kg and $mass_{cell}$ is the gas mass of the cell in kg.

$$\Omega_{i,soot} = \Omega_{i,pi} + \Omega_{i,cond} + \Omega_{i,sg} + \Omega_{i,ox} + \Omega_{i,coag} \quad (3\text{-}98)$$

$$\Omega_{1,pi} = C_{pi} f_{pi}\left(Y_{j=1,soot}^{i,max}, T\right); \Omega_{i \neq 1,pi} = 0 \quad (3\text{-}99)$$

$$\Omega_{i,cond} = C_{cond} f_{cond}\left(Y_{i,soot}, T\right) \quad (3\text{-}100)$$

$$\Omega_{i,sg} = C_{sg} f_{sg}\left(Y_{i-1,soot}, Y_{i,soot}\right) \quad (3\text{-}101)$$

$$\Omega_{i,ox} = C_{ox} f_{ox}\left(Y_{i,soot}, Y_{i+1,soot}\right) \quad (3\text{-}102)$$

$$\Omega_{i,coag} = f_{coag}\left(Y_{j=1,soot}^{i,max}, T, p\right) \quad (3\text{-}103)$$

The subscripts pi, cond, sg, ox and coag denote particle inception, PAH condensation, surface growth, oxidation and coagulation of soot particles, respectively. Ω is the source term for a particular process while C and f are the corresponding scale factor and function describing the process. The source terms are computed on the fly at each time-step from the mass fractions of relevant species and temperatures derived from the Detailed Chemistry model. The inception model is PAH-based whereby the nucleation rate is supplied by the collision rate between two PAH molecules. All the scale factors are tuneable to replicate the experimental results except for coagulation whose function is entirely established on the physical interactions between particles.

By solving the transport equations for soot mass fractions, additional characteristic quantities related to soot particles can be extracted for post-processing as determined using Equations (3-104)–(3-107). Total number density (TOTN) of soot is defined as the total number of particles per unit volume in 1/m^3. Total soot volume fraction (FV) represents the volume fraction occupied by soot in a given cell while the total mass of soot relative to a given cell volume is known as total mass density (MSOOT) in kg/m^3. Assuming soot particles are spherical, average soot diameter (AVGD) in m can be estimated through total number density and volume fraction of soot. The normalised PSDF of soot expressed on a logarithmic scale of diameters is drawn from the model through Equation (3-108).

$$TOTN = \sum_{i=1}^{i_{max}} N_i \; ; \; N_i \approx \frac{\rho_{cell} Y_{i,soot}}{\rho_{soot} V_{i,m}} \tag{3-104}$$

$$FV = \sum_{i=1}^{i_{max}} \frac{\rho_{cell} Y_{i,soot}}{\rho_{soot}} \tag{3-105}$$

$$MSOOT = FV \cdot \rho_{soot} = \sum_{i=1}^{i_{max}} \rho_{cell} Y_{i,soot} \tag{3-106}$$

$$AVGD = \left(\frac{6FV}{TOTN \cdot \pi} \right)^{1/3} \tag{3-107}$$

$$\frac{dN(i)}{d\log(D)\,N} = \frac{N_i / TOTN}{\frac{1}{3}\log\left(\frac{6V_{i,max}}{\pi}\right) - \frac{1}{3}\log\left(\frac{6V_{i,min}}{\pi}\right)} = \frac{3}{\log 2}\frac{N_i}{TOTN} \tag{3-108}$$

3.5 Concluding Remarks

To represent real gasoline fuels, the compositions of TRF surrogates are optimised based on the key properties to be emulated, namely RON, MON and H/C ratio through the improved second order response surface model. With Chemkin-Pro, appropriate 0D and 1D models described are applied to simulate experimental kinetic studies in evaluating the chemistry of TRF mechanisms as summarised in Table 3-4. In-depth understanding of chemical kinetic simulations is drawn through sensitivity and ROP analyses. Subsequently, 3D engine simulations are performed in STAR-CD through an integrated CFD-chemical kinetic modelling approach. Various CFD sub-models defined in the numerical framework to characterise the complex in-cylinder events are summarised in Table 3-5.

Table 3-4 0D and 1D models in Chemkin-Pro used for chemical kinetic simulations.

Measurement	Facility	Model	Section
ID time	ST	Closed Homogenous Batch Reactor	4.4
Flame speed	Flame	Premixed Laminar Flame-Speed Calculation	4.5
Speciation	Flame	Premixed Laminar Burner-Stabilised Flame	4.6.1
	JSR	PSR	4.6.2

Table 3-5 CFD sub-models in STAR-CD adopted for 3D engine simulations.

Process	Model	Description
Turbulence	RNG k-ε	Refined k-ε model via the RNG theory
Breakup	KH-RT	A composite process of competing KH and RT breakup mechanisms
Wall impingement	Bai-ONERA	Forms transition criteria between deposition, rebound and splashing
Liquid film	Numerical	Predicts the dynamic characteristics of fuel films in the Eulerian framework
Ignition	Numerical	Defined in terms of period, position, temperature and kernel size
Combustion	Detailed Chemistry	Solves transport equations for chemical species through reaction mechanisms
Soot emissions	Sectional	Computes soot mass fraction through a volume-based discretisation of particle sizes

CHAPTER 4
EVALUATIVE STUDY OF TRF MECHANISMS

4.1 Introductory Remarks

In this chapter, three TRF mechanisms are identified from the literature based on their applicability and relevance to gasoline engine modelling in Section 4.2. Chemical kinetics of the reaction mechanisms is assessed numerically under various test configurations with GDI engine-like operating conditions from Section 4.3 to Section 4.6. The evaluative study serves to achieve the optimum trade-off between accuracy and computational load, where the limiting factor is the size of mechanism in terms of numbers of species and reactions. The experimental setups employed are ST, JSR and flame burners. The validation criteria cover ID time, species concentration profile and laminar flame speed. In Section 4.7, the performance of each TRF mechanism in replicating the experimental measurements is then compared and contrasted through a dissection of chemical kinetic analyses. Subsequently, the optimal TRF mechanism is selected in Section 4.8 for the integration in GDI engine modelling.

4.2 Reduced Mechanisms of TRF

As compared to isooctane and PRF mechanisms, TRF mechanisms are better suited to emulate real gasoline fuels because they account for fuel sensitivities induced by differences in RON and MON. The available TRF mechanisms listed in Table 2-3 are illustrated graphically in Figure 4-1. It is apparent that there is a linear increasing trend between the numbers of species and reactions. With higher numbers of species and reactions, the enhanced accuracy of chemical kinetics comes at a cost of imposing larger computational loads in numerical simulations. Therefore, the use of reaction mechanisms in CFD engine modelling is generally limited to reduced mechanisms with typically less than 200 species.

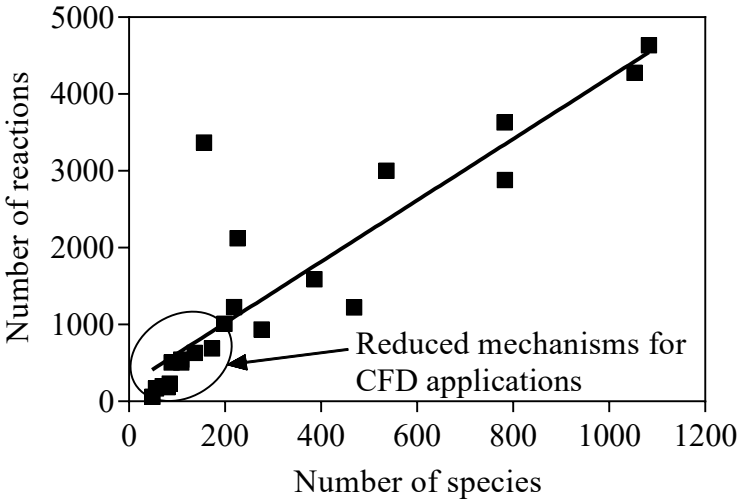


Figure 4-1 TRF mechanisms represented in terms of numbers of species and reactions.

In this study, the selection of TRF mechanisms for further evaluations is carried out based on the following considerations: (1) applicability in GDI combustion systems, (2) incorporation of the PAH chemistry as soot precursor species and (3) compactness of the reaction mechanisms for reasonable computational effort. The wide array of TRF mechanisms has thus been narrowed down to three potential options which fulfil the aforementioned selection criteria as detailed in Table 4-1. They are all reduced TRF mechanisms which have been utilised as gasoline surrogates in CFD modelling studies of engine combustion and emission. For brevity, the mechanisms are referred to in the 'first author-TRF' convention hereafter.

Table 4-1 Potential reduced TRF mechanisms identified.

Mechanism	N_S	N_R	Brief description	Reference
Jiao-TRF	89	506	Models soot formation from liquid films in a stratified-charge GDI engine	[63]
Wang-TRF	109	543	Models combustion and emission in compression ignition engines	[65]
An-TRF	85	232	Models PAH formation and evolution in a GDI engine	[67]

From Table 4-1, the number of species is almost similar for all the three TRF kinetic models with fewer than 110 species. However, both Jiao-TRF and Wang-TRF possess

more than double the number of reactions of An-TRF, thus rendering the number of reactions one of the major elements in the evaluative study. In order to retain and enhance the predictive accuracy for isooctane and TRF surrogates, respectively, the pre-exponential factors of two consumption pathways of isooctane under An-TRF as shown in Table 4-2 were adapted from the original works of Liu et al. [60]. The resulting improvements of chemical kinetics for An-TRF are depicted and discussed in Section 4.4 till Section 4.6.

Table 4-2 Adapted rate coefficients for two reactions of isooctane under An-TRF.

Reaction	A (cm^3/mol/s)	n	E_a (cal/mol)	Reference
$C_8H_{18} + O_2 = C_8H_{17} + HO_2$	6×10^{15}	0	46,000	[60]
$C_8H_{18} + OH \rightarrow C_8H_{17} + H_2O$	2×10^{13}	0	3,000	[60]

4.3 Validation Criteria Based on GDI Engine-Like Operating Conditions

Despite the continuing advancement in chemical kinetics of gasoline surrogates, only a few TRF mechanisms have been applied in CFD modelling of GDI combustion systems [63,67,179,190]. Those models are typically validated under HCCI engine operations without addressing the inherent differences arising from GDI combustion mode. Fundamental understanding of chemical kinetics in GDI engines is further complicated by the indecisive role of turbulence on the chemical processes occurring behind the turbulent flame front [75]. Therefore, it is of utmost importance to establish the critical range of operating conditions and environments within GDI systems to which the development of mechanisms can be tailored to accordingly.

The validation criteria used to evaluate the chemical kinetics of TRF mechanisms are established based on the wall-guided GDI engine under investigation in the present study. It is a four-cylinder and turbocharged engine operating under steady state and fully warm conditions. The combustion mode is of the homogeneous charge type with stoichiometric air-fuel ratio globally. The engine speed was varied from 1600 rpm to 3000 rpm while the torque ranged from 60 N m to 120 N m. Detailed specifications on the engine test bed along with the experimental operating conditions are elaborated in Section 5.2.

The nature of SI in GDI engines directly reflects the significance of high-temperature chemistry in describing the fuel combustion accurately. Additionally, several kinetic studies on octane sensitivity in SI engines pinpoint the lack of low- and intermediate-temperature reactivity for gasoline fuels with high sensitivities [200,201]. Therefore, the subsequent validations focus on the high-temperature regime which is above 900 K. From the in-cylinder pressure curves, the corresponding pressure range during high-temperature combustion is between 30 bar and 50 bar. Since the GDI engine is operating in the homogeneous mode with stoichiometric air-fuel ratio, the resulting equivalence ratio of interest is unity. However, the potential presence of locally fuel-rich regions requires the validations to extend to conditions with equivalence ratios larger than one.

Represented by ID time, auto-ignition behaviour remains the most important target in assessing the accuracy of chemical kinetics. Two common experimental setups for ID time measurements are ST and RCM. Only ST test conditions are modelled so as to emulate the high-temperature regime. Even in the homogenous mode, the combustion in GDI engines is more precisely characterised as the partially premixed type [143]. In this regard, the development of flame surface with its propagation speed is a crucial aspect in combustion modelling. Thus, flame speed is included as a validation goal in evaluating the high-temperature chemistry. Although the flame structure is turbulent in nature, experimentally measured laminar flame speeds in laboratory-scale flame configurations provide useful directions in shaping the chemical kinetics [202]. Last but not least, development of species concentration profiles, particularly PAH, in flame burners and flow reactors is also incorporated in the evaluative study. The validation targets and GDI engine-like operating conditions derived from the engine test bed are shown in Figure 4-2. All the numerical works on validations of chemical kinetics were performed using Chemkin-Pro.

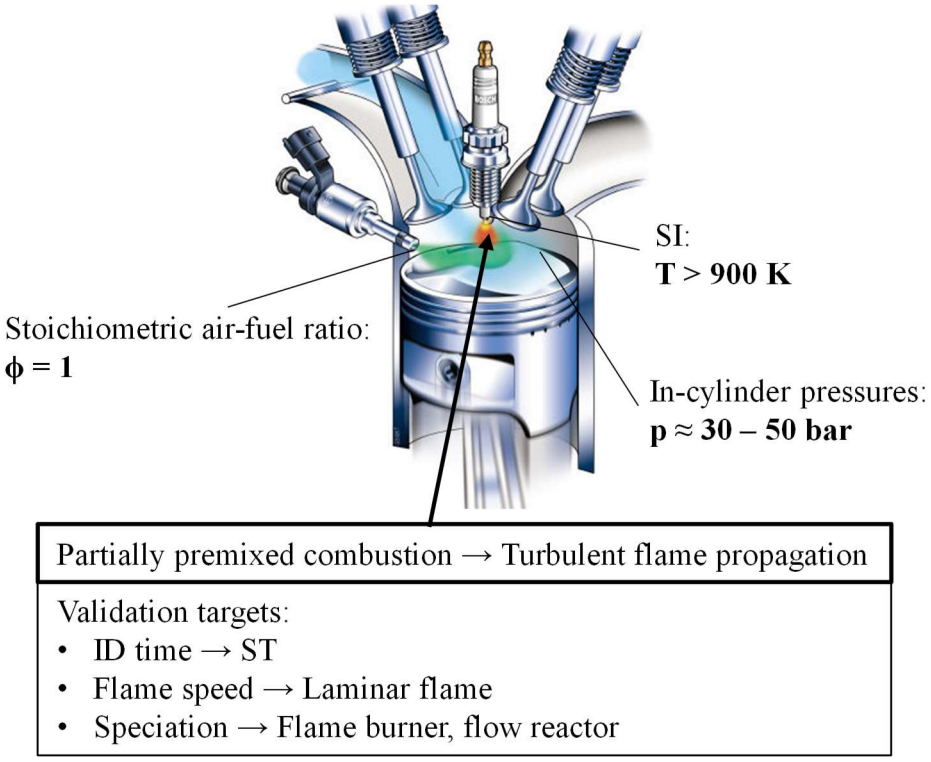


Figure 4-2 Validation criteria established based on the GDI engine combustion mode and operating conditions.

Among all the experiments measuring ID time, flame speed and speciation profiles, the emphasis is placed at those utilising real gasoline fuels and gasoline-like TRF surrogates. This is because the multi-component fuel mixtures allow the assessment on possible kinetic couplings and cross reactions between individual fuel constituents [26]. To further assure robustness of the TRF mechanisms and completeness of the validations, experimental studies on critical fuel components including binary PRF mixtures, isooctane, n-heptane and toluene are also utilised wherever applicable. From the kinetic analyses performed under the GDI engine-like operating conditions, the optimal TRF mechanism is identified to be applied in subsequent CFD modelling.

4.4 ID Time

Under ST test facilities, the ID time is typically defined as the time interval between the arrival of the reflected shock wave and the onset of ignition event at the end wall. The arrival of the reflected shock wave is detected by the step rise in pressure at the observation location while the ignition is determined by the maximum slope in the abrupt rise in pressure and/or chemiluminescence measurements of OH radicals

[203,204]. The associated ST simulations are modelled with a closed homogeneous batch reactor to compute the ID times. Here, the ID time is calculated as the time required to reach the highest rate of change of temperature with respect to time as indicated by the inflection point in the temperature profile. The definition of ID time is used consistently across the kinetic simulations with different fuels and operating conditions as tabulated in Table 4-3.

Table 4-3 Experimental specifications of ST studies of fuel components and mixtures relevant to gasoline fuels used as validation conditions.

Fuel	T (K)	p (bar)	ϕ	Uncertainty (%)	Reference
RD387	850–1280	15–25, 45–60	0.5, 1, 2	15	[205]
Surrogate A	850–1280	15–25, 45–60	0.5, 1, 2	15	[205]
Surrogate B	850–1280	15–25, 45–60	1	15	[205]
PRF 80	700–1300	40	1	-	[206]
PRF 90	700–1300	40	1	-	[206]
Isooctane*	700–1300	13, 34, 45	1	-	[206]
n-Heptane*	660–1350	13.5, 30, 42	1	-	[207]
Toluene*	855–1400	12, 50	1	15	[208,209]

* Validation results for neat hydrocarbons are included in Appendix A for brevity.

4.4.1 Gasoline Fuels and TRF Surrogates

Gauthier et al. [205] investigated the auto-ignition characteristics of a gasoline fuel, RD387 and two ternary TRF surrogates, termed Surrogate A and Surrogate B using the ST facility. RD387 is a regular-grade and non-oxygenated fuel which is blended to have an anti-knock index of 87. Strong agreement is observed between ID time measurements of RD387 and the two ternary surrogates across all the experimental conditions. Due to the lack of information on fuel sensitivity of RD387, the associated TRF surrogate composition was formulated using Equations (3-1)–(3-3) based on the research-grade gasoline supplied by Chevron-Phillips Chemical [210] with the same anti-knock index. With a H/C ratio of 1.94, the fuel has a RON of 90.8 and a MON of 83.2. The compositions of TRF surrogates for RD387, Surrogate A and Surrogate B are tabulated in Table 4-4. It is seen that the proposed composition of TRF surrogate for RD387 is very comparable to those of Surrogate A and Surrogate B.

Table 4-4 Compositions of TRF surrogates for RD387, Surrogate A and Surrogate B.

Component	Composition in mole % (liquid volume %)		
	RD387 surrogate*	Surrogate A	Surrogate B
Isooctane	57.4 (64.1)	56 (63)	63 (69)
n-Heptane	16.8 (16.9)	17 (17)	17 (17)
Toluene	25.8 (19.0)	27 (20)	20 (14)

* Proposed using Equations (3-1)–(3-3).

The comparison between measured and computed ID times of RD387 at pressures of 20 bar and 55 bar under fuel-lean ($\phi = 0.5$), stoichiometric ($\phi = 1$) and fuel-rich ($\phi = 2$) conditions is illustrated in Figure 4-3. The high-temperature region is indicated by temperatures exceeding 900 K ($1000/T \leq 1.11$). As expected, ID times decrease with both increasing pressures and temperatures across the three equivalence ratios. For stoichiometric conditions at 20 bar and 55 bar, experimental ID times are accurately reproduced by Jiao-TRF and An-TRF within approximately 20% deviations. At 55 bar, Wang-TRF under-predicts the ID times by 19–49% at temperatures ranging from 900 K to 1160 K. However, Figure 4-3(b)(ii) clearly displays the convergence of ID time predictions by all the mechanisms at temperatures above 1200 K ($1000/T \leq 0.83$).

Differences between the mechanisms arise for operating conditions with equivalence ratios of non-unity. For fuel-lean conditions, An-TRF predicts the ID times reasonably well (< 30%) while the other two under-predict them with the maximum deviations of 46% observed for Jiao-TRF and 39% for Wang-TRF. On the other hand, all the mechanisms compute nearly similar ID times for fuel-rich conditions at 20 bar except for Wang-TRF at lower-temperature range (46% difference at 935 K). The deviations in computed ID times under fuel-rich conditions become more apparent at the higher pressure of 55 bar. Likewise, better agreement with the experimental data (< 40%) is associated with Jiao-TRF and An-TRF while the under-predictions by Wang-TRF are as high as 57%.

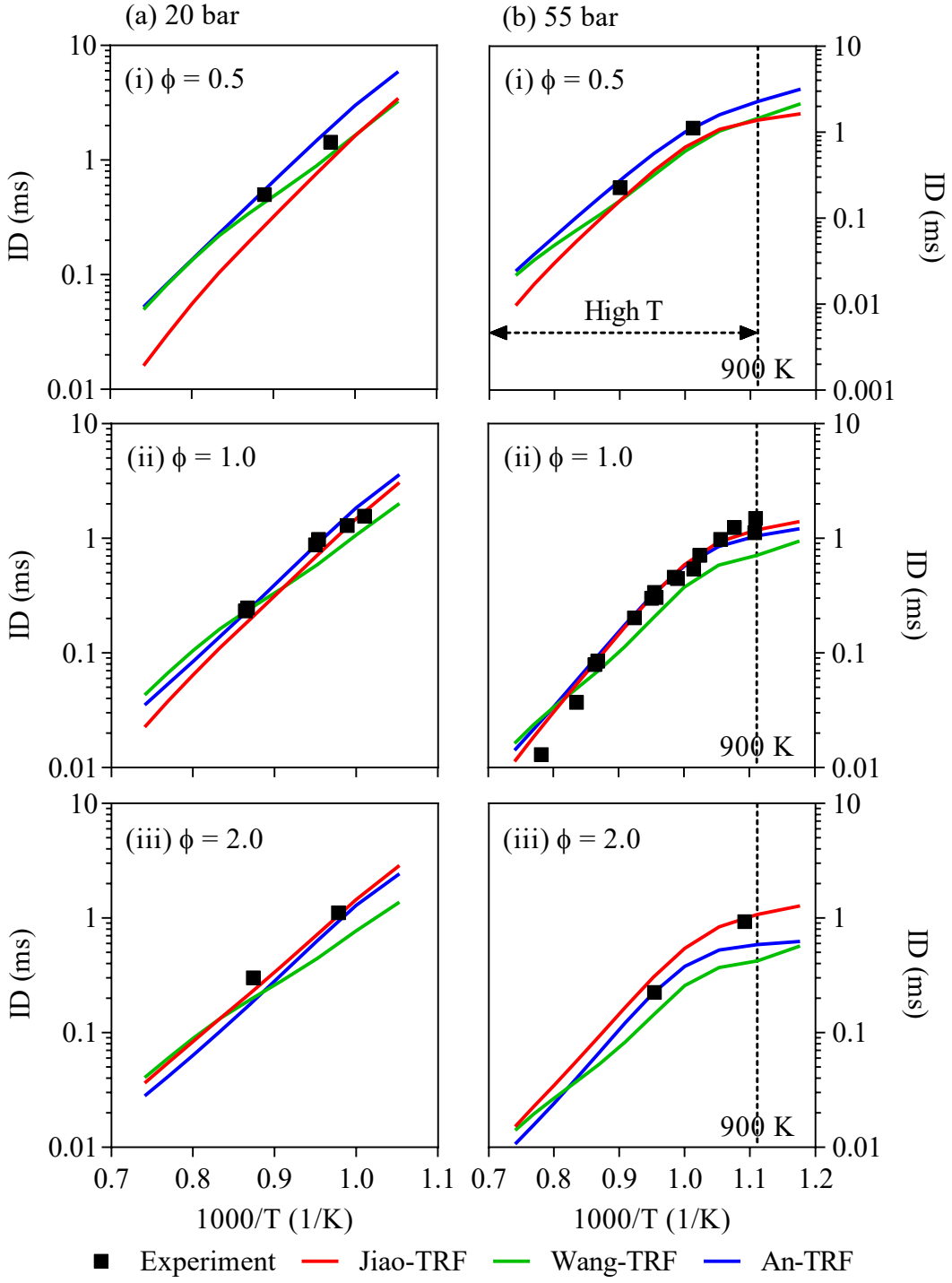


Figure 4-3 Measured [205] and computed ID times of RD387 at pressures of (a) 20 bar and (b) 55 bar with equivalence ratios of (i) 0.5, (ii) 1 and (iii) 2.

Figure 4-4 and Figure 4-5 display the measured and calculated ID times for Surrogate A and Surrogate B. Generally, the predictions of ID times by the three mechanisms resemble those of RD387 in Figure 4-3 across the range of operating conditions. This

is due to the close proximity in TRF surrogate compositions between the three fuels as shown in Table 4-4. Gauthier et al. [205] also pointed that there is no discernible difference in ID times of RD387 and Surrogate A measured experimentally. Hence, the ability of TRF surrogate to replicate the combustion properties of RD387 reassures the reliability of correlations used in Equations (3-1)–(3-3). It is noteworthy that all the mechanisms are able to capture the ignition characteristics of Surrogate A and Surrogate B satisfactorily at stoichiometric conditions for 20 bar and 55 bar with slightly overestimated reactivity observed for Wang-TRF from 860 K to 1140 K.

The significance of negative temperature coefficient (NTC) behaviour of RD387 under low and high pressures at the stoichiometric condition is explored in Figure 4-6. The range of temperatures is extended to cover the typical NTC region (750–900 K) despite the lack of experimental data. From Figure 4-6, RD387 exhibits marginal NTC behaviour at 20 bar and near negligible NTC behaviour at 55 bar. Thus, the effect of NTC behaviour diminishes with increasing pressure. The NTC behaviour of RD387 is primarily suppressed by low reactivity of toluene in the TRF surrogate due to its role as a radical scavenger [202]. This observation directly necessitates the importance of including a representative of aromatics such as toluene in gasoline surrogates.

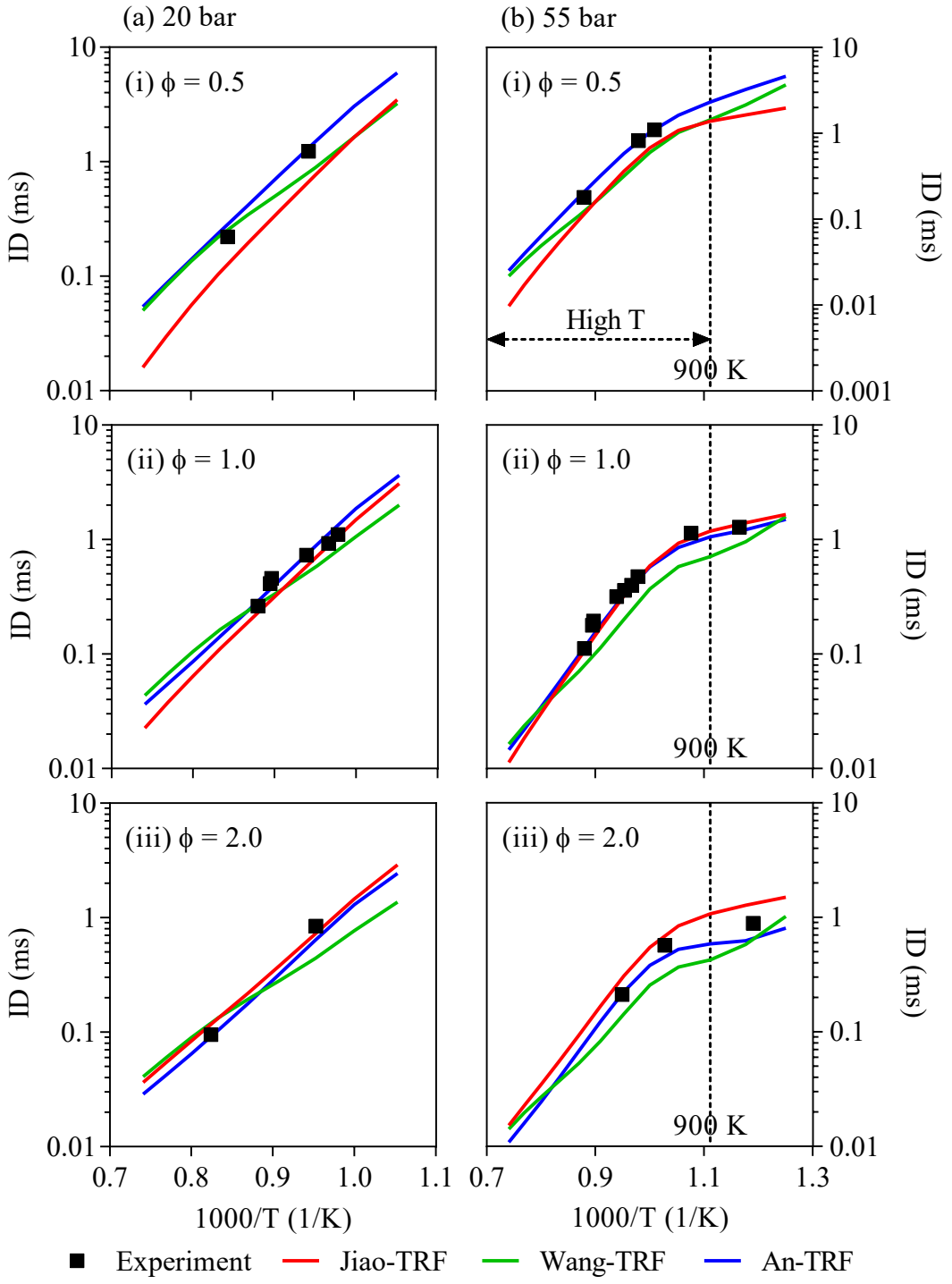


Figure 4-4 Measured [205] and computed ID times of Surrogate A at pressures of (a) 20 bar and (b) 55 bar with equivalence ratios of (i) 0.5, (ii) 1 and (iii) 2.

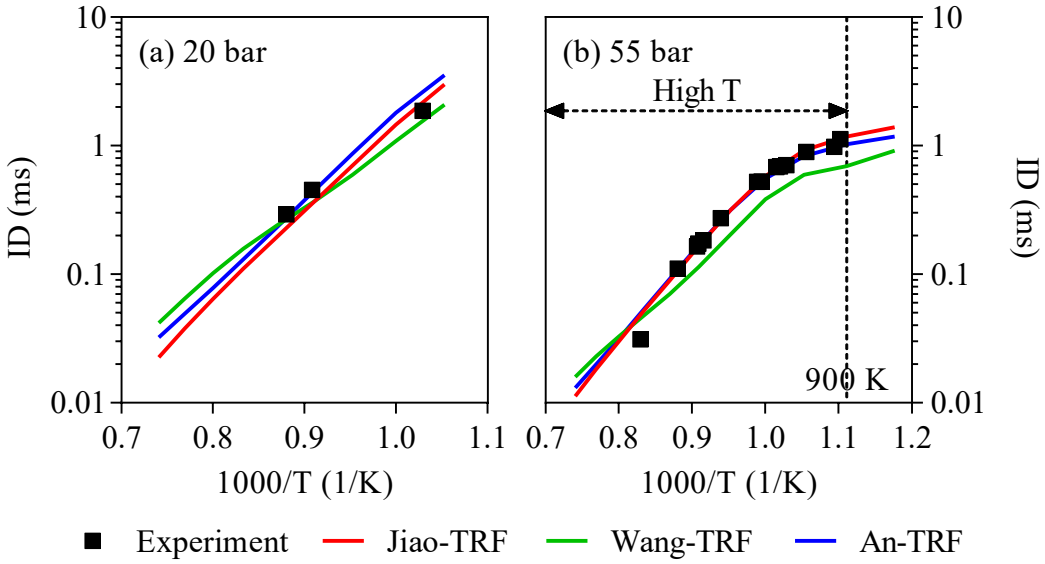


Figure 4-5 Measured [205] and computed ID times of Surrogate B at pressures of (a) 20 bar and (b) 55 bar with the equivalence ratio of 1.

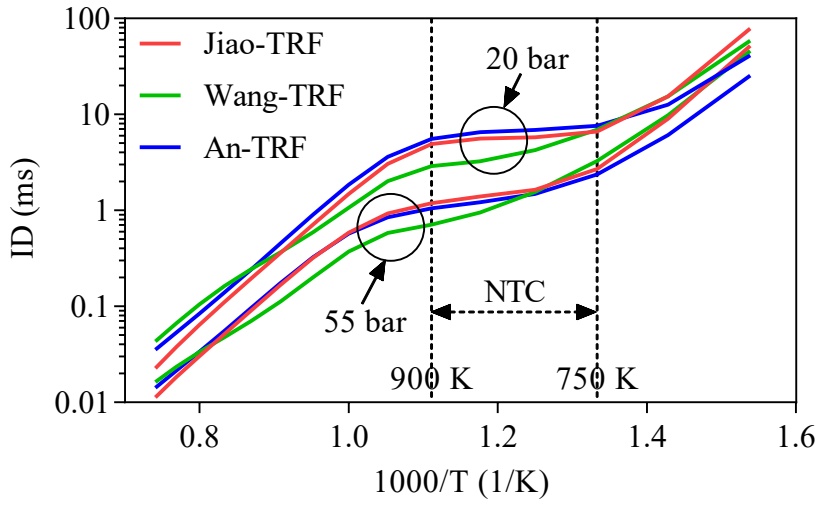


Figure 4-6 Computed ID times of RD387 at pressures of 20 bar and 55 bar with the equivalence ratio of 1 for temperatures ranging from 650 K to 1350 K.

4.4.2 PRF Surrogates

To study the fuel ignition characteristics relevant to SI engines, Fieweger et al. [206] measured the ID times of stoichiometric mixtures of PRF 60, PRF 80 and PRF 90 at 40 bar in ST. The naming convention 'PRF #' means that the PRF mixture contains #% of isooctane and (100 − #)% of n-heptane by liquid volume. Since gasoline fuels

with higher ON are preferable in GDI engines to prevent knocking, only PRF 80 and PRF 90 are examined here. The prediction of ID times of PRF mixtures is compared against the experimental values in Figure 4-7.

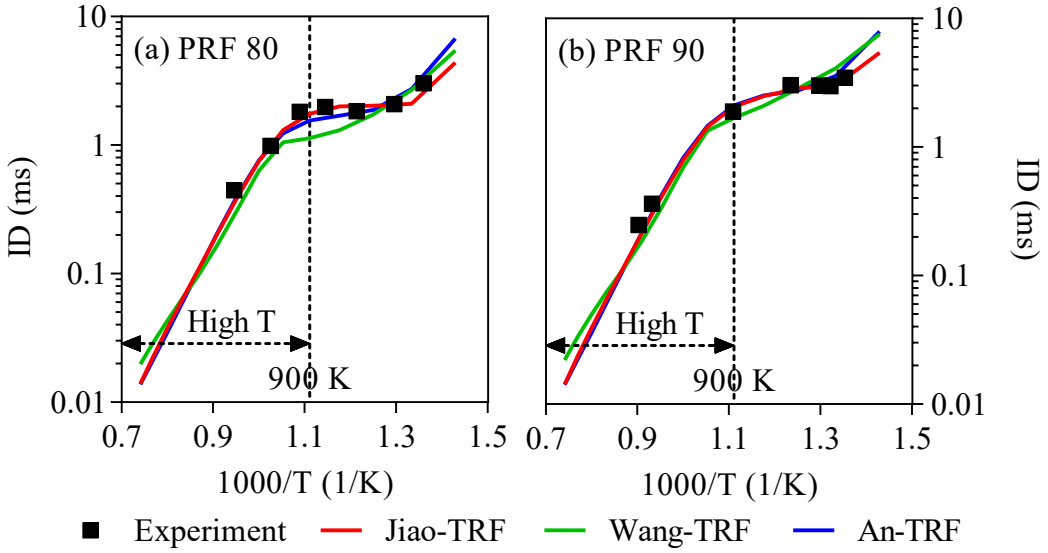


Figure 4-7 Measured [206] and computed ID times of (a) PRF 80 and (b) PRF 90 at the pressure of 40 bar with the equivalence ratio of 1.

Nearly identical ID times are calculated by all the mechanisms at temperatures higher than 1000 K, thus highlighting their similarities in high-temperature chemistry. While all the computed ID times of PRF 90 coincide with the measured values, Wang-TRF under-predicts those of PRF 80 by 18–39% throughout 800–1050 K. As compared to RD387 and TRF surrogates, PRF mixtures demonstrate slightly more pronounced NTC behaviour. Besides, this behaviour prevails for PRF with lower ON. It can then be deduced that high-ON gasoline fuels doped with toluene are generally associated with reduced/removed NTC behaviour.

4.5 Flame Speed

In characterising the complex flame structure and response, laminar flame speed is a vital physicochemical property which provides fundamental knowledge on the reactivity, diffusivity and exothermicity of the combustible mixture [211]. Due to the stochastic nature of turbulence in engines, numerous computational models depend heavily on experimental laminar flame speeds across different operating conditions to

interpret the turbulent counterpart [212]. For flame modelling, laminar flame speeds are computed from the 1D, steady, planar, freely propagating and adiabatic flames in a doubly infinite domain without radiative heat transfer. A mixture-averaged equation is used to determine the species diffusion coefficients and fluxes. The relevant flame configurations with their experimental conditions selected are listed in Table 4-5.

Table 4-5 Experimental specifications of flame speed studies of fuel components and mixtures relevant to gasoline fuels used as validation conditions.

Fuel	Initial T (K)	p (bar)	ϕ	Measurement method	Reference
CR-87	353, 500	1	0.6–1.4	Stagnation flame[a]	[213]
TAE7000 surrogate	358	1	0.6–1.5	Flat burner[b]	[214]
PRF	298	1	1.0	Counterflow[a]	[215]
PRF 87	373	10, 15, 20, 25	0.7–1.2	Spherical flame[a]	[216]
Isooctane[c]	298, 358	1	0.7–1.3	Flat burner[b]	[217]
n-Heptane[c]	298, 358	1	0.7–1.3	Flat burner[b]	[217]
Toluene[c]	298, 358	1	0.7–1.3	Flat burner[b]	[217]

[a] Stretched flame with linear extrapolation to zero stretch rate.
[b] Non-stretched flame.
[c] Validation results for neat hydrocarbons are included in Appendix A for brevity.

4.5.1 Gasoline Fuels and TRF Surrogates

Using the experimental conditions of the stagnation jet-wall flame of an unleaded conventional gasoline, CR-87 by Zhao et al. [213], the predicted laminar flame speeds by the TRF mechanisms are depicted in Figure 4-8. Here, CR-87 is modelled as Surrogate B whose composition is listed in Table 4-4 as the ternary mixture has been demonstrated to reproduce the laminar flame speeds of CR-87 numerically [52,218]. The flame speeds are compared at atmospheric pressure for initial temperatures of 353 K and 500 K over an extensive range of equivalence ratios. Wang-TRF and An-TRF exhibit good quantitative agreement with experimental data (about 10% differences) for equivalence ratios ranging from 0.85 to 1.3. Conversely, Jiao-TRF over-predicts the flame speeds by 17–49% across the entire envelope of operating conditions. The

poor performance of Jiao-TRF is likely caused by the omission of important reaction pathways pertinent to flame speed computations during the mechanism reduction as further discussed in Section 4.7.2.

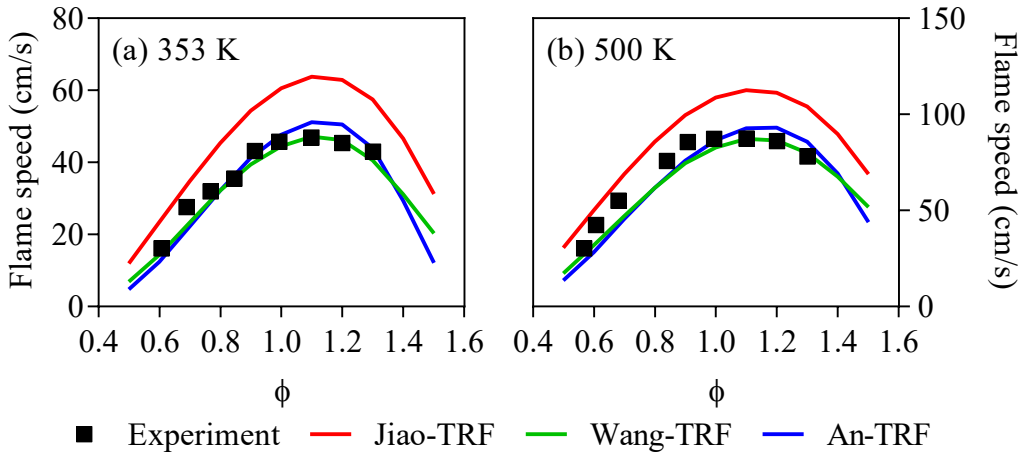


Figure 4-8 Measured [213] and computed flame speeds of CR-87 at the pressure of 1 bar and initial temperatures of (a) 353 K and (b) 500 K.

Dirrenberger et al. [214] utilised the heat flux method to determine the adiabatic flame speeds of a commercial gasoline known as TAE7000 with an estimated RON of 95.6 at atmospheric pressure and initial temperature of 358 K. To emulate the RON, MON, H/C ratio and normal boiling temperature of TAE7000, a TRF surrogate was proposed with a composition of 42.9% isooctane, 13.7% n-heptane and 43.4% toluene by liquid volume. Along with the experimental flame speeds of TAE7000 and its surrogate, the computed ones based on the proposed TRF surrogate are displayed in Figure 4-9. The best agreement between computation and experiment is observed for Wang-TRF, followed by An-TRF and then Jiao-TRF. While Wang-TRF and An-TRF calculate the peak flame speed lower by 3% and 6%, respectively, the over-prediction by Jiao-TRF reaches 27%. The discrepancies associated with Jiao-TRF also increases up to 55% when the conditions become fuel-rich ($\phi > 1$).

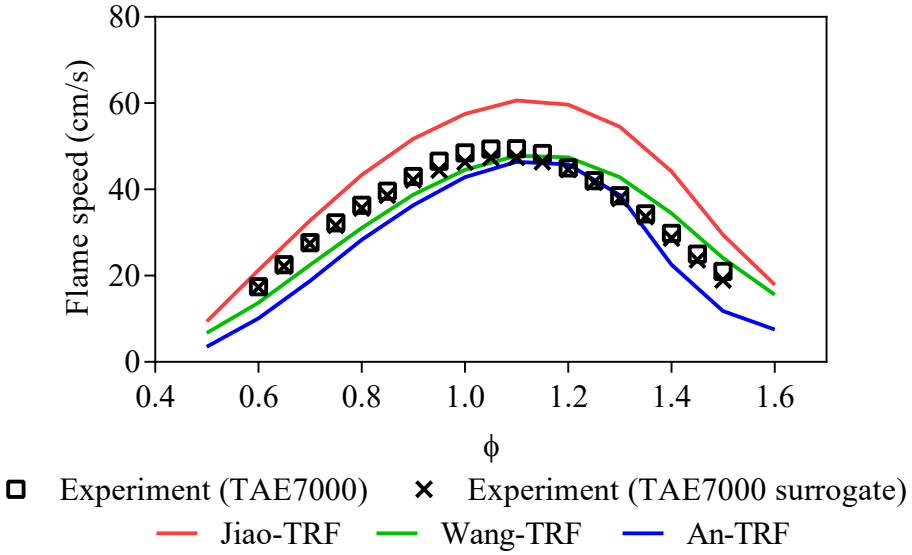


Figure 4-9 Measured [214] and computed flame speeds of TAE7000 and its surrogate at the pressure of 1 bar and initial temperature of 358 K.

4.5.2 PRF Surrogates

Using counterflow configuration, Huang et al. [215] measured the laminar flame speeds of PRF with ON ranging from 0 to 100 at atmospheric pressure and initial temperature of 298 K. The computed flame speeds at the stoichiometric condition are illustrated in Figure 4-10. Significant over-predictions in flame speeds of 43–54% is observed for Jiao-TRF over the range of ON. Wang-TRF and An-TRF demonstrate opposing performances whereby the former shows strong agreement of within 3% deviations for PRF with high ON (ON ≥ 85) while the latter computes flame speeds closer to the measured values (within 8% deviations) for lower-ON PRF (ON ≤ 10). This observation indirectly reveals the higher fidelity of chemical kinetics of isooctane in Wang-TRF and n-heptane in An-TRF, respectively at the stoichiometric condition.

While typical flame configurations are experimented at atmospheric pressure, flame propagation in engines occurs at higher pressures. Thus, the high-pressure laminar flame speed data of PRF 87 obtained by Jerzembeck et al. [216] were used to examine the pressure dependence of chemical kinetics of the TRF mechanisms. At the initial temperature of 373 K, flame speeds of PRF 87 were measured at pressures of 10–25 bar over equivalence ratios of 0.7–1.2. Figure 4-11 depicts the performance of TRF mechanisms in capturing the effect of pressures on flame speeds of PRF 87. For all the pressures, Jiao-TRF calculates higher flame speeds (up to 69%) while Wang-TRF

under-predicts the experimental values, particularly for fuel-rich mixtures with the maximum difference of 41%. Despite the slight discrepancies at the equivalence ratio of 1.2, good agreement with the experimental data is preserved for An-TRF with deviations lower than 23%. So, it can be inferred that An-TRF manages to characterise the high-temperature flame propagation under high pressures.

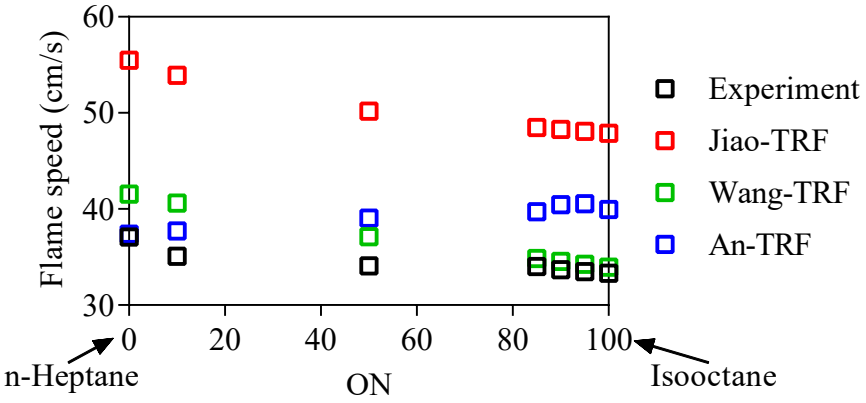


Figure 4-10 Measured [215] and computed flame speeds of different PRF under the stoichiometric condition with the pressure of 1 bar and initial temperature of 298 K.

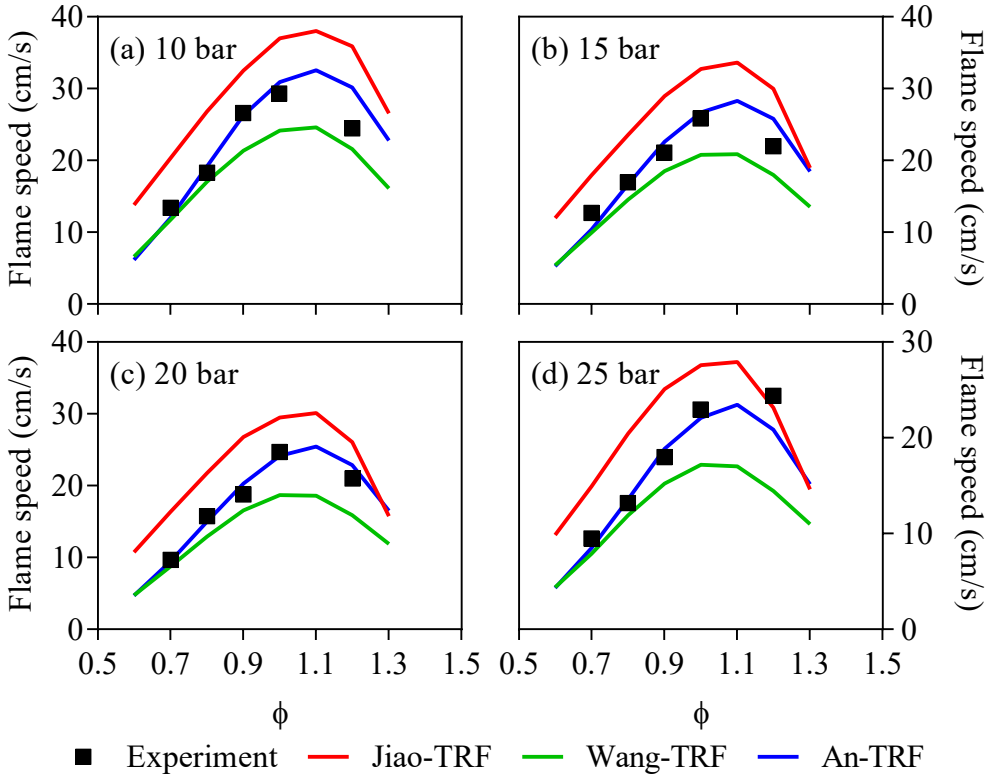


Figure 4-11 Measured [216] and computed flame speeds of PRF 87 at the initial temperature of 373 K and pressures of (a) 10 bar, (b) 15 bar, (c) 20 bar and (d) 25 bar.

4.6 Speciation Profile

Identification and analysis of intermediate species and final products of fuel oxidation generate detailed understanding on the chemical reactions. Commonly, the time- and space-resolved speciation data are obtained in chemical reactors and low-pressure flame systems. Nevertheless, the non-idealities and limitations of optical techniques and measuring devices pose notable uncertainties in the speciation data [202]. Often, such uncertainties in the experimental measurements can reach as high as one or two orders of magnitude [65]. Additionally, Sarathy et al. [202] underlined the increased uncertainties for real fuels and multi-component surrogate mixtures as the interactions between fuel components and their fragments further complicate the quantification and analysis of intermediates and by-products. The experimental configurations to which the speciation profiles were measured and are utilised to validate the TRF mechanisms include laminar premixed flames and JSR. The relevant test conditions and specifications of flame and JSR systems are detailed in Table 4-6 in Section 4.6.1 and Table 4-7 in Section 4.6.2, respectively.

4.6.1 Flame Burners

Table 4-6 Experimental specifications of laminar premixed flames of fuel components relevant to gasoline fuels used as validation conditions.

Fuel	Composition (mole %)			p	ϕ	Gas velocity	Reference
	Fuel	O_2	N_2/Ar	(bar)		(cm/s)	
Isooctane	4.23	27.80	67.97 (N_2)	1	1.9	4.18	[219]
n-Heptane	3.98	23.01	73.01 (N_2)	1	1.9	4.98	[219]
n-Heptane	5.5	28.79	65.71 (Ar)	1	2.1	5.17	[220]

The experimental flames are modelled as premixed laminar burner-stabilised flames which are 1D. The temperature profiles measured experimentally are imposed in the simulations to account for conductive and radiative heat losses. Bakali et al. [219] carried out species identification and concentration measurements in rich premixed flames of isooctane and n-heptane stabilised on a flat flame burner at atmospheric pressure. The speciation profiles, measured and computed, are plotted as a function of height above the burner (HAB) in Figure 4-12 and Figure 4-13 for isooctane and

n-heptane flames, respectively. The species examined include reactants (C_8H_{18}/C_7H_{16}, O_2), major products (CO, CO_2) and crucial species of soot formation (C_2H_2 and A1).

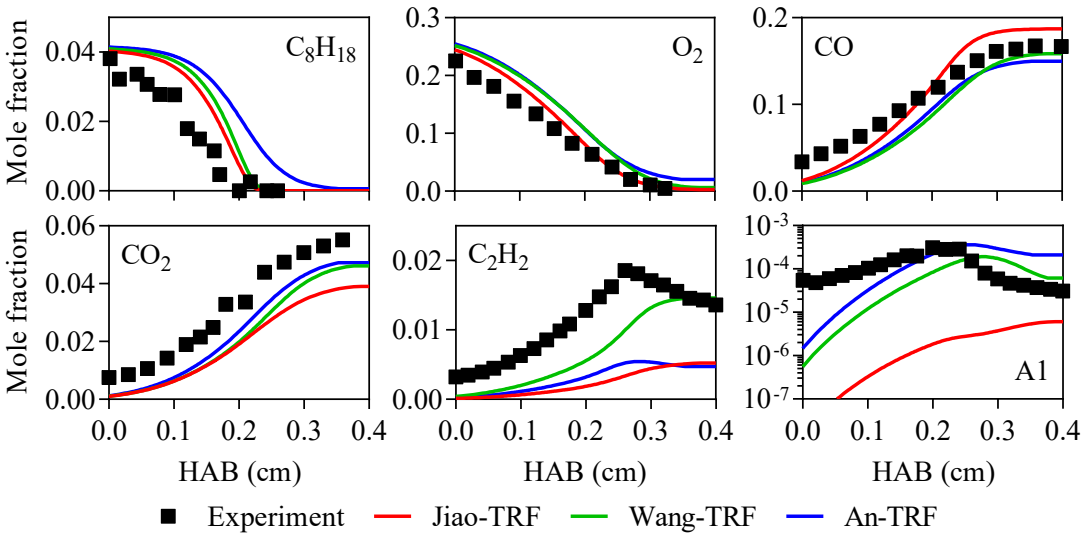


Figure 4-12 Measured [219] and computed speciation profiles in the rich premixed flame of isooctane at atmospheric pressure and equivalence ratio of 1.9.

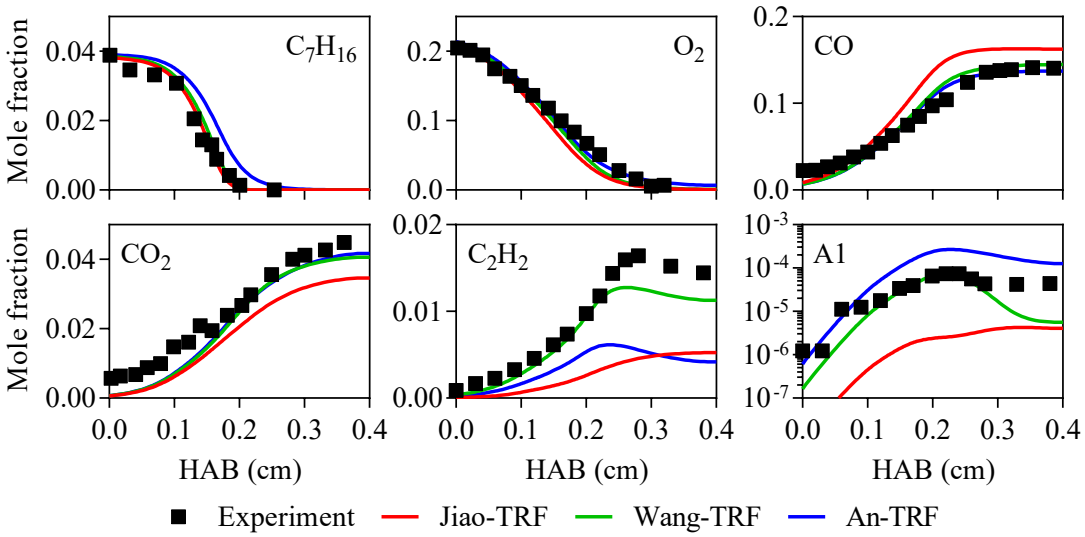


Figure 4-13 Measured [219] and computed speciation profiles in the rich premixed flame of n-heptane at atmospheric pressure and equivalence ratio of 1.9.

Generally, qualitative trends in the speciation profiles are reproduced by each TRF mechanism for both the flames examined. Reasonable agreement in the consumption of fuel species and oxygen and production of CO and CO_2 in both flames implies that

the major pathways for oxidation of isooctane and n-heptane are captured by all the mechanisms under the fuel-rich conditions (ϕ = 1.9). Wang-TRF exhibits the best agreement in the speciation of C_2H_2 with 23–30% differences in the peak values while the other two mechanisms under-predict the peak mole fractions by 63–75%. For the concentration profiles of A1, the computed peak values differ from the measured ones by factors of 1.1–1.4 for Wang-TRF and 1.4–4.2 for An-TRF, respectively. On the other hand, the peak mole fractions computed by Jiao-TRF are 15–43 times lower than those measured experimentally.

The chemistry of PAH embedded in the TRF mechanisms is further validated using the experimental study of rich premixed flames of n-heptane conducted by Inal and Senkan [220] at atmospheric pressure. Absolute concentrations of stable major, minor and trace species associated with PAH and soot were quantified through the direct analysis of samples withdrawn from the flames. They questioned the reliability of speciation data at small HAB (within a few mm) due to possible interactions between sampling probe and burner surface. The measured and computed mole fractions of n-heptane fuel, oxygen and PAH including benzene (A1), A2, A3 and A4 are depicted in Figure 4-14 along the HAB of 1 cm.

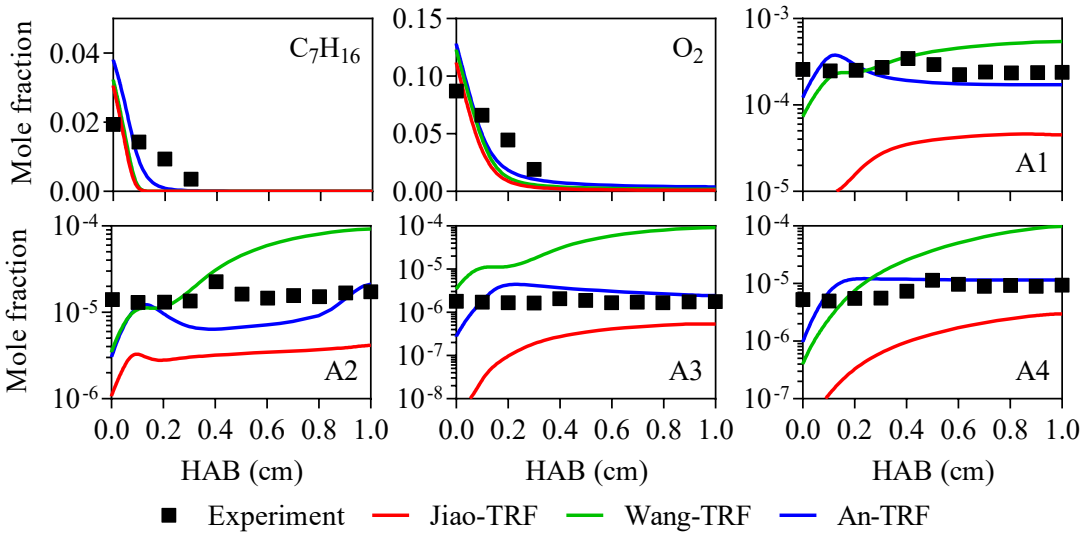


Figure 4-14 Measured [220] and computed speciation profiles in the rich premixed flame of n-heptane at atmospheric pressure and equivalence ratio of 2.1.

Following the experimental observations, reactants (C_7H_{16}, O_2) are entirely consumed at HAB of 0.3–0.4 cm. At HAB larger than 0.6 cm, An-TRF computes mole fractions

of PAH closest to the experimental values within the same order of magnitude. In particular, the peaks in speciation profiles of A1 and A2 are also reproduced by An-TRF at lower HAB. At larger HAB, Wang-TRF predicts higher concentrations of A2, A3 and A4 (up to one order of magnitude) although better agreement is seen for the A1 profile. Meanwhile, all the PAH profiles are consistently under-predicted by Jiao-TRF (within factors of 3–5 at HAB of 1 cm).

4.6.2 JSR

In a JSR, combustible reactants are delivered at high velocity to the reactor maintained at elevated temperatures to induce intense turbulence and homogenise the mixture. Molecular species concentration measurements are obtained from samples of the reacting mixture. A high degree of dilution is used to minimise potential temperature gradients in the JSR [221]. Hence, the mixing process is treated as complete and instantaneous in which the mixing time scale is much smaller than the residence time or the chemical time scale. JSR experiments are modelled as PSR in the simulations. Under well-mixed conditions, the PSR model determines species concentrations from the balance between the net ROP by chemical reactions and the difference in inflow and outflow of the species.

Table 4-7 Experimental specifications of JSR experiments of fuel components and mixtures relevant to gasoline fuels used as validation conditions.

Fuel	Composition (mole %)			T (K)	p (bar)	ϕ	τ (s)	Reference
	Fuel	O_2	N_2					
PRF 90	0.1	1.235	98.665	550–1150	10	1	1	[222]
Isooctane*	0.1	1.25	98.65	550–1150	10	1	1	[221]
n-Heptane*	0.1	1.1	98.8	550–1150	10	1	1	[221]

* Validation results for neat hydrocarbons are included in Appendix A for brevity.

Dagaut et al. [222] examined the oxidation behaviour of stoichiometric PRF mixtures experimentally in a high-pressure JSR at temperatures ranging from 550 K to 1150 K and a mean residence time of 1 s. PRF 90 is chosen in the present study to evaluate the kinetics of TRF mechanisms in emulating the oxidation characteristics of a high-ON fuel. The computed concentration profiles of reactants, intermediates and final

products are presented in Figure 4-15, along with the experimental measurements as a function of temperature.

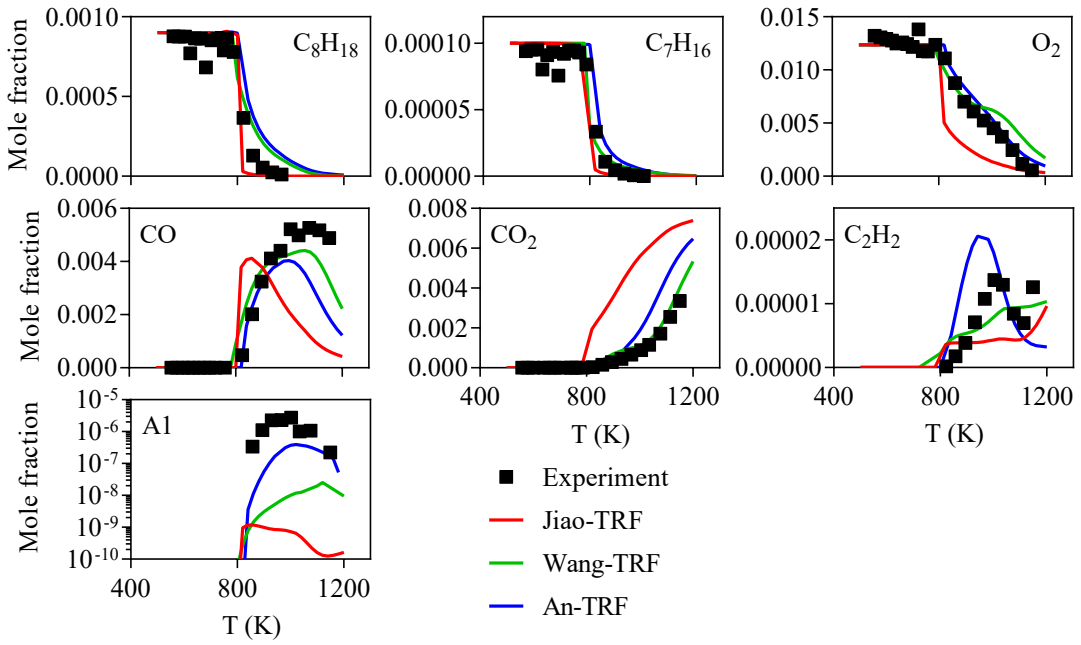


Figure 4-15 Measured [222] and computed speciation profiles of stoichiometric PRF 90 in the JSR at the pressure of 10 bar and mean residence time of 1 s.

The changes in mole fractions of fuel species and oxygen with respect to the variation in temperatures are well replicated by the TRF mechanisms. The rapid consumption of fuel and oxygen becomes apparent at temperatures starting from 800 K which is also supported by the increased production of CO and CO_2. However, the temperature for the peak production of CO predicted by Jiao-TRF is lower by about 220 K while CO_2 is over-computed up to a factor of 17 at temperature higher than 860 K. The peak formation of C_2H_2 observed experimentally is only retained by An-TRF though it is overestimated by 50%. Likewise, An-TRF computes the production of A1 within the same order of magnitude whereas Wang-TRF and Jiao-TRF under-predict the mole fractions by one and two orders of magnitude, respectively.

4.7 Chemical Kinetic Analyses

In order to explicate fundamental differences between the TRF mechanisms, chemical kinetic analyses on computations of ID, laminar flame speed and speciation profile

from premixed flame are conducted at engine-like operating conditions illustrated in Figure 4-2. As tabulated in Table 4-8, the kinetic analyses serve to address the varying levels of accuracy in high-temperature chemistry at a stoichiometric ratio and reaction pathways of PAH pertinent to soot formation. Auto-ignition of RD387 in ST and laminar flame of CR-87 are selected to interpret ID time and flame speed, respectively while premixed flame of n-heptane is utilised for speciation profiles of PAH due to the available experimental measurements.

Table 4-8 Selected engine-like operating conditions for chemical kinetic analyses.

Criterion	Fuel	T (K)	p (bar)	ϕ	Kinetic analysis
ID	RD387	1000	55	1.0	Temperature sensitivity
Flame speed	CR-87	353, 500	1	1.0	Mass flow rate sensitivity
PAH profile	n-Heptane	-	1	2.1	ROP of A1

4.7.1 Temperature Sensitivity for ID Time

Sensitivity analysis of ID time is examined by determining the first-order sensitivity coefficients of gas temperature with respect to the reaction rate constants. Positive sensitivity coefficients indicate a decrease in ID time with increasing reaction rates, thus increasing the overall system reactivity. Conversely, negative coefficients reduce the system reactivity due to longer ID time when the reaction rates are increased. Since GDI system is characterised by high-temperature combustion due to the presence of SI, the stoichiometric condition of RD-387 in the ST at the pressure of 55 bar is used for the sensitivity analysis.

From Figure 4-4(b)(ii), excellent agreement in the measured and computed ID times is observed for Jiao-TRF and An-TRF while shorter times are computed by Wang-TRF throughout the temperature range of 900–1150 K. Wang-TRF under-predicts the ID time at 1000 K by 31%. Percentage deviations in ID time at the same temperature for Jiao-TRF and An-TRF are 9% and 6%, respectively. Thus, sensitivity coefficients of temperature are calculated at 1000 K for all the mechanisms and normalised by their corresponding highest absolute value. Ten reactions which are most sensitive towards ID time are presented in Figure 4-16 whereby the mutual reactions among the three mechanisms are highlighted in colours.

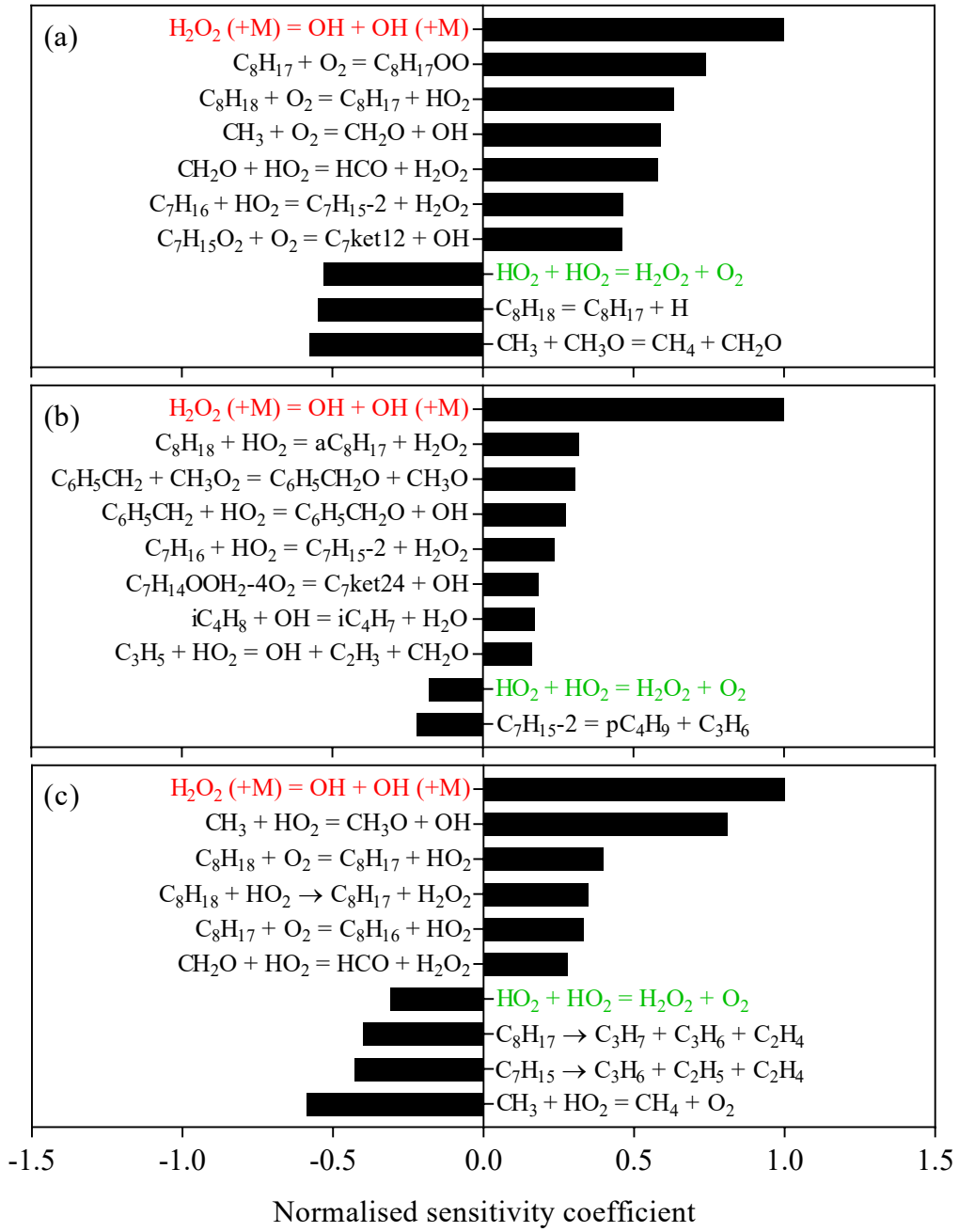


Figure 4-16 Normalised sensitivity coefficients for the ID time of RD387 at the pressure of 55 bar, temperature of 1000 K and equivalence ratio of 1 for (a) Jiao-TRF, (b) Wang-TRF and (c) An-TRF.

For all the mechanisms, thermal chain branching of hydrogen peroxide (H_2O_2) into two OH radicals remains the top contributor to initiate the ignition process. The role of hydrogen atom (H) abstraction from fuel species (isooctane and n-heptane) and alkyl radicals (such as C_8H_{17} and C_7H_{15}) in promoting the reactivity is also prominent.

These fuel-specific reactions are responsible for the initial generation of radical pool that governs the auto-ignition chemistry [29]. Conversely, conversion of hydroperoxyl radicals (HO_2) into H_2O_2 and oxygen represents a chain termination, thus exhibiting negative sensitivity coefficient. Besides, chain-terminating reactions involving alkyl radicals such as unimolecular decomposition into smaller alkanes and alkenes inhibit the system reactivity.

From Figure 4-16(b), a large portion of the most sensitive reactions for Wang-TRF causes an increase in the reactivity whereas the diminishing effects of reactions with negative coefficients are significantly lower. Particularly, promoting effects of alkoxy benzyl radicals ($C_6H_5CH_2O$) formation from benzyl radicals ($C_6H_5CH_2$) related to toluene decomposition in Wang-TRF are not observed in the other two mechanisms. Also, reactions involving methyl radicals (CH_3) with the highest negative coefficients in Jiao-TRF ($CH_3 + CH_3O = CH_4 + CH_2O$) and An-TRF ($CH_3 + HO_2 = CH_4 + O_2$) are not captured by Wang-TRF. These jointly lead to an overestimation of the reactivity and hence the lower ID time predicted by Wang-TRF at 1000 K.

4.7.2 Mass Flow Rate Sensitivity for Flame Speed

To quantify the contribution of important reactions in sensitivity analysis of laminar flame speed, the first-order sensitivity coefficients of mass flow rate with respect to the reaction rate constants are applied. As the reaction rates become higher, positive sensitivity coefficients suggest a rise in flame speed whereas negative coefficients are linked to decreased flame speed [223]. For the sensitivity analysis, the atmospheric laminar flame of CR-87 is chosen for two initial temperatures of 353 K and 500 K at the stoichiometric condition to emulate homogenous combustion in the GDI engine.

As seen in Figure 4-8, flame speeds of the stoichiometric fuel-air mixture for both initial temperatures are accurately reproduced by Wang-TRF and An-TRF with the maximum percentage error of 5%. On the other hand, flame speeds predicted by Jiao-TRF are higher by 32% at 353 K and 25% at 500 K, respectively. To acquire the rationale behind the observed discrepancies, sensitivity coefficients of mass flow rate at the equivalence ratio of unity are determined and normalised by the highest absolute value for both initial temperatures. Ranked in descending order of sensitivity towards flame speed, the top ten reactions are identified in Figure 4-17 with the common reactions from the mechanisms coloured.

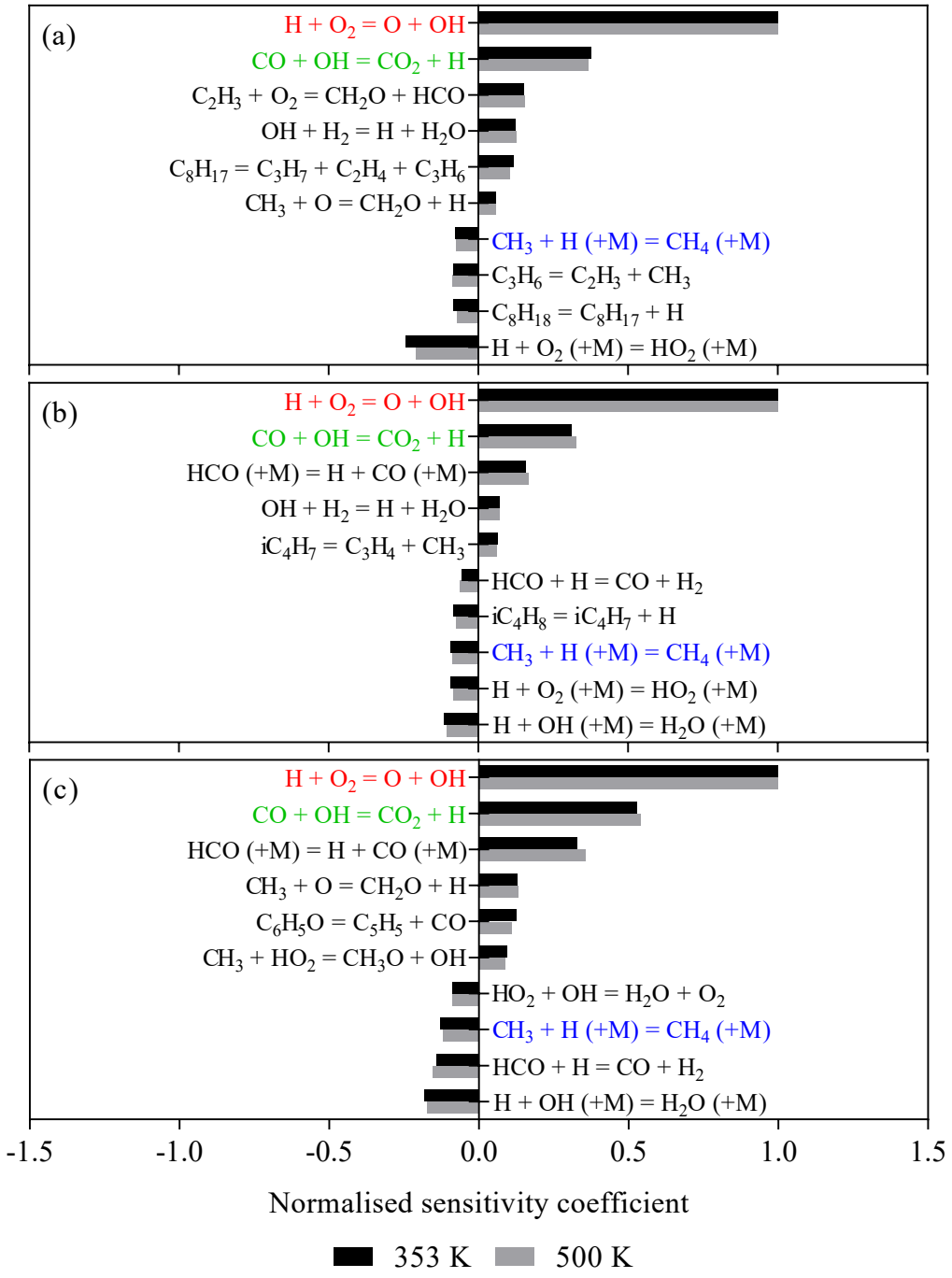


Figure 4-17 Normalised sensitivity coefficients for the laminar flame speed of CR-87 at atmospheric pressure, initial temperatures of 353 K and 500 K and equivalence ratio of 1 for (a) Jiao-TRF, (b) Wang-TRF and (c) An-TRF.

Overall, there is no drastic effect of initial temperatures on the sensitivity of laminar flame speed with slightly higher positive normalised coefficients found at 500 K. So, the effect of initial temperature is mainly thermal rather than chemical [224]. Flame

speed is mainly controlled by the chemistry of H and/or OH radicals originating from beta-scission reactions and oxidations of small alkyl radicals [29]. The largest positive coefficient at all the mechanisms is exhibited by the chain-branching reaction between H and oxygen to generate OH radicals. In addition, oxidation of CO to CO_2 increases the flame speed by supplying H required by the former reaction. These reactions cause high heat release and raise the temperature of the system. On the other hand, negative coefficient of recombination reaction of CH_3 and H to form methane (CH_4) appears to be consistent across all the mechanisms.

A deeper look at Figure 4-17 discloses distinct differences among the mechanisms in flame speed computation. The role of unimolecular dissociation of octyl radicals (C_8H_{17}) and isooctane pinpointed in Jiao-TRF remains questionable as Babushok and Tsang [225] have demonstrated the relatively low sensitivity of reactions with large hydrocarbon species (C_5–C_7) towards flame speed. In addition, inhibiting effects of chain-terminating reactions of HCO + H = CO + H_2 and H + OH (+M) = H_2O (+M) detected in Wang-TRF and An-TRF are not captured by Jiao-TRF. Elimination of the reactions during mechanism reduction of Jiao-TRF is potentially the reason of large overestimation in flame speed of stoichiometric mixture of CR-87 and air.

4.7.3 ROP of A1 for Speciation Profile of PAH

To understand reaction pathways of PAH which are critical for soot formation, ROP analysis distinguishes the role of chemical reactions in production or destruction of a species. Positive ROP implies directly species formation from the reactions whereas negative ROP reflects the species consumption pathways. ROP of A1 is carried out under the premixed flame of n-heptane at atmospheric pressure and equivalence ratio of 2.1. This is because formation of large PAH depends heavily on that of small PAH due to the sequential nature of PAH growth [65].

The associated speciation profiles of PAH from A1 to A4 have been plotted in Figure 4-14 in which the best agreement between measured and computed mole fractions is observed for An-TRF. At HAB larger than 0.6 cm, percentage errors in the speciation of A1 by An-TRF are approximately 29%. Meanwhile, differences resulted in Jiao-TRF and Wang-TRF reach as high as 83% and 125%, respectively within the same range of HAB. Hence, ROP of A1 contributed by five reactions with the highest

absolute value for each mechanism are plotted as a function of HAB in Figure 4-18 with the mutual reaction expressed in bold.

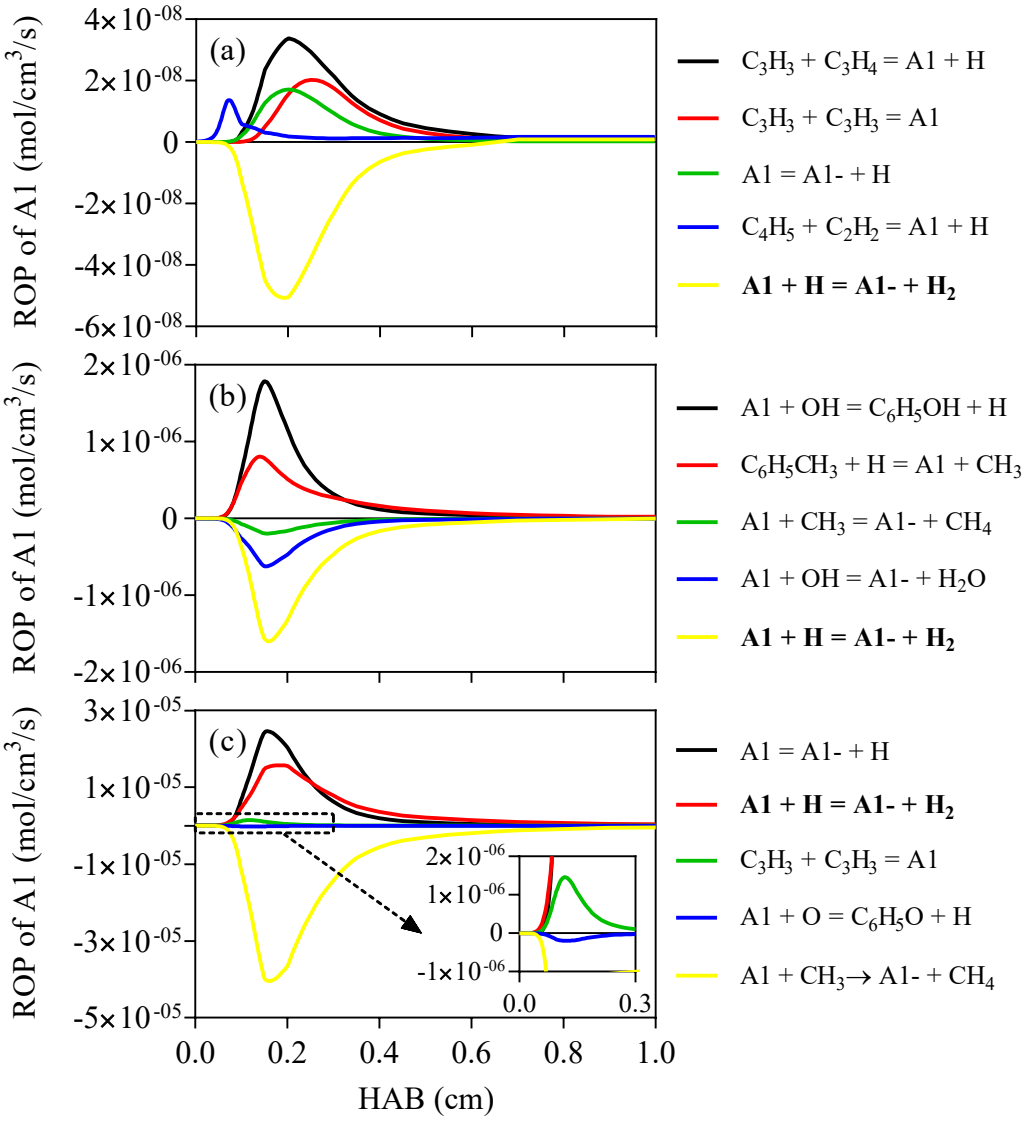


Figure 4-18 ROP of A1 for the rich premixed flame of n-heptane as a function of HAB at atmospheric pressure and equivalence ratio of 2.1 for (a) Jiao-TRF, (b) Wang-TRF and (c) An-TRF.

ROP of A1 depends primarily on H-abstraction reactions of A1 through free active radicals including H, CH_3, OH and O to yield phenyl radicals (A1-). Essentially, the net production of A1 is controlled by the competing rates of formation between A1 and A1- from the corresponding reversible reactions. While consuming A1 in both Jiao-TRF and Wang-TRF, the reaction A1 + H = A1- + H_2 promotes the formation of A1 in An-TRF by the reverse path. Additionally, crucial pathways of A1 formation

through C_2H_2 addition to butadienyl radicals (C_4H_5) [226] and recombination of propargyl radicals (C_3H_3) [227] are preserved in Jiao-TRF and An-TRF. The reaction pathways concerning A1 for all the three mechanisms are generally agreeable to the fundamental studies of PAH chemistry [59,73].

However, the quantitative discrepancies in speciation of A1 for different mechanisms can be correlated to the degree of ROP shown in Figure 4-18. The range of ROP of A1 for Jiao-TRF is lower than those for Wang-TRF and An-TRF by 2–3 orders of magnitude, thus explaining the significant under-prediction of A1 mole fractions by Jiao-TRF. On the other hand, higher mole fractions of A1 computed by Wang-TRF at HAB of 0.4 cm and beyond is presumably contributed by A1 + OH = C_6H_5OH + H and $C_6H_5CH_3$ + H = A1 + CH_3 at smaller HAB. The A1-promoting effects of these aromatic-specific reactions may be overestimated in a premixed laminar flame of the non-aromatic fuel, n-heptane examined.

4.8 Selection of the Optimal TRF Mechanism

Selection of the most appropriate TRF mechanism for subsequent CFD modelling is targeted at operating mode of the GDI engine. The relevant conditions in the present study cover high-temperature (> 900 K) and high-pressure (30–50 bar) homogeneous combustion of a stoichiometric mixture of gasoline and air (ϕ = 1). In addition, fuel-rich conditions and speciation of relevant species of PAH for soot formation are taken into account. Table 4-9 summarises the important operating conditions with resulting validations performed on the three mechanisms. It is noted that experimental studies on real fuels and multi-component surrogates are prioritised wherever applicable to provide a more realistic representation of gasoline.

Given the nature of simplified chemistry of multi-component reduced mechanisms, compromise in the levels of accuracy for various validation targets is expected. Better agreement in computed ID time is observed for Jiao-TRF at 20 bar, particularly during stoichiometric and fuel-rich conditions. The flame speed prediction is conversely poor with percentage differences exceeding 50%. General performances of Wang-TRF and An-TRF in terms of ID time and flame speed are somewhat comparable. However, speciation profiles of PAH in premixed flames and JSR computed by An-TRF are preserved within the same order of magnitude as the measurements whereas those by

Wang-TRF differ by one order of magnitude. From the overall validations, An-TRF is therefore, deemed the optimal reaction mechanism to be integrated in the following GDI engine modelling works. The chemical reactions included in An-TRF are listed in Appendix B with their individual rate coefficients.

Table 4-9 Summary of chemical kinetic validations on the three TRF mechanisms at important operating conditions.

Validation target	Jiao-TRF	Wang-TRF	An-TRF
ID time of RD387 (ST)[a]			
20 bar; 1030–1125 K; ϕ = 0.5	🟡	🟢	🟡
20 bar; 986–1158 K; ϕ = 1.0	🟢	🟡	🟡
20 bar; 1023–1144 K; ϕ = 2.0	🟢	🟡	🟡
55 bar; 988–1111 K; ϕ = 0.5	🟡	🟡	🟢
55 bar; 902–1160 K; ϕ = 1.0	🟢	🟡	🟢
55 bar; 916–1048 K; ϕ = 2.0	🟡	🔴	🟡
ID time of Surrogate B (ST)[a]			
20 bar; 972–1136 K; ϕ = 1.0	🟢	🟢	🟡
55 bar; 907–1136 K; ϕ = 1.0	🟢	🟡	🟢
Flame speed of CR-87 (laminar flame)[a]			
1 bar; 353 K; ϕ = 0.6–1.3	🔴	🟢	🟢
1 bar; 500 K; ϕ = 0.6–1.3	🔴	🟢	🟡
Flame speed of PRF 87 (laminar flame)[a]			
10–15 bar; 373 K; ϕ = 0.7–1.2	🔴	🟢	🟢
20–25 bar; 373 K; ϕ = 0.7–1.2	🔴	🟡	🟢
Speciation of n-heptane (premixed flame)[b]			
1 bar; 695–1530 K; ϕ = 2.1; A1–A4	🟢	🟡	🟢
Speciation of PRF 90 (JSR)[b]			
10 bar; 550–1150 K; ϕ = 1.0; A1	🔴	🟡	🟢

Legends	🟢	🟡	🔴
Maximum absolute deviation (%)[a]	≤ 25	26–50	≥ 51
Maximum absolute deviation (order of magnitude)[b]	0	1	> 1

[a] Against experimental data of ID time and flame speed.
[b] Against experimental data of speciation profile.

4.9 Concluding Remarks

Three TRF mechanisms, coupled with PAH chemistry, are evaluated through 0D and 1D chemical kinetic simulations of various experimental configurations at engine-like operating conditions. The validation targets include ID time measured from ST, laminar flame speed and concentration profiles of crucial species such as reactants, major products, C_2H_2 and PAH from flame burners and JSR. In order to emulate the gasoline fuel closely, kinetic studies on real fuels and multi-component surrogates are prioritised before extending to those on pure components. Derived from the operating mode of the GDI engine, high-temperature conditions of a stoichiometric mixture of fuel and air establish the main validation criteria.

To address the discrepancies between the mechanisms, numerical tools of sensitivity and ROP analyses are employed at chosen operating points. The exclusion of critical reactions involving H and OH radicals in Jiao-TRF is likely responsible for the over-predictions in flame speed of more than 50%. The shortened ID time of RD387 and increased mole fractions of A1 from premixed n-heptane flame computed by Wang-TRF may be attributed to the overestimated toluene reactivity. The overall validations deduce that An-TRF is the optimal reaction mechanism for the CFD modelling works. The ID times of stoichiometric RD387-air mixture at 55 bar are predicted with the largest deviation of 13% throughout 900–1160 K while the computed flame speeds of PRF 87 differ by a maximum value of 14% at higher pressures of 20 bar and 25 bar. Speciation profiles of PAH as functions of HAB and temperature are also captured within the same order of magnitude.

CHAPTER 5
DEVELOPMENT OF INTEGRATED CFD-CHEMICAL KINETIC MODELLING FOR GDI ENGINES

5.1 Introductory Remarks

This chapter discusses the development of integrated CFD-chemical kinetic modelling for the wall-guided GDI engine, detailing both formulation and validation procedures. Understanding the experimental setup including the engine test bed, gasoline fuel and operating variables is crucial so that the experimental conditions can be emulated as closely as possible in the numerical simulations to minimise any uncertainties. Fuel properties and GDI engine specifications are described in Section 5.2, along with the five part-load operating conditions examined. In Section 5.3, the integrated approach is formulated by first generating the computational mesh, selecting the time-step sizes and setting up the initial and boundary conditions. A complete set of CFD sub-models is then developed to characterise the whole panoply of in-cylinder engine phenomena with emphasis placed on combustion and soot modelling. Eventually, the numerical results are validated against the experimental findings in terms of spray properties, fuel surrogate, combustion behaviour and PM production under operating conditions of the selected reference case.

5.2 Experimental Setup of GDI Engine Test Bed

5.2.1 Fuel Specifications

The fuel employed throughout the entire experimental testing was 95 RON reference gasoline. It is a pump-grade unleaded gasoline fuel with a stoichiometric air-fuel ratio (AFR) of 14.4. Important fuel properties in formulating the composition of a suitable TRF surrogate are summarised in Table 5-1.

Table 5-1 Fuel properties of 95 RON reference gasoline.

Property	Value
RON	95
MON	85
H/C ratio	1.89
Density at 15 °C (kg/m^3)	743–756
Aromatics (volume %)	29–35
Olefins (volume %)	3–13

5.2.2 Engine Specifications and Data Acquisition

The test engine is a turbocharged and intercooled wall-guided GDI engine of Euro 4 standard. It is a four-stroke and four-cylinder engine with its technical specifications listed in Table 5-2. Installed on a laboratory test bed, the engine is controlled by a Schenck W150 eddy-current dynamometer via Sierra-CP Engineering CADET automated control and data acquisition system. The overview of the engine test rig is illustrated schematically in Figure 5-1. The engine control unit optimises SI timing in an open-loop process for maximum thermal efficiency and controls fuel injection strategy to achieve homogeneous stoichiometric combustion.

Table 5-2 Technical specifications of the GDI test engine.

Specification	Value/Description
Cylinder displacement (cm^3)	399.5
Bore (mm)	77
Stroke (mm)	85.8
Compression ratio	10.5
Connecting rod length (mm)	138.4
Combustion chamber	4-valve, central spark plug, pent-roof design
Maximum engine speed (rpm)	6000
Maximum rated torque (N m)	240
Number of nozzle holes	7 (circumferential arrangement)
Diameter of nozzle hole (mm)	0.165

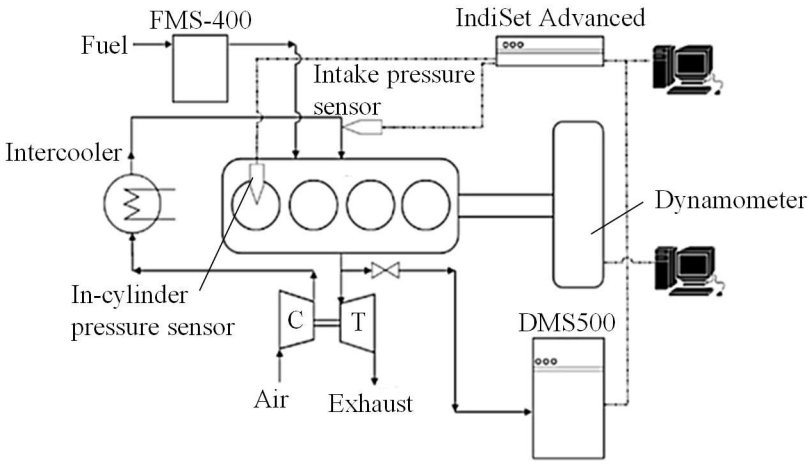


Figure 5-1 Schematic diagram of the engine test rig [228].

The fuel is delivered via a common-rail direct injection system into the combustion chamber by a side-mounted injector. The charge propagates towards the spark plug region through reverse tumble motion assisted by a spoon-shaped piston crown. Injection pressure is regulated as a function of engine speed and load through the engine control unit with a maximum value of 120 bar. Sierra-CP Engineering FMS-400 gravimetric system is utilised to measure the fuel consumption.

A Kistler piezoelectric pressure transducer is mounted on the spark plug of one of the cylinders to acquire in-cylinder pressure measurements with 1 crank angle degree (CAD) resolution. Intake and exhaust pressures are recorded from the same cylinder using Kistler piezo-resistive pressure sensors. The measuring devices are connected to an AVL IndiSet Advanced data acquisition system which works in conjunction with AVL IndiCom 1.6 software for data visualisation and post-processing. At each steady-state condition, batches of 100 consecutive pressure cycles are obtained to determine the ensemble-averaged pressure trace.

Parallel measurements of engine-out PM are made using a fast-response Cambustion DMS500 system which allows real-time classification of PM in the size range of 5–1000 nm based on the aerodynamic drag-to-charge ratio of particles. The sampling point for the exhaust gas stream is fitted into the exhaust manifold, close to the exhaust port of the cylinder. The gas sample passes through a capillary tube into a heated switch valve kept at 190 °C. The switch unit is connected to the PM measurement unit via a heated sampling line maintained at 58 °C to prevent condensation. The sample is drawn at a constant mass flow rate using a scroll vacuum pump.

The corresponding PM measurements are collected under a primary dilution ratio of 5 and a secondary dilution ratio of 25. The exhaust stream is sampled for 5 min in steady state and the data are time-averaged to generate the size-resolved PSDF. The particle mass is then deduced under the assumption that the particles are spherical with a density of 1800 kg/m^3. The PM data acquisition is repeated three times under nominally identical conditions during different days to reduce random errors and increase repeatability. The averaged data of PM are then computed in terms of number density, mass concentration and particle diameter. It is noted that the particles with diameters below 10 nm are excluded due to increased variance within that size range.

5.2.3 Experimental Operating Conditions

Engine testing was carried out experimentally under fully-warm and steady-state operating conditions. The mode of engine operations was targeted to be homogeneous with the stoichiometric global AFR. The five operating conditions under investigation cover a portion of the part-load running regime to represent typical urban and cruise driving situations. They were derived from the classic grid of equally-spaced speed-load points as shown in Figure 5-2. Engine speeds were varied between 1600 rpm, 2300 rpm and 3000 rpm at a fixed load. A variation in engine load at a constant speed was achieved by introducing three levels of torque in the range of 60 N m to 120 N m with an increment of 30 N m. The operating point at the speed of 2300 rpm with a torque of 90 N m was selected as the reference case to which the effects of an increase or a decrease in speed and torque were benchmarked against and correlated to.

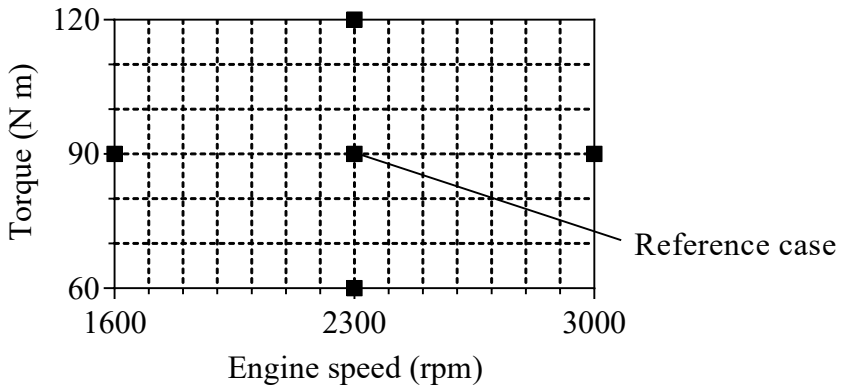


Figure 5-2 Classic grid of equally-spaced speed-load points studied experimentally.

For brevity, the five part-load operating conditions are denoted by the 'speed (in rpm)-torque (in N m)' convention hereafter. To enable the homogeneous combustion mode, fuel injections for all the cases took place during the intake stroke when the piston moved from the top dead centre (TDC) to the bottom dead centre (BDC). Detailed information on the fuel injection and SI events is tabulated in Table 5-3. The intake and exhaust valve timings are summarised in Table 5-4 and illustrated graphically in Figure 5-3. The average pressures and temperatures during intake and exhaust phases acquired experimentally are listed in Table 5-5. The experimental configurations of and related measurements from the engine test bed were provided by the collaborators at Oxford Brookes University in Oxford, England.

Table 5-3 Detailed information on fuel injection and SI events from the experiment.

Case	Speed (rpm)	Torque (N m)	SOI[a] (CAD ATDC[b])	EOI[a] (CAD ATDC[b])	Fuel mass (mg)	SI (CAD BTDC[b])
1600-90	1600	90	68	85	18	22
2300-60	2300	60	58	78	13	35
2300-90	2300	90	59	78	18	25
2300-120	2300	120	55	74	23	15
3000-90	3000	90	45	75	18	25

[a] SOI and EOI represent start and end of injections, respectively.
[b] ATDC and BTDC represent after and before TDC, respectively.

Table 5-4 Intake and exhaust valve timings from the experiment.

Case	IVO[a] (CAD BTDC)	IVC[a] (CAD ABDC[c])	EVO[b] (CAD BBDC[c])	EVC[b] (CAD ATDC)
1600-90	21	14	28	18
2300-60	3	32	16	30
2300-90	7	28	16	30
2300-120	11	24	16	30
3000-90	16	19	22	24

[a] IVO and IVC represent intake valve opening and closing, respectively.
[b] EVO and EVC represent exhaust valve opening and closing, respectively.
[c] ABDC and BBDC represent after and before BDC, respectively.

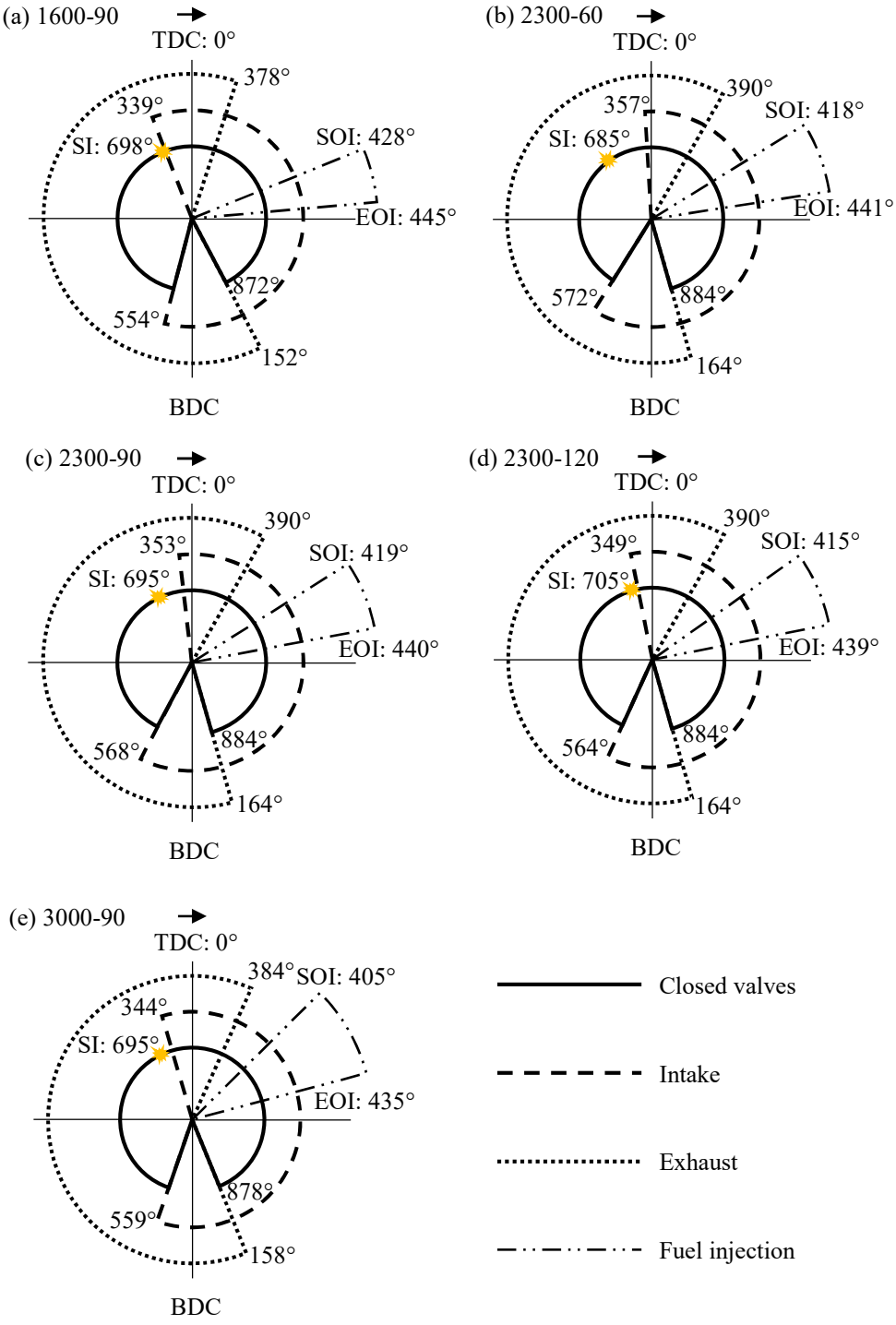


Figure 5-3 Valve timing diagrams including the injection and ignition events for the five part-load operating conditions examined experimentally.

Table 5-5 Average pressures and temperatures during intake and exhaust phases from the experiment.

Case	Intake p (bar)	Exhaust p (bar)	Intake T (K)	Exhaust T (K)
1600-90	0.820	1.096	298.2	822.6
2300-60	0.618	1.080	297.8	820.1
2300-90	0.788	1.106	299.6	907.0
2300-120	0.914	1.133	301.5	959.4
3000-90	0.764	1.150	300.3	965.2

5.3 Numerical Formulation of GDI Engine Modelling with Integrated CFD-Chemical Kinetics

5.3.1 General Numerical Setting

The computational domain of the wall-guided GDI engine consists of intake and exhaust ports, valves and combustion chamber with the piston. Only half of the engine geometry is modelled due to symmetry of the pent-roof design of combustion chamber and the fuel injector nozzle. Following the common practice among GDI engine modelling works [176,228,229], the present computational grid features a typical cell size of 1 mm with local refinements of approximately 0.5 mm in the vicinity of valve seat and spark plug regions. The resulting optimised mesh totals up to 212272 cells when the piston is at TDC and 365720 cells when the piston is at BDC. Cross sections of the computational mesh are illustrated in Appendix C when the piston is at TDC and BDC. The dynamic volume mesh is created within es-ice interface through the trimming approach and automatic generation of engine motion events. To improve mesh quality and reduce the effect of grid topology on the computations, regular hexahedral cells are primarily utilised whenever applicable.

Numerical simulations of GDI engine operations begin at 40 CAD BTDC during the exhaust stroke of the previous cycle (i.e. 320 CAD) and complete at EVO during the power stroke of the current modelled cycle (i.e. 884 CAD for the reference case). The modelling period hence covers all the major in-cylinder events including gas exchange, spray, mixture preparation, ignition, combustion and emission. As listed in Table 5-6, time-step sizes are set and varied accordingly to provide sufficient temporal

resolution in capturing the transient engine processes accurately. It is noteworthy to highlight that more refined time-steps (0.01 CAD) are defined for the valve opening and closing events, fuel injection and combustion processes to account for the more rapid flow changes. To ensure the accuracy of numerical results, the mean Courant numbers at all computational cells are monitored to be always below unity throughout the time-steps in the modelling.

Table 5-6 Time-step sizes employed for different in-cylinder engine events.

Event	Time-step size (CAD)	Time-step size* (μs)
40 BTDC to before IVO	0.1	7.25
IVO	0.01	0.72
After IVO to before EVC	0.1	7.25
EVC	0.01	0.72
After EVC to before SOI	0.1	7.25
SOI to EOI	0.01	0.72
After EOI to before IVC	0.1	7.25
IVC	0.01	0.72
After IVC to before SI	0.1	7.25
SI to 15 CAD ATDC	0.01	0.72
15 CAD ATDC to before EVO	0.1	7.25
EVO	0.01	0.72

* Time-step size is converted from CAD to μs based on the engine speed of 2300 rpm (reference case).

The initial conditions of the cylinder, intake and exhaust ports in terms of pressure and temperature are based on Table 5-5 for each speed-load operating point. The boundary conditions set for the cylinder, ports and valves are provided in Table 5-7 in terms of their temperatures. Near-wall treatments to model in-cylinder heat transfer are described by the wall function proposed by Angelberger [230] which gives a more realistic representation of wall heat fluxes as compared to the standard wall function. The resulting algebraic finite-volume equations are solved implicitly through the PISO algorithm. The method implements a predictor-corrector strategy enabled by the use of operator splitting to temporarily decouple the flow equations and solve them

sequentially. In the present work, all the 3D engine simulations were run in parallel using a hyper-threaded Intel Xeon hexa-core processor with a speed of 3.30 GHz.

Table 5-7 Boundary conditions in terms of designated temperatures for different regions of the cylinder, ports and valves.

Region	Designated temperature (K)	
Cylinder		
Combustion dome	443	
Piston crown	443	
Cylinder liner	423	
Spark plug	500	
Port and valve	Intake	Exhaust
Valve stem	370	443
Valve face	443	443
Port wall	340	443

5.3.2 CFD Sub-models for In-Cylinder Processes

Each engine event is defined and characterised mathematically through appropriate CFD sub-models. The underlying assumptions and governing equations of the models have been elaborated in Section 3.4. The in-cylinder turbulence is described by RNG k-ε model due to its ability to better capture effects of compression, expansion and rapid strain on the turbulence scales. To model fuel injection, the nozzle diameter is specified as 0.165 mm while the spray cone is defined with an inner angle of 0° and an outer angle of 10°. Fuel injection profiles inputted in terms of the mass flow rates are derived to emulate the experimental profiles measured by Montanaro et al. [231] through AVL Fuel Mass Flow Meter in a constant volume vessel with optical access. As depicted in Figure 5-4, the realistic time-resolved profiles feature a drastic increase in the flow rate at the SOI and stabilise to a lower value throughout until the EOI. Initial droplet size distribution of the fuel is expressed mathematically as the Rosin-Rammler distribution function with a characteristic diameter of 50 μm, in line with the range of 20–80 μm examined by Huang and Lipatnikov [132] to model the hollow-cone gasoline sprays.

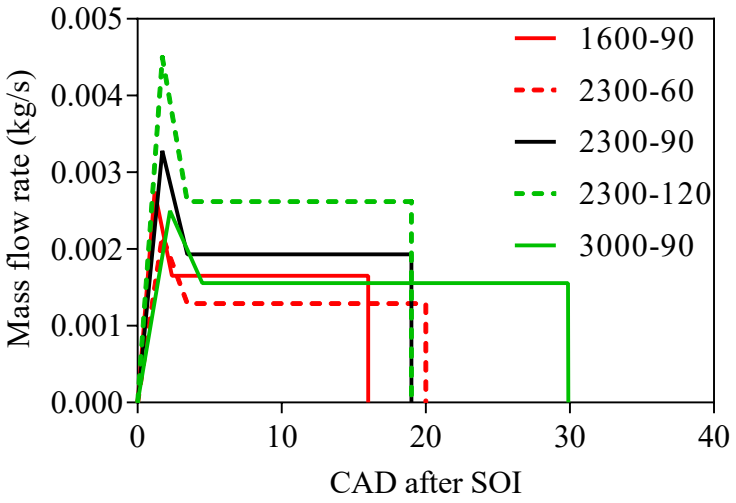


Figure 5-4 Modelled fuel injection profiles for all the operating conditions studied.

Within the Lagrangian framework, the rate of computational parcels injected at each predefined location is set to be 3000000 to represent groups of particles sharing the same droplet parameters and physical properties. As corroborated in spray modelling studies of GDI engines [111,114,232], the KH-RT model is selected in the present work to describe the breakup of fuel droplets as a result of interfacial forces. Also, the impingement events due to spray-wall interactions are governed by the Bai-ONERA model to predict the outcome of a droplet impact as deposition, splashing or rebound. Consequently, the numerical model describing the dynamic behaviours of liquid films formed follows the Eulerian formulation in which film detachment from the wall can occur by surface and/or edge stripping. Upon ignition, the spark is treated numerically by specifying the spark parameters and duration. The selection of numerical models for combustion and emission is elaborated in Section 5.3.2.1 and Section 5.3.2.2. The overview of CFD sub-models adopted in the numerical simulations of the GDI engine has been compiled in Table 3-5 and is illustrated graphically in Figure 5-5.

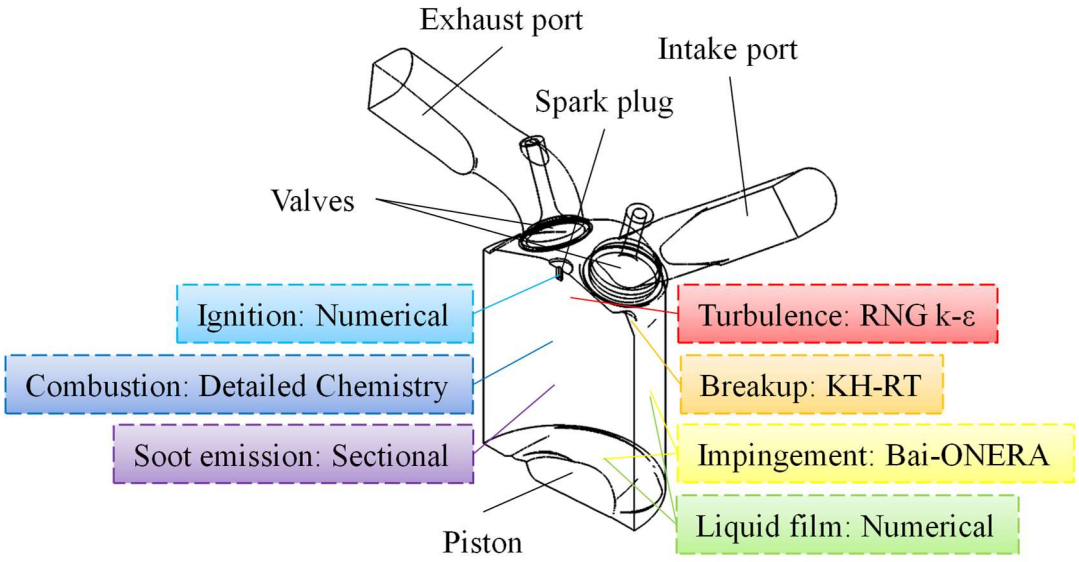


Figure 5-5 Illustration of CFD sub-models adopted along with the geometrical parts of the GDI engine.

5.3.2.1 Appraisal of Combustion Models

For GDI engines, the combustion process is often classified as partially premixed type to which the extent depends on the operating modes (homogenous or stratified). As compiled in Table 2-4 and Table 2-5, several combustion models have been developed and adapted to simulate various configurations of GDI combustion systems. Among all, the family of CFM is the most widely utilised option, particularly the variant of 3-zone ECFM. Based on the concept of flame area, the 3-zone ECFM treats the flame as an infinitesimally thin surface propagating in space which is subjected to physical activities such as stretching, curvature and cusp formation.

Within the model, three zones are distinguished based on the levels of mixing, namely unmixed fuel zone, mixed gases zone and unmixed air plus EGR zone. Combustion takes place in the mixed zone which is the result of turbulent and molecular mixing between gases in the other two zones. Flame propagation is then modelled by solving the transport equation of flame surface density. The transport equation incorporates the theoretical flame speed which is expressed as functions of fuel and equivalence ratio. For post-flame and emission phases, the associated reactions are represented by simplified chemistry of post-oxidation, dissociation and radical formation.

On the other hand, the Detailed Chemistry model relies on the description of chemical kinetics in a reaction mechanism to characterise the combustion and emission events. The model solves transport equations of mass fractions for all species using the time-split numerical solution method due to the large differences in time scale between different reactions. The transport equation of a species depends on the diffusion flux component which is expressed in terms of turbulent viscosity, Schmidt number, molecular diffusivity and thermal diffusion coefficient of the species. To achieve the correct flame propagation speed, scaling factors for enthalpy, species diffusion and rate of reactions can be calibrated accordingly. Table 5-8 compares the applicability of the 3-zone ECFM and the Detailed Chemistry model as combustion models.

Table 5-8 Comparisons of the 3-zone ECFM and the Detailed Chemistry model as combustion models.

3-zone ECFM	Model	Detailed Chemistry model
Flame area	Concept	Chemical kinetics
Flame surface density	Transport equation	Mass fractions of species
Library tables	**Chemistry effect**	**On-the-fly computation**
One-step global mechanism	Reaction mechanism	Reduced mechanism with typically 100 species or less
'Mean fuel' based on individual constituents	Multi-component fuel	In terms of each individual constituent
Lower	Computational load	Higher
Empirical coefficients for production and destruction	Calibration	Scaling factors for enthalpy, species diffusion and rate of reactions

The main distinguishing feature between the models lies within the manner in which the effects of chemistry are incorporated. Based on a storage-retrieval strategy, the 3-zone ECFM makes use of precompiled library tables to compute laminar flame speed which in turn, enables the characterisation of flame propagation. The tabulated library tables are typically generated ahead from reaction mechanisms using simplified 0D and 1D models based on a wide range of varying parameters including conditional temperature of unburnt gases, pressure, mole fraction of residual gases, equivalence

ratio and fuel composition. Despite the lower computational cost, the comparison by Aubagnac-Karkar [25] under a 0D 3-zone ECFM reactor revealed that mass fraction of soot calculated through tabulated chemistry was lower by a factor of two than that using the detailed kinetic solver when they were coupled to the same soot model.

Such a limitation is overcome in the Detailed Chemistry model as the reaction kinetics is directly implemented through pre-validated reduced mechanisms to compute the speciation data arising from chemical source terms. Also, the model describes the fuel oxidation and decomposition more accurately through a series of elementary reactions as compared to the global mechanism used in the 3-zone ECFM with a limited number of species. The multi-component nature of fuel is modelled in the 3-zone ECFM as a 'mean fuel' with its properties averaged from all the constituents whereas the Detailed Chemistry model allows specification of the proportions of individual constituents, thus better emulating the real fuel. Nonetheless, the computational load to run the Detailed Chemistry model in CFD simulations becomes the bottleneck as it is at least a linear [233] or a cubic [43] function of the number of species included, burdened with the level of solution accuracy within the numerical schemes.

Hence, the DMZ partitioning method is introduced to expedite the computations and render the integrated approach feasible. The partitioning method has been previously applied in the combustion modelling of compression-ignition engines [234–236]. In particular, Liang et al. [234] demonstrated a 19-fold reduction in the computational time with the proposed DMZ scheme while reproducing identical in-cylinder pressure and major speciation profiles obtained from the fully resolved calculations (without partitioning). The reaction mechanism of isooctane employed comprised 29 species and 60 reactions. It is highlighted that the relative efficiency gain from using the DMZ partitioning method increases when larger mechanisms are utilised. Essentially, the Detailed Chemistry model, together with the reaction kinetics from An-TRF, forms the backbone of the integrated CFD-chemical kinetic approach in the present work.

5.3.2.2 Appraisal of Soot Models

While the current soot modelling practices in GDI engines commonly utilise multi-step semi-empirical models to describe the entire envelope of PM formation, accurate description of the aerosol dynamics in terms of PSDF is also necessary to understand the inherent intricacy of the related processes. To this end, two well-known numerical

approaches yet with limited applications in GDI engine setups are available, namely the method of moment and the sectional method. They have been extensively applied to predict soot formation in simplified flame configurations [23,24,169] with several integrations in engine environments [25,178,180].

In the method of moments, the PSDF is expressed as a series of moments to be computed whereby the zeroth and first moments correspond to the mean number density and mean volume fraction of soot, respectively. The transport equation for a moment depends on the averaged source term derived from a PDF integration of the instantaneous source term over the mixture fraction and scalar dissipation rate. Conversely, the sectional method divides the size range of interest of soot particles into discrete intervals known as sections and solves the transport equation of soot mass fraction based on the source terms for each individual section.

Wen et al. [237] compared the performance of soot prediction between the method of moments and the sectional method for a plug flow reactor fuelled by a rich C_2H_4-air mixture. It is found that the former under-predicted the soot mass concentration by a factor of three and failed to provide the PSDF. With particle inception, surface growth and oxidation included, the associated computational time for the method of moments was about 1.5 min while that for the sectional method was 287 min. Despite the better computational efficiency, the method of moments requires additional assumptions of mathematical closure to solve the transport equations of a finite number of moments. This is typically attained by presuming a functional form of the PSDF or through moment interpolations which are not generally valid [238].

Unlike the method of moments which mainly provides statistical information on soot particles, the sectional method resolves the PSDF directly by discretising the entire particle ensemble into several sections. However, the major drawback is attributed to the enormous computational cost incurred [23], on top of the intensive reactive flow calculations in 3D engine simulations. Fortunately, the aforementioned computational speedup offered by the DMZ partitioning method allows the coupling of the sectional method with the selection of adequate sections to CFD modelling in describing soot processes in a cost-effective manner numerically.

5.3.3 Validation of Integrated CFD-Chemical Kinetic Modelling

The integrated CFD-chemical kinetic modelling approach developed to simulate homogenous charge operations of the GDI engine is validated thoroughly from spray targeting, combustion progress up to PM formation and emission phases eventually. Related CFD sub-models are calibrated accordingly to capture the in-cylinder events accurately by replicating the available experimental measurements from the reference case of 2300-90 based on the operating conditions listed in Table 5-3 till Table 5-5. The general framework in validating combustion and emission modelling is illustrated in Figure 5-6. Subsequently, the optimised numerical settings are imported, wherever applicable, to the remaining speed-load points to study the effects of engine speed and load on combustion and PM emission characteristics.

In the present study, one complete engine simulation case (until the EVO timing) took approximately 85 h. The computational time appears to be reasonable as compared to related CFD modelling studies as tabulated in Table 5-9. Seo et al. [239] investigated the application of split injection strategies in a GDI engine with the 3-zone ECFM while Hepkaya et al. [240] modelled the combustion process in a PFI engine through the CFM. The former lacked experimental validation of soot emissions while emission modelling was not included in the latter. Thus, considering the direct incorporation of fuel chemistry and the sectional method, the computational cost of the present integrated approach in modelling GDI combustion is deemed highly comparable to those relying on the tabulated chemistry given the constraint in computing power.

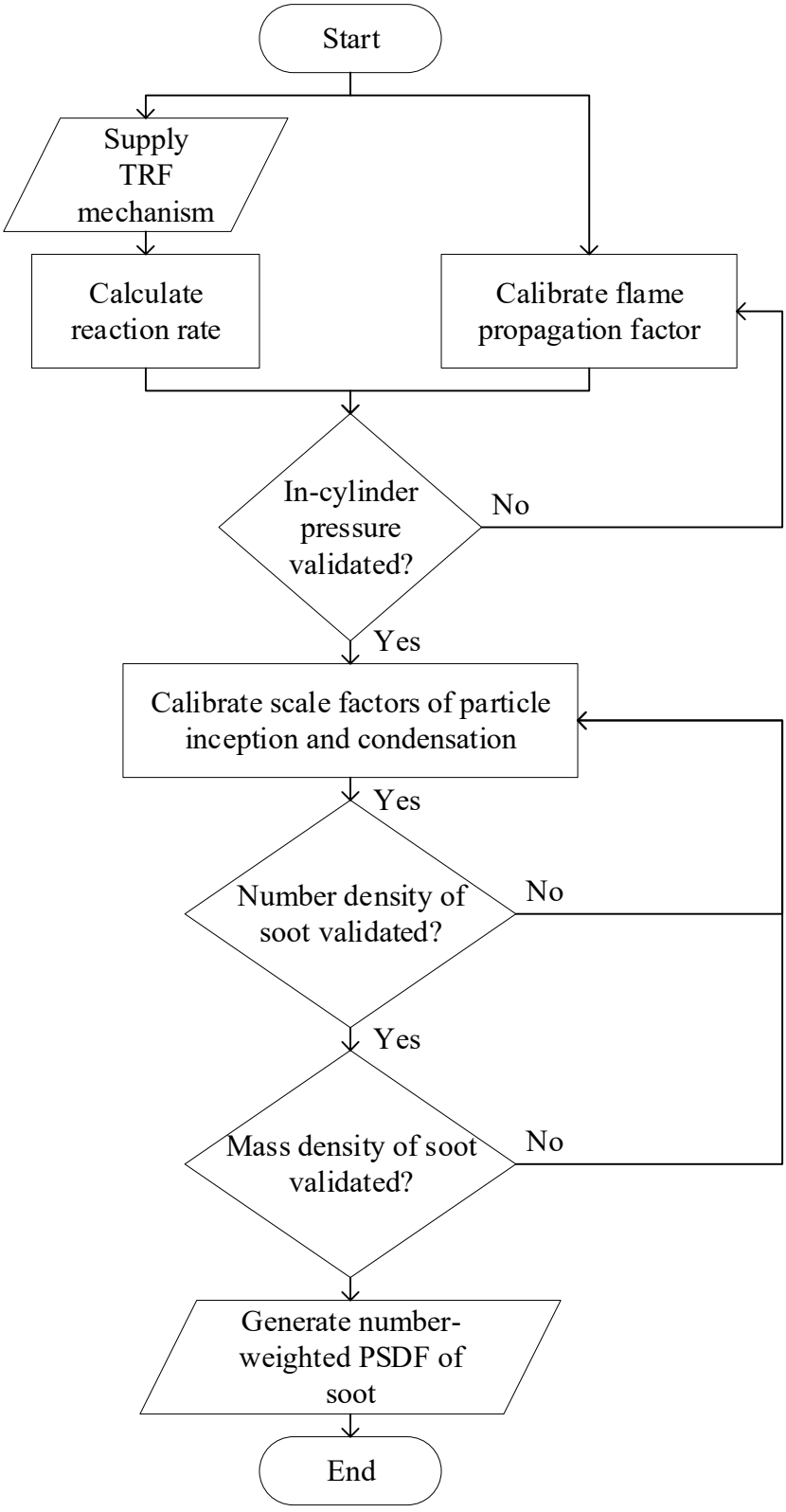


Figure 5-6 General framework in validating combustion and emission modelling.

Table 5-9 Comparisons between computing facilities and the associated costs for 3D engine modelling.

Author(s)	Present	Seo et al. [239]	Hepkaya et al. [240]
Number of cores	12	16	24
Random-access memory (GB)	16	16	24
Computational time (h)	85	75	56
Number of cells at BDC	365720	344000	693124

5.3.3.1 Spray Modelling

The spray modelling is initially calibrated based on the experimental works carried out by Whelan [241] using the similar 7-hole fuel injector in a static spray vessel with optical access. The vessel was filled with nitrogen and kept at ambient pressure of 1 bar to provide a non-evaporative environment. Via a downward-facing injector, the fuel was delivered at an injection pressure of 120 bar over a duration of 0.32 ms. The KH-RT model is tuned accordingly to replicate the experimental spray tip penetration length which is defined as the distance between the nozzle and the bulk of the spray containing 90% of the mass of fuel droplets. Spray tip penetration is the key parameter governing fuel distribution, mixing and potential spray-wall impingement [78]. As seen in Figure 5-7, the excellent agreement between the measured and predicted spray penetration lengths with estimated deviations of 1 mm indicates that the transient process of spray development has been accurately modelled.

Despite the lack of experimental measurements of SMD of droplets by Whelan [241], the predicted SMD stabilised towards the EOI exhibits fair agreement with commonly reported values of SMD as tabulated in Table 5-10. The lower value of SMD predicted here as compared to that measured by Lucchini et al. [31] is attributed to the higher injection pressure as increasing injection pressure has a diminishing effect on the droplet diameter [242]. Overall, the spray modelling is properly validated in terms of liquid penetration and droplet diameter under a designated spray environment. The setup is then implemented within the engine simulations to model the corresponding spray breakup. Accurate characterisation of spray targeting establishes a fundamental prerequisite to ensure precise modelling of the resulting air-fuel mixing process.

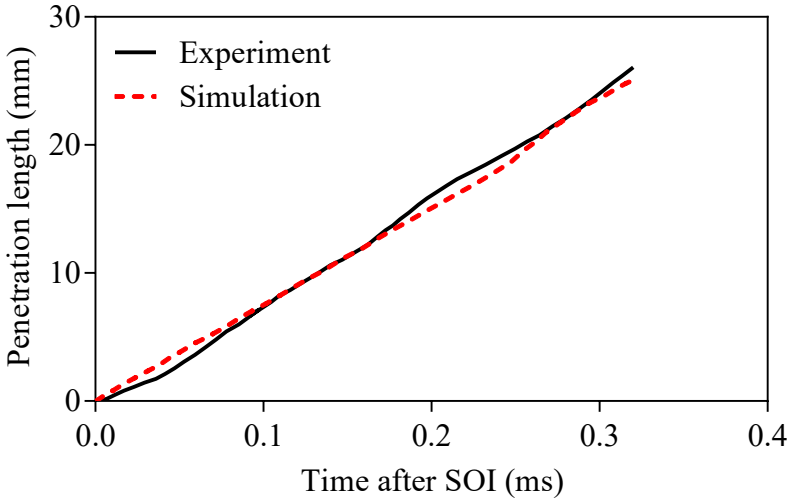


Figure 5-7 Measured and computed spray tip penetration length as a function of time after SOI at the injection pressure of 120 bar over the period of 0.32 ms.

Table 5-10 Predicted SMD in the present work compared to reported experimental values of SMD.

Author(s)	Injection pressure (bar)	SMD (μm)
Present work	120	16*
Yi and DeMinco [133]	-	11
Lucchini et al. [31]	100	21

* Predicted SMD of droplets based on the calibrated KH-RT model.

5.3.3.2 Fuel Modelling

While TRF surrogates are becoming the norm in representing gasoline fuels, isooctane is more commonly utilised in CFD simulations of SI engines in general. The former results in larger complexity due to the interactions between different components and the need to optimise their individual proportions based on selected targets of the real fuel. Although simplified, the use of isooctane neglects other essential constituents, particularly aromatics which have been highly associated to PM formation. Hence, a comparative study is performed on isooctane and TRF to justify the proper choice of fuel surrogate in the engine simulations.

To formulate a TRF surrogate for the 95 RON reference gasoline described in Section 5.2.1, the similar set of equations outlined in Section 3.2 is applied to determine its composition. In terms of liquid volumes, the appropriate TRF surrogate consists of

64% isooctane, 14% n-heptane and 22% toluene. The performance in using isooctane and TRF as fuels is compared in terms of pressure, temperature, fuel consumption, fuel evaporated, liquid film mass, number density and mass density of soot as shown in Figure 5-8 till Figure 5-10. From Figure 5-8(a) and (b), combustion initiates and proceeds faster for the single component of isooctane as compared to the ternary TRF mixture. Peak pressure and temperature increase by 40% and 12%, respectively when the fuel is switched from TRF to isooctane. This is because the overall fuel reactivity is suppressed by the presence of toluene in TRF as previously elucidated in Section 4.4.1.

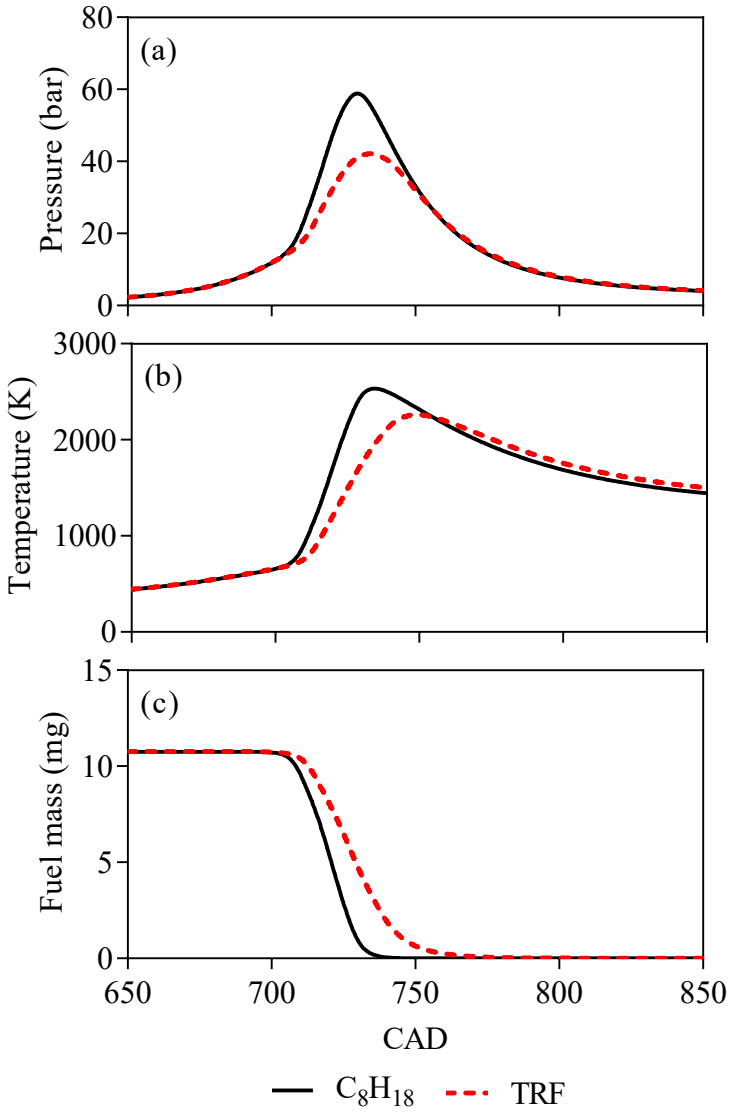


Figure 5-8 Computed in-cylinder (a) pressure, (b) temperature and (c) fuel mass as a function of CAD when the fuel is represented as isooctane and TRF surrogate.

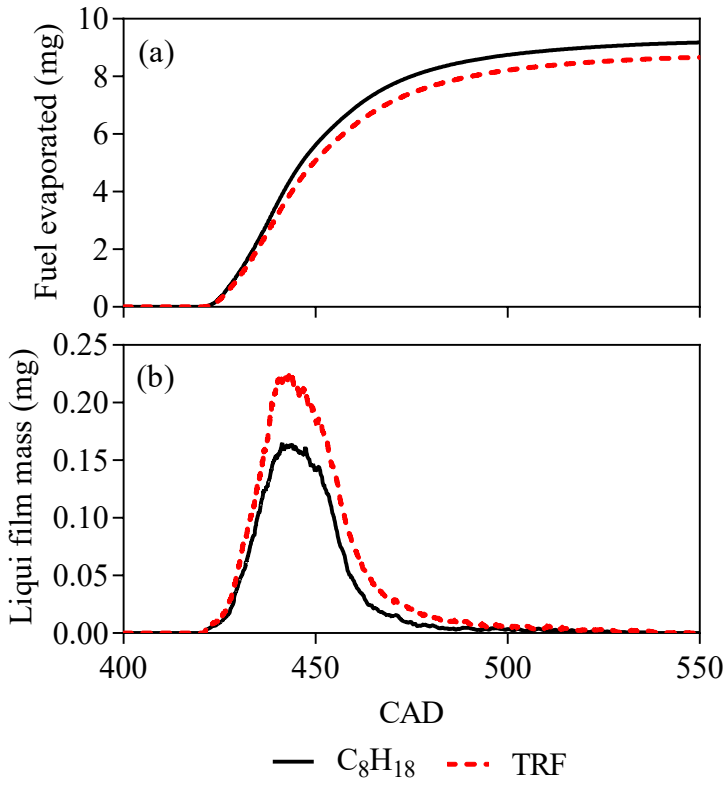


Figure 5-9 Computed (a) mass of fuel evaporated and (b) mass of liquid film as a function of CAD when the fuel is represented as isooctane and TRF surrogate.

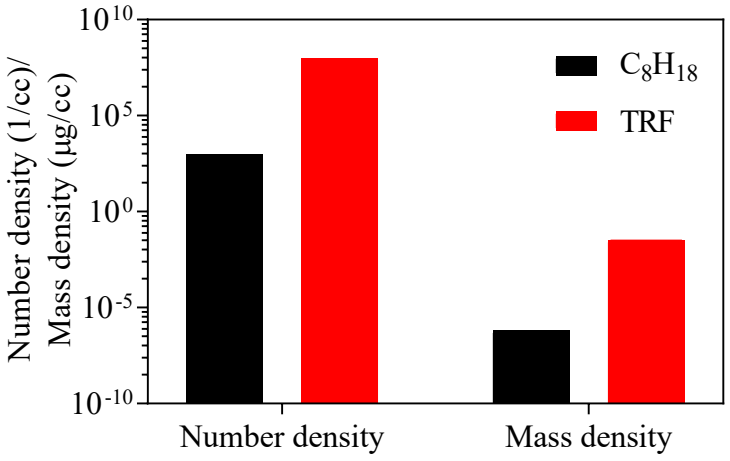


Figure 5-10 Computed number density and mass density of soot at EVO when the fuel is represented as isooctane and TRF surrogate.

Higher fuel reactivity of isooctane is also evident from the earlier and more rapid fuel consumption profile illustrated in Figure 5-8(c) as compared to that of TRF. This can

be partly attributed to the better vaporisation properties of isooctane shown in Figure 5-9(a) due to its higher volatility. As a result of enhanced vaporisation, the maximum liquid film mass formed, when using isooctane, is lower by 27% as compared to that when using TRF as the fuel. Furthermore, the lack of aromatics in isooctane affects the soot production drastically as seen in Figure 5-10. Both number density and mass density of soot for isooctane are five orders of magnitude lower than those of TRF.

Therefore, TRF remains a more appropriate fuel surrogate for gasoline when it comes to engine simulations. Using isooctane as a single fuel component leads to inaccurate modelling of combustion behaviour and unrealistic estimation of PM formation due to dissimilar fuel properties and lack of aromatic compounds, respectively. The need to include aromatics in a gasoline surrogate is also corroborated by the counterflow flame experiment conducted on a laboratory scale to reproduce the critical conditions of extinction and auto-ignition of real fuels [76].

5.3.3.3 Combustion Modelling

In the Detailed Chemistry model, the chemistry effect is computed on the fly based on the supplied reaction mechanism to describe the fuel combustion as a whole. The computational load typically increases drastically with higher numbers of species and reactions. Substantial savings in computational time can be achieved if the calculation is initiated only when the chemistry effects become dominant. Hence, two approaches to combustion modelling are carried out in which

i. the Detailed Chemistry model is activated at SOI and
ii. the Detailed Chemistry model is activated at the onset of SI.

The computed in-cylinder pressures and temperatures are depicted in Figure 5-11, along with rates of change of the pressures and mass of fuel species as a function of CAD for both approaches.

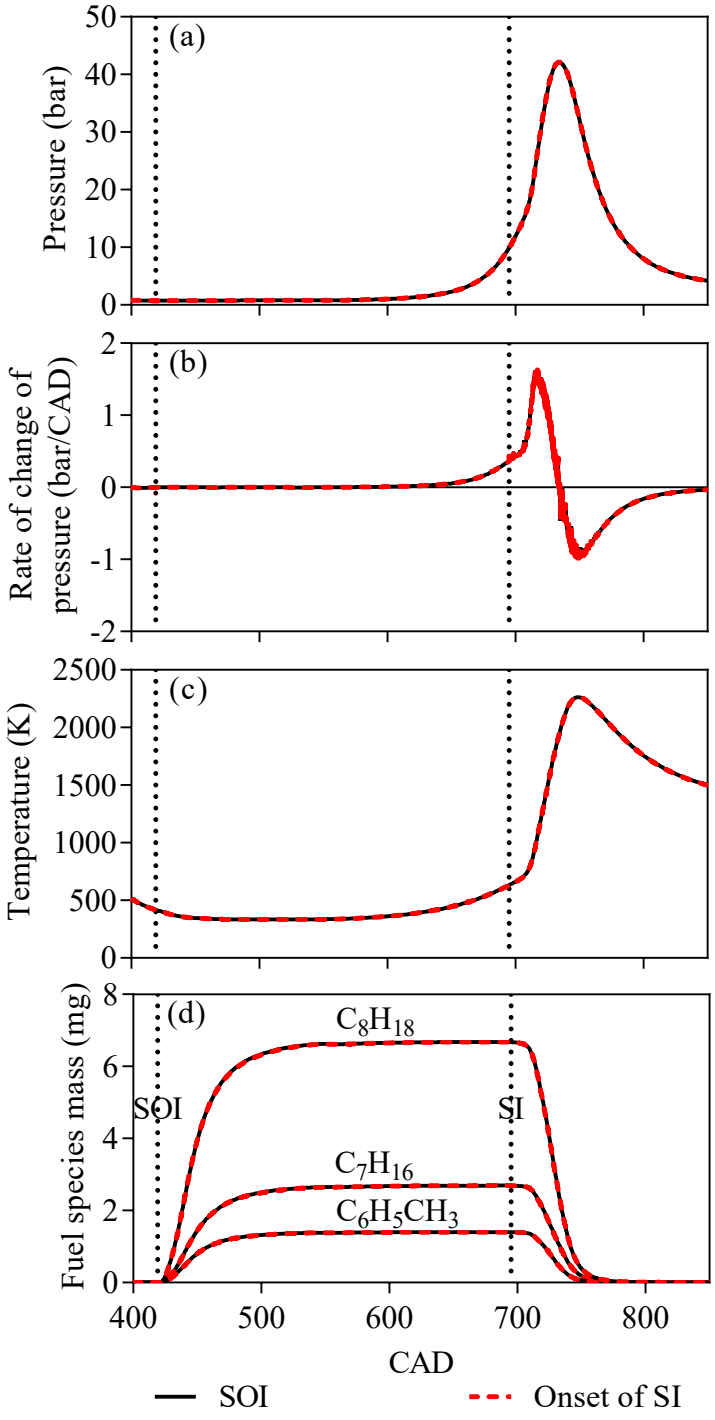


Figure 5-11 Computed in-cylinder (a) pressure, (b) rate of change of pressure, (c) temperature and (d) mass of fuel species as a function of CAD when the Detailed Chemistry model is activated at SOI and at the onset of SI.

The differences in computational results of combustion modelling when the Detailed Chemistry model is activated at SOI and at the onset of SI are indiscernible. In both

cases, the temporal developments of in-cylinder pressures and temperatures are essentially identical. As shown in Table 5-11, peak pressure and temperature predicted by the Detailed Chemistry model for both approaches vary by less than 1%. Hence, it can be deduced that the fuel chemistry effects only take place effectively after SI as evidenced by the rapid rises in pressure and temperature in Figure 5-11(a) and (c).

Table 5-11 Computed peak pressure and temperature when Detailed Chemistry model is activated at SOI and at the onset of SI with the computational time required.

Detailed Chemistry model	SOI	Onset of SI	Difference (%)
Peak pressure (bar)	42.12	42.16	0.09
Peak temperature (K)	2263.74	2263.33	0.02
Computational time (h)	114.4	84.9	25.79

Furthermore, fuel consumption profiles for all three components as illustrated in Figure 5-11(d) reveal that the fuel decomposition begins at about 15 CAD after the event of SI for both modelling approaches. This directly reflects the insignificance of low-temperature chemistry of TRF under the GDI engine operation when the average in-cylinder temperature is below 500 K before the ignition. It is also supported by the kinetic simulations in Section 4.4.1 which highlight the low reactivity of high-ON TRF within the low-temperature regime. Activating the Detailed Chemistry model upon SI provides the same level of accuracy in combustion modelling as activating it earlier at SOI with an added advantage of computational speedup. Therefore, the Detailed Chemistry model is activated at the onset of SI for the engine simulations to achieve the computational saving of nearly 26% as depicted in Table 5-11.

As discussed previously, the DMZ partitioning method expedites the calculations by grouping computational cells based on their local thermo-chemical states and solving them in groups. The criteria for group construction need to be properly established to capture the combustion process accurately. As an improvement to the earlier works [234,235] which only utilised temperature and equivalence ratio, four flow variables pertinent to GDI combustion are proposed in Table 5-12 to segregate and assemble the cell groups. For each variable, two available options to divide the computational cells are to:

i. specify an interval within the predefined range of values
ii. specify the total number of bins within the range determined by the solver based on the local conditions at each time-step

For temperature and mixture fraction, a lower limit and an upper limit are assigned, along with a suitable interval within the range. Meanwhile, the total number of bins are specified for enthalpy and mass fraction of H as their values vary drastically depending on the local cell conditions.

Table 5-12 Flow variables proposed as criteria for group construction in the DMZ partitioning method.

Flow variable	Significance
Temperature	To represent the combustion progress
Mixture fraction	To characterise the mixing process
Enthalpy	To represent the energy level
Mass fraction of H	To capture the SI process

To identify the optimal setting for DMZ partitioning, three ways of group construction are tested within the Detailed Chemistry model as detailed in Table 5-13. The intervals and numbers of bins for each way of group construction differ by a factor of two with increasing total number of cell groups going from DMZ 1 to DMZ 3. The resulting computed in-cylinder pressures, temperatures and changes in total fuel mass are plotted in Figure 5-12 whereas the predicted number density and mass density of soot at different CAD ATDC are illustrated in Figure 5-13 for all three ways of group construction. The peak values of pressures and temperatures, their locations as well as the number density and mass density of soot at EVO are tabulated in Table 5-14.

From Figure 5-12, the computed pressures and temperatures after the event of SI of DMZ 1 are relatively lower while DMZ 2 and DMZ 3 exhibit significantly closer agreement. The maximum deviation in pressures between DMZ 1 and DMZ 3 is 6.1 bar while that between DMZ 2 and DMZ 3 is 1.8 bar. For temperature, the difference between DMZ 1 and DMZ 3 reaches as high as 308 K whereas the differences between DMZ 2 and DMZ 3 stay within 87 K. The magnitudes and CAD of peak pressure and temperature computed by DMZ 2 also resemble those by DMZ 3 with deviations less

than 3.5%. Additionally, the rates of fuel consumption estimated by DMZ 2 and DMZ 3 are nearly similar while relatively slower fuel decomposition is obtained with DMZ 1 as illustrated in Figure 5-12(c).

Meanwhile, larger deviations in number density and mass density of soot are observed across different ways of group construction. Notably, the decreasing trends in number density and mass density after 20 CAD ATDC are consistent for all cases except for DMZ 1 whose number density increases slightly from 20 CAD to 40 CAD ATDC. Due to lower in-cylinder pressures and temperatures, significantly lower amount of soot is predicted by DMZ 1 up to EVO. As compared to DMZ 3, the number density computed by DMZ 1 and DMZ 2 at EVO differs by 52% and 17%, respectively. The deviation in mass density at EVO between DMZ 2 and DMZ 3 is about 20% while that between DMZ 1 and DMZ 3 is as high as 55%.

Table 5-13 Setting of group construction for the DMZ partitioning method.

Flow variable	Range	Interval	Number of bins
		DMZ 1	
Temperature (K)	500–3000	4	-
Mixture fraction	0–0.1	0.0002	-
Enthalpy (J)	-*	-	100
Mass fraction of H	-*	-	50
		DMZ 2	
Temperature (K)	500–3000	2	-
Mixture fraction	0–0.1	0.0001	-
Enthalpy (J)	-*	-	200
Mass fraction of H	-*	-	100
		DMZ 3	
Temperature (K)	500–3000	1	-
Mixture fraction	0–0.1	0.00005	-
Enthalpy (J)	-*	-	400
Mass fraction of H	-*	-	200

* Determined by the solver based on the local cell conditions.

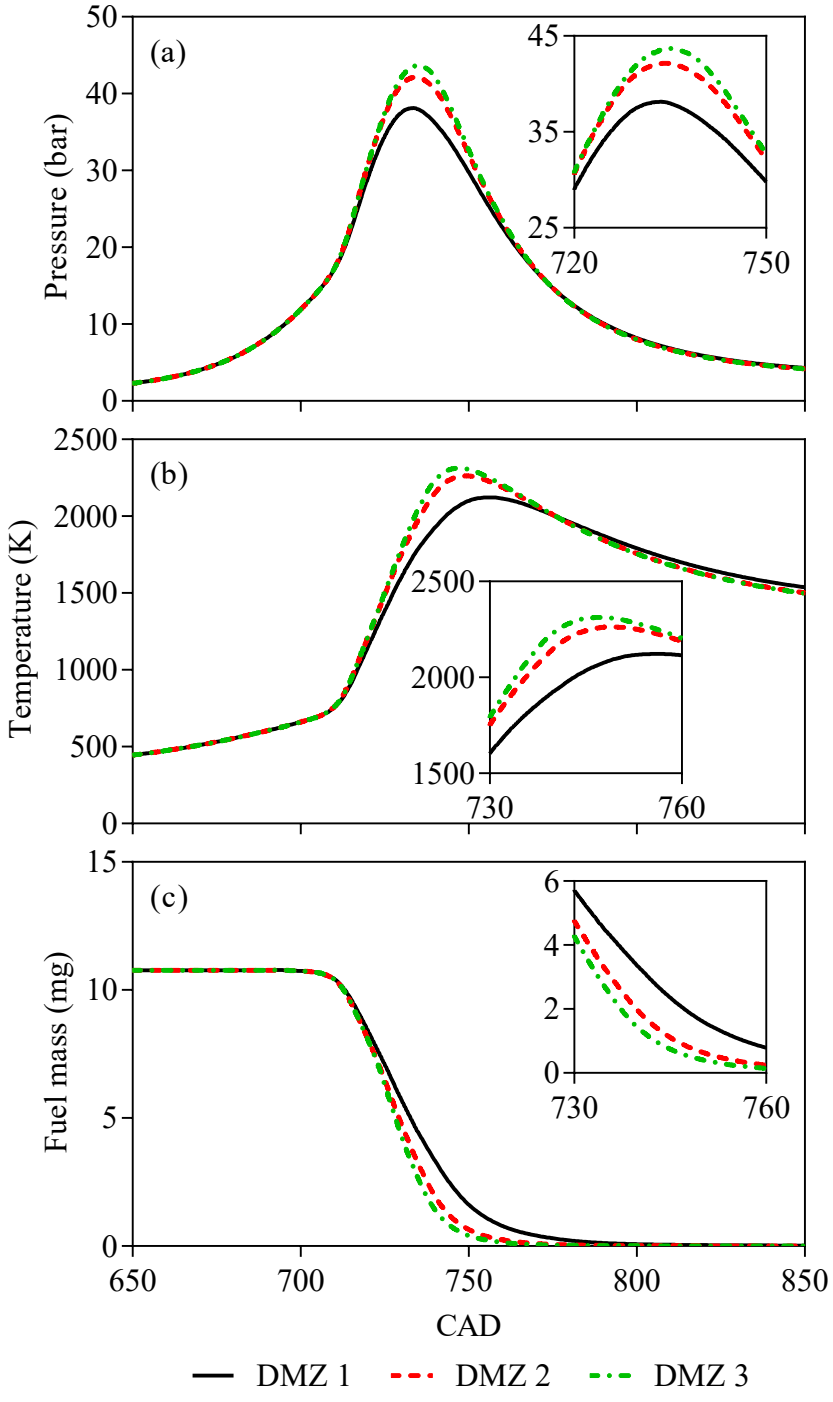


Figure 5-12 Computed in-cylinder (a) pressure, (b) temperature and (c) change in fuel mass for different ways of group construction in the DMZ partitioning method.

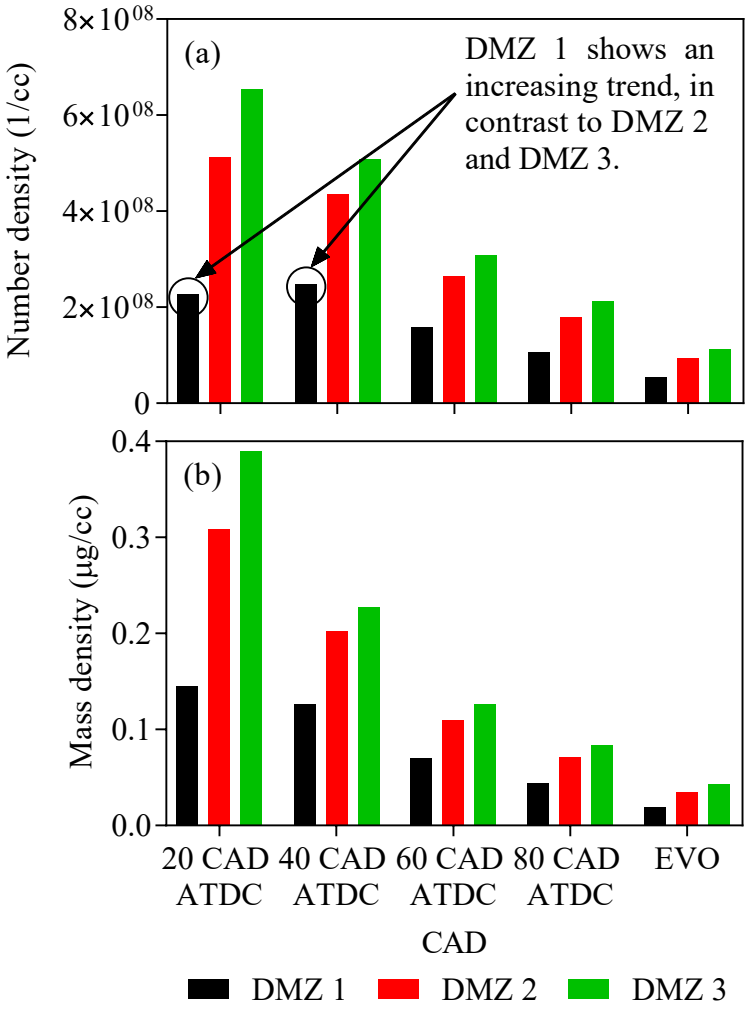


Figure 5-13 Computed (a) number density and (b) mass density of soot at different CAD ATDC for different ways of group construction in the DMZ partitioning method.

Table 5-14 Computed peak pressure, temperature and their locations as well as number density and mass density of soot at EVO for different ways of group construction in the DMZ partitioning method.

DMZ partitioning	DMZ 1	DMZ 2	DMZ 3
Peak pressure (bar)	38.14	42.16	43.71
Location of peak pressure (CAD)	733.55	734.10	735.00
Peak temperature (K)	2123.03	2263.33	2313.07
Location of peak temperature (CAD)	756.60	749.00	747.30
Number density at EVO (1/cc)	5.38×10^{7}	9.33×10^{7}	1.13×10^{8}
Mass density at EVO (µg/cc)	0.01956	0.03440	0.04319

To sum up, with its simplistic segregation of computational cells, DMZ 1 is deemed insufficient to capture the combustion and emission processes adequately. At the same time, DMZ 2 and DMZ 3 display reasonably close agreement for all the characteristic quantities computed. Therefore, DMZ 2 is selected as the appropriate setting for the DMZ partitioning method to be used in conjunction with the Detailed Chemistry model. Further refinements in group construction through decreasing the intervals and/or increasing the numbers of bins for the flow variables are unnecessary as they impose higher computational load.

By activating the Detailed Chemistry model with the defined setting of DMZ partitioning at the onset of SI, flame propagation factor within the combustion model is calibrated to emulate the actual flame propagation and development, hence reproducing the experimental in-cylinder pressures. Figure 5-14 shows both simulated and measured pressure curves for the reference case, together with the rate of pressure change. Good agreement in temporal development of in-cylinder pressures is seen, particularly at the peak value. In general, the computed pressures appear to be slightly higher with the maximum percentage difference approximated at 20%. Figure 5-14(b) reveals that initiation of combustion is faster during the simulation as evidenced by the earlier rapid rise in rate of pressure change as compared to the experiment. The predicted trend then becomes consistent with the measured one after 15 CAD ATDC, signalling that the stage of late combustion is adequately captured.

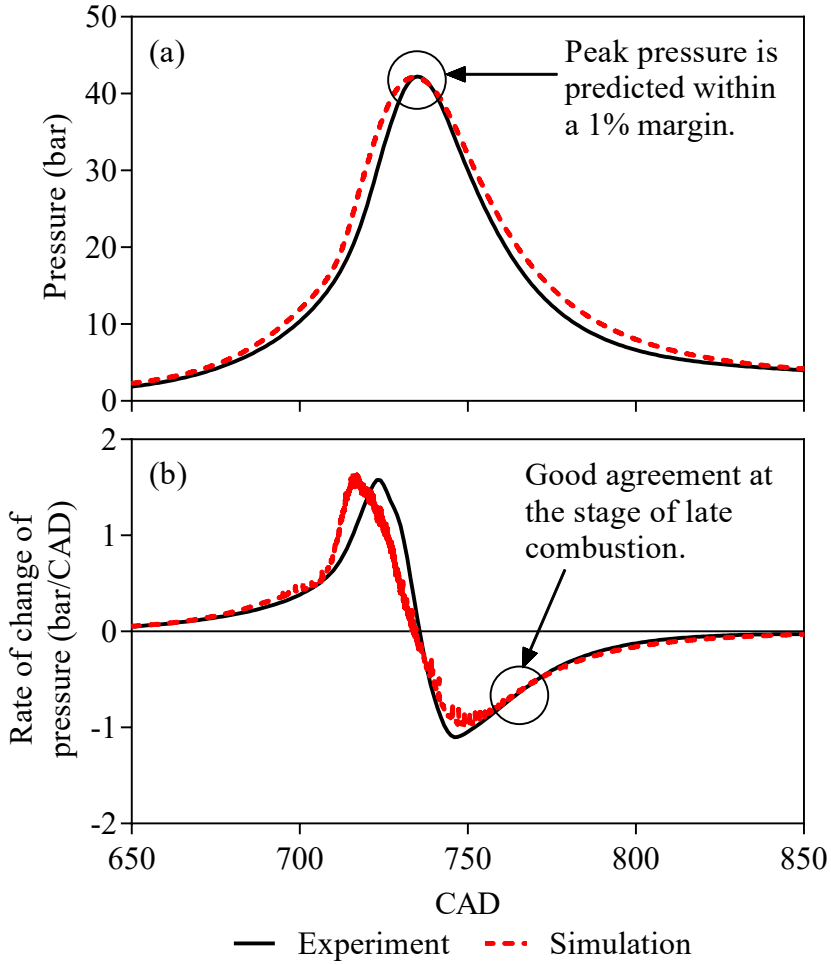


Figure 5-14 Measured and computed in-cylinder (a) pressure and (b) rate of change of pressure for the reference case.

5.3.3.4 Soot Modelling

The population of soot particles is evaluated using the sectional method in which the particles are grouped based on their volumes into discrete sections. The present work treats soot particles as solids and models them as a distinct dispersed phase which interacts with the gaseous phase within the turbulent reactive flow. The phenomena involved in the net soot formation process can be classified into the following two categories:

i. Collisional source terms include particle inception, PAH condensation and coagulation.
ii. Chemical source terms cover surface growth and oxidation.

For particle inception, formation of a nascent soot particle is governed by the collision rate between two PAH molecules which act as the precursors. The nucleation of soot particles from PAH is also supported by transmission electron microscopy [21] and molecular dynamics simulations [243]. In this context, A4 is selected as the gaseous precursor species as it is widely utilised in soot modelling studies [159,244,245] under the assumption that incipient particles are of the sizes of dimers of A4. Condensation and coagulation both contribute to an increase in particle size. However, condensation depends on the rate of collision between soot particles and PAH whereas coagulation takes place from the collisions among soot particles.

On the other hand, computing surface growth and oxidation depends on the reactions describing the surface chemistry of soot particles. Surface growth increases particle size through carbon addition from the gaseous phase. In contrast, oxidation involves taking carbon from soot particles by oxygen and OH radicals, thus diminishing the particle size. The present work adopts the HACA ring closure (HACARC) mechanism developed by Mauss et al. [246] in which the surface chemistry reactions are listed as follows.

i. $C_{soot,i}H + H = C^*_{soot,i} + H_2$
ii. $C_{soot,i}H + OH = C^*_{soot,i} + H_2O$
iii. $C^*_{soot,i} + H \rightarrow C^*_{soot,i}H$
iv. $C^*_{soot,i} + C_2H_2 = C^*_{soot,i}C_2H_2$
v. $C^*_{soot,i}C_2H_2 = C_{soot,i+1}H + H$
vi. $C^*_{soot,i} + O_2 \rightarrow C^*_{soot,i-1} + 2CO$
vii. $C^*_{soot,i}C_2H_2 + O_2 \rightarrow C^*_{soot,i} + 2CHO$
viii. $C_{soot,i}H + OH \rightarrow C^*_{soot,i-1} + CH + CHO$

$C_{soot,i}H$ represents an 'armchair' site on the soot particle surface while $C^*_{soot,i}$ is the corresponding radical in section i. The HACARC mechanism is a modified version of that initially proposed by Frenklach and Wang [247] to take into account the effects of reaction reversibility.

Within the sectional method, the number of sections assigned is 20. The threshold temperature above which soot source terms are computed is set to be 900 K as the nucleation of soot particles typically begins at around 1000–2800 K in the presence of UHC [21]. To replicate the measured number density and mass density of soot,

scale factors for particle inception and condensation are calibrated accordingly. It is noteworthy that chemical source terms of surface growth and oxidation are calculated based on the surface chemistry in the HACARC mechanism without additional tuning. The computational results for the reference case based on the optimised setting of sectional method is illustrated graphically in Figure 5-15 with the experimental data. Tailpipe measurements of PM at the exhaust phase are compared against the computed soot results at EVO under the commonly adopted assumption during modelling that soot particle physics and chemistry remain frozen beyond EVO.

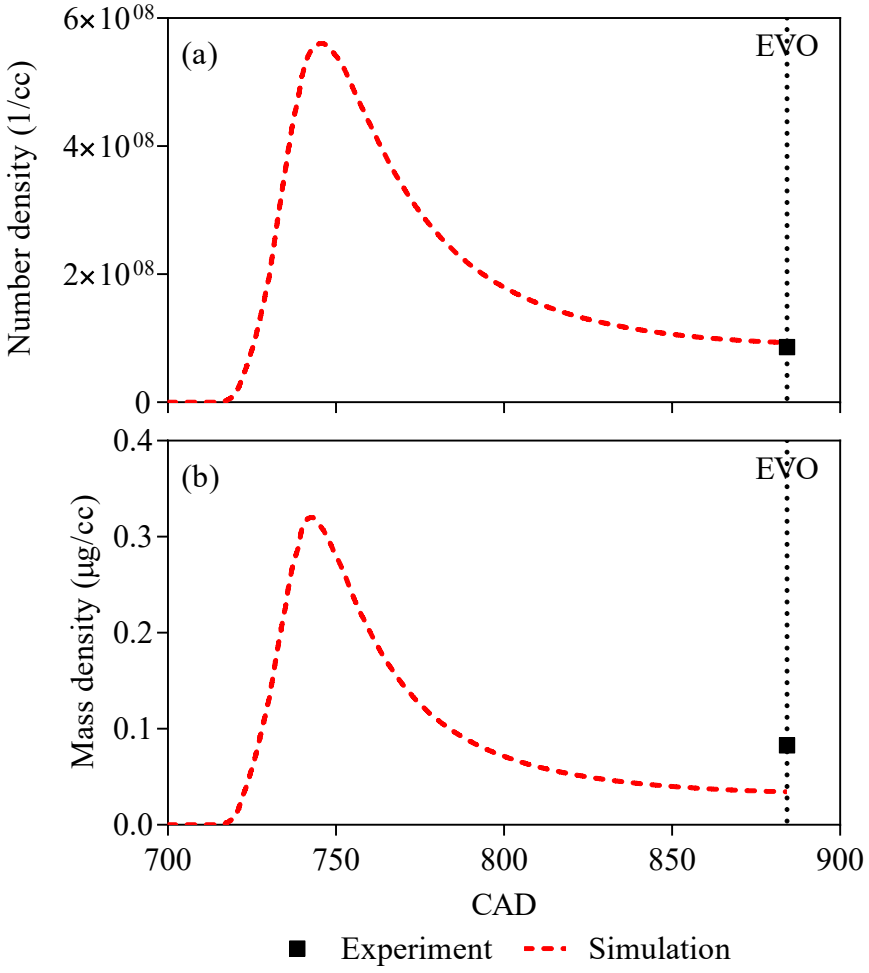


Figure 5-15 Computed (a) number density and (b) mass density of soot for the reference case along with the experimental data compared at EVO.

From Figure 5-15, excellent agreement between the measured and computed number density of soot is observed at EVO with a percentage difference of 8%. In contrast, mass density of soot is under-predicted roughly by a factor of two as compared to the

measured value. The underestimation in soot mass is commonly observed in the few soot modelling studies with validations against experimental data in GDI engines [173,180,182,190]. For instance, the computed soot mass fraction by Wallesten et al. [173] was lower by a factor of 3.4 at 2000 rpm while the work of Kim et al. [180] under-predicted the mass density of soot by factors of 1.8–5.9 across the injection pressures examined at 1600 rpm. Potential causes of the observed deviations include:

i. Since engine-out measurements of PM are taken past the valve into the exhaust manifold, the particles are subjected to further condensation and coagulation which are not captured in the simulations after EVO.
ii. The simulations do not take into account the presence of volatile fraction of organic and inorganic compounds. The volatile components can be absorbed upon the solid particles during the experiment.
iii. Agglomeration results in soot aggregates with a fractal-like structure, thus increasing the overall size. Underestimation of soot mass can be attributed to the lack of modelling of aggregation dynamics in the simulations.

Particularly, engine-out PM are typically emitted in the form of agglomerates. The lack of agglomeration modelling by treating soot particles as spherical primarily contributes to the underestimation of particle size and hence, the total mass. Moreover, the volatile components can be transformed into PM in solid phase through nucleation, condensation and adsorption as the exhaust is diluted and cooled at the measurement system [190]. Though to a lesser extent, PM experiences further condensation and coagulation past the exhaust valve after EVO. These jointly cause increases in particle diameter and mass within the accumulation mode which are not modelled currently.

To understand the soot aerosol dynamics, the present sectional method is capable of extracting detailed information on the PSDF of soot. The measured and computed number-weighted PSDF are illustrated in Figure 5-16 which are normalised by their respective number density during the exhaust phase. An overview of Figure 5-16 reveals that the predicted curve fails to replicate the experimentally observed bimodal distribution. However, particle diameter at the peak of nucleation mode shows good agreement which corresponds to about 15 nm. When the particle size exceeds 50 nm, the number of particles is under-predicted. The lower peak of accumulation mode at particle diameter of approximately 65 nm is not captured by the model.

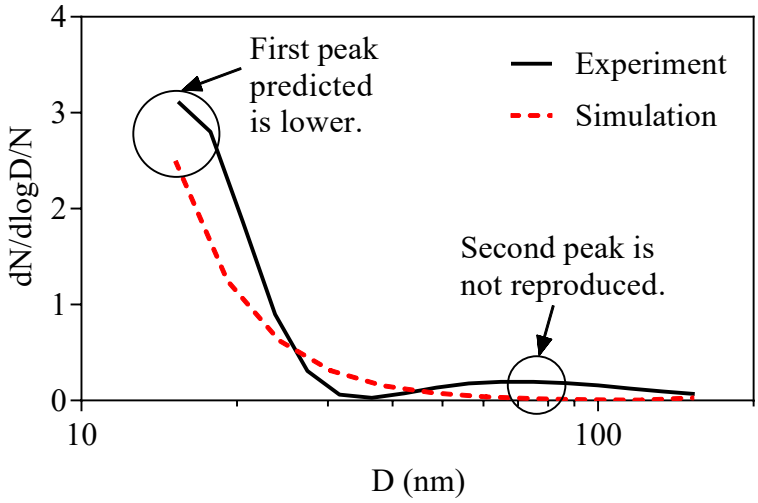


Figure 5-16 Measured and computed number-weighted PSDF normalised with total number density of soot for the reference case.

As explained previously, the main reason for the lower number of large particles estimated is associated to the lack of agglomeration in the soot model utilised. On the other hand, the sectional method inherently includes small particles with diameters lower than 10 nm while particles of this size range are difficult to be detected reliably at the experimental scale. This partly explains the better agreement in number density than in mass density observed in Figure 5-15. From the PSDF of soot, number density is primarily governed by the count of smaller particles while larger particles contribute mostly towards mass density.

Taking into account the inherent and fundamental discrepancies between experiment and simulation, the PSDF calculated in the present work is considered to be acceptable as it captures the higher peak of nucleation mode with the decreasing trend in particle number when the diameter changes across the range of 10–100 nm. Furthermore, as far as ultra-fine PM is concerned, accurate predictions in number density of soot particles provide confidence in the validity and fidelity of the computational outcome on soot emissions from the GDI engine.

5.4 Concluding Remarks

Detailed specifications of the GDI test engine and experimental operating conditions serve to provide necessary inputs for the numerical simulations so as to minimise any

potential uncertainties. The integrated CFD-chemical kinetic modelling approach is formulated, combining the pre-validated mechanism, An-TRF and development of CFD sub-models to characterise the entire engine operations. The modelled processes cover fuel injection and spray, mixing induced by turbulence, fuel impingement and liquid film formation, ignition and flame propagation and PM emission.

The spray tip penetration length measured in the static spray vessel using the similar multi-hole fuel injector is accurately replicated by the KHRT model, thus ensuring the correct modelling of spray formation and development. Regarding gasoline surrogate, it is evident that TRF provides a more realistic representation as using pure isooctane computes lower soot emissions (by five orders of magnitude). The Detailed Chemistry model, coupled with the DMZ partitioning method, allows direct incorporation of the chemical kinetics in 3D engine model with affordable computational load. Owing to the insignificance of low-temperature chemistry of high-ON fuels, activating the model at the onset of SI reduces the required computational time by 26% as compared to activating it at SOI without compromising the level of accuracy. DMZ partitioning of the cells is carried out based on their local thermo-chemical states described by temperature, mixture fraction, enthalpy and mass fraction of H. With the optimised numerical setting, in-cylinder pressures of the reference case are correctly reproduced, particularly the peak pressure which is computed within a 1% margin.

To model soot emissions, the sectional method divides each computational cell into 20 sections and determines the source terms contributed by particle inception, surface growth, condensation, coagulation and oxidation. Calibrated scale factors of particle inception and condensation which are collisional in nature replicate the number density of soot with a deviation of only 8%, but underestimate its mass density by a factor of about two. Considering the uncertainties of measurement systems and the inherent limitations of modelling approach, the agreement with experimental values within the same order of magnitude is reasonably acceptable. Besides, the normalised number-weighted PSDF extracted captures the peak of nucleation mode at particle size of 15 nm and the overall trend of declining number of particles when the diameter increases even though the lower peak of accumulation mode is not emulated.

CHAPTER 6
INVESTIGATION OF PM FORMATION MECHANISMS UNDER DIFFERENT SPEED-LOAD POINTS

6.1 Introductory Remarks

In this chapter, integrated CFD-chemical kinetic modelling formulated based on the reference case of 2300-90 is extended across different speed-load operating points to examine the effects of engine speed and load on PM emissions. The range of engine speed is from 1600 rpm to 3000 rpm with intervals of 700 rpm while engine load is altered through changing the torque from 60 N m to 120 N m in 30 N m increments. Validations of numerical modelling are performed in terms of in-cylinder pressures, number density, mass density and PSDF of soot for each speed-load point. The effects of speed and load on PM emissions are linked to the resulting flow field, spray formation, fuel impingement, air-fuel mixture distribution and combustion properties in Section 6.2 and Section 6.3, respectively. Crucial operating parameters, in-cylinder conditions and engine phenomena contributing to increased or decreased emissions as a result of changes in speed and load are identified and highlighted.

6.2 Effect of Engine Speed on PM Formation Mechanisms

By fixing the engine torque at 90 N m, the effect of engine speed on the resulting PM formation mechanisms is examined across three speeds at a constant load. The running speeds of 1600 rpm, 2300 rpm and 3000 rpm represent the low-, medium- and high-speed conditions, respectively in which the correlations arising due to a decrease and an increase in speed from the reference case can be established. Model calibration at different engine speeds follows the formulated approach described in Figure 5-6 based on their respective experimental measurements. Despite the inherent differences in process specifications and operating conditions, the implications of engine speed are evaluated based on fluid flow distributions, spray characteristics, quality of mixture preparation and progress of combustion with the overall influence on PM formation.

6.2.1 Spray Development and Mixture Formation

Engine speed influences the quality of spray and mixture preparation directly through induced flow intensity and time availability of the mixing process before SI. The level of mixture homogeneity is governed by the in-cylinder flow velocity and the overall period of a complete engine cycle. Higher flow velocity and shorter cycle time are associated with higher engine speed. As illustrated in Figure 6-1(a), there is an increase in velocity of air intake within the overall flow field at the maximum valve lift during the intake stroke when the engine speed increases from 1600 rpm to 3000 rpm. Despite the slight variation in CAD at which the maximum valve lift occurs for each speed, the in-cylinder tumble flows consistently feature a counter-clockwise rotating flow mechanism across all cases.

Besides, higher engine speed generates higher tumble velocity and larger turbulence kinetic energy as shown in Figure 6-2 due to faster piston movement. These directly lead to increased turbulence intensity, thus providing a more favourable condition for air-fuel mixing. From Figure 6-2(a), tumble speeds for all engine speeds gradually increase to their peak magnitudes after SOI of fuel with the highest rate of increase observed at 3000-90. The maximum value of tumble speed at engine speeds of 2300 rpm and 3000 rpm increases by 37% and 79%, respectively as compared to that at 1600 rpm. The maximum turbulence kinetic energy after fuel injection is also higher by a factor of 2.4 and 3.9 at 2300 rpm and 3000 rpm, respectively than that at 1600 rpm. Similar observation was also reported in which the maximum turbulence kinetic energy became higher by a factor of 2.9 when the speed increased from 2000 rpm to 4000 rpm [248]. As the piston moves closer to TDC, both tumble speed and turbulence kinetic energy diminish slowly due to the restriction of air motion across all engine speeds.

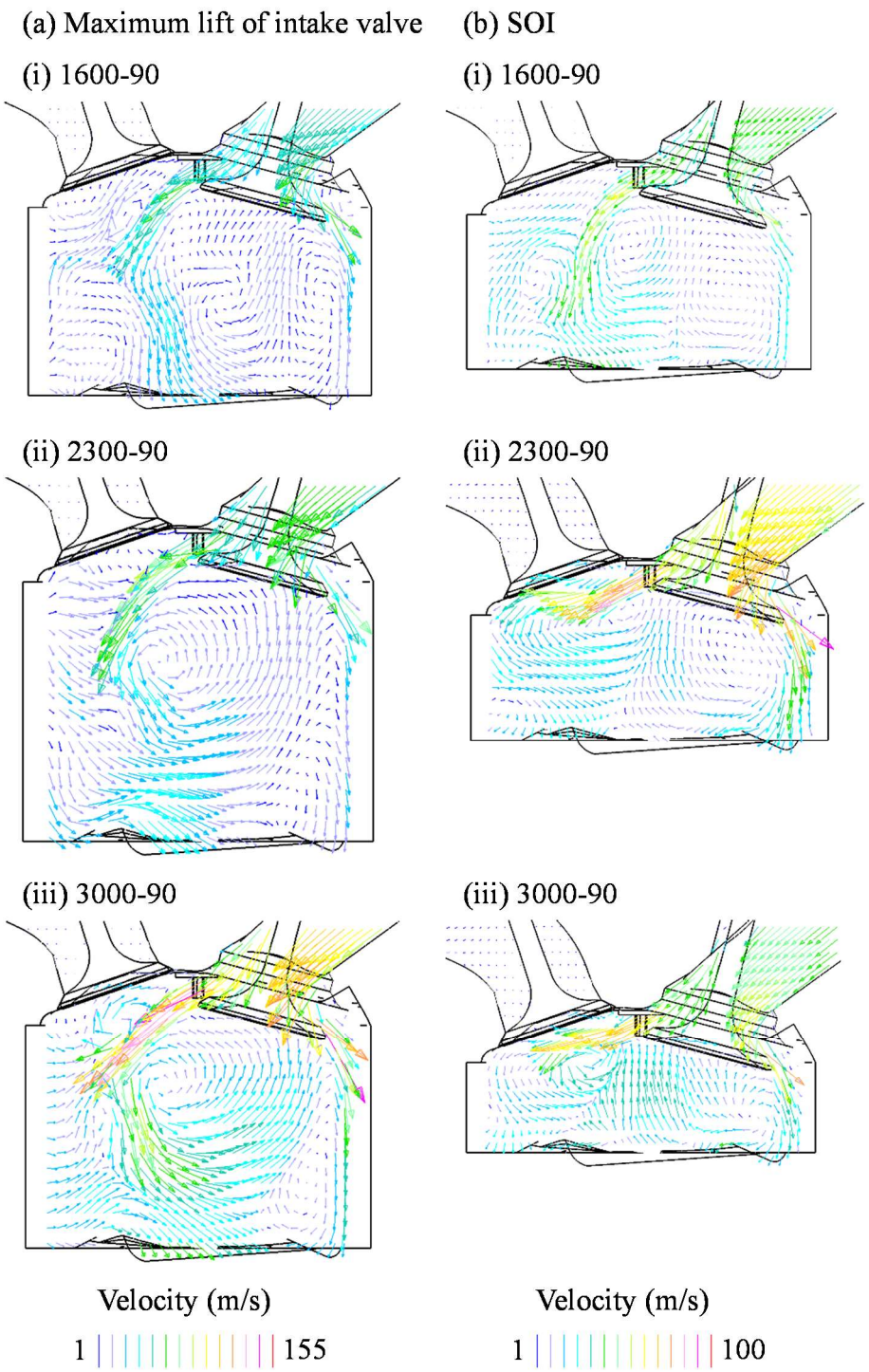


Figure 6-1 In-cylinder flow velocity at (a) maximum lift of intake valve and (b) SOI for engine speeds of (i) 1600 rpm, (ii) 2300 rpm and (iii) 3000 rpm.

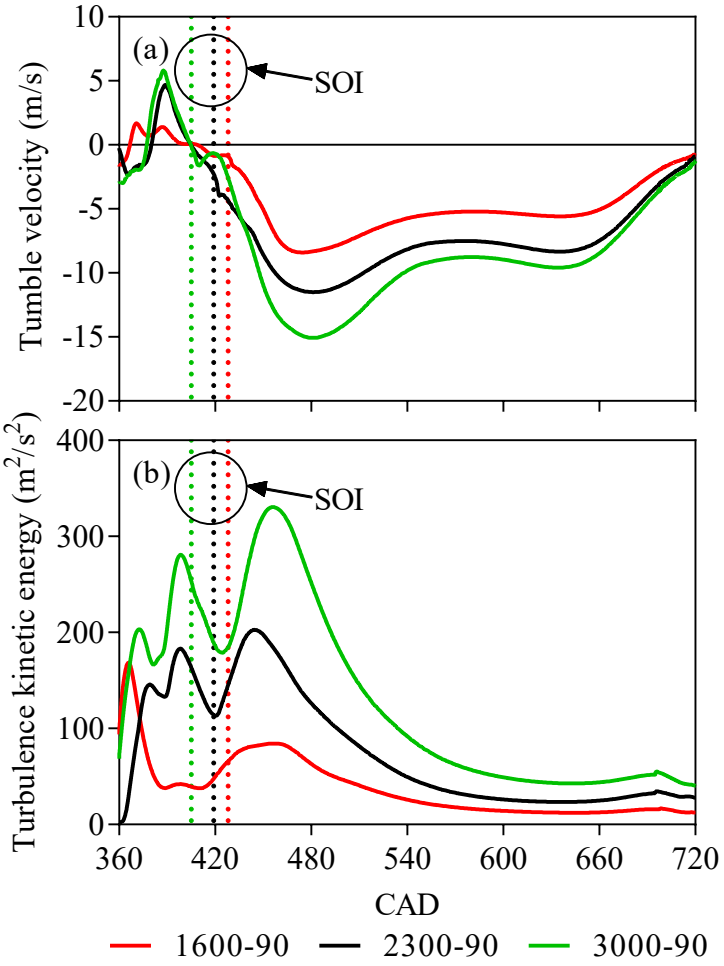


Figure 6-2 (a) Tumble velocity and (b) turbulence kinetic energy as a function of CAD for different engine speeds.

Spray characteristics for different engine speeds are compared in terms of SMD of droplets as displayed in Figure 6-3(a). Since nozzle with identical geometry is used, the SMD of droplets peaks to the same maximum value of 56 µm after fuel injection before decreasing in size due to spray breakup. As expected, at 20 CAD ABDC during the compression stroke, the lowest SMD of droplets is observed for 3000-90 at about 21 µm as a result of increased flow velocity at higher engine speed. However, predicted SMD of droplets at the particular CAD varies by less than 1.5 µm across the change in engine speed. The effect of engine speed on fuel vaporisation becomes more apparent as plotted in Figure 6-3(b) which expresses the ratio of fuel evaporated to fuel injected as a function of CAD. For higher engine speed, fuel vaporisation initiates earlier as the SOI timing is advanced correspondingly. Subsequently, enhanced flow

intensity facilitates the droplet breakup and vaporisation, thus allowing higher amount of fuel injected to vaporise at the beginning of compression stroke as compared to the low-speed condition at 1600 rpm. The improvement in total fuel vaporised diminishes when the engine speed increases from 2300 rpm to 3000 rpm.

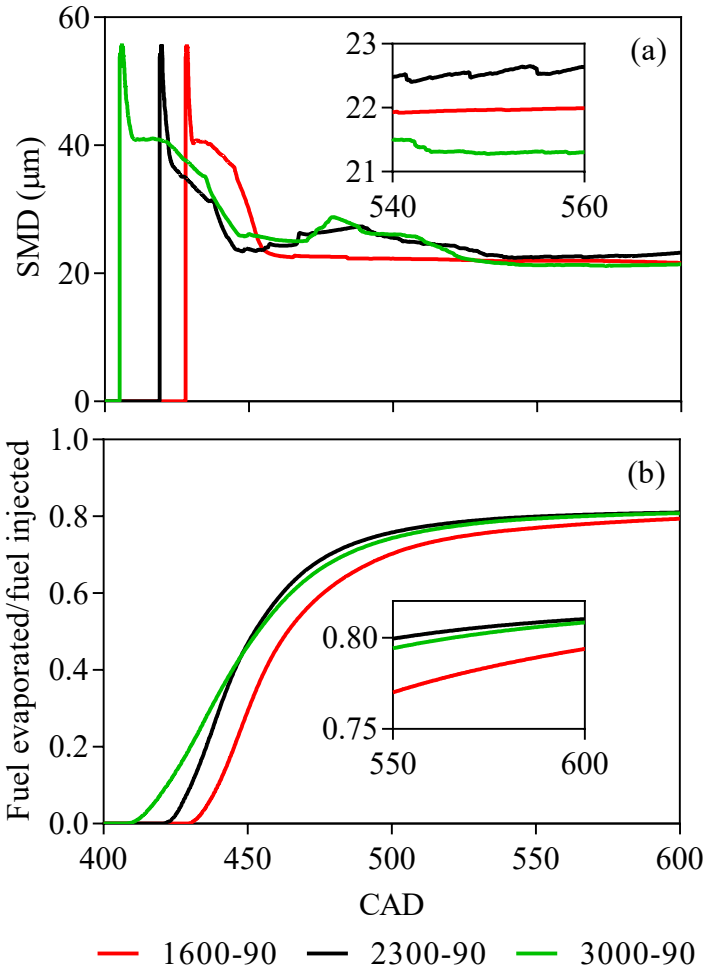


Figure 6-3 (a) SMD of fuel droplets and (b) ratio of fuel evaporated to fuel injected as a function of CAD for different engine speeds.

The extent of spray-wall impingement depends largely on the SOI timing and flow field which are controlled by the engine speed. Figure 6-4 displays the in-cylinder distributions of equivalence ratio at 10 CAD and 20 CAD after SOI for each engine speed. The cross-sectional profiles feature a fuel-rich core region within the spray pattern and leaner areas around the periphery as a result of mixing with air. Comparatively, the core within the spray profile at the engine speed of 1600 rpm is richer than those of the high-speed conditions at 10 CAD after SOI. Moreover, flow

velocity plays a prominent role in the spatial distributions of fuel and air. The stronger in-cylinder flow at 2300 rpm and 3000 rpm directs the fuel injected towards the lower part of the cylinder, following the counter-clockwise rotating motion. On the other hand, the distribution of equivalence ratio at 1600 rpm is more widespread throughout the whole cylinder, reaching even the combustion dome as visualised in Figure 6-4(b)(i).

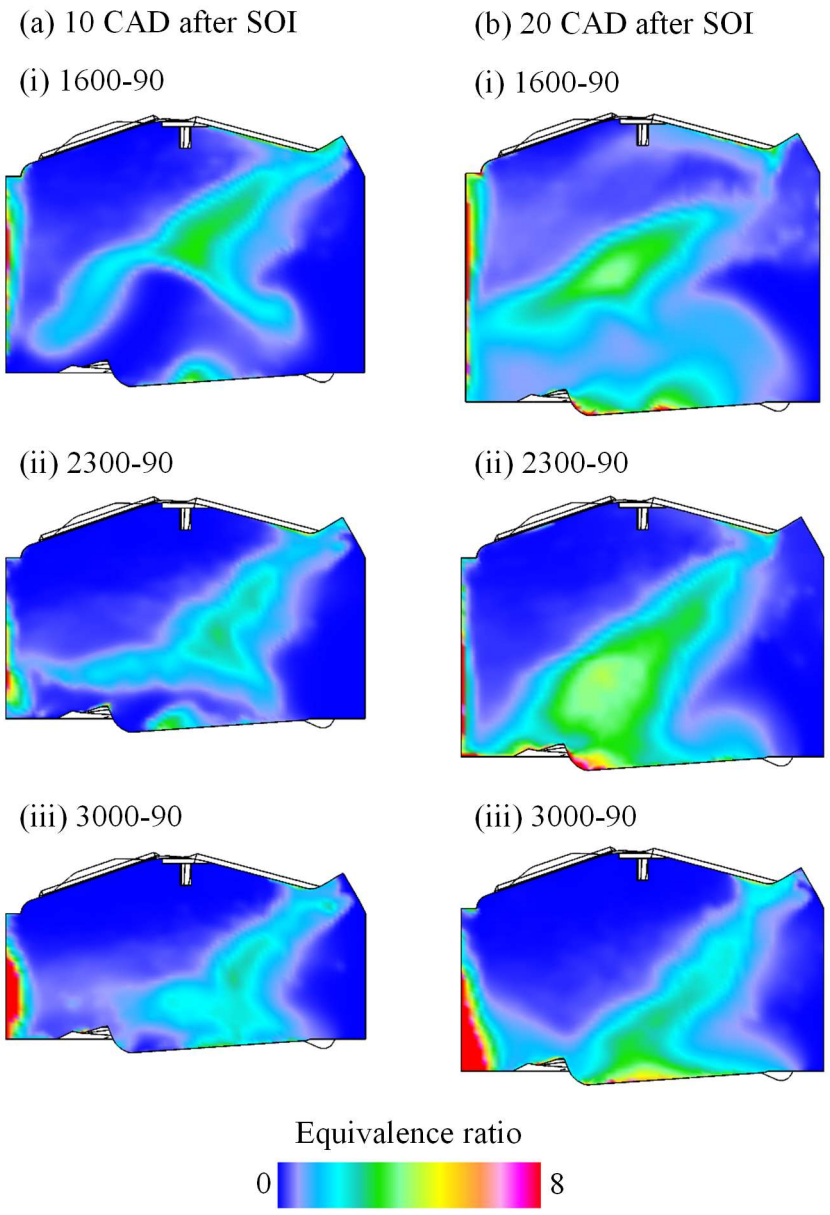


Figure 6-4 In-cylinder distributions of equivalence ratio at (a) 10 CAD and (b) 20 CAD after SOI for engine speeds of (i) 1600 rpm, (ii) 2300 rpm and (iii) 3000 rpm.

The impingement process is evident from regions near the cylinder surfaces having high equivalence ratios after SOI. The in-cylinder locations which are susceptible to fuel impingement include cylinder wall, piston crown and combustion dome. Formation and development of liquid fuel film within the cylinder is expressed in terms of total film mass as a function of CAD for all the engine speeds in Figure 6-5 with their respective SOI timings shown. The highest mass of total film formed is observed at 2300-90, followed by 3000-90 and subsequently 1600-90. The larger film mass at higher engine speeds of 2300 rpm and 3000 rpm is attributed to the earlier SOI timing during the intake stroke when the position of piston is closer to the fuel injector. The spray tip penetration, hence, is likely to reach the piston crown and cylinder wall, causing more fuel to be deposited on the surfaces. However, improved fuel vaporisation due to stronger flow field at 3000 rpm reduces the maximum fuel film mass formed by 24% as compared to that at 2300 rpm as seen from Figure 6-5. On the other hand, the retarded SOI timing at 1600 rpm minimises the impingement despite the lower in-cylinder flow velocity. For all engine speeds, the film evaporates completely before 10 CAD ABDC during the compression stroke with the fastest process observed at 1600 rpm and the slowest at 3000 rpm.

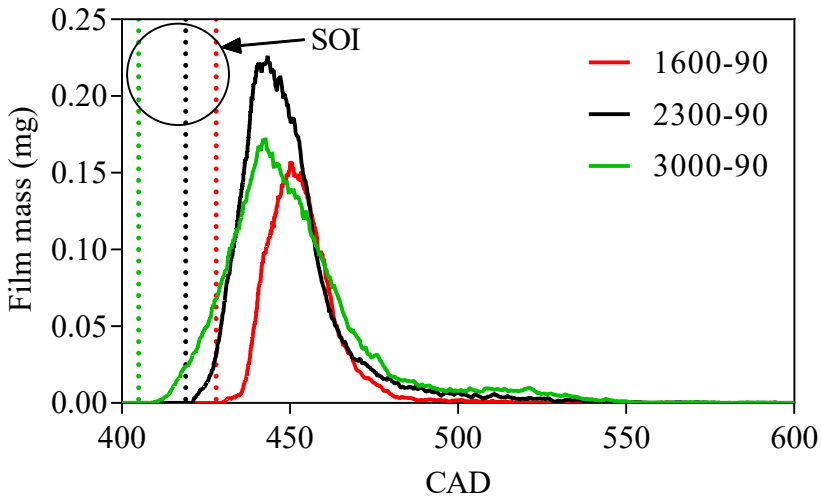


Figure 6-5 Total mass of liquid fuel film formed within the cylinder as a function of CAD for different engine speeds.

To further analyse the formation of liquid film, individual proportions of the total film mass deposited on combustion dome, piston crown and cylinder wall are displayed in Figure 6-6 for different engine speeds within 10–50 CAD after their respective SOI

timings. An overview of Figure 6-6 reveals that the piston surface is most prone to fuel impingement, accounting for the highest proportion of total film mass at each CAD examined across all the engine speeds. This is because the tumble motion within the cylinder increases the ease of droplet impact on the piston crown as compared to on other engine components. A significant amount of fuel film is also found on the cylinder wall while relatively lower film mass is deposited on the combustion dome. Since less fuel impinges on the wall and dome surfaces, the associated film evaporates quicker into fuel vapour. Larger mass of fuel film on the piston surface persists longer in the engine cycle before evaporating completely.

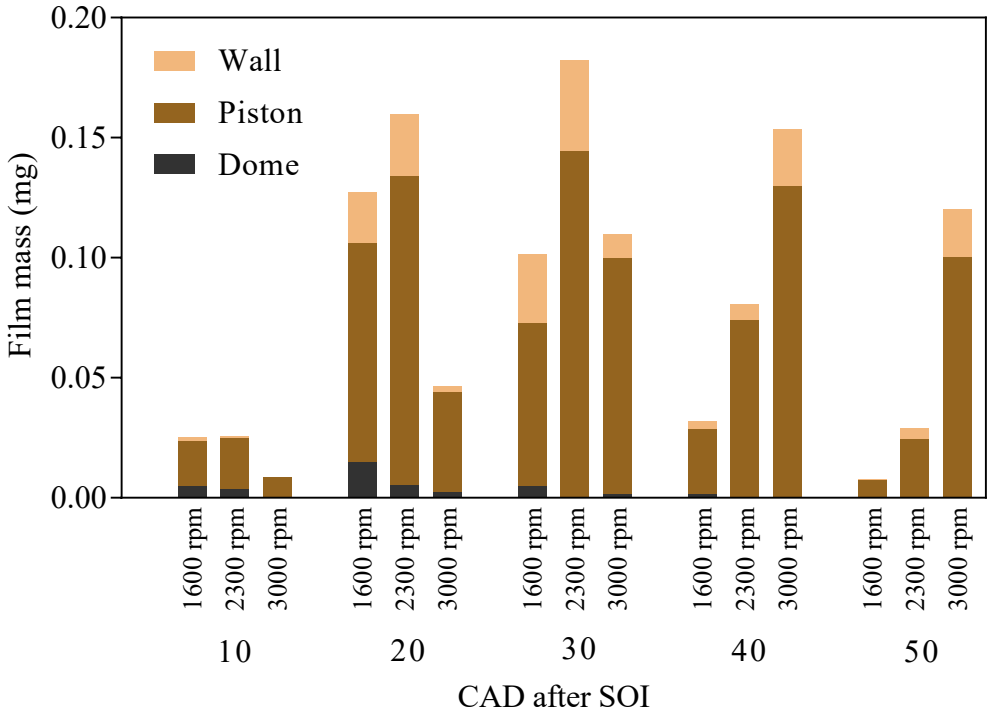


Figure 6-6 Proportions of total film mass formed on combustion dome, piston crown and cylinder wall as a function of CAD after the respective SOI of different engine speeds.

Among the three cases, noticeable amount of film mass on the combustion dome is present only at 1600 rpm. As corroborated by Figure 6-4(b)(i), fuel distribution at the low-speed condition spreads out widely within the cylinder whereby potential fuel impingement on the dome surface is observed. In addition, wall wetting is more severe at 20 CAD and 30 CAD after SOI for 1600 rpm and 2300 rpm. This is linked to poorer droplet vaporisation at lower speeds which allows more liquid fuel to impact and form

film on the wall surfaces. In contrast, better droplet breakup and atomisation due to higher in-cylinder flow velocity at 3000 rpm result in near-wall regions with high fuel vapour concentration as shown in Figure 6-4(a)(iii) and (b)(iii), thus reducing the amount of liquid fuel deposited on the wall surfaces. Enhanced droplet vaporisation at 3000 rpm also slows down the rate of film formation as the film mass reaches its peak at about 40 CAD after SOI. Meanwhile, the maximum film mass is detected at about 20 CAD after SOI when the engine speed is 1600 rpm.

The mixing intensity and level of mixture homogeneity at 90 CAD BTDC during the compression stroke are characterised in Figure 6-7 by flow velocity and equivalence ratio distribution. It is apparent that the in-cylinder flow velocity becomes higher as the engine speed increases. The maximum flow velocity increases by 58% going from 1600 rpm to 2300 rpm and 28% from 2300 rpm to 3000 rpm, respectively. Due to the counter-clockwise motion of bulk flow, fuel-rich pockets are swept from the piston area at the bottom towards the regions of intake valve and spark plug at the top of the cylinder. Figure 6-7(b) highlights the direct correlation between engine speed and mixture homogeneity in which increased flow velocity promotes the mixing between fuel and air to generate a more homogeneous mixture. The region around the spark plug at lower engine speeds of 1600 rpm and 2300 rpm comprises fuel-rich conditions whereas that at 3000 rpm appears to be closer to the stoichiometric mode.

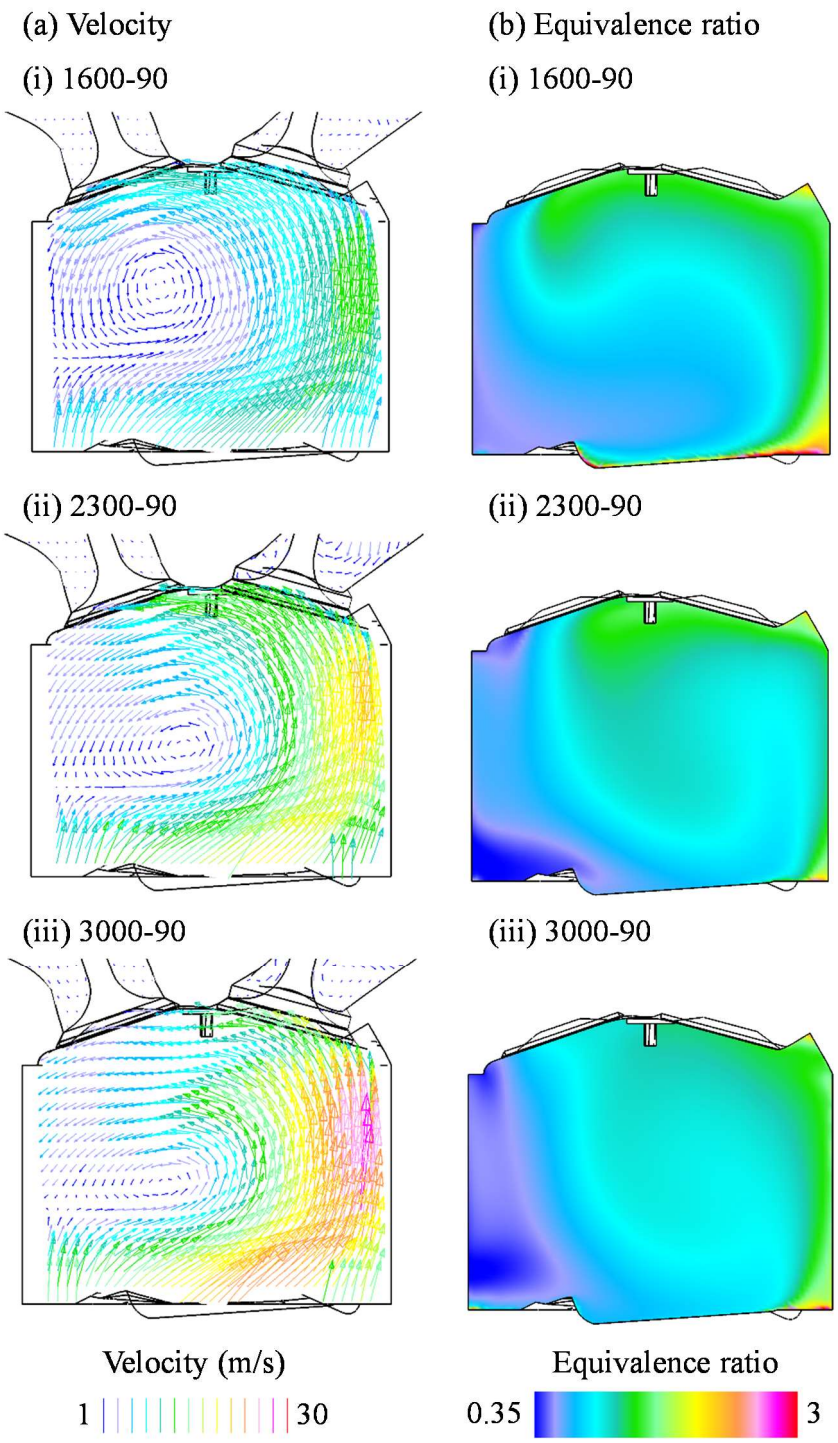


Figure 6-7 In-cylinder (a) flow velocity and (b) distribution of equivalence ratio at 90 CAD BTDC during the compression stroke for engine speeds of (i) 1600 rpm, (ii) 2300 rpm and (iii) 3000 rpm.

6.2.2 Combustion Progress

Numerical modelling of the combustion process is validated with development of experimental in-cylinder pressures in which the measured and computed values are

compared in Figure 6-8 for each engine speed. Good agreement is observed between measured and simulated pressure curves in general. The slight over-prediction of pressures at the early stages of combustion is consistent across the engine speeds. The simulations also manage to capture the variation in pressure with respect to the change in engine speed whereby the pressure increases going from 3000 rpm to 1600 rpm and then to 2300 rpm. From Table 6-1, measured peak pressures are replicated accurately with the maximum percentage deviation of 1.5% determined for 1600-90.

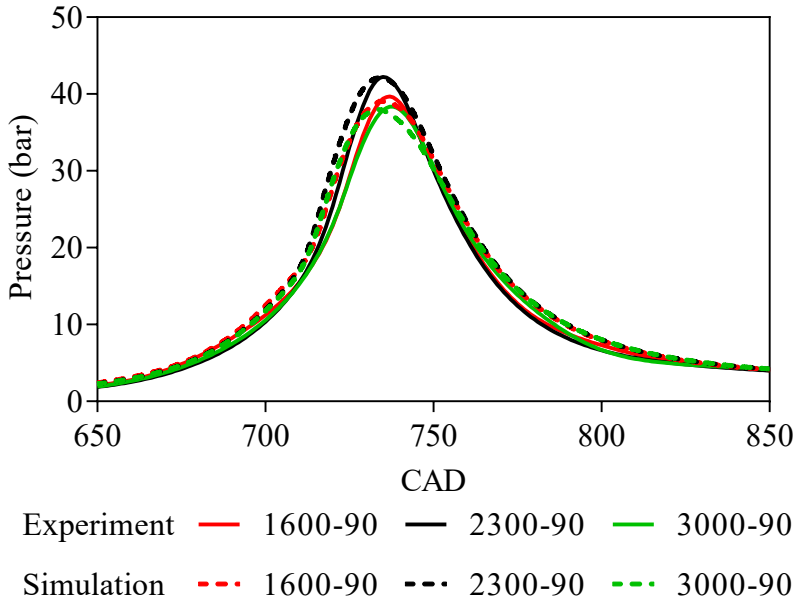


Figure 6-8 Measured and computed in-cylinder pressures for different engine speeds.

Table 6-1 Measured and computed peak pressures and their locations in CAD for different engine speeds.

Speed (rpm)	Peak pressure (bar)		Location of peak pressure (CAD)	
	Experiment	Simulation	Experiment	Simulation
1600	39.68	39.08	737	735
2300	42.23	42.16	735	734
3000	38.37	37.99	738	734

Fuel combustion behaviours after initiation of spark including flame development and propagation heavily rely on the level of mixture homogeneity at SI timing. As depicted in Figure 6-9, increasing the engine speed has a positive influence on the overall

uniformity of mixture distribution which in turn promotes homogeneous combustion. There are more fuel-rich pockets within the mixture under low-speed conditions of 1600 rpm and 2300 rpm. The presence of such pockets is attributed to the weaker flow fields which fail to mix the fuel with air evenly before the spark initiation is activated. These fuel-rich regions are typically found near wall and piston surfaces due to the reduced air entrainment.

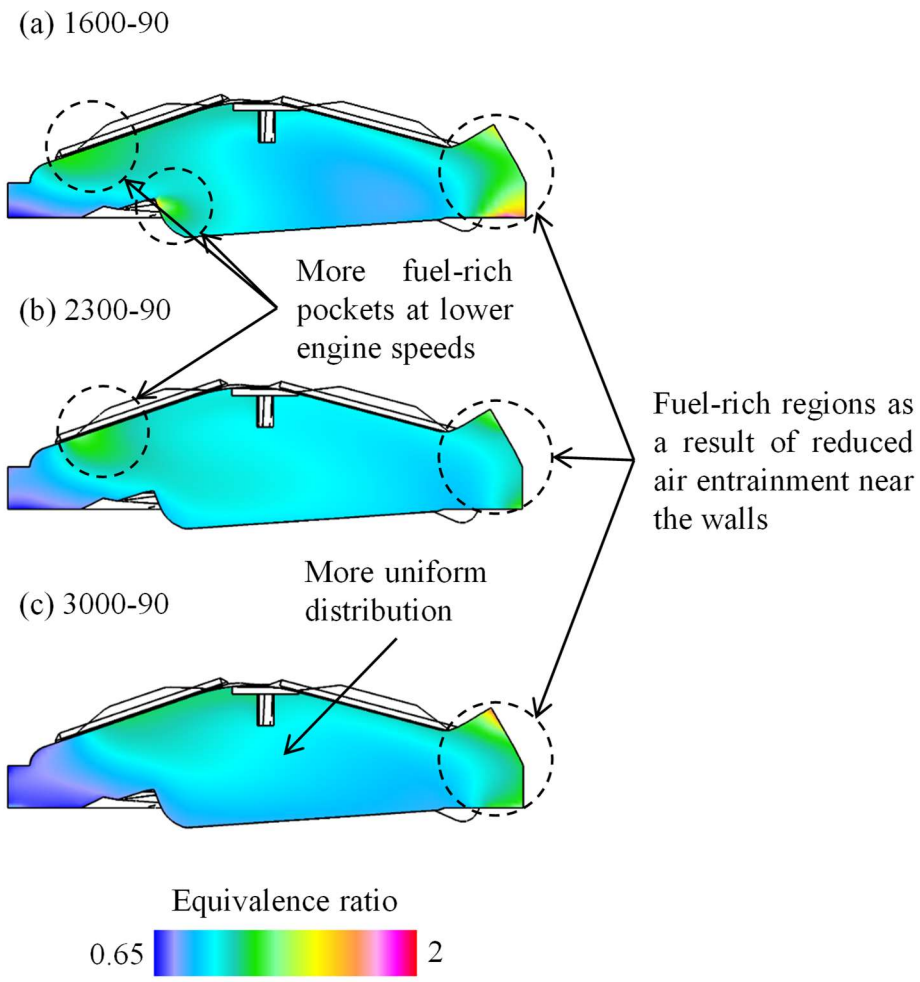


Figure 6-9 In-cylinder distributions of equivalence ratio at SI timing for engine speeds of (a) 1600 rpm, (b) 2300 rpm and (c) 3000 rpm.

The resulting computed in-cylinder temperature profiles are plotted in Figure 6-10 for all the engine speeds. Consistent with the pressure variation, higher temperatures are associated with 2300-90, followed by 3000-90 and 1600-90. The peak temperature at 2300 rpm is higher by 5.8% and 3.4% than those calculated at 1600 rpm and 3000 rpm, respectively. Figure 6-11 demonstrates the temporal evolution of temperature contours for different engine speeds after their corresponding SI timings. Combustion

commences and proceeds the fastest at 2300 rpm as the flame front, characterised by the high-temperature region, spreads out the furthest into the cylinder peripheries at 40 CAD after SI. As the combustion continues at 60 CAD and 80 CAD after SI, the temperature distribution at 3000 rpm resembles that at 2300 rpm while that at 1600 rpm consists of relatively lower temperatures. The observation is coherent with the reported in-cylinder temperature curves in Figure 6-10 whereby temperatures during the late stage of combustion at low speed of 1600 rpm are lower than those at the high-speed conditions.

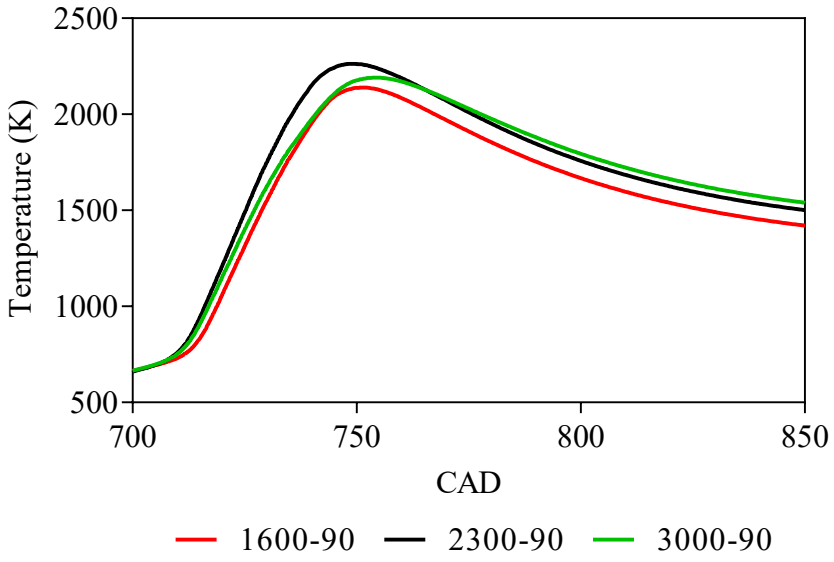


Figure 6-10 Computed in-cylinder temperatures for different engine speeds.

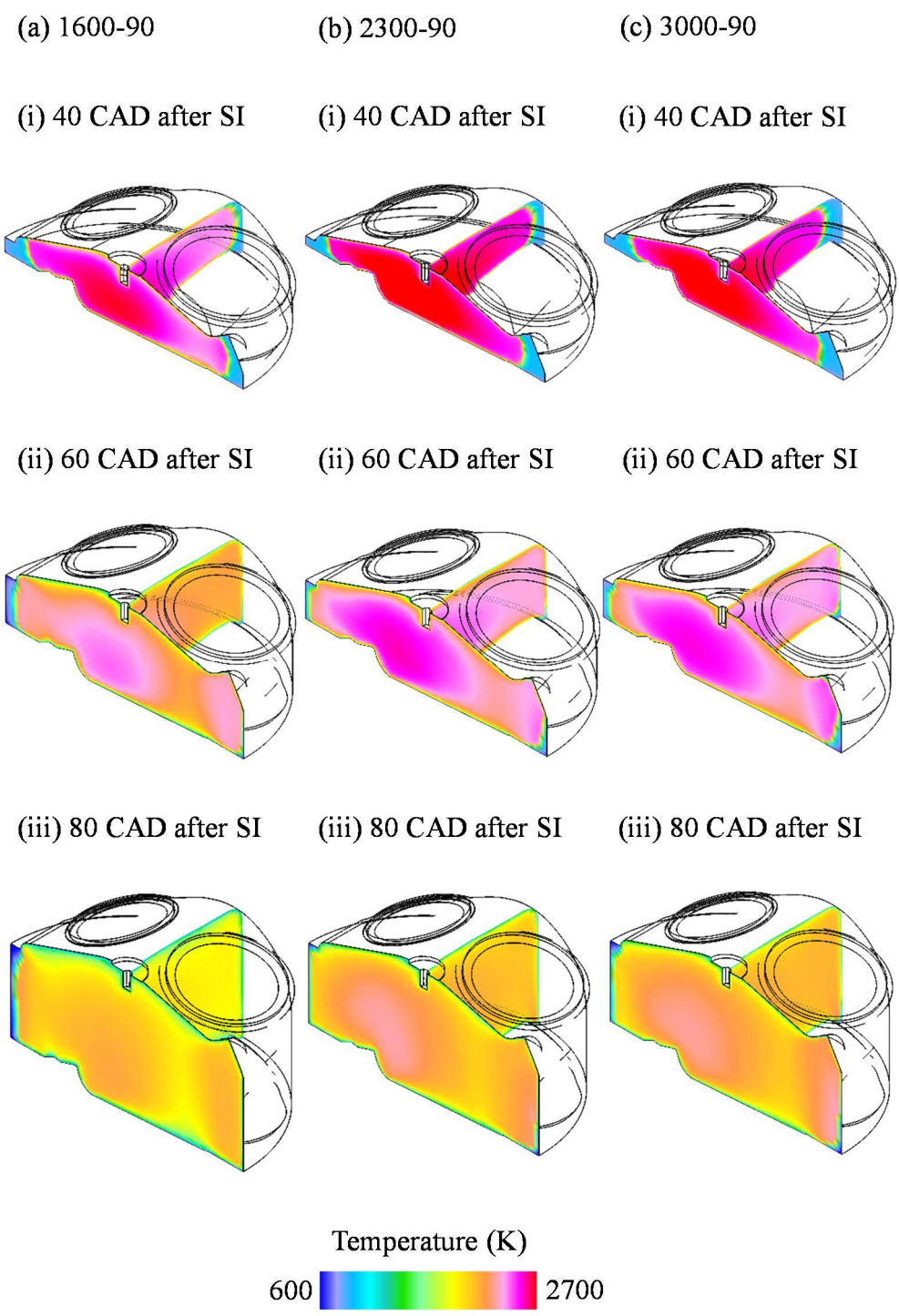


Figure 6-11 In-cylinder temperature contours for engine speeds of (a) 1600 rpm, (b) 2300 rpm and (c) 3000 rpm at (i) 40 CAD, (ii) 60 CAD and (iii) 80 CAD after SI.

6.2.3 PM Formation and Emissions

Modelled PM formation and emission processes at different engine speeds are validated in terms of number density and mass density of soot against experimental tailpipe measurements as demonstrated in Figure 6-12. Good agreement is observed

between measured and computed number density of soot while lower values of mass density are calculated consistently across all the engine speeds. The underestimation of soot mass has been previously addressed in Section 5.3.3.4 which is mainly attributed to modelling limitations and inherent differences between experimental and numerical setups. Nevertheless, replicated experimental trends in number density and mass density as portrayed by the close agreement in normalised results based on the reference case of 2300-90 suggest that the simulations capture the variation in PM emissions with respect to the change in engine speed properly.

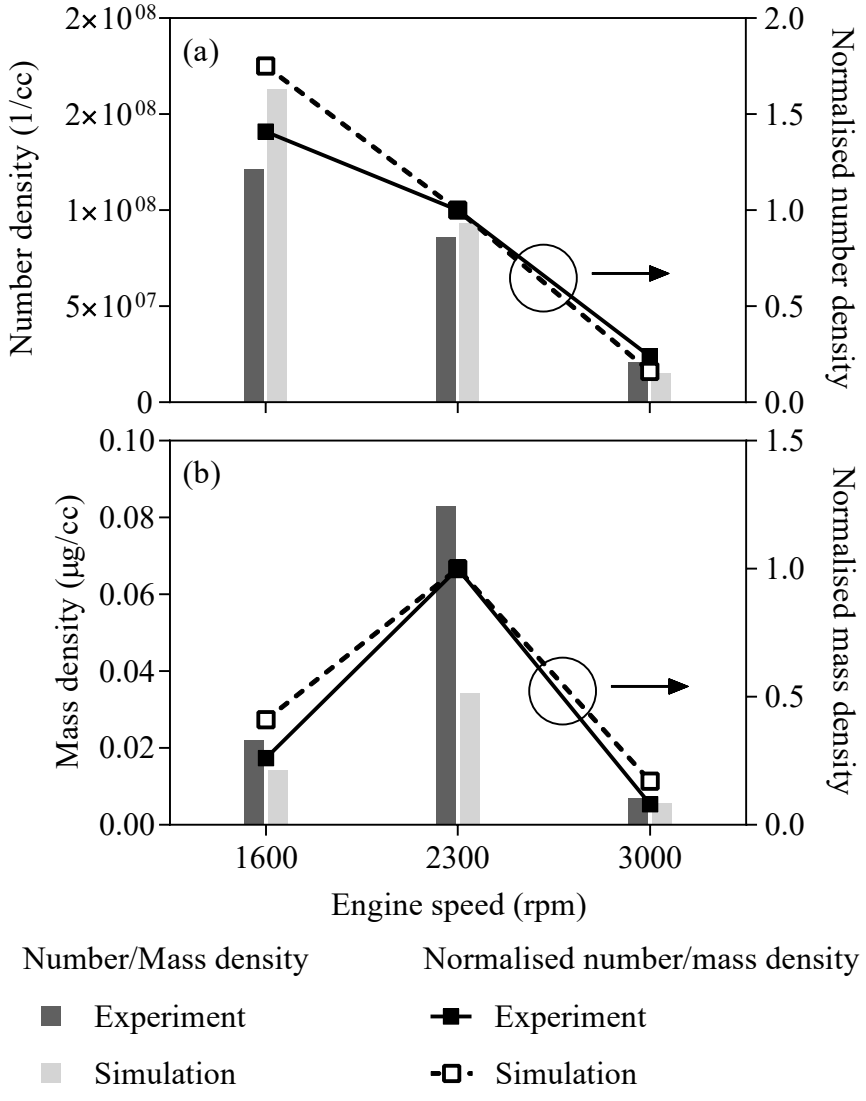


Figure 6-12 Measured and computed (a) number density and (b) mass density of soot and their normalised values based on the reference case for different engine speeds.

When the engine speed increases, number density of soot decreases with a larger drop observed going from 2300 rpm to 3000 rpm. The reduction in number density was also observed in the work of Lucchini et al. [31] when the speed was increased from 1500 rpm to 5500 rpm for two different spray patterns. On the other hand, the highest mass density is detected at 2300 rpm, followed by 1600 rpm and then 3000 rpm. This exhibits good conformity with the experimental study by An et al. [249] which found the highest mass concentrations of PAH and soot at 2000 rpm for the range of 1000–3000 rpm investigated at the fixed torque of 120 N m.

Figure 6-13 shows both normalised number-weighted PSDF of soot based on the total number density determined experimentally and numerically for engine speeds at 1600 rpm and 3000 rpm whereas those of 2300 rpm have been plotted in Figure 5-16. For the two engine speeds, the general trend in particle number with increasing diameter is captured with over-predicted peak of the nucleation mode and underestimation in particle count of the accumulation mode. Better agreement is observed at 1600 rpm and the deviations amplify when particle number within the range of accumulation mode becomes significant at higher engine speeds. Similar to 2300-90, the lower peak of accumulation mode is not reproduced at lower and higher engine speeds. From Figure 5-16 and Figure 6-13, it is noted that the normalised PSDF computed from the current sectional method exhibits no sensitivity towards the change in engine speed.

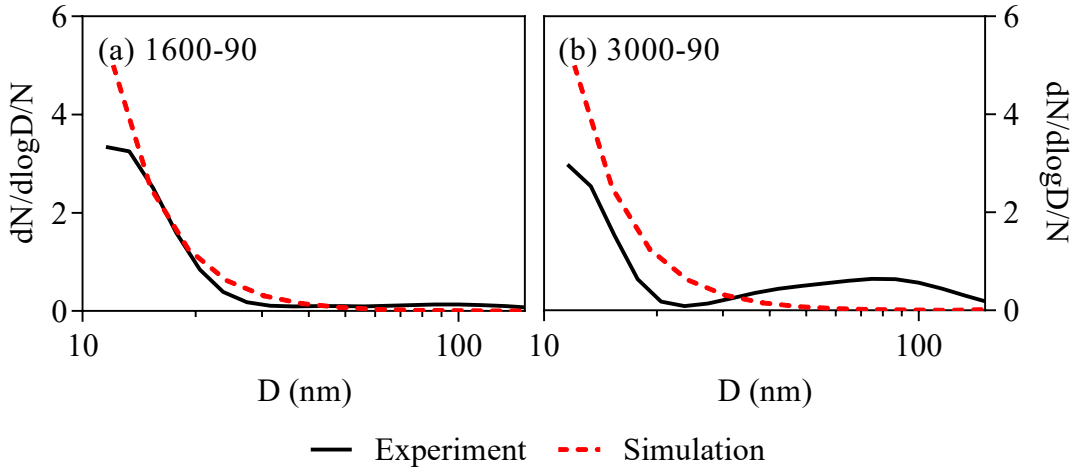


Figure 6-13 Measured and computed number-weighted PSDF normalised with total number density of soot at engine speeds of (a) 1600 rpm and (b) 3000 rpm.

In-cylinder distributions of number density and mass density of soot at 40 CAD, 60 CAD and 80 CAD after SI for different engine speeds are depicted in Figure 6-14 and Figure 6-15, respectively. At any particular CAD after SI, the highest number of soot particles is associated with the low-speed condition at 1600 rpm while the high engine speed of 3000 rpm corresponds to the lowest particle count. Spatial distributions of number density at 40 CAD after SI in Figure 6-14 are a direct manifestation of the benefits of improved mixture homogeneity at higher engine speeds as highlighted in Figure 6-9. The presence of more fuel-rich regions at lower speeds gives rise to the nucleation of higher particle number. As the combustion proceeds, there is an apparent reduction in particle number due to oxidation at 80 CAD after SI for all cases. For 1600-90, significantly high number density is observed at near-wall region on the right side of combustion chamber as shown in Figure 6-14(a)(iii). This can be attributed to the lower in-cylinder temperature within the region from Figure 6-11(a)(iii) which in turn reduces the rate of soot oxidation.

In-cylinder distributions of mass density of soot in Figure 6-15 reveal that the mass contours at 2300 rpm are the most widespread near the cylinder walls. As compared to 1600-90 which exhibits higher number density but lower mass density, 2300-90 experiences greater rates of surface growth and PAH condensation, thus resulting in an overall increase of soot mass. Furthermore, higher flow velocity at 2300 rpm contributes to coagulation which leads to increased mass density by enhancing the rate of collision between soot particles. Consistent with the number density, minimal mass density is observed at the engine speed of 3000 rpm. The reduced oxidation rate at low speed of 1600 rpm is also evident from the higher concentration of mass density near the right cylinder walls as illustrated in Figure 6-15(a)(iii).

Figure 6-16 displays the net production of soot as a function of CAD at varied engine speeds with their associated EVO timings indicated. The rapid rise in particle number of soot at 1600 rpm to a peak value of 4.68×10^{10} indicates the accelerated particle inception due to localised fuel-rich regions. By contrast, the drastic spike in soot mass at 2300 rpm highlights the dominance of surface growth, PAH condensation and coagulation at higher speed. Unlike 1600-90 and 2300-90, there is no visible peak in both particle number and mass of soot at 3000-90. Improved spray characteristics and enhanced mixture homogeneity at high speed of 3000 rpm bring about an order of magnitude lower in particle number and a six-fold decrease in mass as compared to

the maximum values recorded at lower engine speeds, respectively. Additionally, the shortest residence time of soot at 3000 rpm inhibits further potential nucleation and growth of particles, thus minimising the eventual soot emissions at EVO.

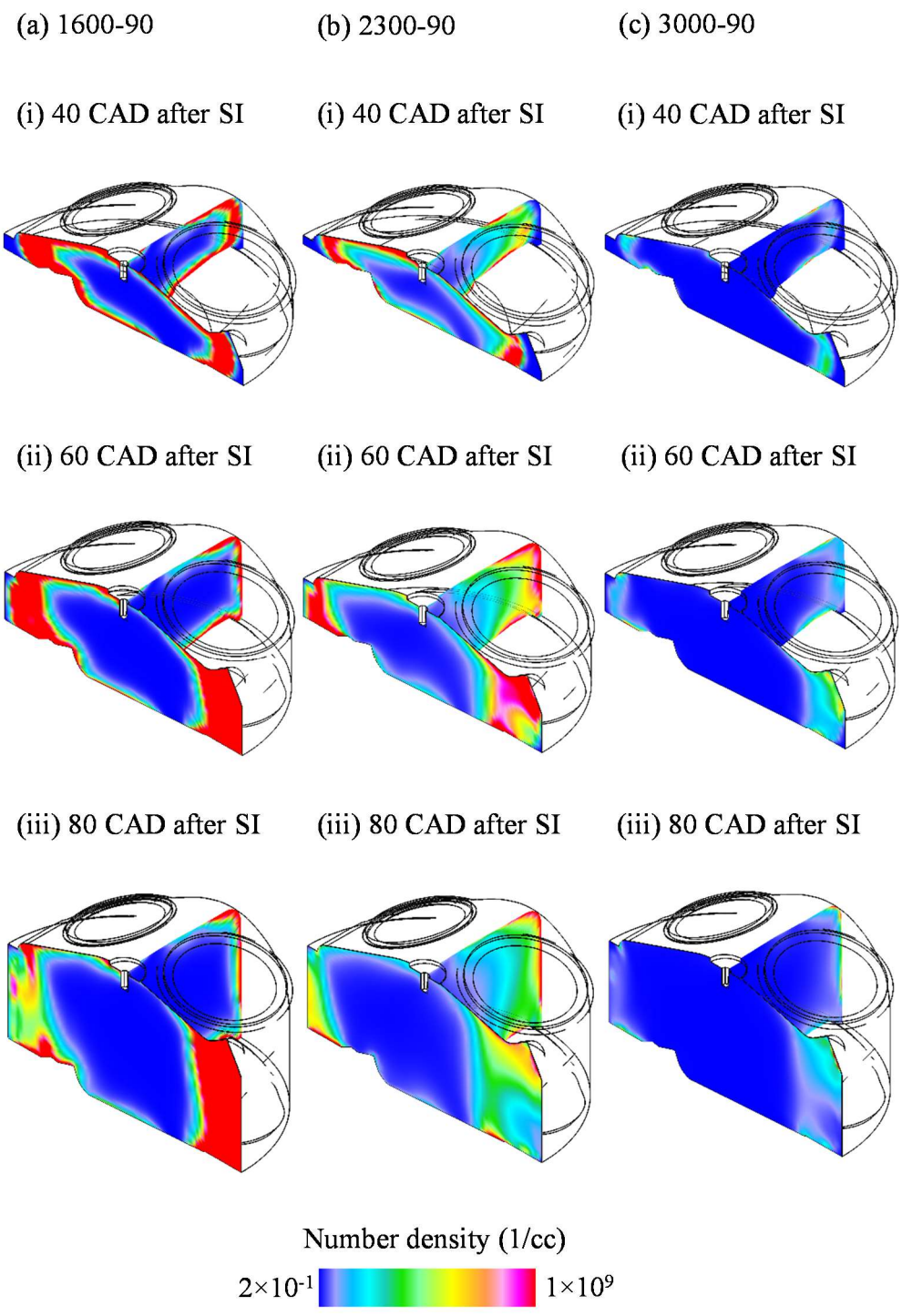


Figure 6-14 In-cylinder distributions of number density of soot for engine speeds of (a) 1600 rpm, (b) 2300 rpm and (c) 3000 rpm at (i) 40 CAD, (ii) 60 CAD and (iii) 80 CAD after SI.

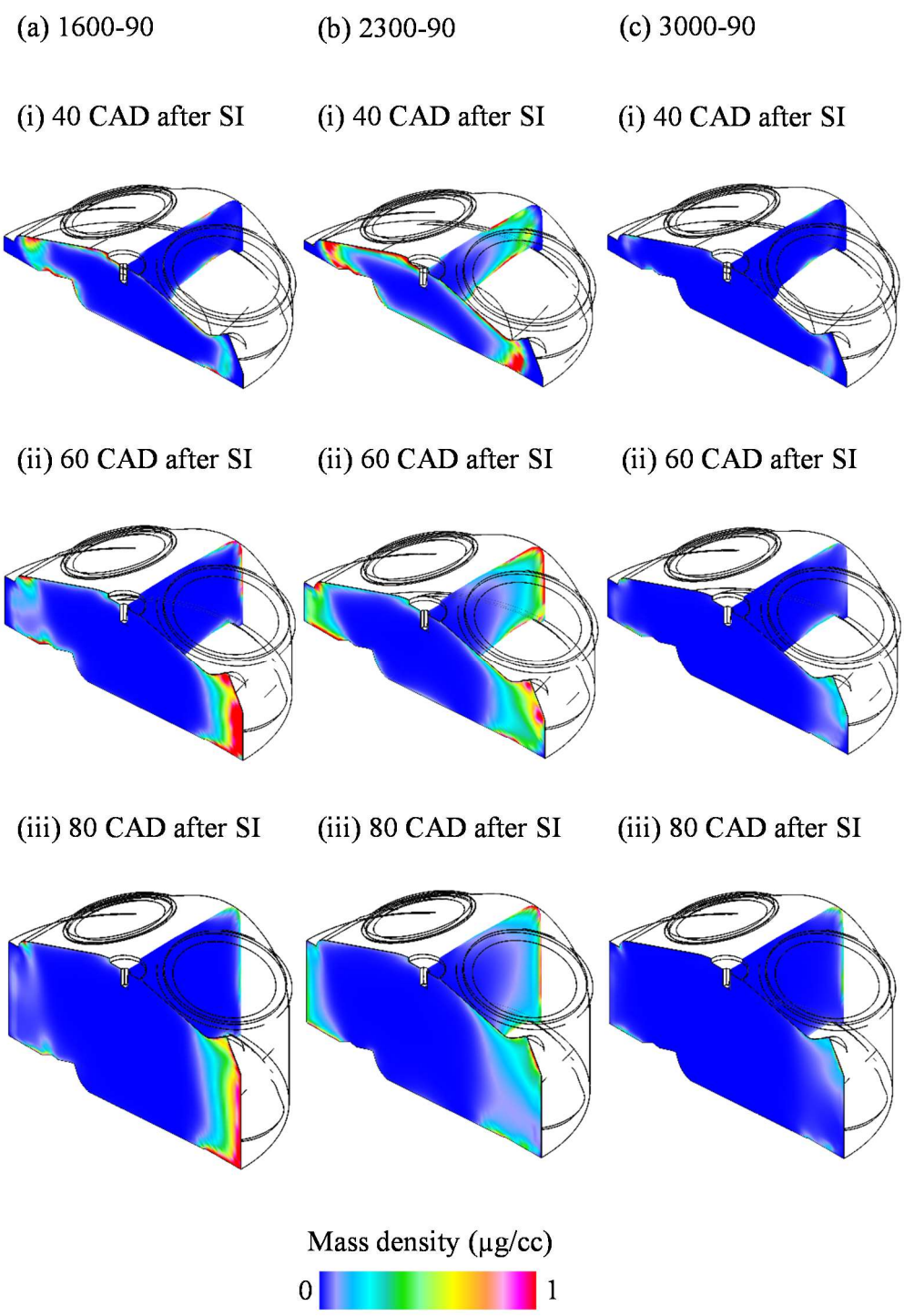


Figure 6-15 In-cylinder distributions of mass density of soot for engine speeds of (a) 1600 rpm, (b) 2300 rpm and (c) 3000 rpm at (i) 40 CAD, (ii) 60 CAD and (iii) 80 CAD after SI.

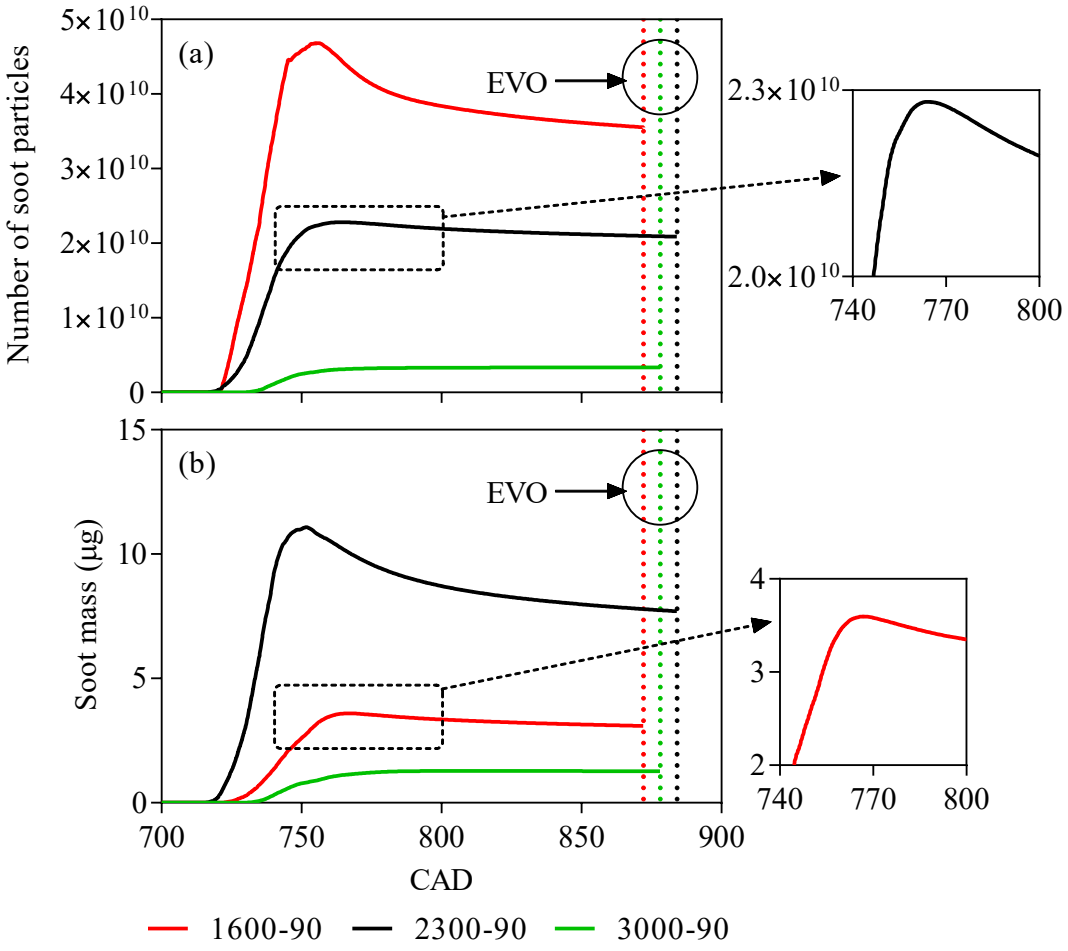


Figure 6-16 Computed in-cylinder (a) number of soot particles and (b) soot mass as a function of CAD up to EVO for different engine speeds.

6.3 Effect of Engine Load on PM Formation Mechanisms

The effect of engine load on PM emissions is studied by varying the engine torque from 60 N m to 120 N m with intervals of 30 N m to represent the low-, medium- and high-load conditions correspondingly at the fixed engine speed of 2300 rpm. The associated brake mean effective pressure (BMEP) for each engine load is determined as tabulated in Table 6-2 from Equation (6-1).

$$BMEP = \frac{2\pi n_r T}{V_d} \tag{6-1}$$

where n_r is the number of rotations of crankshaft for a complete engine cycle, T is the engine torque while V_d is the total engine displacement. Employing the same approach

outlined in Figure 5-6, the formulated models are calibrated based on the experimental measurements taken at different engine loads. The overall influence of engine load on PM emissions is inspected through the changes in in-cylinder flow conditions, spray properties, mixture distributions and combustion development as the engine torque is altered.

Table 6-2 BMEP at different engine loads with the fixed engine speed of 2300 rpm.

Engine torque (N m)	60	90	120
BMEP (bar)	4.72	7.08	9.44

6.3.1 Spray Development and Mixture Formation

The change in engine load is accompanied by necessary modifications in terms of the amount of fuel injected, injection pressure and intake pressure as governed by the position of throttle body. Increasing the engine load requires a larger amount of fuel to be injected and higher pressure at the intake manifold to facilitate spray atomisation and air-fuel mixing. In addition, higher injection pressure for fuel spray is utilised at increased engine load, thus intensifying the flow field during the injection period. As visualised in Figure 6-17(a), flow velocity into the cylinder at SOI increases at higher engine loads due to the combined effect of higher intake and injection pressures. However, from Figure 6-17(b), this enhanced mixing intensity does not persist late in the engine cycle. At 90 CAD BTDC during the compression stroke, the differences in maximum flow velocity across all the cases are less than 2 m/s.

Both higher intake and injection pressures contribute to the increase of in-cylinder pressure at higher engine loads as depicted in Figure 6-18. The pressure at 200 CAD after SOI for 2300-120 is higher than that for 2300-60 by 43%. The role of injection pressure in affecting in-cylinder mixing level is clearly pinpointed in Figure 6-19. Upon SOI, swirl motion becomes stronger in which the swirl ratio reaches a peak value before decreasing after EOI timing. The swirl intensity is commensurate with the injection pressure and engine load. Likewise, there is an apparent rise in turbulence kinetic energy during fuel injection across all engine loads. At the highest load of 120 N m, the maximum turbulence kinetic energy after SOI is larger by 33% and 25% as compared to those at 60 N m and 90 N m, respectively. The increase in turbulence

intensity during fuel injection due to increased injection pressure was also captured in the work by Kim et al. [250] for all the SOI timings studied.

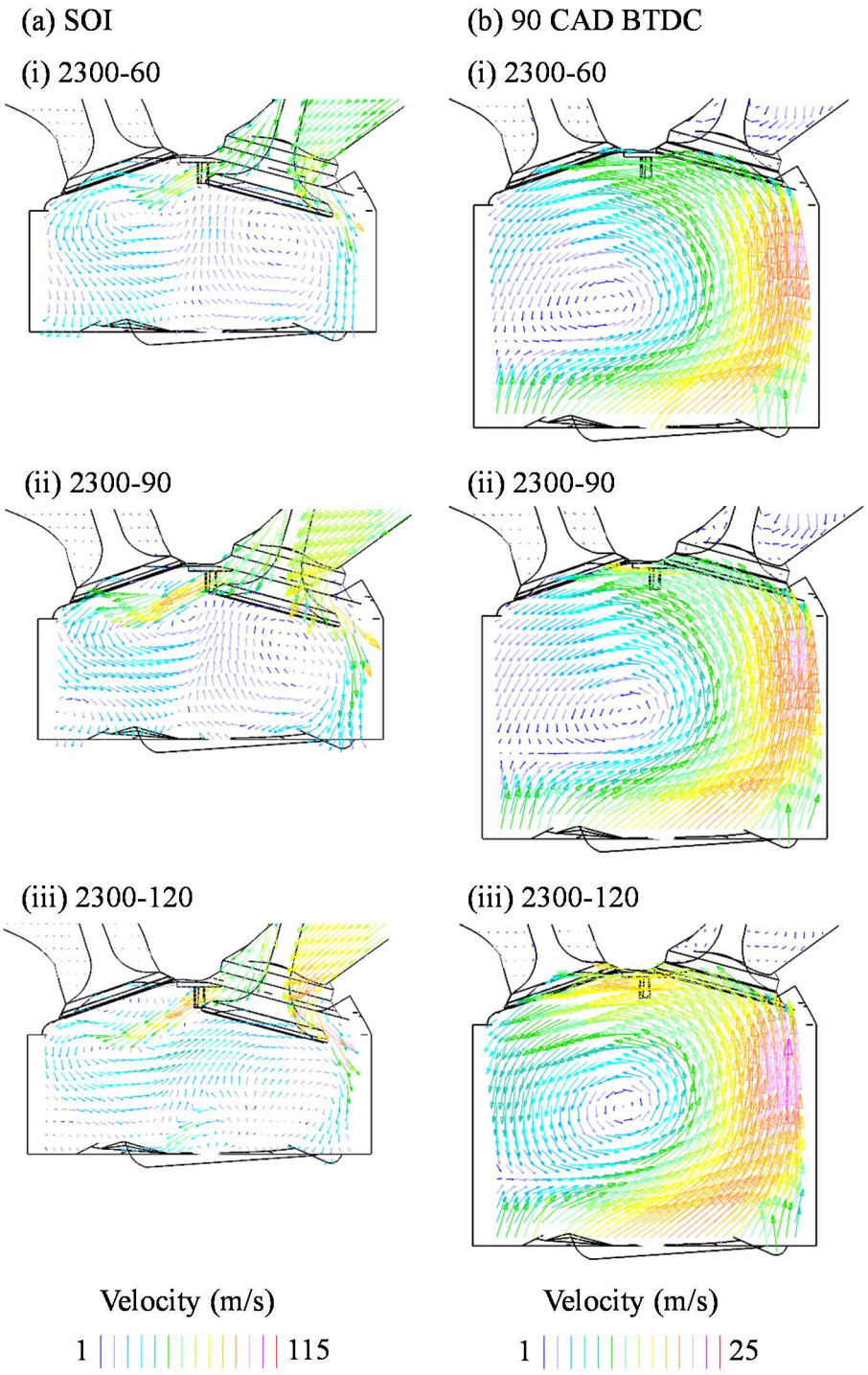


Figure 6-17 In-cylinder flow velocity at (a) SOI and (b) 90 CAD BTDC for engine loads of (i) 60 N m, (ii) 90 N m and (iii) 120 N m.

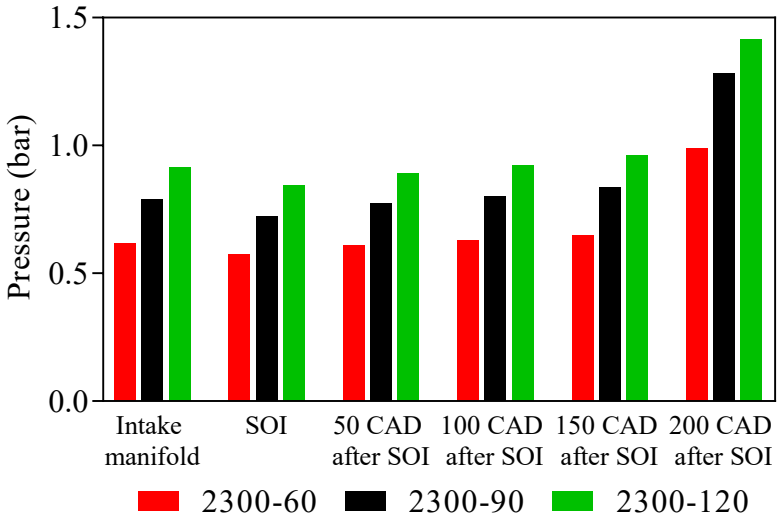


Figure 6-18 In-cylinder pressure at intake manifold, SOI and 50–200 CAD after SOI for different engine loads.

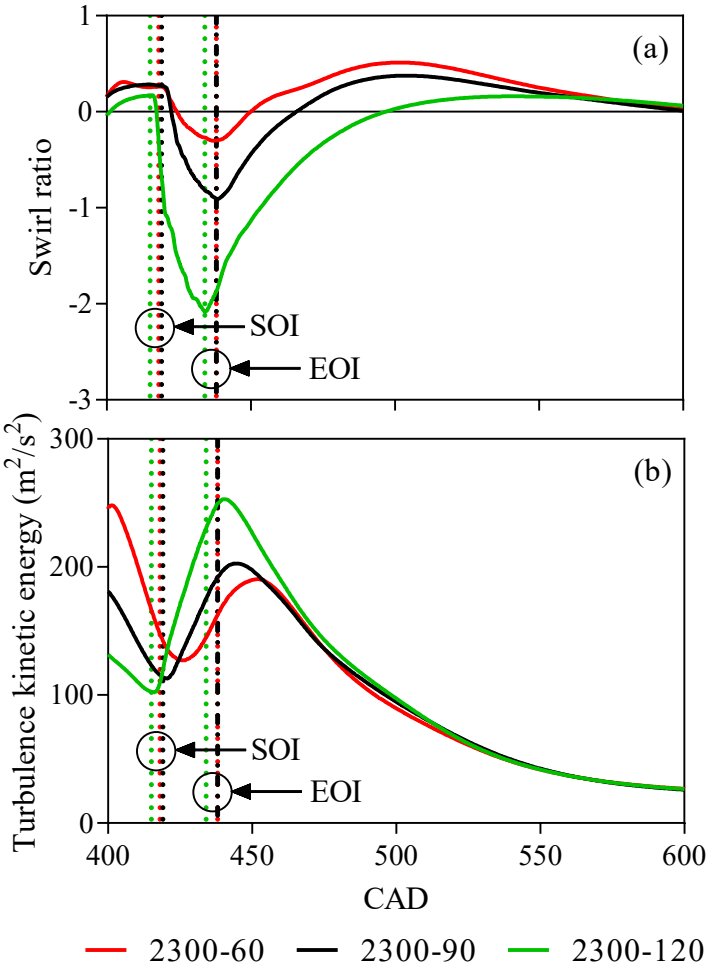


Figure 6-19 (a) Swirl ratio and (b) turbulence kinetic energy as a function of CAD for different engine loads.

Even though the flow fields exhibit no distinct differences during the compression stroke approaching the event of SI as shown in Figure 6-17(b) and Figure 6-19, flow intensity at the injection period is crucial to determine spray and droplet vaporisation characteristics. As shown in Figure 6-20(a), the decrease in SMD of fuel droplets is more rapid with increased engine load right after SOI. As the compression stroke initiates at 540 CAD, the SMD of droplets at 90 N m and 120 N m is about 22–23 µm while that at 60 N m is close to 25 µm. Furthermore, despite the higher amount of fuel injected at higher engine loads, Figure 6-20(b) reveals that fuel vaporisation takes place the earliest and fastest at 2300-120, followed by 2300-90 and 2300-60. Hence, higher injection and intake pressures supplied at increased engine load improve spray characteristics and enhance fuel evaporation [250], particularly during the injection period, thus facilitating the concurrent air-fuel mixing process.

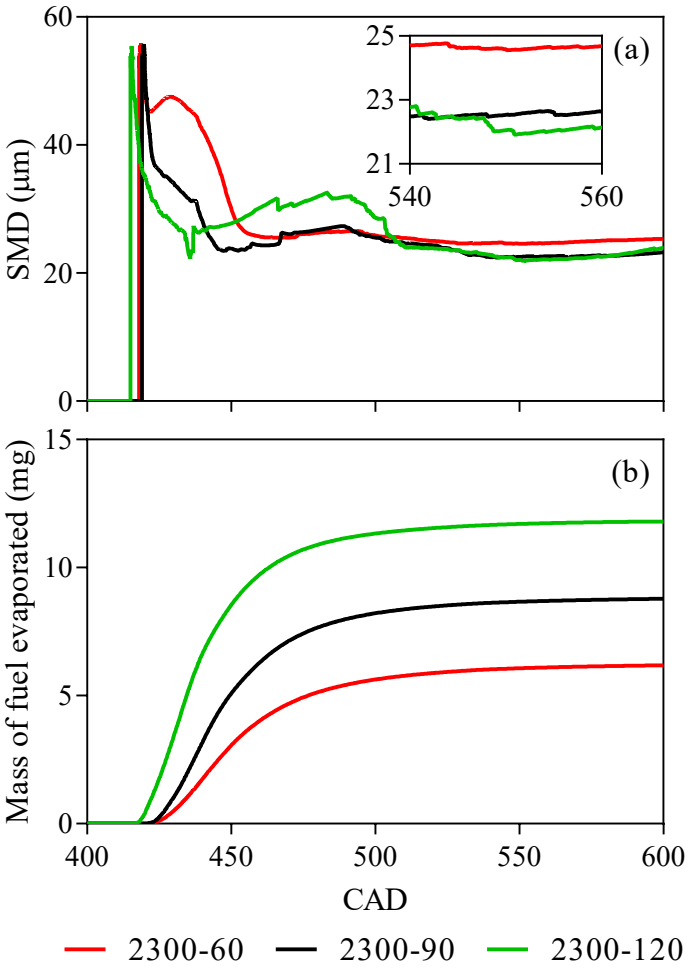


Figure 6-20 (a) SMD of fuel droplets and (b) mass of fuel evaporated as a function of CAD for different engine loads.

In-cylinder distributions of equivalence ratio in Figure 6-21 highlight the effect of injection pressure on spray development and impingement as the engine load varies. From the cross-sectional profiles at 10 CAD after SOI, the spray formation appears to be wider and more developed as the injection pressure increases during the high-load conditions. At the same time, the core region within the spray are richer in fuel, owing to the larger amount of fuel injected and better droplet vaporisation. At 20 CAD after SOI, the air-fuel distributions skew from central area to left side of the combustion chamber as the engine torque is increased from 60 N m to 120 N m. This is because at 60 N m, the spray resulting from low injection pressure follows the established in-cylinder counter-clockwise rotating flow, thus shifting the air-fuel mixture formation away from the left side of cylinder.

Figure 6-22 describes the development of liquid film mass as a consequence of fuel impingement as a function of CAD at different engine loads. As expected, the highest film mass is detected for 2300-120 due to the strongest droplet impact on surfaces caused by the highest injection pressure. The peak film mass at 120 N m is higher than those at 60 N m and 90 N m by a factor of 2.3 and 1.4, respectively. Intensified spray impingement at high load of 120 N m is characterised by the early and rapid rise in film mass right after SOI. The degree of spray-wall interactions clearly declines with decreasing engine load. At the same time, film evaporation occurs the fastest at 120 N m which can be attributed to higher in-cylinder pressure and enhanced turbulence as shown in Figure 6-18 and Figure 6-19. Thus, the effect of injection pressure on the overall spray and mixture formation is double-edged. On the one hand, high injection pressure promotes spray impingement which increases liquid fuel deposition. On the other, it improves mixing intensity and turbulence, thus facilitating film stripping and evaporation.

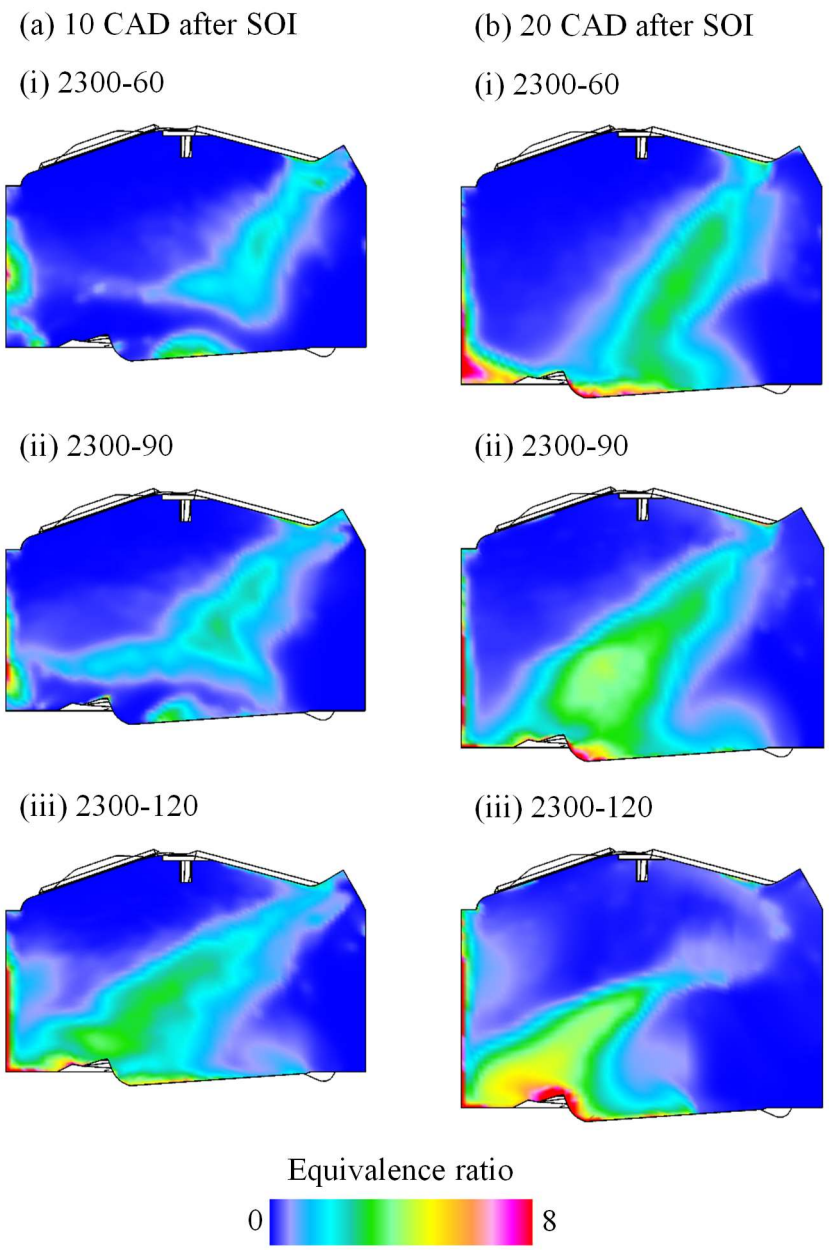


Figure 6-21 In-cylinder distributions of equivalence ratio at (a) 10 CAD and (b) 20 CAD after SOI for engine loads of (i) 60 N m, (ii) 90 N m and (iii) 120 N m.

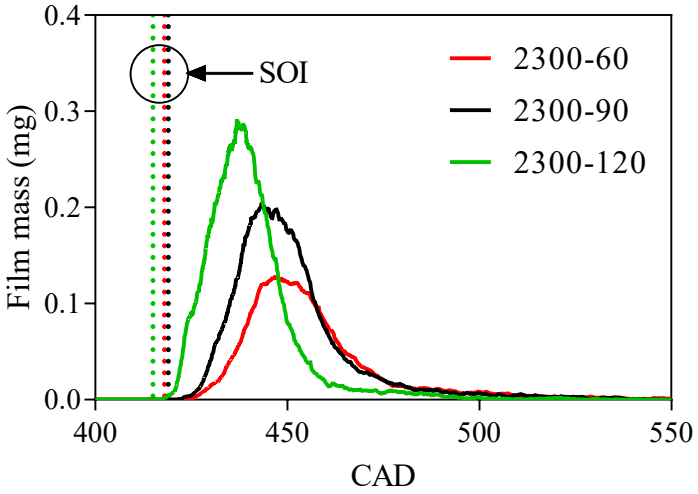


Figure 6-22 Total mass of liquid fuel film formed within the cylinder as a function of CAD for different engine loads.

At all engine loads, piston crown remains as the engine part that is most susceptible to fuel impingement as illustrated in Figure 6-23 after SOI. A fair portion of liquid fuel film is deposited on the cylinder wall while minimal film mass is observed on the combustion dome which evaporates beyond 20 CAD after SOI. Wall wetting is severe at high load of 120 N m, particularly during 20–30 CAD after SOI. This phenomenon is supported by the spray formation and development displayed in Figure 6-21(b)(iii) which leads to strong impingement on both piston and wall surfaces of the left side of combustion chamber. Spatial distributions of liquid film and film mass breakdowns at the corresponding peaks at different engine loads are depicted in Figure 6-24 and Figure 6-25, respectively. While piston wetting is common across all conditions, wall wetting becomes more critical as the engine load increases. Film thickness distributed within the cylinder surfaces exhibits coherent agreement with the amount of film mass computed on each engine part across all engine loads.

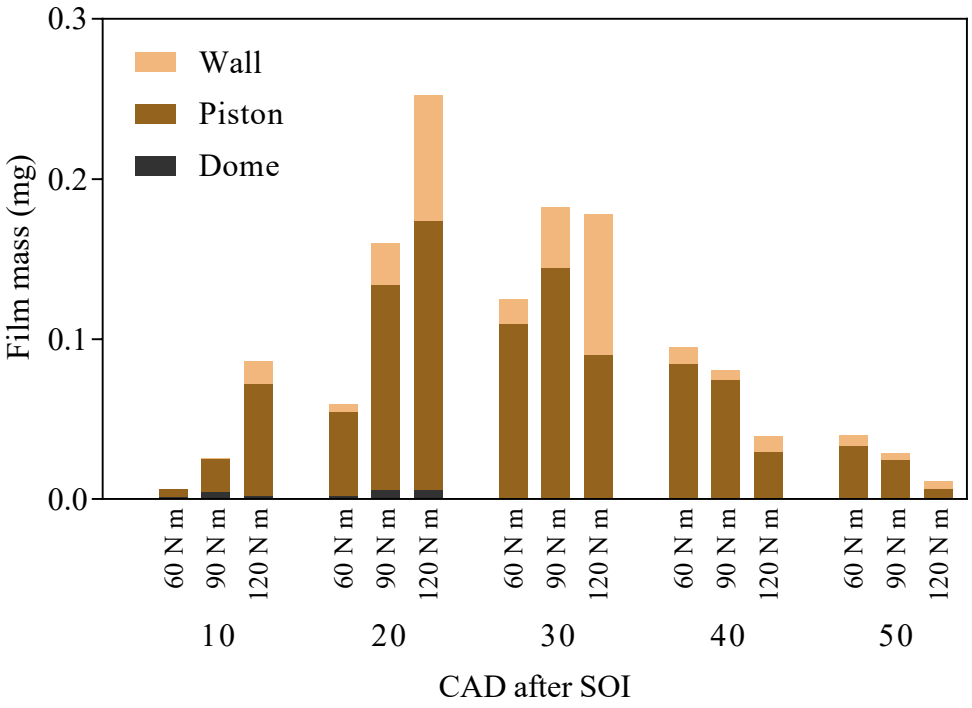


Figure 6-23 Proportions of total film mass formed on combustion dome, piston crown and cylinder wall as a function of CAD after the respective SOI of different engine loads.

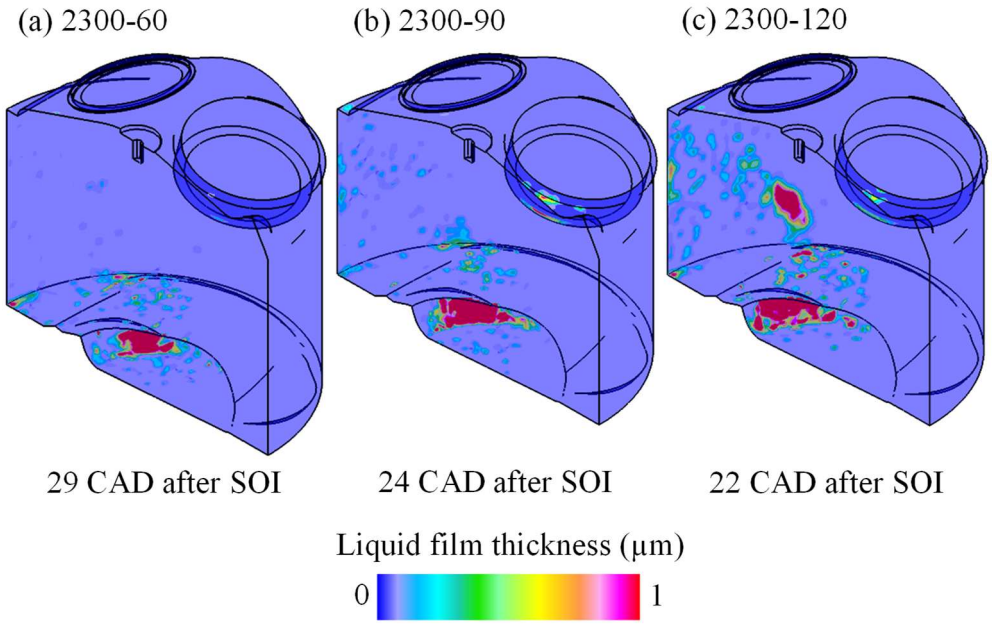


Figure 6-24 In-cylinder distributions of liquid film expressed in film thickness at the respective maximum film mass for engine loads of (a) 60 N m, (b) 90 N m and (c) 120 N m.

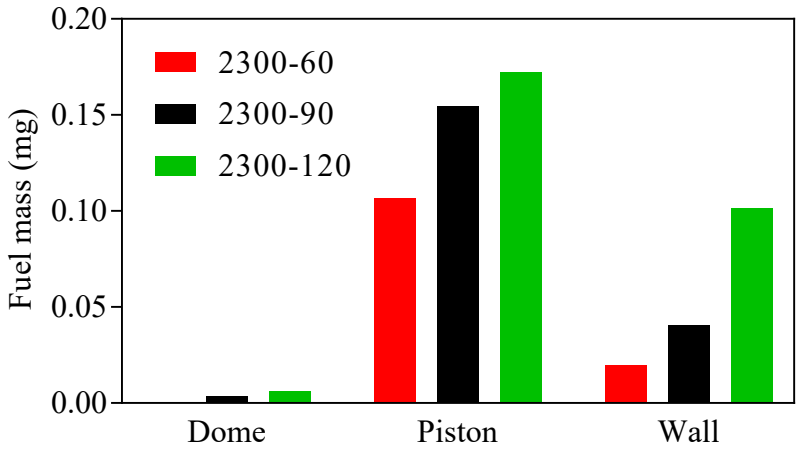


Figure 6-25 Proportions of total film mass formed on combustion dome, piston crown and cylinder wall at the respective maximum film mass for different engine loads.

6.3.2 Combustion Progress

Validation of the modelled combustion process at all engine loads is carried out by comparing the computed in-cylinder pressures against their respective measurements in Figure 6-26. Generally, both simulated and measured pressure curves exhibit close resemblance with each other despite the slight over-predictions before the peak values across the engine loads. The estimated peak pressures as listed in Table 6-3 stay within a 1% margin from the corresponding experimental values. Importantly, the trend of pressure developments with respect to the change in engine load is well captured in the simulations. As the engine load increases, the in-cylinder pressures increase in which the peak pressure becomes higher by 56% going from 60 N m to 120 N m. The delayed peak observed at 120 N m as compared to low-load conditions is attributed to the retarded SI timing.

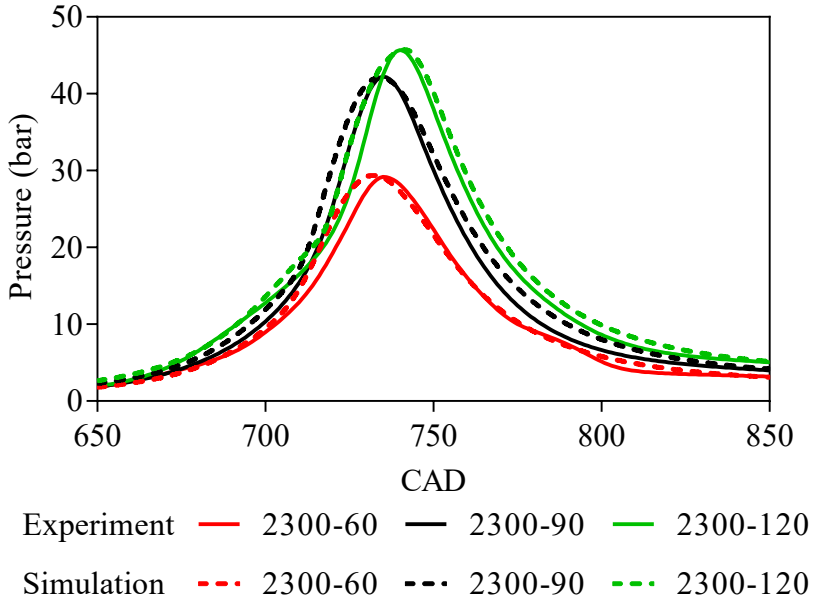


Figure 6-26 Measured and computed in-cylinder pressures for different engine loads.

Table 6-3 Measured and computed peak pressures and their locations in CAD for different engine loads.

Load (N m)	Peak pressure (bar)		Location of peak pressure (CAD)	
	Experiment	Simulation	Experiment	Simulation
60	29.17	29.37	735	732
90	42.23	42.16	735	734
120	45.70	45.71	740	742

The outcome of air-fuel mixing at different engine loads is manifested through in-cylinder spatial distributions of equivalence ratio at SI timing in Figure 6-27. Due to the larger amount of fuel injected, the overall in-cylinder equivalence ratio increases slightly at higher engine loads. While small fuel-rich pockets are present near the right cylinder walls, critical fuel-rich region is located close to the combustion dome on the left side of cylinder. As the engine load increases, the rich region is shifted further away from the spark plug towards the left periphery. This subsequently turns out to be beneficial for fuel combustion as the areas near the ignition source need to be kept close to the stoichiometric condition to minimise PM formation.

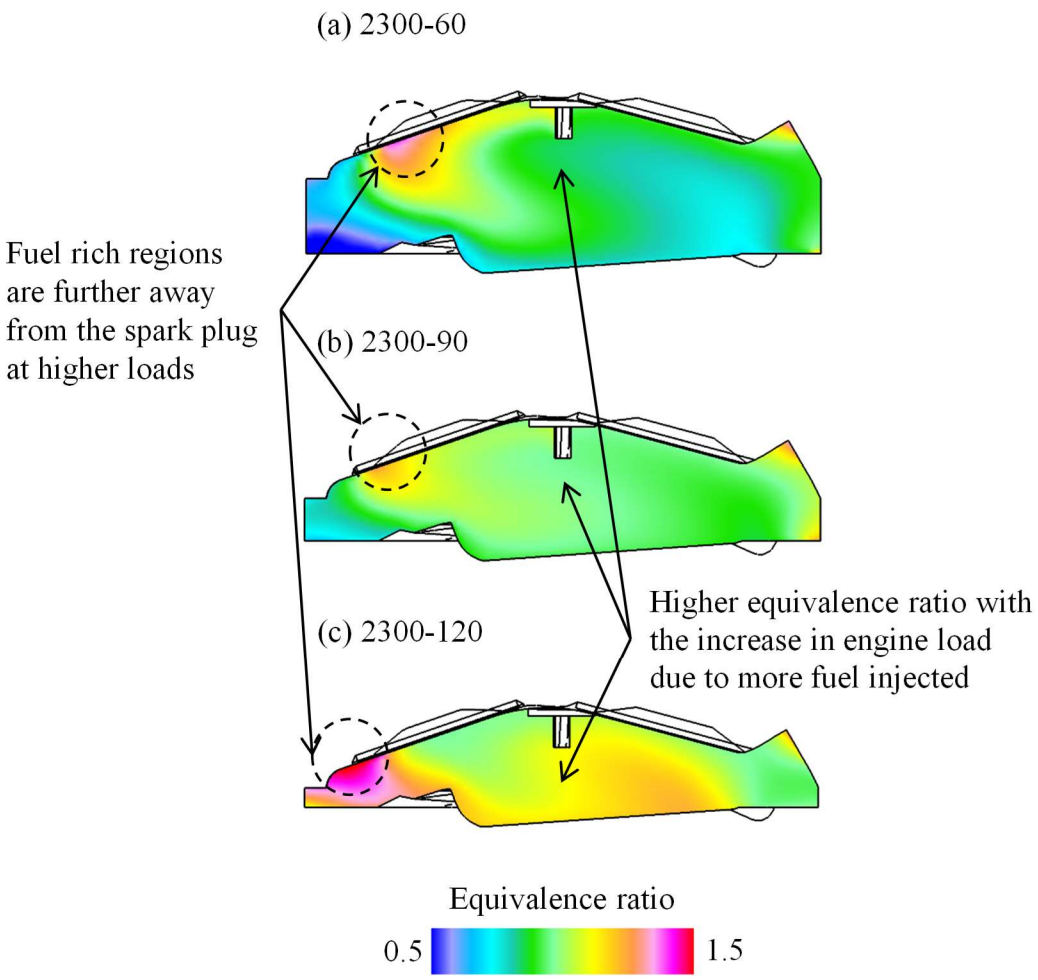


Figure 6-27 In-cylinder distributions of equivalence ratio at SI timing for engine loads of (a) 60 N m, (b) 90 N m and (c) 120 N m.

Unlike those at high-load conditions, the equivalence ratio distribution at 60 N m as displayed in Figure 6-27(a) features relatively leaner regions at bottom part and right side of the combustion chamber. The uneven mixture distribution with higher level of stratification at low load is a direct consequence of advanced SI timing which shortens the time for proper mixture preparation. Furthermore, as visualised in Figure 6-28(a), a larger count of fuel droplets remains not volatilised at SI timing for the lowest load of 60 N m. There is an apparent reduction in the amount of fuel droplets present at SI timing as the engine load is increased to 120 N m. Apart from the delayed SI, enhanced mixing intensity due to increased injection pressures at higher engine loads improves fuel vaporisation, thus diminishing the amount of remaining fuel droplets as the cycle approaches the event of SI.

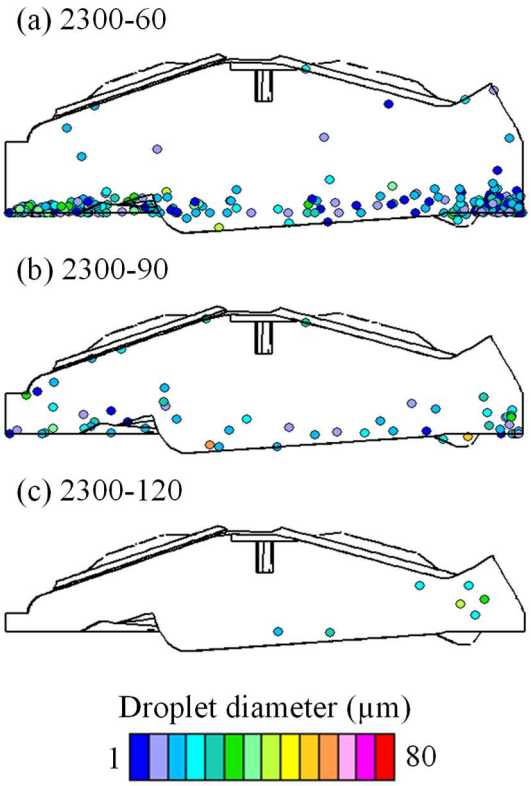


Figure 6-28 Fuel droplets coloured by their diameters at SI timing for engine loads of (a) 60 N m, (b) 90 N m and (c) 120 N m.

From Figure 6-29, although the temperature rise for 2300-120 is slower, the maximum in-cylinder temperature increases with the increase in engine load which is coherent with the pressure variation. Changing the load from 60 N m to 90 N m and 120 N m scales up the computed peak temperature by 14% and 20%, respectively. Temporal evolutions of temperature contours after SI across all engine loads are depicted in Figure 6-30. The flame front propagates the fastest at 120 N m as the high-temperature region expands the furthest into the cylinder peripheries at 40 CAD after SI. This is corroborated by the experimental observation of increasing propagation speed of the flame front extracted from planar flame images as the load became higher [85].

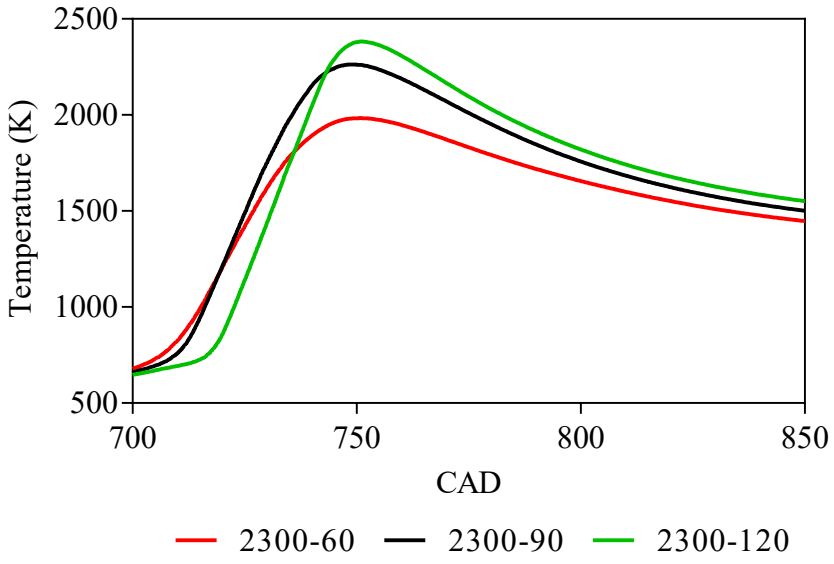


Figure 6-29 Computed in-cylinder temperatures for different engine loads.

Besides, the progress of combustion is faster at 120 N m as the temperature contour at 80 CAD after SI (see Figure 6-30(c)(iii)) appears to be more uniformly distributed than those at lower engine loads. In contrast, the rate of combustion is significantly lower at 60 N m as signified by the reduced high-temperature core. At 80 CAD after SI, near-wall regions on the right side of cylinder remain at low temperature as shown in Figure 6-30(a)(iii). The lowered rates of combustion and flame propagation at low-load condition can be partly linked to the delayed vaporisation of fuel droplets initially present at SI timing illustrated in Figure 6-28(a).

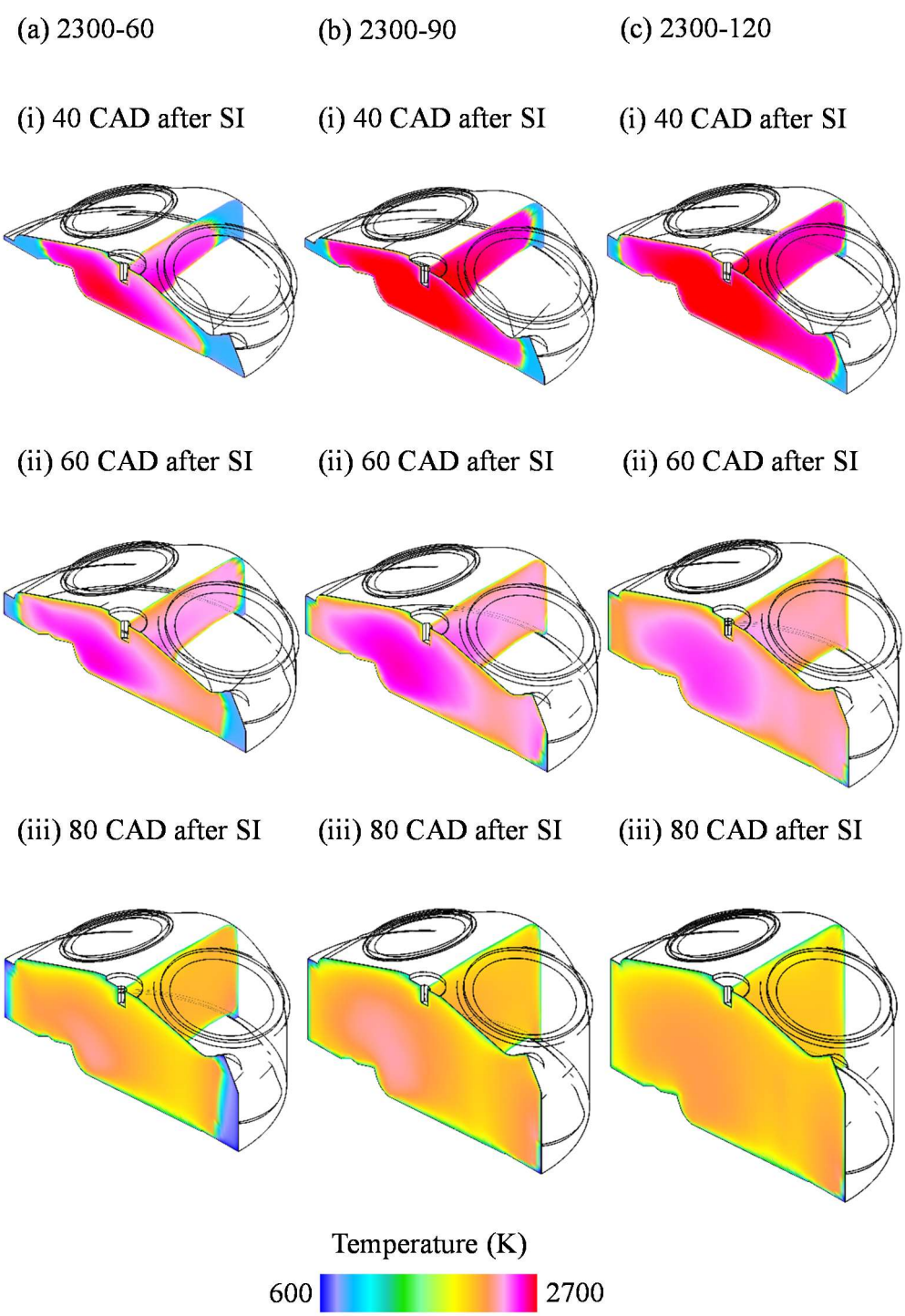


Figure 6-30 In-cylinder temperature contours for engine loads of (a) 60 N m, (b) 90 N m and (c) 120 N m at (i) 40 CAD, (ii) 60 CAD and (iii) 80 CAD after SI.

6.3.3 PM Formation and Emissions

Computed number density and mass density of soot at EVO are validated against their experimental tailpipe measurements in Figure 6-31 for all the engine loads. Excellent agreement between computed and measured number density is preserved across the

loads. However, mass density is under-predicted at lower loads of 60 N m and 90 N m while slight overestimation is observed at high load of 120 N m. The computational results stay within the same order of magnitude as the measured values regardless. The comparison of normalised results based on the reference case of 2300-90 reflects the accurate replication of experimental trends of number density and mass density due to the change in engine load.

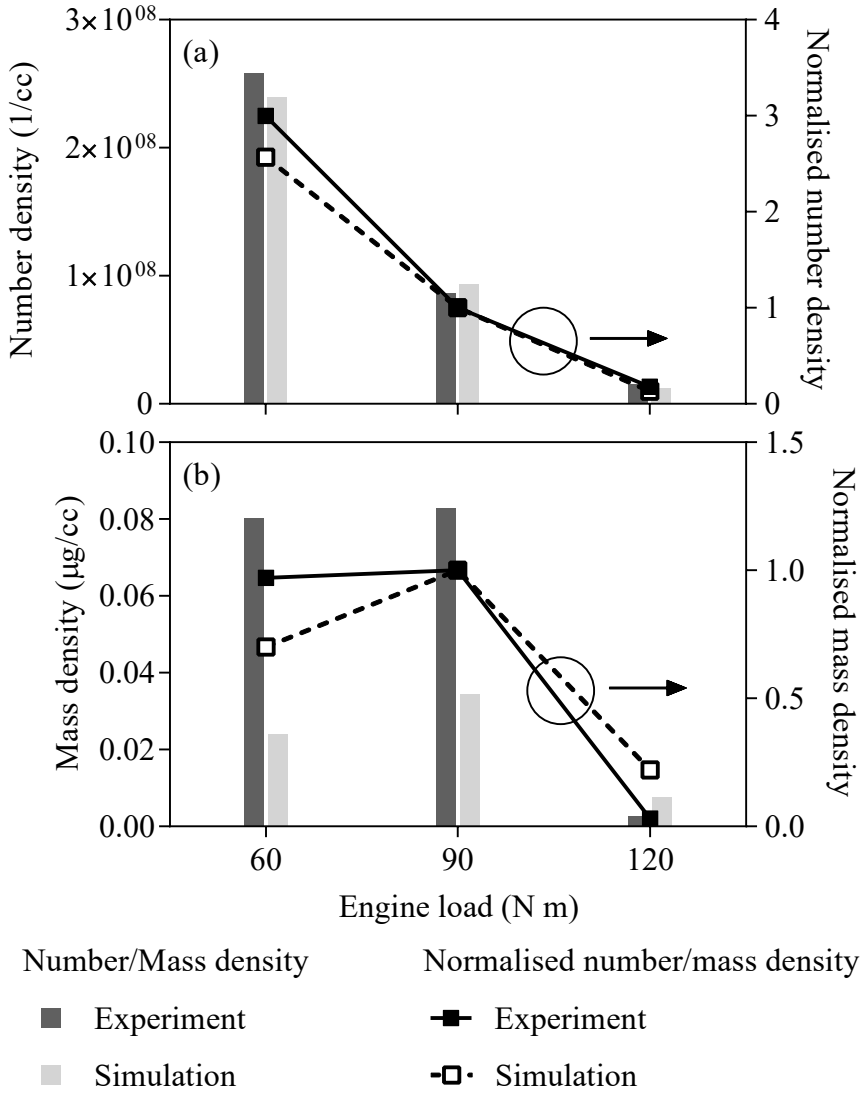


Figure 6-31 Measured and computed (a) number density and (b) mass density of soot and their normalised values based on the reference case for different engine loads.

When the engine load decreases from 120 N m to 60 N m, number density increases significantly. Large mass density is generated at 2300-60 and 2300-90 with the latter

being slightly higher than the former whereas high-load condition of 2300-120 forms remarkably lower mass density. Similar trends in PM emissions were measured by Wang et al. [251] in which number density declined with increasing IMEP (6.5–8.5 bar) while the highest mass density was detected at the medium-load condition with IMEP of 7.5 bar. In contrast, the experimental work by An et al. [249] demonstrated that mass density at 120 N m was consistently higher than that at 60 N m for engine speeds ranging from 1000 rpm to 3000 rpm. Thus, it can be inferred that the effect of engine load on PM emissions depends highly on the associated operating parameters such as injection pressure, SOI and SI timings.

In terms of normalised number-weighted PSDF of soot plotted in Figure 6-32 for engine loads of 60 N m and 120 N m, the general trend of decreasing particle number with increasing diameter observed experimentally is retained numerically. However, the peak of nucleation mode is overestimated for both engine loads. The reasonable agreement exhibited at low load of 60 N m vanishes at high load of 120 N m when the number of particles within the accumulation mode is comparatively notable. Like the PSDF of soot at 90 N m shown in Figure 5-16, the bimodal distributions at higher engine loads are not reproduced. Therefore, the normalised PSDF of soot generated from the current sectional method also lacks sensitivity towards the effect of varying the engine load.

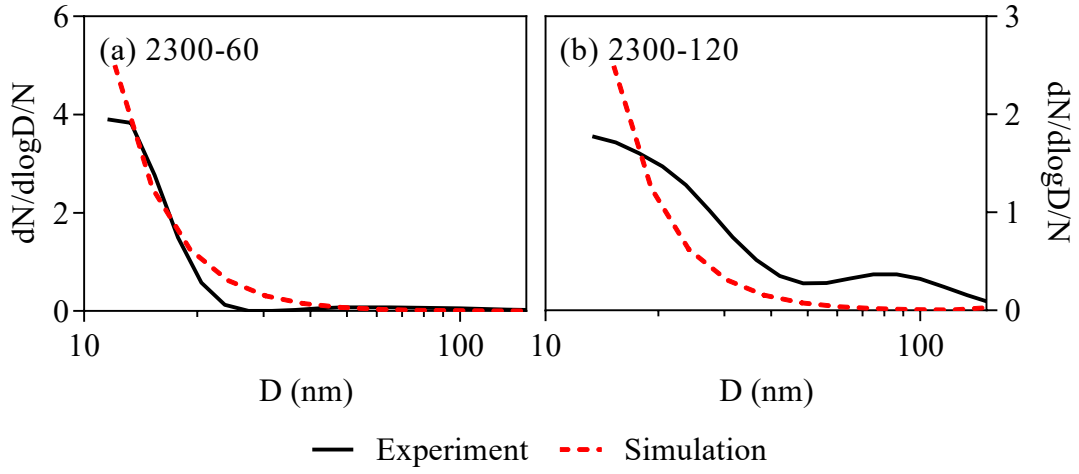


Figure 6-32 Measured and computed number-weighted PSDF normalised with total number density of soot at engine loads of (a) 60 N m and (b) 120 N m.

Figure 6-33 and Figure 6-34 illustrate the temporal development of number density and mass density of soot at different CAD after the respective SI timings for all the engine loads. The emergence of high number density at 60 N m is clearly visible at all CAD after SI examined within the regions surrounding the high-temperature core. Lower number density is found at higher engine loads which experiences apparent reductions at 60 CAD and 80 CAD after SI as a result of enhanced soot oxidation. On the other hand, high number density for 2300-60 persists late in the engine cycle. It is noticed that soot formation ceases before reaching the right end of cylinder walls in Figure 6-33(a)(ii) and (a)(iii). This is because low temperature at the region shown in Figure 6-30(a)(ii) and (a)(iii) inhibits the inception of nascent soot particles.

Inspecting Figure 6-33(a)(i) to (c)(i) across all engine loads reveals that the regions with concentrated number density of soot are located further away from the spark plug as the engine load increases from 60 N m to 120 N m. This, in fact, coincides with the spatial distributions of fuel-rich regions at varied engine loads shown in Figure 6-27. Similar to number density, mass density for 2300-120 is minimal as evidenced from Figure 6-34(c)(i) to (c)(iii) with higher concentration observed on the left cylinder periphery. The associated in-cylinder equivalence ratio distribution in Figure 6-27(c) corroborates that the fuel-rich region acts as the main source of soot formation under the condition. On the other hand, wider distribution of high soot mass density at 90 N m as compared to that at 60 N m suggests that particle growth through surface growth and PAH condensation dominates under higher engine load.

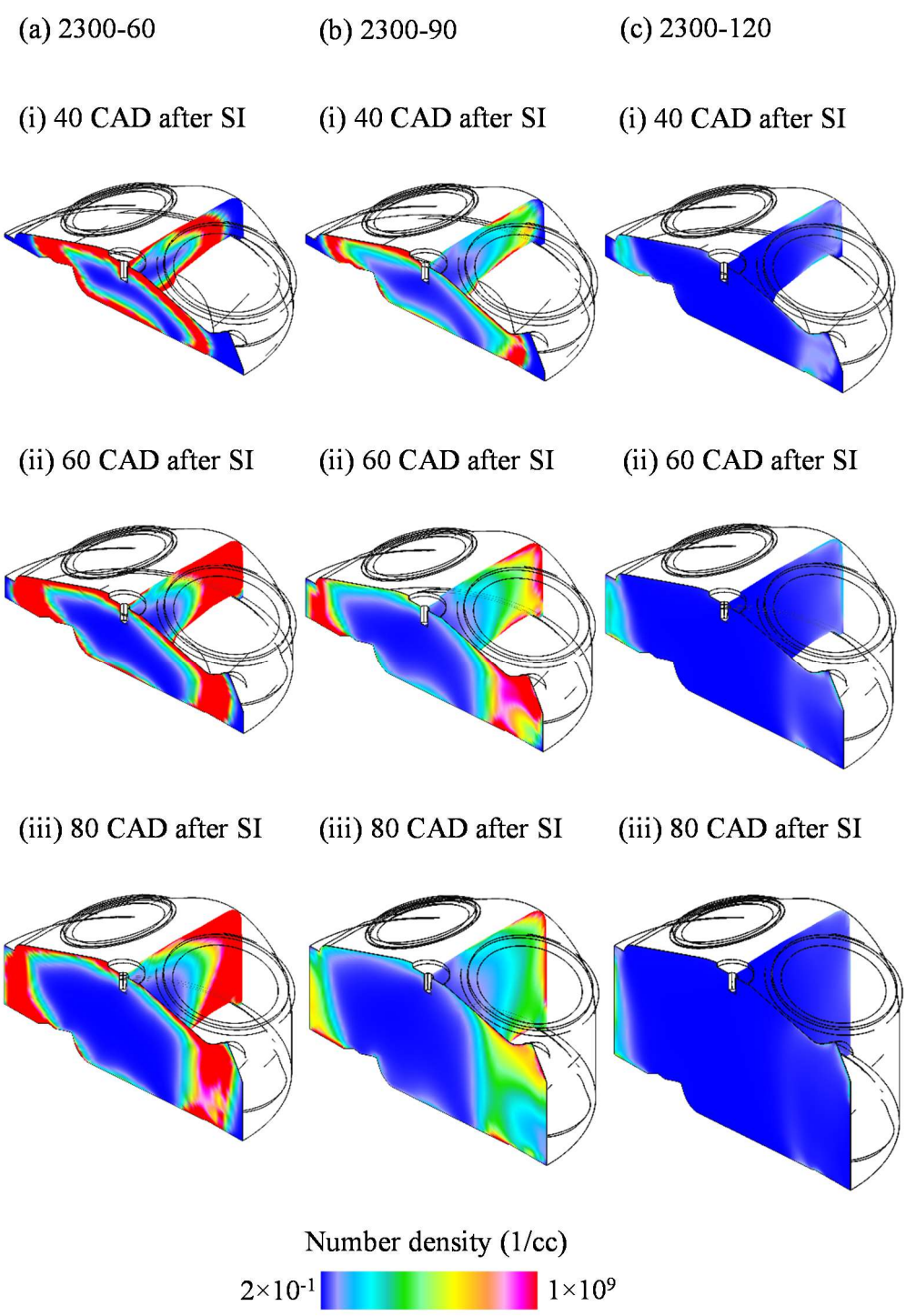


Figure 6-33 In-cylinder distributions of number density of soot for engine loads of (a) 60 N m, (b) 90 N m and (c) 120 N m at (i) 40 CAD, (ii) 60 CAD and (iii) 80 CAD after SI.

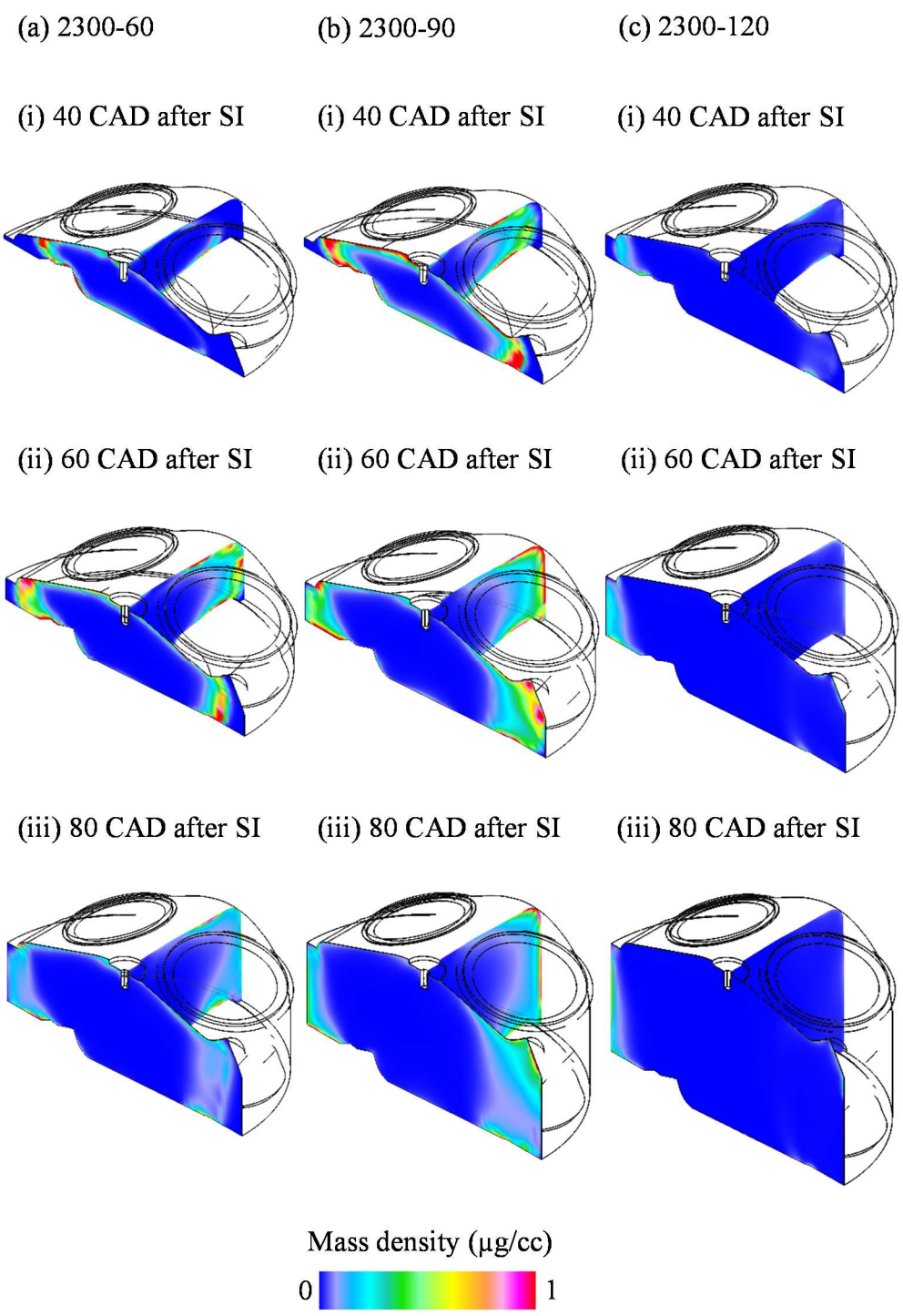


Figure 6-34 In-cylinder distributions of mass density of soot for engine loads of (a) 60 N m, (b) 90 N m and (c) 120 N m at (i) 40 CAD, (ii) 60 CAD and (iii) 80 CAD after SI.

The net production of soot in terms of particle number and mass is plotted in Figure 6-35 as a function of CAD up to EVO timing for different engine loads. Due to the advanced SI timing, there is an accelerated rate of particle inception at low load of 60

N m as supported by the early and rapid rise in particle number. The increase in soot mass is comparable for both 60 N m and 90 N m with the peak at 90 N m exceeds that at 60 N m by 32%, emphasising the increased particle growth rate at higher load. Despite higher mass of injected fuel at 120 N m, both particle number and mass stay at the minimum level until EVO without any visible peaks. Reduced PM emissions at high load of 120 N m can be primarily attributed to the enhanced droplet atomisation and fuel vaporisation provided by higher intake and injection pressures. This in turn, lowers the count of remaining fuel droplets near SI timing which potentially translate to a direct source of soot formation. Moreover, the retarded SI timing at 120 N m cuts down the residence time of PAH and soot particles to prevent further inception and growth before EVO.

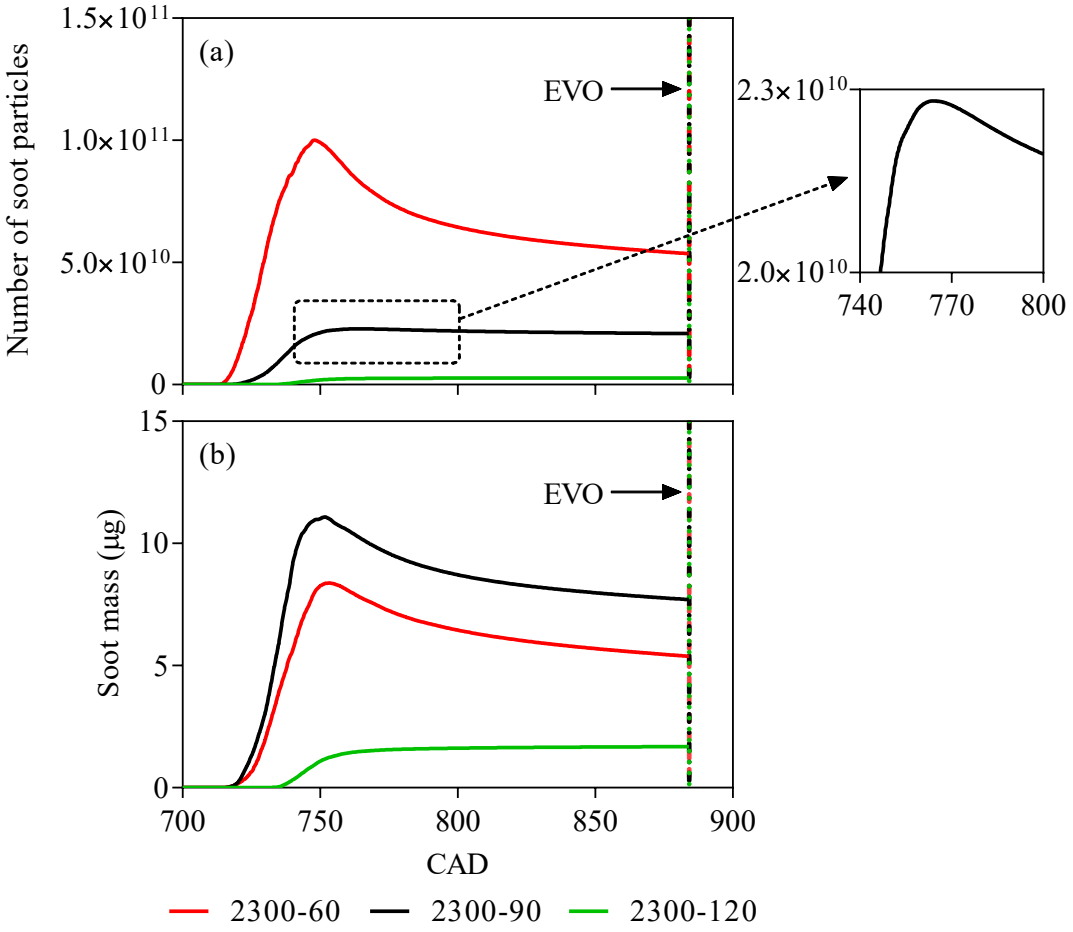


Figure 6-35 Computed in-cylinder (a) number of soot particles and (b) soot mass as a function of CAD up to EVO for different engine loads.

6.4 Concluding Remarks

PM formation mechanisms are studied under varying engine speeds and loads through integrated CFD-chemical kinetics. Measured in-cylinder pressures across the speed-load domain are reasonably replicated with the maximum discrepancy of 1.5% in peak pressures. Predicted number density and mass density of soot at EVO are within the same order of magnitude as the experimental tailpipe measurements. The variations in pressure, number density and mass density of soot with respect to the changes in speed and load are also successfully captured by the numerical simulations. Number-weighted PSDF of soot generated from the sectional method emulates the general experimental trend of decreasing particle number as the diameter increases from 10 nm to 100 nm, but fails to reproduce the lower peak of accumulation mode. It is noted that the shapes of normalised PSDF computed exhibit no sensitivity towards changes in speed or load. Main changes (increases or decreases) in operating parameters, in-cylinder conditions and engine phenomena pertinent to PM emissions due to varied speeds and loads are summarised in Table 6-4.

Table 6-4 Main changes in operating parameters, in-cylinder conditions and engine phenomena as a result of varying engine speed and load from the reference case.

1600-90 (low speed)	2300-60 (low load)	2300-90 (reference case)	2300-120 (high load)	3000-90 (high speed)
▼	-	Speed	-	▲
-	▼	Load	▲	-
-	▼	Intake pressure	▲	-
-	▼	Injection pressure	▲	-
▼	▼	Turbulence kinetic energy	▲	▲
▼	▼	Maximum film mass	▲	▼
▲	▼	Mixing time[a]	▲	▼
-	▲	Fuel droplets at SI	▼	-
▼	▼	Peak pressure	▲	▼
▼	▼	Peak temperature	▲	▼
▲	▲	Soot residence time[b]	▼	▼
▲	▲	Soot number density	▼	▼
▼	▼	Soot mass density	▼	▼

[a] Defined as the duration between EOI and SI timings.
[b] Defined as the duration between SI and EVO timings.

Engine speed mainly affects in-cylinder flow intensity and available mixing time, thus determining the uniformity of mixture distribution. From Table 6-4, as engine speed increases, higher flow velocity contributes to intensified tumble motion and larger turbulence kinetic energy. Consequently, stronger mixing intensity promotes droplet breakup and vaporisation which benefit the attainment of homogenous mixture. Fuel impingement is more severe at higher speeds due to earlier SOI timings when the piston is closer to the fuel injector. The maximum liquid film mass formed is lower at 3000 rpm than that at 2300 rpm owing to better droplet vaporisation for the former. At SI timing, the level of mixture homogeneity clearly improves with the increase in speed as more fuel-rich pockets are present at low-speed condition. Furthermore, shorter residence time of soot particles is linked to higher speed. Thus, high speed of 3000 rpm demonstrates reductions of an order of magnitude in number density and a factor of six in mass density of soot from those registered at lower engine speeds.

Increasing engine load inherently requires injecting greater fuel mass, accompanied by an elevated intake pressure as tabulated in Table 6-4. Besides, increased injection pressure at higher load improves flow field and accelerates droplet atomisation and vaporisation. Such an enhancement in flow intensity typically diminishes during the compression stroke at constant engine speed. Nevertheless, good spray characteristics during fuel injection phase is essential to ensure the completeness of fuel vaporisation so as to minimise the count of remaining droplets near SI timing. While larger film mass is deposited on part surfaces due to stronger droplet impact, film stripping and evaporation occur the fastest at high engine load of 120 N m. Approaching the event of SI, prolonged mixing time at higher load shifts fuel-rich regions further away from the vicinity of spark plug. Retarded SI timing also decreases in-cylinder residence time of soot particles. As a result, number density and mass density of soot experience a drop by an order of magnitude and 78%, respectively as the engine load is increased to 120 N m.

CHAPTER 7
NUMERICAL STUDY ON EFFECTS OF ENGINE OPERATING PARAMETERS ON PM EMISSIONS

7.1 Introductory Remarks

To deepen the understanding of PM formation mechanisms in GDI engines for further development of mitigation strategies, the reference case of 2300-90 is selected to be analysed and scrutinised in detail in this chapter. This is because the speed-load point lies within the part-load operating envelope, thus serving as a representative condition under the actual urban driving cycle [252]. In addition, as depicted in Figure 7-1, the operating conditions of 2300-90 are associated with the largest mass density and relatively high number density of soot particles. Hence, a conceptual model describing the relevant ultra-fine PM processes within the wall-guided GDI engine is proposed based on the chosen operating point of 2300-90 in Section 7.2.

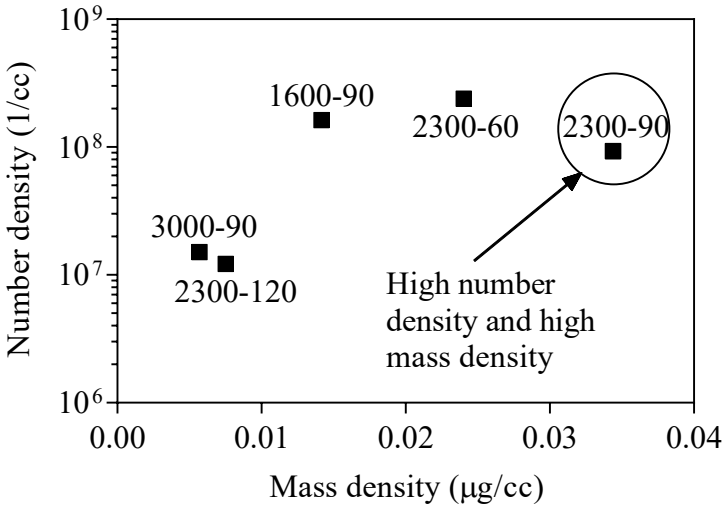


Figure 7-1 Computed number density of soot plotted against mass density for all part-load operating points varying in engine speeds and loads.

Under the fixed running point at 2300 rpm with 90 N m, the effects of engine operating parameters including SOI timing, SI timing and rate of EGR on PM emissions from

the GDI engine are studied numerically in Section 7.3 till Section 7.5. Each operating parameter is varied in isolation so as to build the correlations between the combustion and emission behaviours induced by a change in the particular parameter. Relevance of the parameters on PM mitigation is ranked based on their sensitivities towards soot number density and mass density. The former is emphasised as the particle number of ultra-fine PM rather than the mass is linked to adverse impacts on public health [253].

7.2 Conceptual Model for Ultra-Fine PM Processes in GDI Engines

For the operating point of 2300-90, generation of strong in-cylinder flow field arises at the onset of IVO when there is a rapid entry of air into the combustion chamber. As visualised by the velocity field at the maximum lift of intake valve in Figure 7-2(a), the highest flow velocity occurs around the valve curtain for the incoming air motion. Due to geometrical configurations of the intake port and valve, the flow which is directed towards the left part of the cylinder induces circular rotational motions after impacting wall and piston surfaces. The counter-clockwise rotating flow develops as the air is drawn into the chamber continuously. At the instant of IVC shown in Figure 7-2(b), a fully-developed tumble motion in the counter-clockwise fashion is attained within the cylinder, featuring higher flow velocity at the right side of the cylinder.

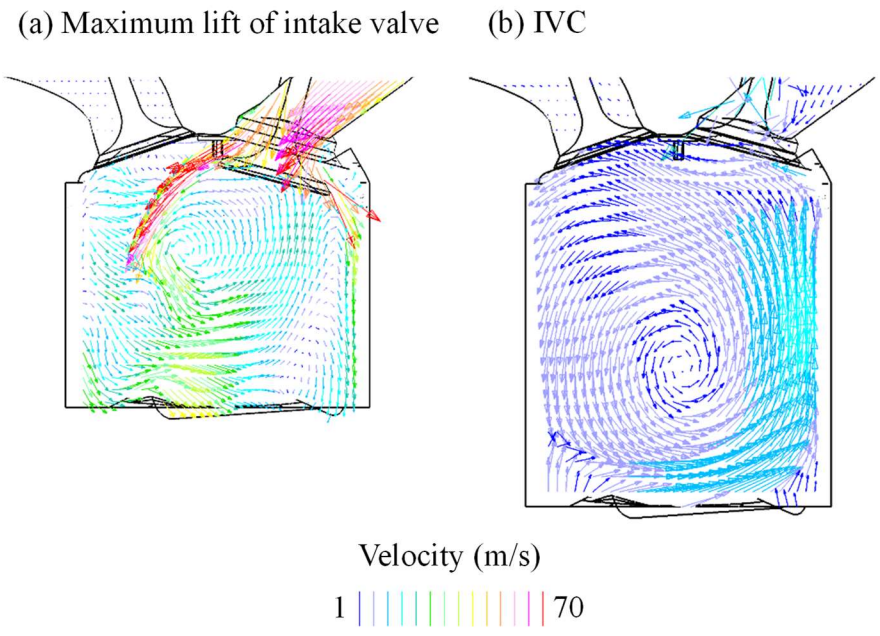


Figure 7-2 In-cylinder flow velocity at (a) maximum lift of intake valve and (b) IVC.

During the intake stroke, directed energy from the incoming jet is mainly converted into turbulence [254], thus causing a rapid spike in turbulence kinetic energy after IVO as plotted in Figure 7-3(a). Subsequently, during the injection timing window, there is an apparent increase in turbulence kinetic energy up to its peak value towards EOI. As the engine cycle proceeds, the intensity of turbulence declines markedly due to turbulent transport and viscous decay [254] in aiding uniform air-fuel mixing. As seen in Figure 7-3(b), tumble and swirl motions become significant after SOI when fuel is injected at an elevated pressure. For the wall-guided GDI engine, tumble flow is the dominant mechanism governing the in-cylinder organised motion with higher ratio shown throughout the mixture preparation phase. Hence, the counter-clockwise nature of tumble flow plays a decisive role in distributing fuel and air spatially within the cylinder to achieve a homogenous charge.

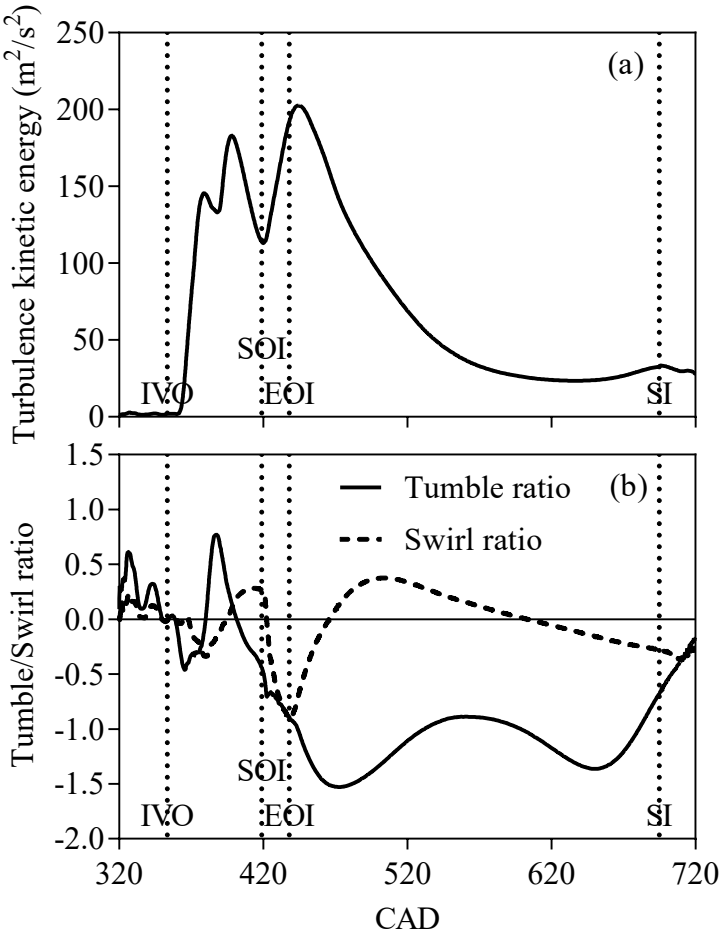


Figure 7-3 (a) Turbulence kinetic energy, (b) tumble ratio and swirl ratio as a function of CAD with IVO, SOI, EOI and SI timings indicated.

At the onset of SOI shown in Figure 7-4(a)(i), region with high flow velocity emerges close to the intake port and fuel injector as a result of the incoming air stream and fuel spray. At 10 CAD after SOI, while fuel primarily vaporises within the spray core, droplet impacts on surfaces of left cylinder wall and piston crown are visible in Figure 7-4(b)(ii). The impingement outcomes cover film deposition, rebound and splashing. Thus, the areas of fuel impingement also correspond to having high equivalence ratio which is indicative of strong fuel evaporation. Towards EOI, fuel impingement clearly amplifies with increased droplet count and broadened impacting surfaces as illustrated in Figure 7-4(b)(iii). Fuel droplets are more uniformly scattered within the high flow field while they are lumped together near the left cylinder wall and piston where the flow is slower.

As a result of intense spray-wall impingement, temporal development of liquid fuel film is represented by mass deposited on combustion dome, piston crown and cylinder wall in Figure 7-5. After SOI, the film mass increases continuously and reaches its peak value of 0.2 mg at about 5 CAD after EOI. Along with Figure 7-4(b)(ii) and (b)(iii), piston and wall surfaces are prone to fuel impingement with piston wetting being more severe. Through laser-induced fluorescence imaging, Stevens and Stepper [164] captured the film formation on piston top for an early fuel injection during the intake stroke. Here, 76% of the maximum mass of total film is formed on the piston while that on the cylinder wall accounts for roughly 20%. Minimal amount of film is found on the combustion dome with the peak mass of 0.006 mg. At 10 CAD ABDC into the compression stroke, the total film vanishes completely through film stripping and breakup.

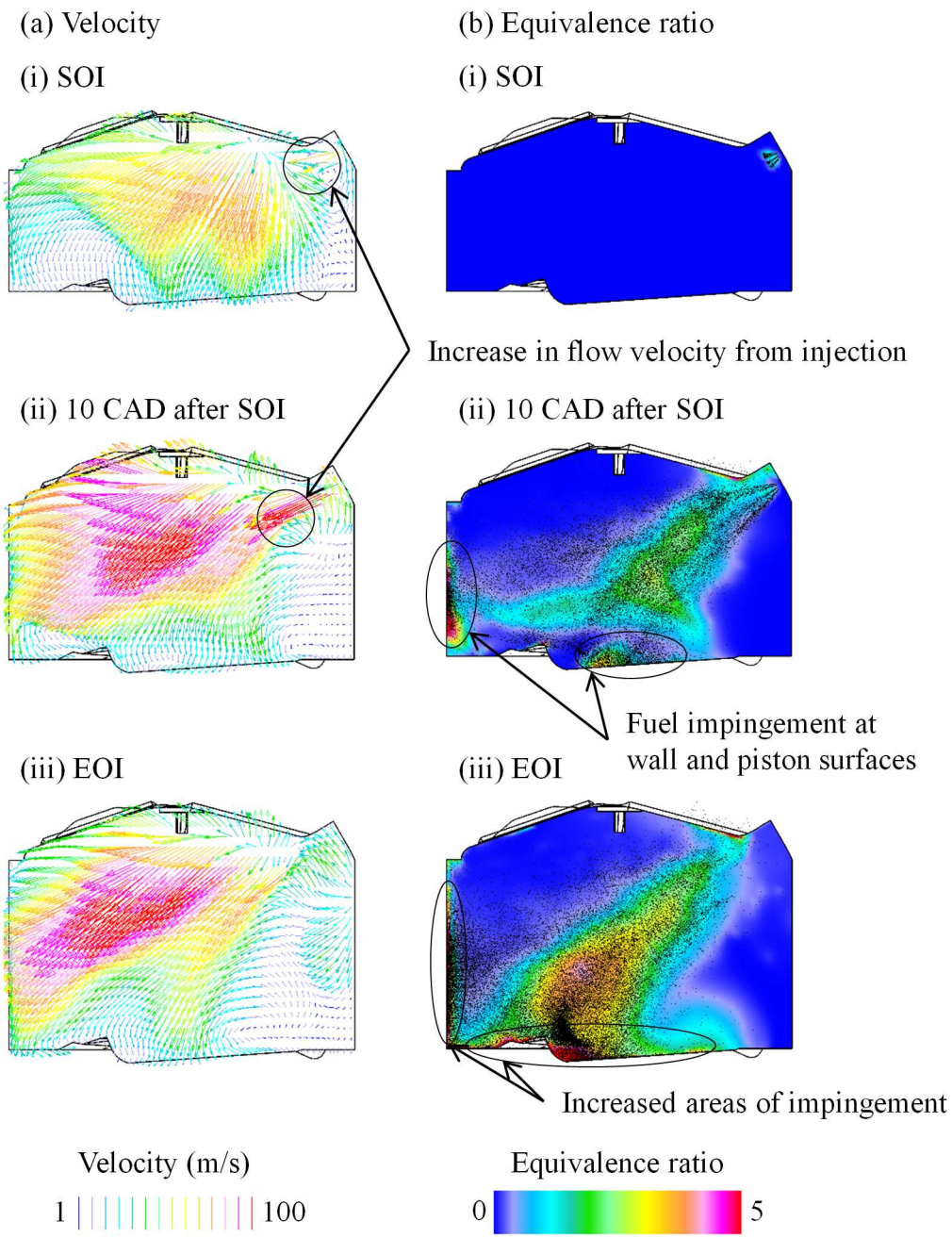


Figure 7-4 In-cylinder (a) flow velocity and (b) distribution of equivalence ratio superimposed with fuel droplets injected at (i) SOI, (ii) 10 CAD after SOI and (c) EOI.

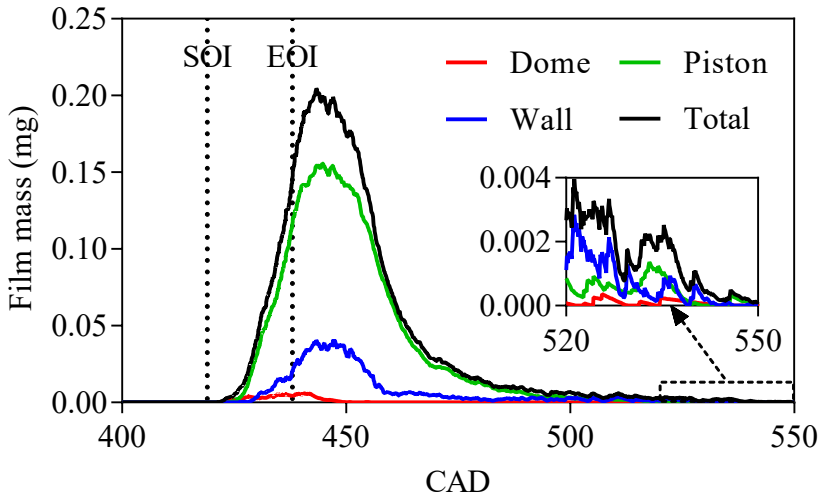


Figure 7-5 Total mass of liquid fuel film formed and the respective proportions on combustion dome, piston crown and cylinder wall as a function of CAD with SOI and EOI timings indicated.

After EOI, film stripping and evaporation take place effectively, thus leading to a net reduction in total liquid film mass. Temporal evolution of in-cylinder distributions of equivalence ratio and fuel droplets is illustrated in Figure 7-6 from 30 CAD to 100 CAD after SOI. At 30 CAD after SOI, fuel droplets rebounded, splashed and stripped from the film are accumulated close to the wall and piston surfaces. These fuel-rich regions are denoted by very high equivalence ratio due to ongoing fuel vaporisation. Within 40–50 CAD after SOI, the fuel-rich region grows and spreads into the bulk of combustion chamber with an apparent decline in droplet number. The size of fuel-rich region near the piston as compared to that near the wall further highlights the severity of piston wetting.

Starting at 60 CAD after SOI, air-fuel mixing prepares the mixture towards the state of homogenous charge. As the mixing continues, air is drawn into the fuel-rich core which lowers the associated equivalence ratio to enable uniform mixture distribution. Fuel-rich pockets and fuel droplets are swept upwards from the piston surface by the counter-clockwise tumble flow, thus causing the equivalence ratio distribution shown in Figure 7-6(f). Hence, the presence of fuel-rich regions within the cylinder is mainly contributed by liquid film stripping due to critical piston wetting.

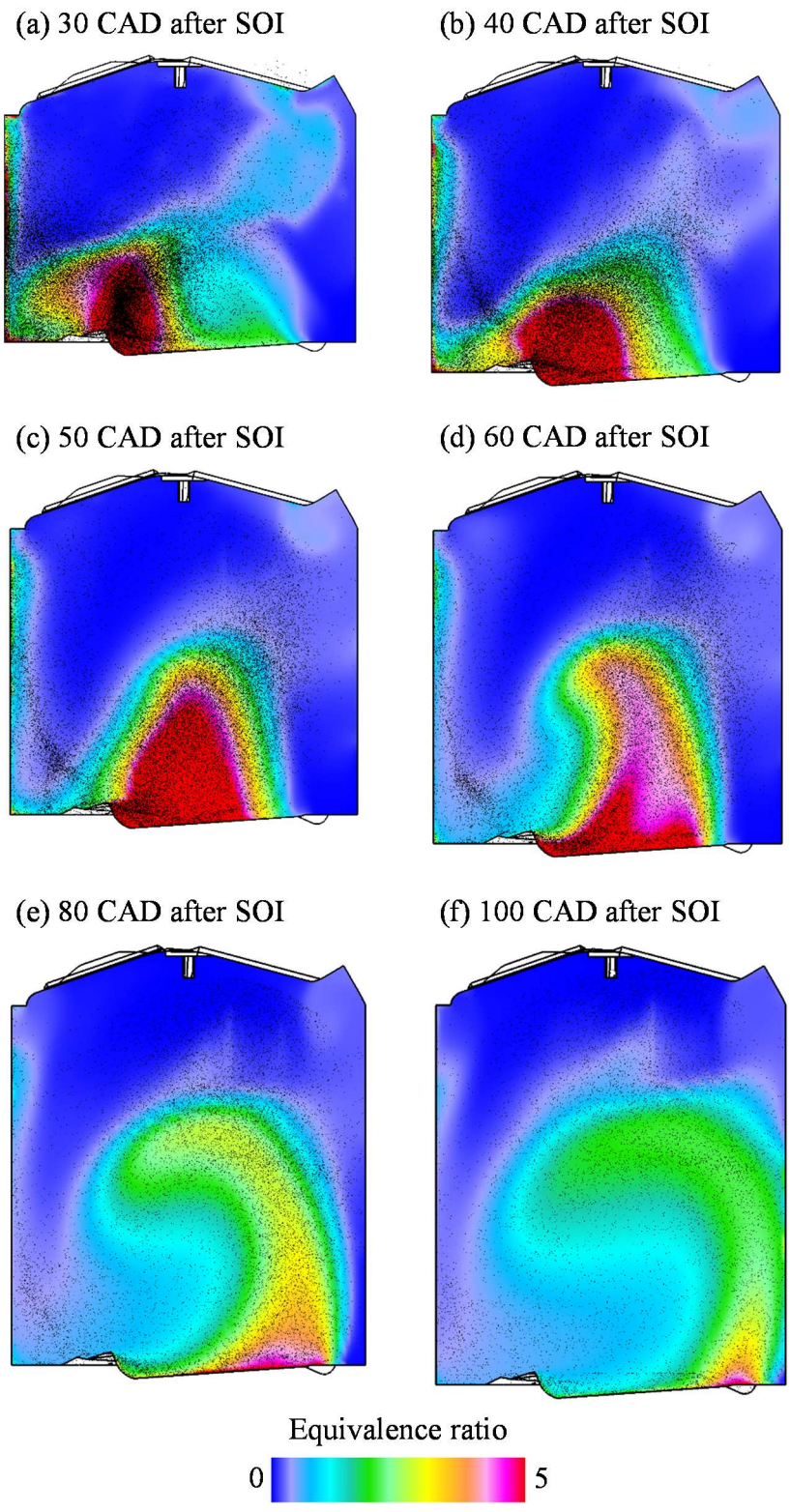


Figure 7-6 In-cylinder distributions of equivalence ratio superimposed with fuel droplets injected at (a) 30 CAD, (b) 40 CAD, (c) 50 CAD, (d) 60 CAD, (e) 80 CAD and (f) 100 CAD after SOI.

Hentschel et al. [255] visualised fuel distribution in a GDI engine with optical access using laser-induced fluorescence. The optical images of fuel vaporisation for an early injection (50 CAD ATDC during the intake stroke) are set as a benchmark to evaluate the simulated mixing process in the present work as illustrated in Figure 7-7. The field of view was located centrally in the cylinder. The comparisons are made qualitatively due to the differences in engine specifications and operating parameters. Nonetheless, temporal development of computed fuel distribution is in coherent agreement with the optical diagnostics, leading to the formation of a nearly homogeneous charge. During the compression stroke depicted in Figure 7-7(a)(iii)–(iv) and (b)(iii)–(iv), higher fuel concentration is transported and located on the left side of cylinder (near the exhaust port).

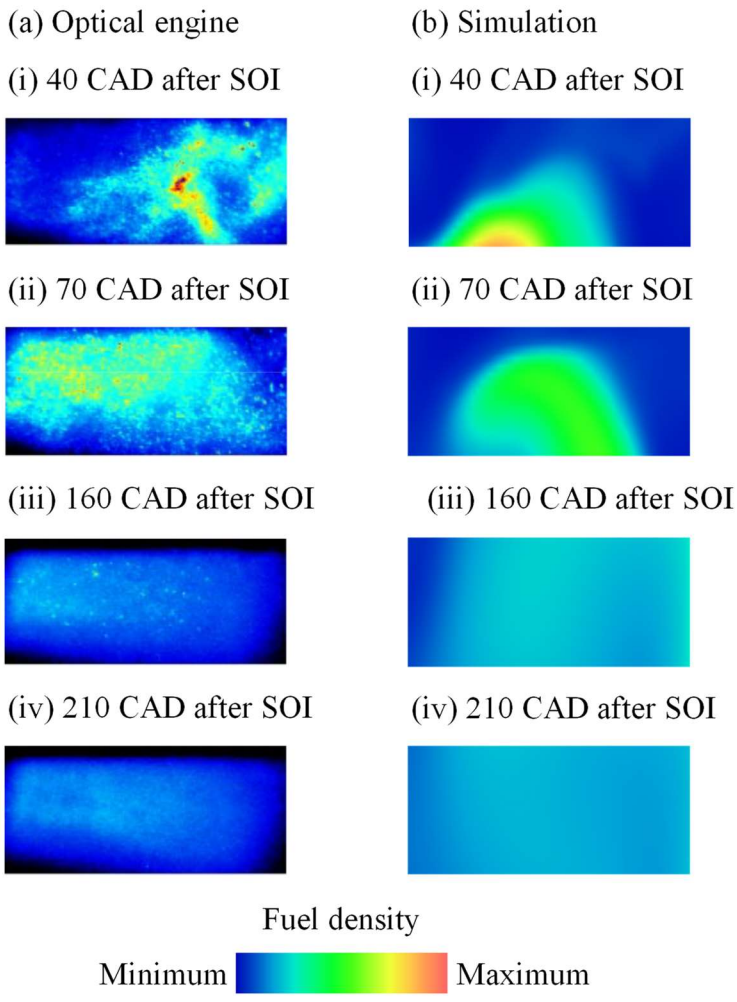


Figure 7-7 (a) Laser-induced fluorescence of liquid and gaseous phases of fuel and (b) simulated fuel mass fraction at (i) 40 CAD, (ii) 70 CAD, (iii) 160 CAD and (iv) 210 CAD after their respective SOI timings.

Fuel droplets which remain unevaporated during SI timing are visualised in Figure 7-8. The droplets are mainly scattered around the piston crown with diameters ranging from 4 μm to 60 μm. The source of fuel droplets surviving up to the event of SI can be associated with the following in-cylinder engine phenomena:

i. Fuel droplets fail to undergo further breakup and vaporise after injection and spray atomisation. This reflects poor in-cylinder conditions to facilitate fuel vaporisation and mixing.
ii. Fuel droplets rebound or splash into smaller droplets after impacting wall surfaces. Along with the newly injected fuel, they remain as liquid droplets as the engine cycle continues.
iii. Fuel droplets stripped from the liquid film are subjected to shortened time for evaporation, thus persisting till the event of SI.

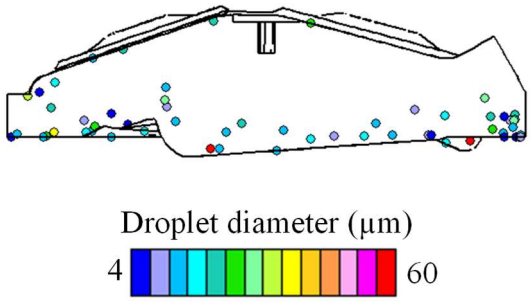


Figure 7-8 Fuel droplets coloured by their diameters at SI timing.

The resulting in-cylinder mixture distribution at SI timing is represented through top, front and side views of equivalence ratio at three cross sections in Figure 7-9. While the overall mixture approaches the stoichiometric state within the cylinder, areas of inhomogeneity and stratification can be observed near the cylinder peripheries. Spatial distribution of increasing equivalence ratio from the bottom right piston region to the upper left exhaust port region is a direct ramification of the tumble motion carrying the fuel-rich charge in the counter-clockwise direction. High degree of stratification in mixture located close to the left end of cylinder wall is due to inadequate mixing time before SI.

Moreover, the presence of fuel-rich pockets at the right wall is caused by reduced air entrainment and lowered flow velocity at the region. Coherently, the top view of equivalence ratio demonstrates that the left domain of combustion chamber is richer

in fuel than that of the right counterpart. Meanwhile, the side view of central plane of the cylinder reveals lowered mixture inhomogeneity with slightly higher equivalence ratio observed at the piston region as a consequence of piston wetting. The combustion mode of the GDI engine is, therefore, more accurately characterised as theoretically homogeneous or quasi-homogeneous due to the inevitable mixture stratification to a certain extent near the event of SI.

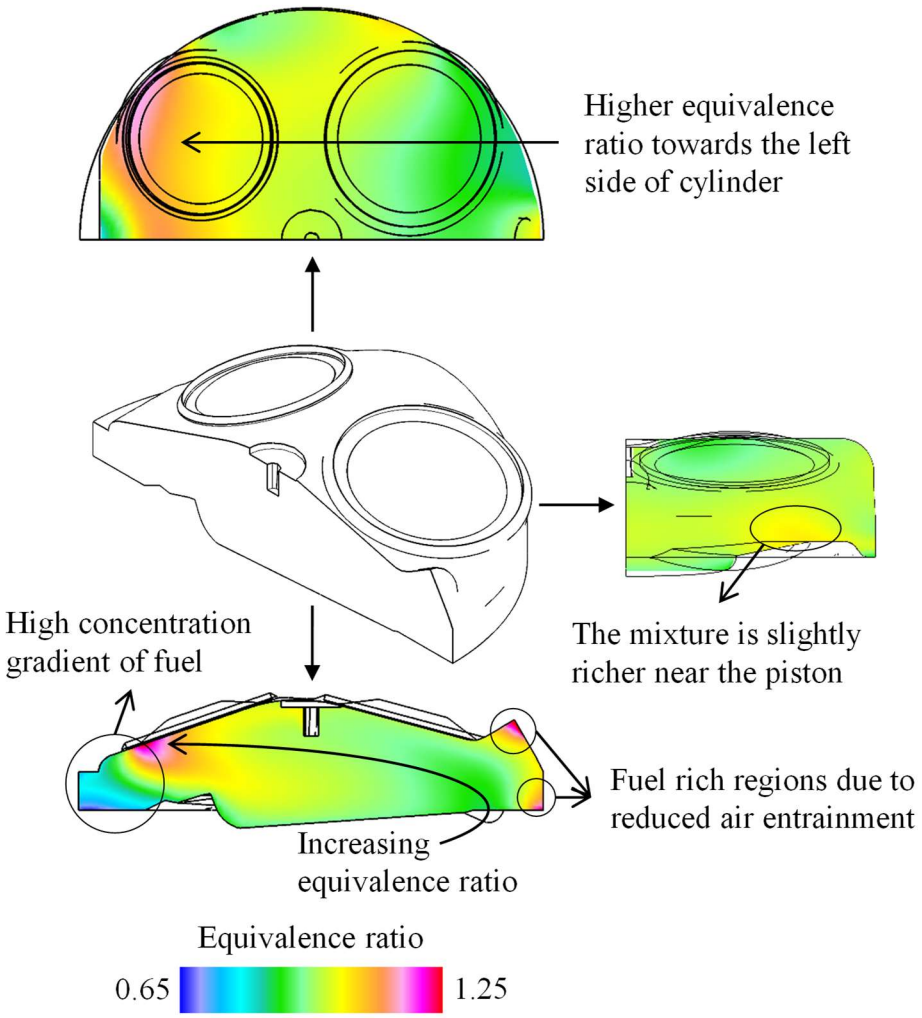


Figure 7-9 In-cylinder distributions of equivalence ratio across three cross-sectional planes at SI timing.

At SI timing, the spark plug is activated, thus initiating flame kernel formation and development from the central point of the cylinder. In-cylinder spatial distributions of temperature and mass fractions of key species pertinent to soot formation at 5 CAD after SI are displayed in Figure 7-10. Production of OH radicals in Figure 7-10(b) is enclosed within the temperature boundary of approximately 900–1000 K. The H_2O_2

reaction loop proposed by Kuwahara and Ando [256] is critical in the initiation of thermal ignition. The loop becomes active when OH radical formation from the decomposition of H_2O_2, H_2O_2 (+ M) = OH + OH (+ M) dominates at about 950 K. At the thermal-ignition range when the temperature is higher than 1500 K, OH radicals are mainly contributed by the hydrogen-oxygen system, $H + O_2 = O + OH$. The spatial contours of high-temperature core and OH radicals serve as good indicators of flame front development and propagation.

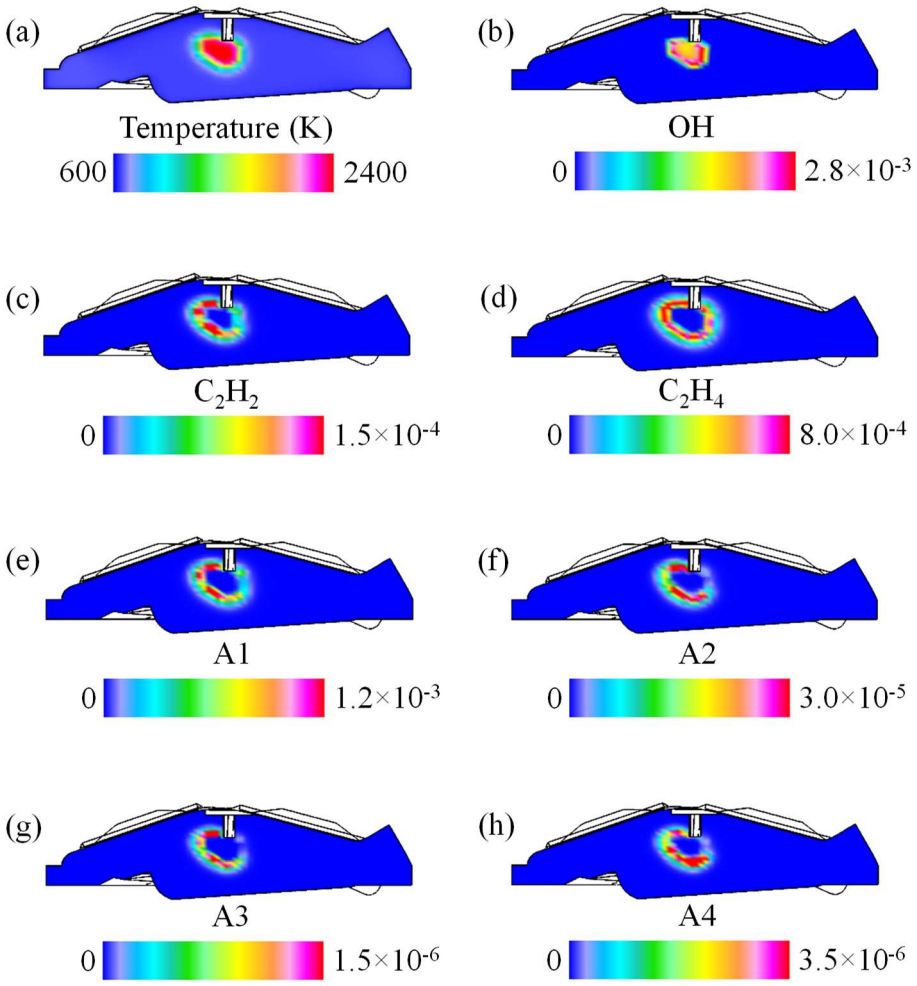


Figure 7-10 In-cylinder distributions of (a) temperature, mass fractions of (b) OH radicals, (c) C_2H_2, (d) C_2H_4, (e) A1, (f) A2, (g) A3 and (h) A4 at 5 CAD after SI.

As seen in Figure 7-10(c)–(h), speciation profiles of C_2H_2, C_2H_4, A1, A2, A3 and A4 possess the similar ring-like distributions surrounding the high-temperature core with slight differences in the temperature boundary where the species formation begins. Similar observation was reported by An et al. [257] with different spatial distributions due to varied orientation of the spark plug and direction of flame propagation. The

distribution of C_2H_2 is larger than that of C_2H_4 as C_2H_4 undergoes oxidation by OH radicals and simultaneous decomposition to generate C_2H_2. C_2H_2 contributes to the formation of A1 primarily through $C_4H_5 + C_2H_2 = A1 + H$. C_2H_2 also aids in the HACA mechanism to build up larger PAH from A1 up to A4. Consequently, there is an accumulated amount of A4 produced at the bottom region in Figure 7-10(h) which depletes C_2H_2 and smaller PAH within the same region.

Increasing A4 concentration promotes molecular collisions between the precursors, thus giving rise to nascent soot particles. The net soot production becomes detectable at approximately 19 CAD after SI as depicted in Figure 7-11. At the instant, the flame has spread halfway through the combustion chamber with the highest temperature of 2600 K. Both C_2H_2 and A4 form around the high-temperature core at about 1000–2000 K. The concentration of A4 is significantly lower than that of C_2H_2 since it is the precursor species for particle nucleation. As shown in Figure 7-11(e) and (f), the distribution of soot cloud somewhat resembles those of C_2H_2 and A4 with slightly wider coverage on the left side of cylinder, thus suggesting the consumption of the two species in soot formation.

Moreover, soot is mainly generated on the left side of cylinder which can be attributed to the fuel-rich zones resulting from imperfect mixing as corroborated by Figure 7-9. At the same time, high number density and mass density of soot near the piston surface are potentially the undesirable outcome of direct carbonisation of remaining liquid fuel droplets shown in Figure 7-8. The number density and mass density distributions appear to be highly similar as this is the early phase of soot formation with vigorous particle nucleation. The abundance of C_2H_2 reflects relatively low surface growth rate at the current stage.

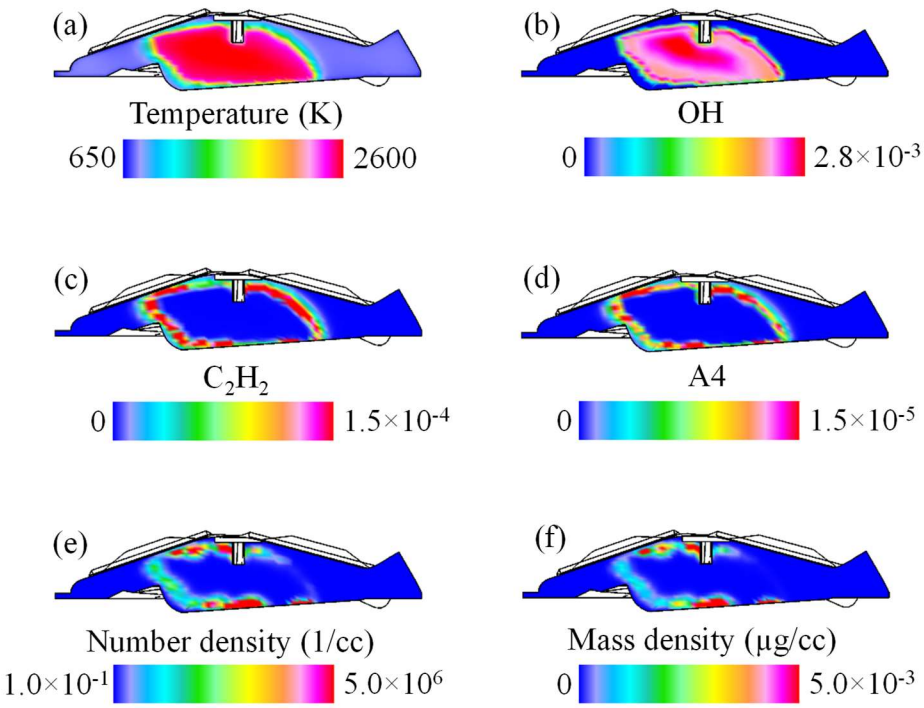


Figure 7-11 In-cylinder distributions of (a) temperature, mass fractions of (b) OH radicals, (c) C_2H_2 and (d) A4, (e) number density and (f) mass density of soot at 19 CAD after SI.

Production and consumption of C_2H_2 and A4 are represented by the changes in mass as a function of CAD in Figure 7-12(a) while the resulting particle number and soot mass are plotted in Figure 7-12(b). The maximum mass of C_2H_2 formed is higher than that of A4 by nearly a factor of four. Besides, C_2H_2 reaches its peak value earlier than A4 by approximately 11 CAD. This is because C_2H_2 contributes to formation and growth of large PAH including A4. Soot particles nucleate and grow in number and mass along with increasing mass of C_2H_2 and A4. It is noteworthy that soot peaks to its maximum mass earlier than reaching its highest particle number by 12 CAD. This is coherent with the aforementioned observation that the peak mass of C_2H_2 is attained earlier as compared to that of A4. Thus, the increase in soot mass is caused by the surface growth of high amount of C_2H_2 whereas particle number is controlled by the availability of A4 acting as the soot precursor.

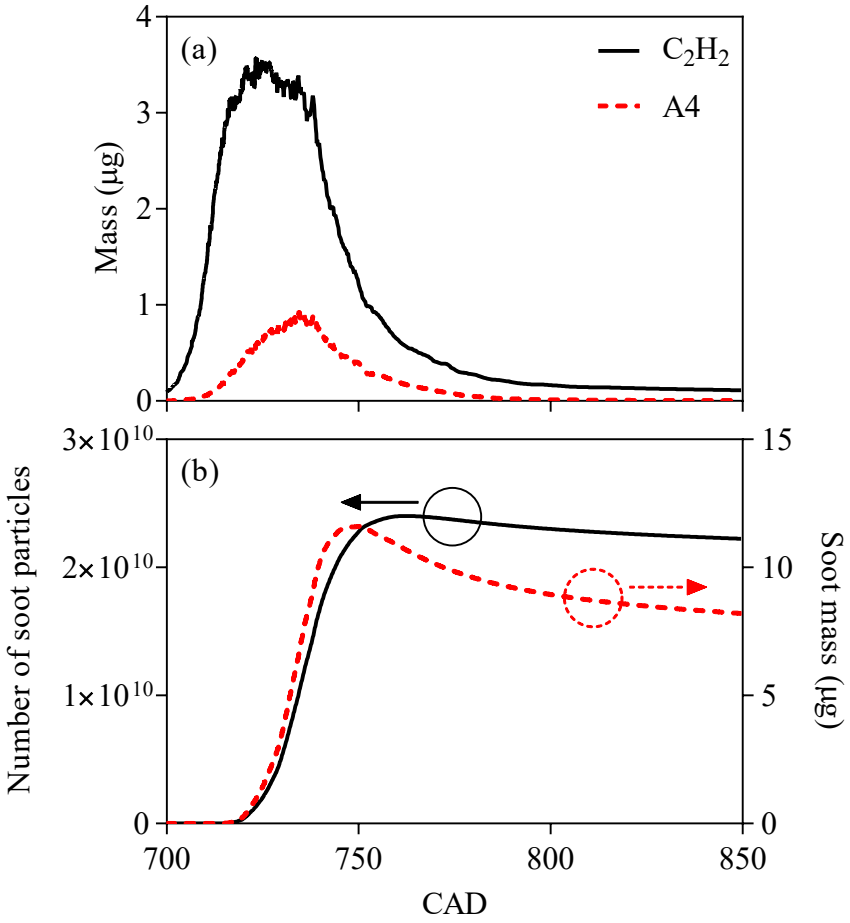


Figure 7-12 In-cylinder (a) mass of C_2H_2 and A4 and (b) number of soot particles and soot mass as a function of CAD.

Figure 7-13 to Figure 7-15 illustrate the temporal evolutions of spatial distributions of temperature, mass fractions of OH radicals, C_2H_2 and A4, number density and mass density of soot within the cylinder from 40 CAD to 80 CAD after SI. At 40 CAD after SI, the flame almost spreads throughout the entire combustion chamber with the core reaching 2800 K. C_2H_2 and A4 are distributed around the cylinder peripheries, surrounding the high-temperature core. Likewise, high mass fraction of A4 is located at regions where the temperatures are 900–2000 K. Regions of high number density and mass density of soot coincide with those having high concentrations of A4 and C_2H_2.

At 60 CAD after SI, it is apparent that C_2H_2 and A4 have been mainly consumed. The consumption of A4 is more rapid as it is used for nucleation and PAH condensation on the soot particles. The residues are found only at the near-wall regions where the

temperatures are lower than 800 K, thus hindering any potential particle inception and growth. With reduced mass fractions of C_2H_2 and A4, soot oxidation becomes the dominant mechanism to decrease particle number and size, thus lowering the overall mass. Particularly, effective oxidation takes place under in-cylinder conditions of high temperature and large OH radical concentration. Hence, number density and mass density of soot increase moving away from the central region of cylinder. Moreover, as shown by the circled zones in Figure 7-14(e) and Figure 7-15(e), the decline in soot number density is associated directly to the high-temperature region with copious OH radicals.

Towards 80 CAD after SI, the core temperature within the cylinder drops to 2300 K. Despite the high OH radical mass fraction at the back of cylinder depicted in Figure 7-15(b), there is no marked cutback on soot due to the presence of C_2H_2 within the same region. Oxidation by OH radicals and surface growth due to C_2H_2 compete with one another and affect the soot distribution. At the same time, the left-skewed high-temperature region with concentrated OH radicals in Figure 7-15(a)–(b) explains the wider distributions of soot on the right side of cylinder as shown in Figure 7-15(e)–(f). The overall conceptual model detailing the ultra-fine PM processes in the wall-guided GDI engine is portrayed in Figure 7-16, elucidating the roles and contributions of spray formation, mixture preparation, combustion and emission from the integrated point of view of CFD and chemical kinetics.

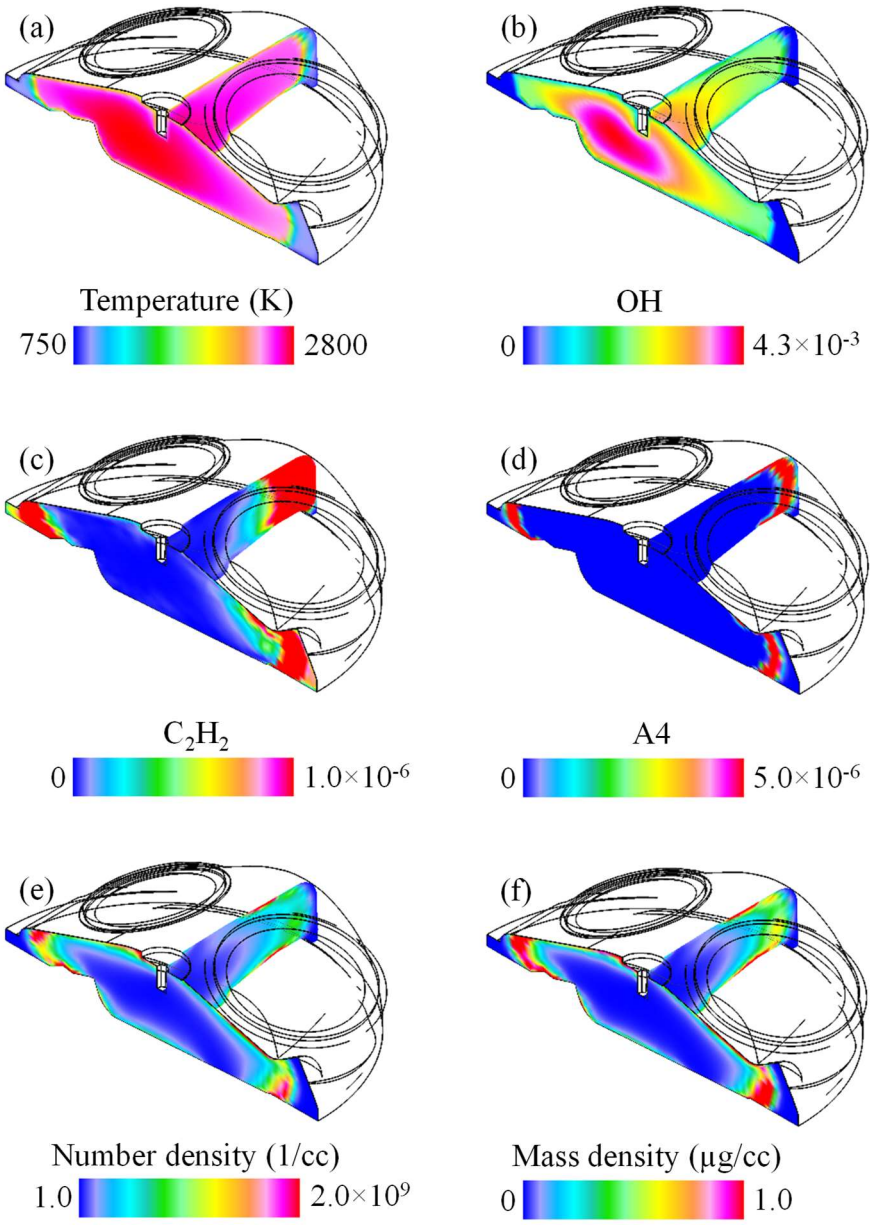


Figure 7-13 In-cylinder distributions of (a) temperature, mass fractions of (b) OH radicals, (c) C_2H_2 and (d) A4, (e) number density and (f) mass density of soot at 40 CAD after SI.

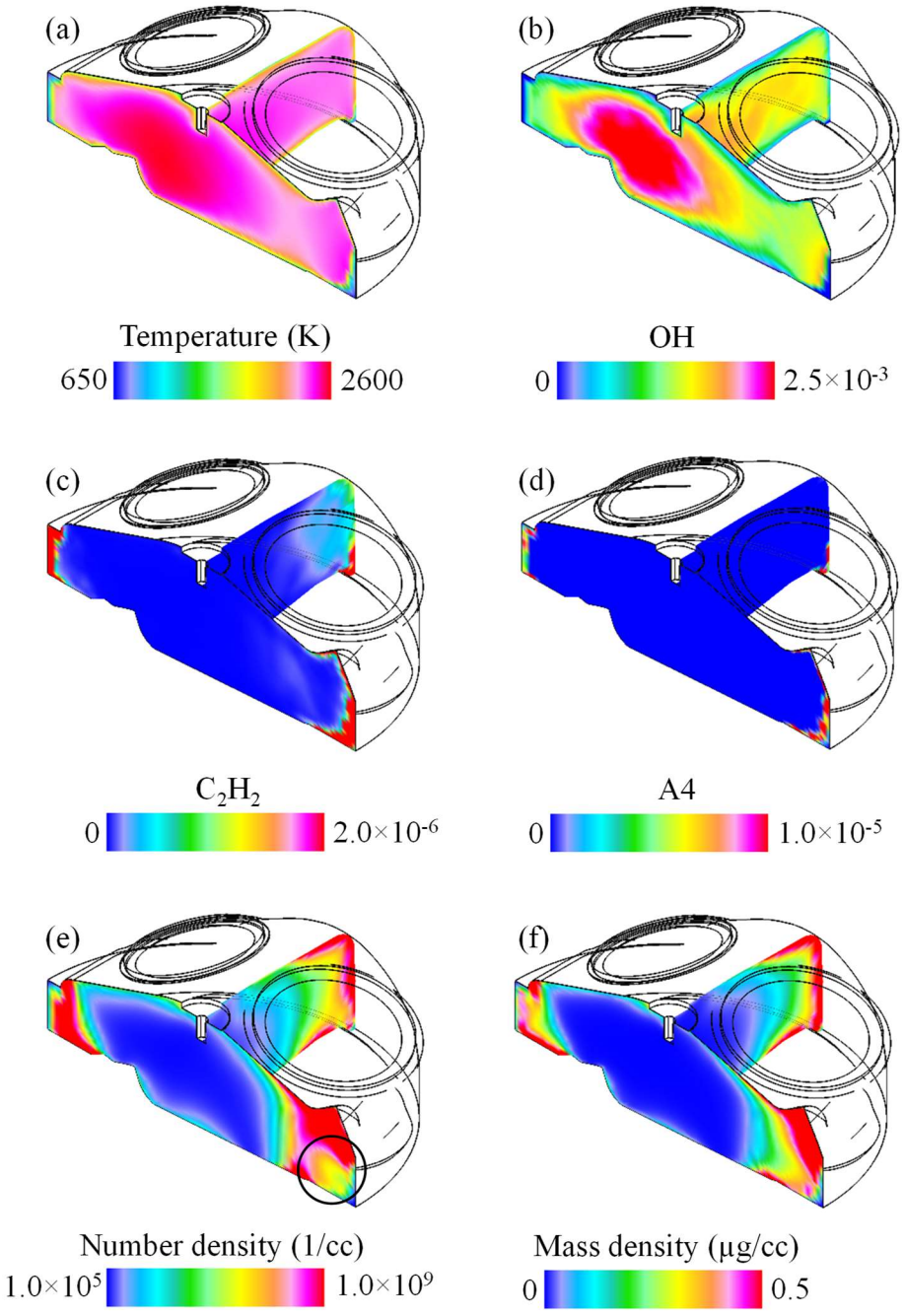


Figure 7-14 In-cylinder distributions of (a) temperature, mass fractions of (b) OH radicals, (c) C_2H_2 and (d) A4, (e) number density and (f) mass density of soot at 60 CAD after SI.

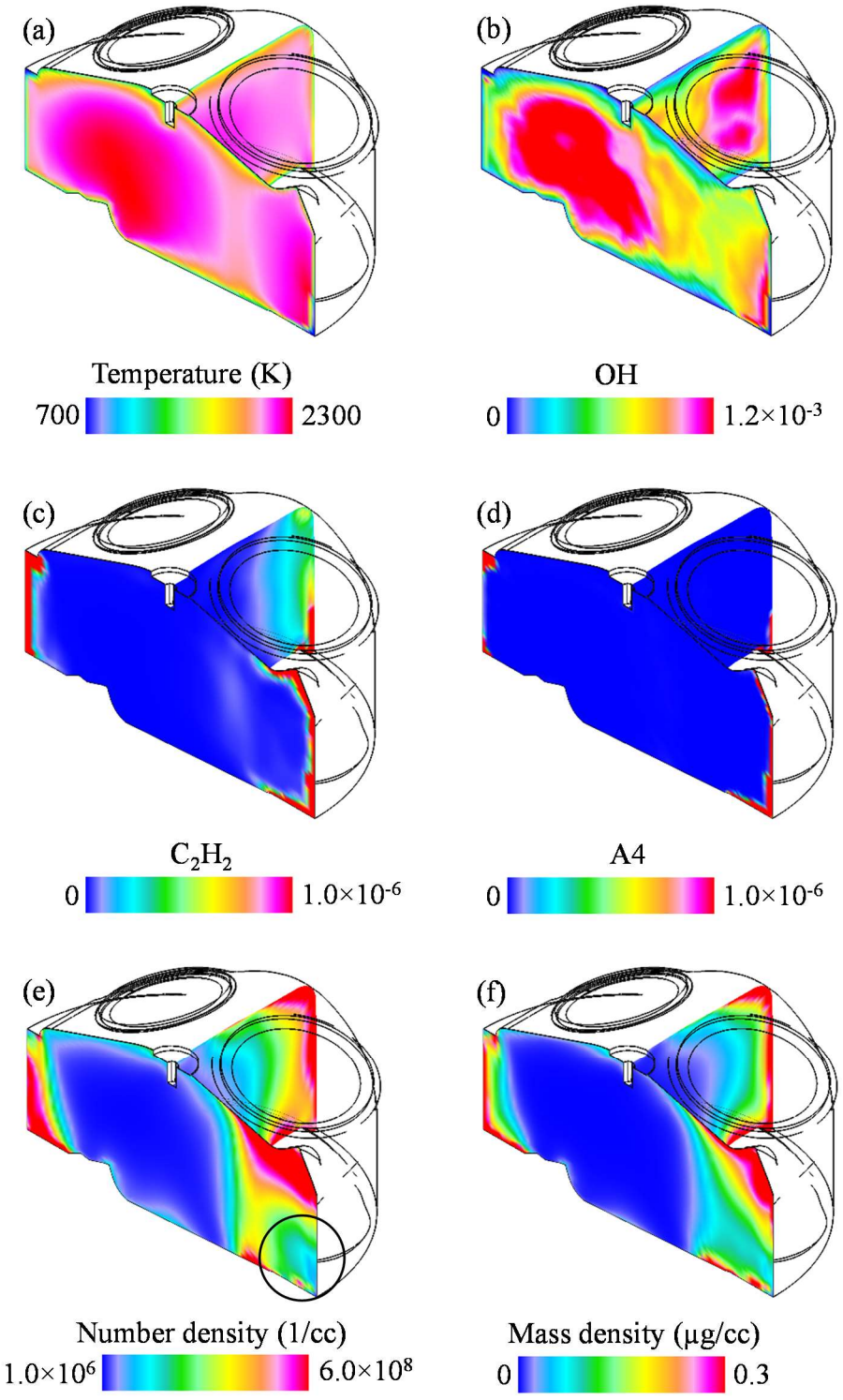


Figure 7-15 In-cylinder distributions of (a) temperature, mass fractions of (b) OH radicals, (c) C_2H_2 and (d) A4, (e) number density and (f) mass density of soot at 80 CAD after SI.

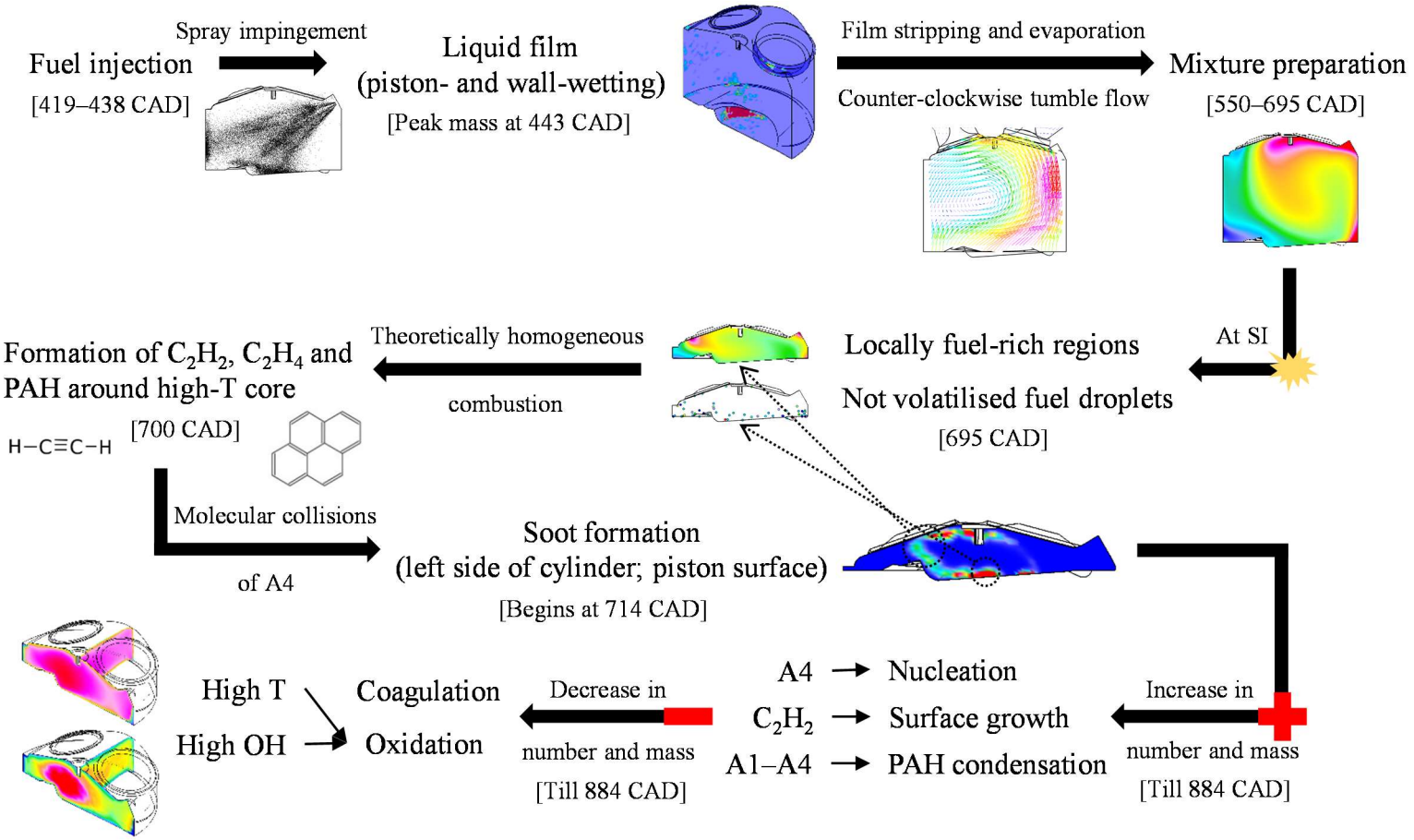


Figure 7-16 Conceptual model describing the ultra-fine PM processes in the wall-guided GDI engine.

The conceptual model identifies the dominant mechanisms of ultra-fine PM formation within GDI engines operating under homogeneous stoichiometric mode which covers a significant portion of the speed-load operating map (see Figure 1-2). Previous soot modelling studies focussing on stratified charge operations [63,173,182] postulated that liquid fuel films on the wall surfaces persist up to the event of SI and associated the secondary fuel evaporation with potential pool fires as the main contributor to PM emissions. This is primarily attributed to the insufficient mixing time as fuel is injected late during the compression stroke.

The present study distinguishes the contributing role of liquid films when the engine operates in quasi-homogeneous mode. Owing to advanced fuel injection during the intake stroke, liquid films generally disintegrate completely by SI timing. The fuel-rich pockets formed through the earlier film stripping are transported within the flow field. Consequently, in-cylinder mixture distribution features local stratifications in which these fuel-rich regions act as the source of PM formation. The level of mixture inhomogeneity depends on the amount and residence time of the liquid films. Though to a lesser extent, direct carbonisation of liquid fuel droplets which are not volatilised at SI timing to PM is also captured accordingly.

The modelling work described here employs an up-to-date selection of A4 as the soot precursor as opposed to the traditional C_2H_2 [176] and fuel vapour [175]. Unlike the over-simplistic soot models [181,183] which only consider nucleation and oxidation of soot particles, major phases of surface growth, condensation and coagulation are taken into account in the present approach. Importantly, temporal development and spatial distributions of critical species and soot based on the in-cylinder conditions concur with the numerical findings reported [175,179,180] in general. As compared to those adopting the method of moments [179,180], the sectional method reproduces the overall trend of experimentally observed PSDF of soot numerically with better agreement retained at the low-diameter range. This, thus, provides confidence in the computational results of soot emissions, particularly when ultra-fine PM is the main consideration.

7.3 Effect of SOI Timing on PM Emissions

Injection timing of fuel is one of the crucial operating parameters in determining the engine combustion and emission behaviours. The manner in which SOI timing affects in-cylinder mixture formation and preparation is twofold [258]:

i. Despite longer air-fuel mixing time, early SOI leads to intense spray-wall impingement, thus resulting in high mass of liquid fuel film deposited.
ii. Late SOI, on the other hand, reduces the available mixing time before SI, thus hindering the attainment of homogenous state of air-fuel charge.

The effect of SOI timing on PM emissions in the wall-guided GDI engine is hence examined by advancing and retarding the SOI timing of the reference case at 59 CAD ATDC during the intake stroke by 20 CAD as tabulated in Table 7-1. The remaining operating parameters are kept constant as those reported for 2300-90.

Table 7-1 Parametric sweep of SOI timing at engine speed of 2300 rpm and engine load of 90 N m.

Case	SOI-39	SOI-59	SOI-79
SOI timing (CAD ATDC*)	39	59	79
	◄——— advancing		retarding ———►

* During the intake stroke.

Formation and development of spray profiles at different SOI timings are represented through in-cylinder distributions of fuel droplets injected depicted in Figure 7-17 from 10 CAD to 30 CAD after SOI. From Figure 7-17(a)(i)–(c)(ii), fuel impingement on piston crown particularly is more critical as the SOI timing is advanced due to closer position of the piston to the fuel injector. This is supported by the breakdown of film mass in Figure 7-18 in which liquid film found on the piston at 10 CAD after SOI for SOI-79 is negligible. Across the SOI timings, piston wetting dominates the formation of liquid film at 20 CAD after SOI and beyond. Fuel droplets impact the combustion dome at early CAD after SOI at retarded SOI timing for SOI-79 whereas liquid film deposited on dome for SOI-39 is noticed later at 40 CAD after SOI as shown in Figure 7-18. This is because the established tumble flow at retarded SOI timing interacts with the incoming fuel stream and directs the fuel droplets towards the dome.

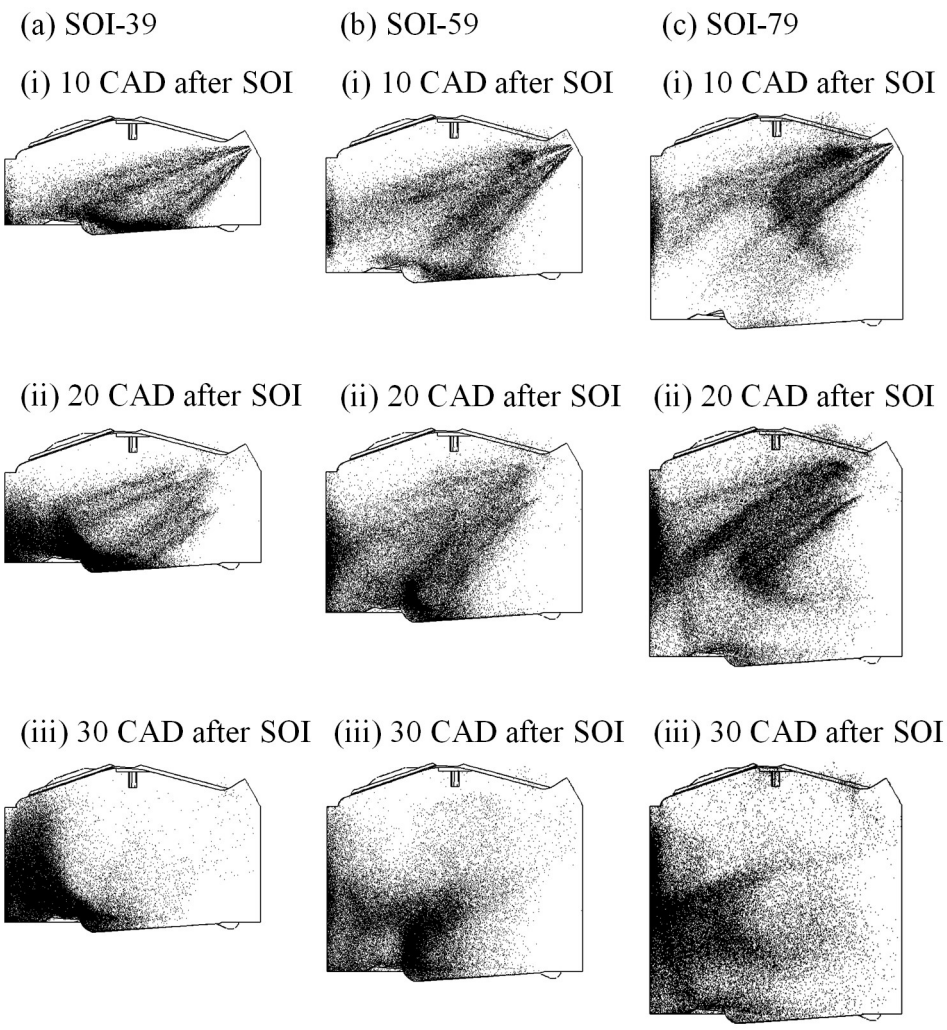


Figure 7-17 In-cylinder distributions of fuel droplets injected for SOI timings at (a) 39 CAD, (b) 59 CAD and (c) 79 CAD ATDC at (i) 10 CAD, (ii) 20 CAD and (iii) 30 CAD after SOI.

From Figure 7-19, the maximum liquid film mass for SOI-39 is higher than those for SOI-59 and SOI-79 by 44% and 26%, respectively as a result of advancing SOI timing. As expected, early SOI causes early liquid film formation to its peak mass. At the same time, it is associated with early film disintegration through film stripping and evaporation. This, in turn, provides sufficient time for the fuel-rich charge near the liquid film to mix homogenously with air. At the CAD with the maximum film mass for SOI-79, the film mass for SOI-39 and SOI-59 has dropped by approximately 98% and 88% from their respective peak values. Despite reduced spray-wall impingement, retarded SOI timing prolongs the residence time for liquid film which deteriorates the subsequent mixture preparation.

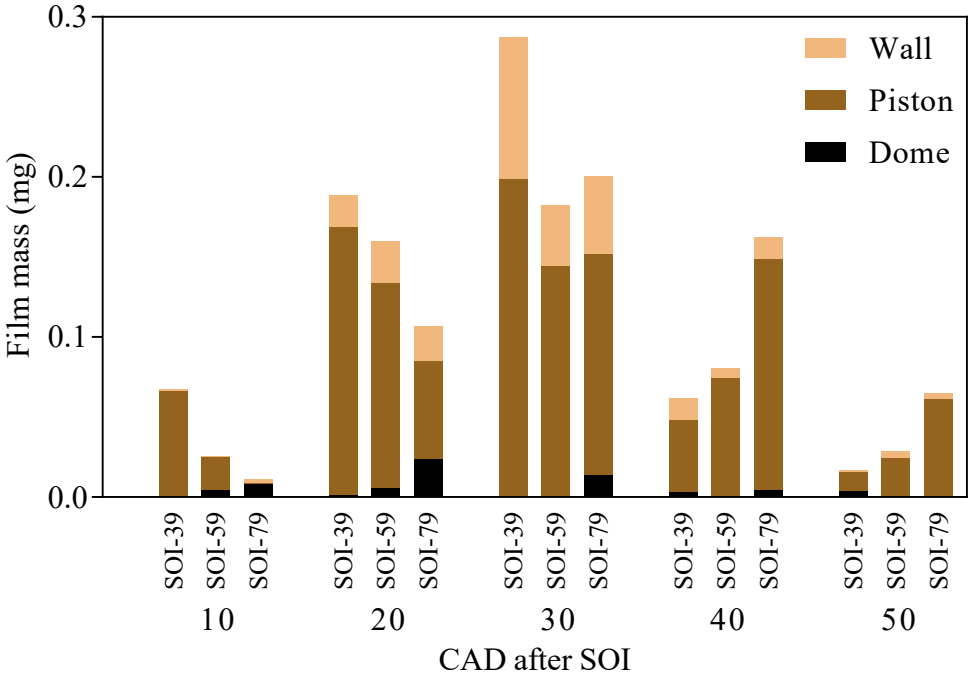


Figure 7-18 Proportions of total film mass formed on combustion dome, piston crown and cylinder wall as a function of CAD after SOI for different SOI timings.

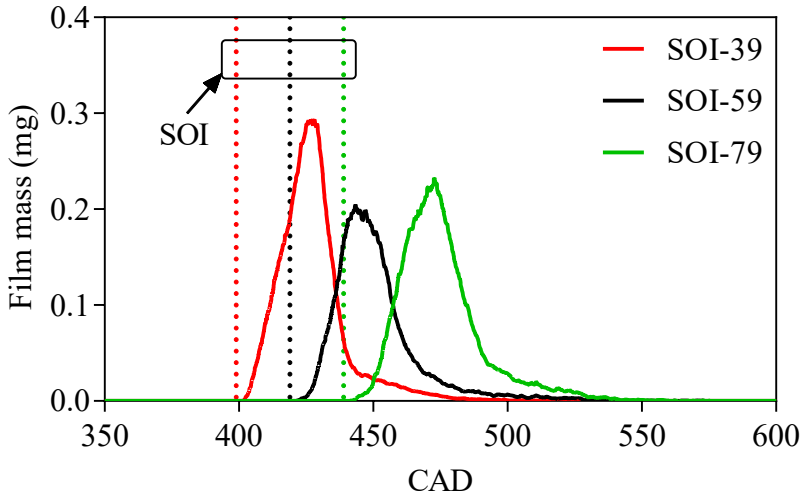


Figure 7-19 Total mass of liquid fuel film formed within the cylinder as a function of CAD for different SOI timings.

The variations in in-cylinder distribution of equivalence ratio at SI timing due to the changes in SOI timing is shown in Figure 7-20, along with the remaining fuel droplets which are not volatilised. Uniformity of air-fuel mixture distribution clearly improves

as SOI timings are advanced from 79 CAD to 39 CAD ATDC. Due to the insufficient mixing time for SOI-79, the in-cylinder mixture exhibits relatively higher level of local stratification whereby the fuel-rich region near the right wall has an equivalence ratio as high as two. Furthermore, the number of fuel droplets present up to the event of SI increases at retarded SOI timings. This is also attributed to the shorter mixing time in which the droplets originating from fuel injection and film stripping fail to evaporate completely before the spark initiation.

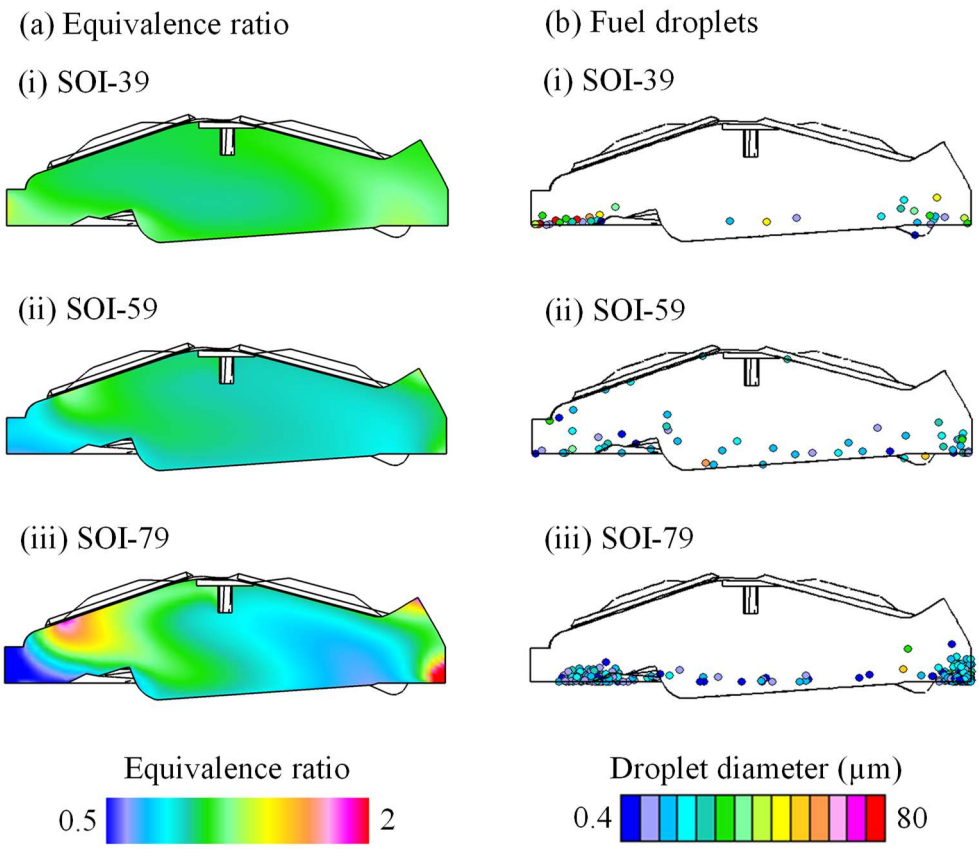


Figure 7-20 In-cylinder distributions of (a) equivalence ratio and (b) fuel droplets coloured by their diameters at SI timing for SOI timings at (i) 39 CAD, (ii) 59 CAD and (iii) 79 CAD ATDC.

As seen in Figure 7-21, retarding the SOI timing from 59 CAD to 79 CAD ATDC does not induce distinct differences in in-cylinder pressure and temperature curves. However, peak pressure increases by about 18% while an increment of 103 K in peak temperature is observed when the SOI timing is advanced to 39 CAD ATDC. This is because better mixture homogeneity for SOI-39 shown in Figure 7-20(a)(i) allows complete combustion upon SI. In terms of C_2H_2 production plotted in Figure 7-22, the

highest peak mass is associated with SOI-39, followed by SOI-79 and then SOI-59. The trend is, however, inconsistent with the A4 formation in which the peak mass increases with retarding SOI timings. The maximum mass of A4 for SOI-79 is higher than those of earlier SOI by 25%. Apart from the contribution of C_2H_2, formation and growth of large PAH rely heavily on the presence of fuel-rich condition which is caused by retarding the SOI timing.

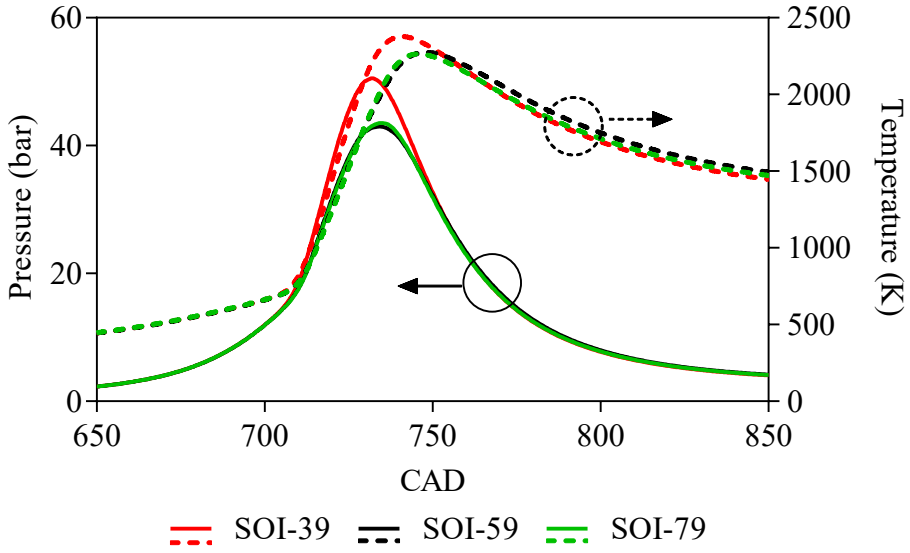


Figure 7-21 In-cylinder pressures and temperatures for different SOI timings.

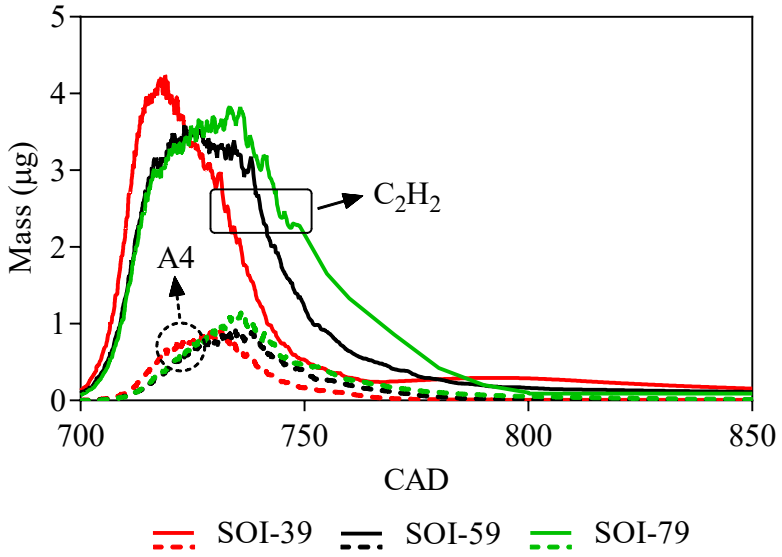


Figure 7-22 In-cylinder mass of C_2H_2 and A4 as a function of CAD for different SOI timings.

From Figure 7-23, advancing the SOI timing to 39 CAD ATDC increases soot number density by 13% and mass density by a factor of 1.5 at EVO. The slight increase can be attributed to the higher peak temperature and increased amount of C_2H_2 for SOI-39 which promote nucleation and surface growth of soot particles. On the other hand, number density increases by 78% while mass density is scaled up by a factor of three as the SOI timing is retarded to 79 CAD ATDC. The presence of fuel-rich regions with a high degree of mixture stratification, combined with the remaining liquid fuel droplets, at SI timing is the prime contributor in the drastic spike of soot at later SOI.

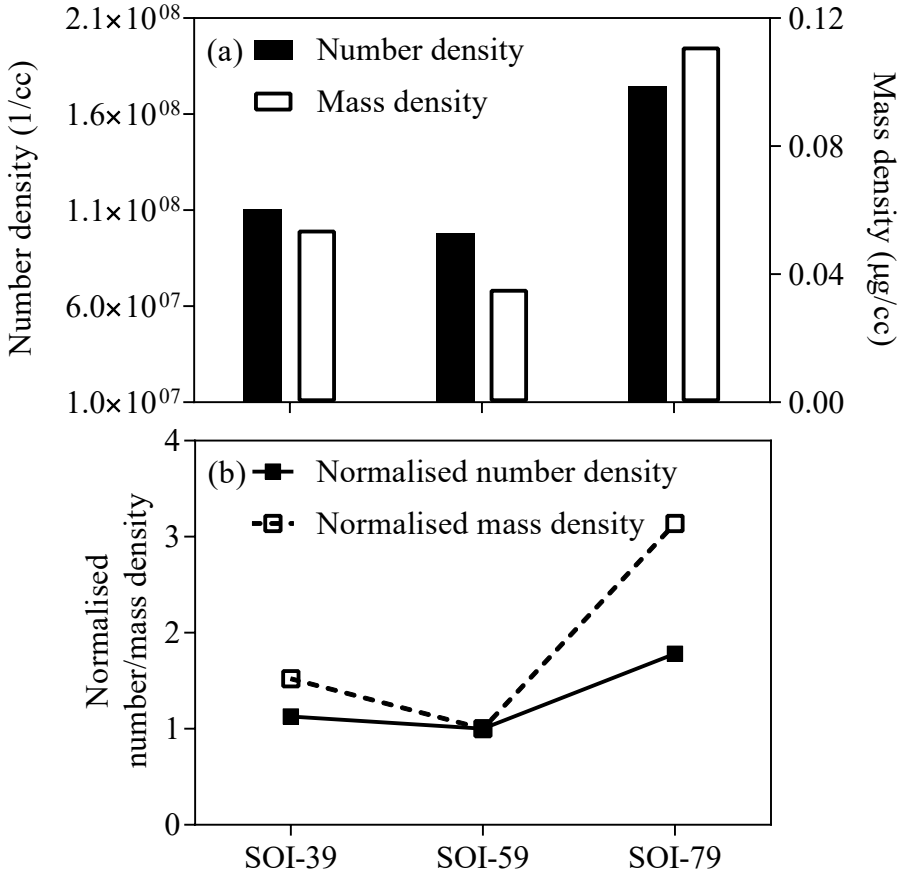


Figure 7-23 (a) Number density and mass density of soot at EVO timing and (b) their normalised values based on the reference case for different SOI timings.

To summarise, varying SOI timings of fuel necessitates a trade-off between prolonged mixing time and reduced spray impingement to minimise PM emissions. From Figure 7-23, it can be deduced that mixing time defined as the interval between EOI and SI timings is the key component to achieve homogenous combustion in the GDI engine.

Despite severe piston and wall wetting, injecting fuel earlier provides sufficient time for liquid film stripping, evaporation and fuel-air mixing to achieve uniform mixture distribution. Longer mixing time also diminishes the number of fuel droplets which are not volatilised by SI timing. These then lead to a more complete combustion, thus resulting in lower amount of PM emitted.

The present study corroborates the role of SOI timing in affecting fuel impingement and fuel-air mixing as inferred by Szybist et al. [259] from their measured filter smoke number across the parametric sweep of SOI. Additionally, several experimental works of GDI engines [258,260–262] reveal the existence of an optimised range of fuel injection window in which advancing or retarding the SOI timing leads to increased number density of soot. The trend is captured in the current simulations as shown in Figure 7-23 whereby the lowest number density is observed when the SOI timing is 59 CAD ATDC. This is comparable to the optimised SOI timing at 60 CAD ATDC reported by Qin et al. [261] who examined PM emissions across SOI timings spanning from 20 CAD to 100 CAD ATDC under the engine speed of 2000 rpm. Sabathil et al. [260] and He et al. [258] found their optimised SOI timings to be slightly retarded at 80 CAD and 69 CAD ATDC, respectively which is potentially due to the lower speed at 1000 rpm.

7.4 Effect of SI Timing on PM Emissions

Ignition timing of in-cylinder combustible mixture governs spark initiation, flame kernel formation and flame front propagation. Varying SI timings influences the preceding fuel-air mixing and the succeeding combustion performance and post-flame behaviours. In a study of pollutant emissions from the first combustion cycle in a GDI engine by Rodriguez and Cheng [263], they alluded that delaying the SI timing beyond TDC of the power stroke causes a sharp decline in the net IMEP and hence, work output of the engine. Thus, the range of SI timings examined is set before the TDC initiating the power stroke to avoid significant deterioration in engine performance. As listed in Table 7-2, the SI timing of the reference case at 25 CAD BTDC is advanced and retarded by 10 CAD while retaining the rest of the operating parameters.

Table 7-2 Parametric sweep of SI timing at engine speed of 2300 rpm and engine load of 90 N m.

Case	SI-35	SI-25	SI-15
SI timing (CAD BTDC*)	35	25	15
	◄——— advancing		retarding ———►

* During the compression stroke.

In-cylinder distributions of equivalence ratio and remaining liquid fuel droplets at all the SI timings examined are illustrated in Figure 7-24. As shown in Figure 7-24(a)(i)–(iii), the mixture distributions are similar across the range of SI timings, featuring a contour of decreasing equivalence ratio from the upper left of cylinder to the bottom right portion. Nevertheless, the effect of SI timing is manifested in magnitudes of the fuel-rich regions. Retarding SI timing extends the fuel-air mixing time which favours the preparation of homogenous charge as same SOI timing is employed consistently. As a result, equivalence ratios of the fuel-rich regions near the exhaust port and right cylinder walls decrease when SI timing is retarded from 35 CAD to 15 CAD BTDC. At the same time, prolonged mixing time at retarded SI timing facilitates the process of fuel evaporation, thus reducing the number of fuel droplets remained as seen in Figure 7-24(b)(i)–(iii).

From Figure 7-25, both peak pressure and peak temperature decrease as the SI timing is retarded. Peak values of pressure and temperature also occur later as expected when the event of SI is postponed with a more obvious delay observed for the temperature. The peak pressures for SI-35 and SI-25 drop by 53% and 37%, respectively when the SI timing is retarded to 15 CAD BTDC for SI-15. Likewise, the maximum in-cylinder temperature is reduced by 20% when the SI timing is changed from 35 CAD to 15 CAD BTDC. It is noted that the in-cylinder temperature approaching EVO for SI-15 towards the end of power stroke is relatively higher as compared to those of advanced SI timings.

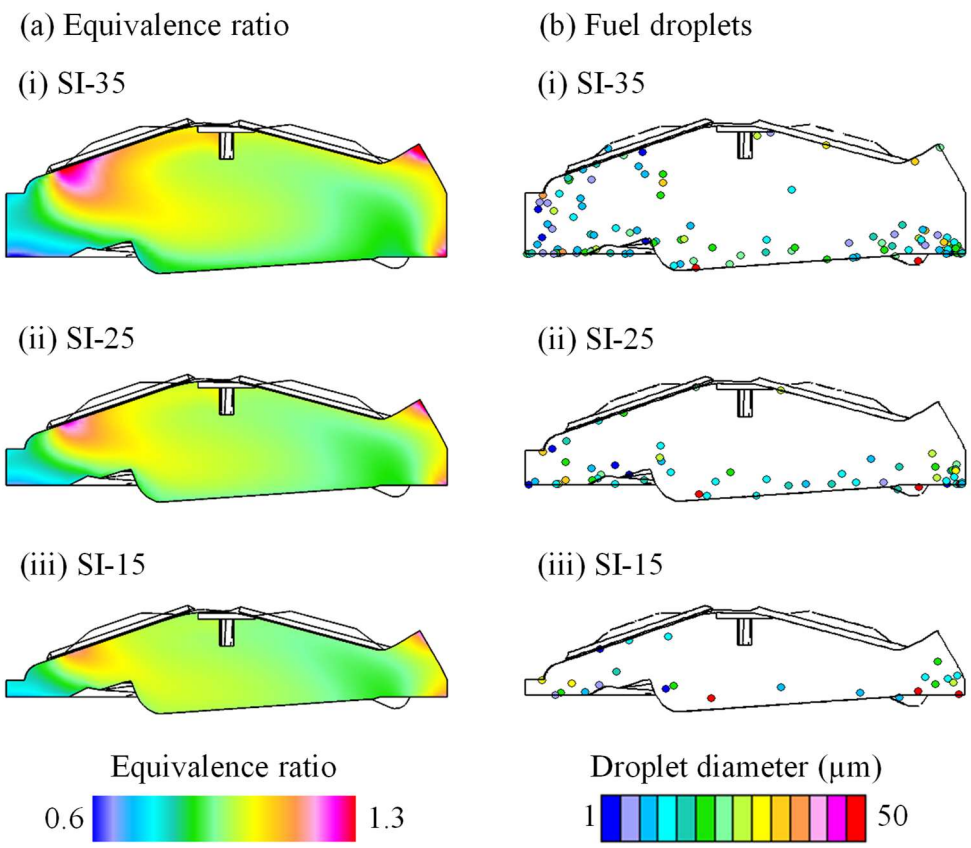


Figure 7-24 In-cylinder distributions of (a) equivalence ratio and (b) fuel droplets coloured by their diameters at SI timings at (i) 35 CAD, (ii) 25 CAD and (iii) 15 CAD BTDC.

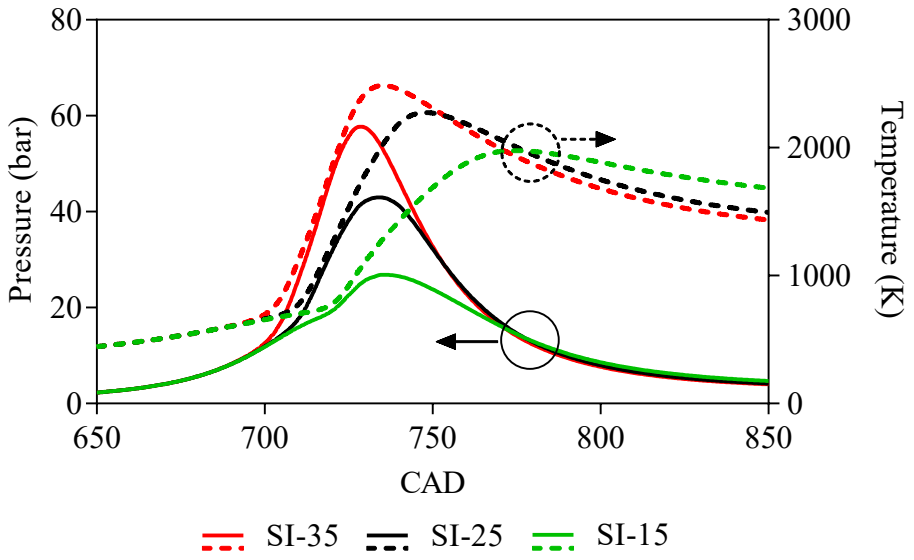


Figure 7-25 In-cylinder pressures and temperatures for different SI timings.

From Figure 7-26, retarding the SI timing delays the production of C_2H_2 and A4 up to their peak values. The maximum in-cylinder mass of C_2H_2 across all the SI timings differs by only 12%. Meanwhile, the maximum mass of A4 at earlier SI timings at 35 CAD and 25 CAD BTDC is approximately 0.9 µg while that for SI-15 is lower by 20% at 0.7 µg. Although the peak masses of these species are relatively close, the speciation profiles exhibit apparent differences during late combustion. Consumption of C_2H_2 at the advanced SI timing at 35 CAD BTDC is very rapid as evidenced by the drastic drop in mass after reaching its peak. When the SI timing is retarded, the consumption of C_2H_2 clearly slows down as the peak mass persists for longer CAD before undergoing a sharp decline. Similar trend across the variations in SI timing is observed for the consumption of A4. By EVO, about 9% of the peak mass of C_2H_2 is left unconsumed for the retarded SI timing at 15 CAD BTDC.

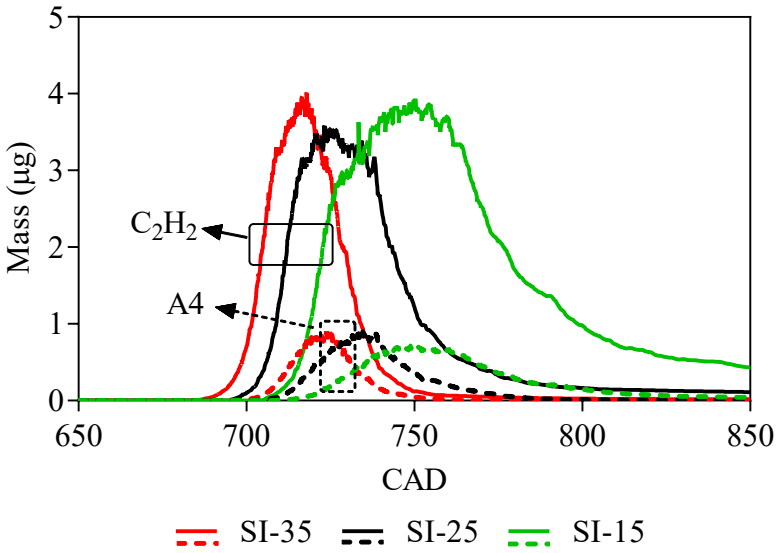


Figure 7-26 In-cylinder mass of C_2H_2 and A4 as a function of CAD for different SI timings.

Inspecting Figure 7-27 reveals the decreasing trend in number density of soot as the SI timing is retarded from SI-35 to SI-15. Mass density, on the other hand, increases slightly going from SI-35 to SI-25, but decreases drastically when the SI timing is further retarded to SI-15. The overall change in number density and mass density by advancing SI timing from 25 CAD BTDC is less than 10% while retarding it to 15 CAD BTDC results in reductions of 65% and 57% in number density and mass density, respectively. At earlier SI, higher in-cylinder temperature, coupled with fuel-

rich regions with larger equivalence ratios, promotes the nucleation of soot particles. Higher peak mass of A4 for SI-35 and SI-25 corresponds to higher number density at the EVO timing.

On the contrary, lower peak temperature at the SI timing at 15 CAD BTDC reduces particle inception as supported by the slower consumption of A4 in Figure 7-26. Also, higher temperature during latter half of the power stroke (beyond 810 CAD) depicted in Figure 7-25 enhances soot oxidation by OH radicals, thus lowering both number density and mass density. Exhaust temperature determined at EVO for SI-15 is larger than those at advanced SI timings by 184–241 K. Given same EVO timing, delaying SI cuts down residence time of soot particles within the cylinder. This is beneficial in preventing further particle formation and growth, thus partly explaining the higher residuals of C_2H_2 and A4 at EVO for SI-15 shown in Figure 7-26.

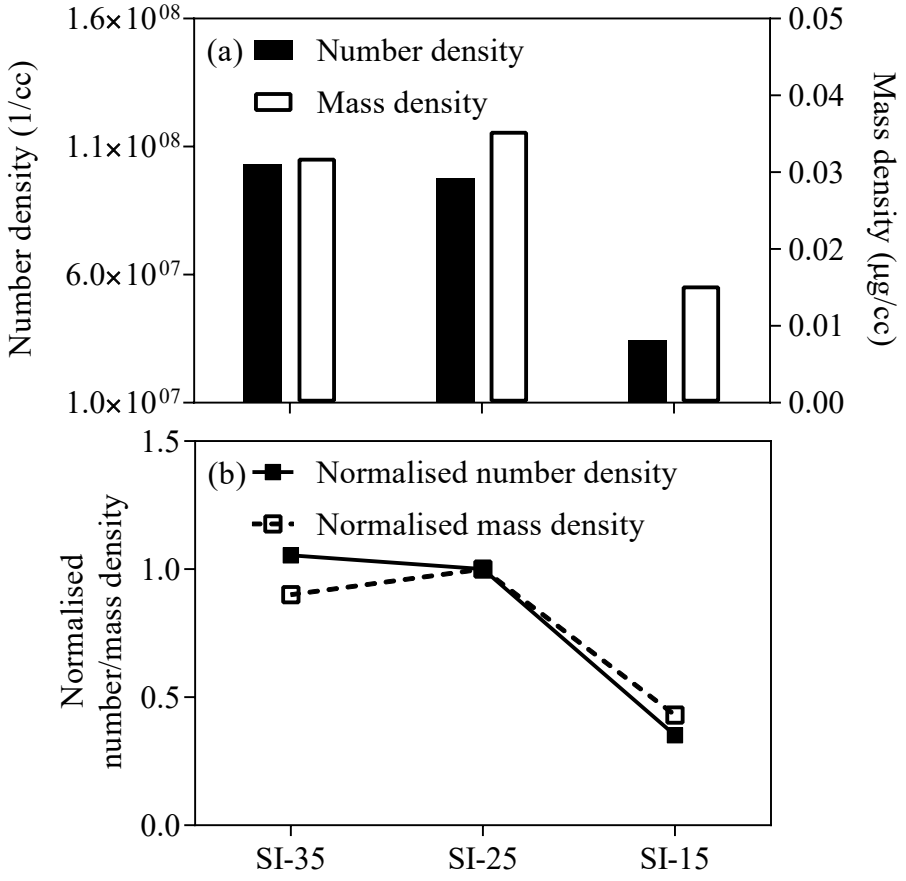


Figure 7-27 (a) Number density and mass density of soot at EVO timing and (b) their normalised values based on the reference case for different SI timings.

Selection of SI timing decides the available time for fuel-air mixing and the residence time of soot particles. Delaying the event of SI lengthens the mixing time to improve mixture homogeneity, thus reducing the fuel-rich pockets by the time ignition begins. Furthermore, shortened residence time of soot minimises the likelihood of further nucleation and particle growth. Higher in-cylinder exhaust temperature also leads to increased soot oxidation rate. Therefore, reduction in PM emissions can be achieved by retarding SI timing. Care should, however, be exercised to avoid retarding the SI timing excessively (over TDC of the power stroke) so as not to compromise the engine performance severely.

In general, the effect of SI timing on number density of soot reported in the present numerical study agrees with the experimental findings [18,258,261,264]. However, the sensitivity of the parameter on number density varies across the experiments. He et al. [258] suggested the low impact of SI timing on PM emissions as the average change in number density is about 20% throughout the range of SI timings of 18–28 CAD BTDC. Meanwhile, the work by Qin et al. [261] demonstrated a decrease of 62% in number density when the SI timing is retarded from 38 CAD to 18 CAD BTDC at 2000 rpm which is comparable to the present study. The low sensitivity of SI timing in the study of He et al. [258] may be attributed to the limited range investigated and lower engine speed at 1000 rpm.

7.5 Effect of EGR Rate on PM Emissions

EGR is defined as the percentage of mass flow rate of recirculated exhaust gas to the total mass flow rate of fresh air and recirculated exhaust gas. By recycling a fraction of exhaust gas back to the intake system where it mixes with fresh air before entering the combustion chamber, EGR acts as a diluent in the unburned gas mixture and lowers the peak combustion temperature in the cylinder [265]. Significant reductions in regulated pollutant emissions including CO and NO have been observed in GDI combustion systems utilising EGR [266,267]. To examine the effect of EGR on PM emissions, it is hence applied at two different rates of 5% and 10% to the current GDI engine as tabulated in Table 7-3 without altering the operating parameters of the reference case.

Table 7-3 Parametric sweep of EGR rate at engine speed of 2300 rpm and engine load of 90 N m.

Case	EGR-0	EGR-5	EGR-10
EGR rate (%)	0	5	10
	increasing ⟶		

Introducing EGR into the cylinder lowers the amount of oxygen delivered from the intake port as depicted in Figure 7-28. EGR rates at 5% and 10% reduce the available mass of oxygen after IVC by 5% and 10%, correspondingly. After the event of SI, the combustion initiates as evidenced by the drastic drop in the mass of fuel and oxygen. It is observed that the rate of fuel decomposition and oxygen consumption declines when the EGR rate is increased to 10%. In terms of spray impingement, the processes of fuel deposition to form liquid film and fuel stripping for evaporation are similar across different EGR rates as shown in Figure 7-29 due to identical injection timing and in-cylinder conditions. However, the maximum film mass is higher with EGR by 8–10% than that without EGR.

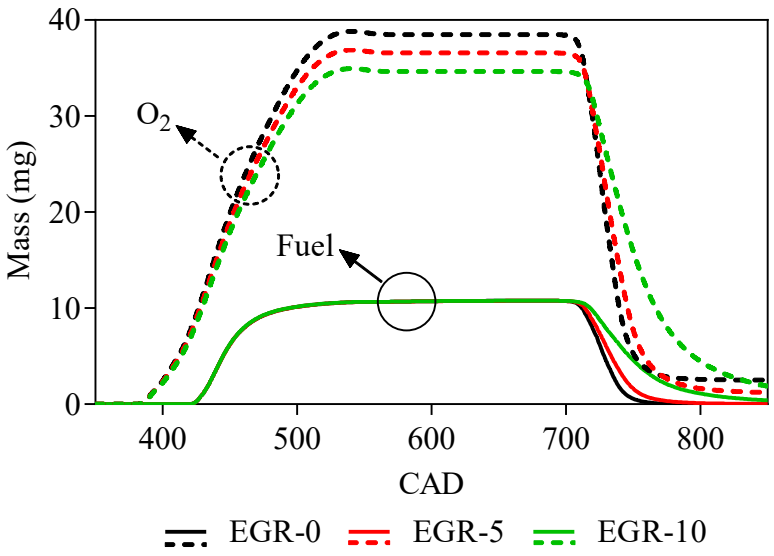


Figure 7-28 In-cylinder mass of fuel and oxygen as a function of CAD for different EGR rates.

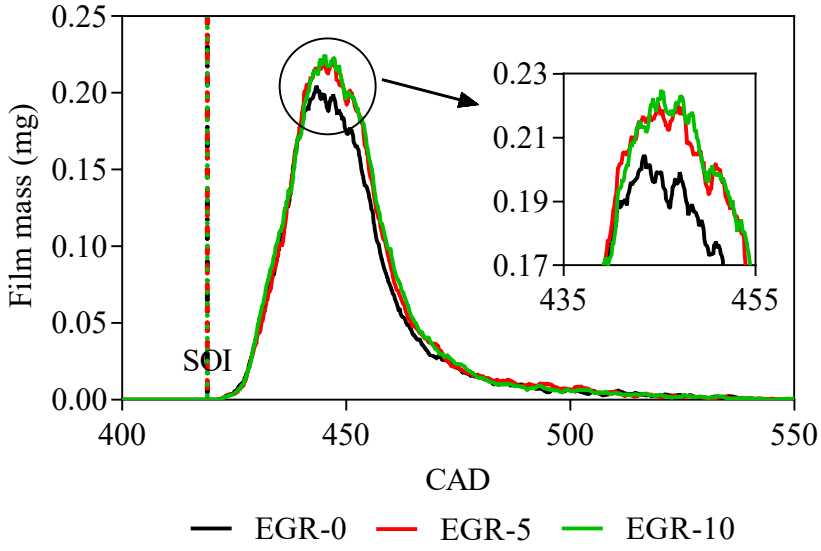


Figure 7-29 Total mass of liquid fuel film formed within the cylinder as a function of CAD for different EGR rates.

Figure 7-30 illustrates in-cylinder distributions of equivalence ratio and liquid fuel droplets present at SI timing for different EGR rates. Spatial distributions of fuel-rich and fuel-lean regions as seen in Figure 7-30(a)(i)–(iii) are alike across the cases with an overall increase in equivalence ratio when the EGR rate becomes higher. This is primarily attributed to the lower oxygen intake shown in Figure 7-28 at higher EGR rate while the similar amount of fuel is injected. A few experimental works on engines with EGR systems demonstrated that global [268] and local [269] equivalence ratios both increase with increasing rate of EGR applied. On the other hand, EGR does not significantly impact the fuel vaporisation characteristics. There is no obvious change in the amount of fuel droplets which remain not volatilised by SI timing as shown in Figure 7-30(b)(i)–(iii).

When EGR is introduced and increased from 5% to 10%, both in-cylinder pressures and temperatures decrease accordingly as plotted in Figure 7-31. EGR rates at 5% and 10% lower peak pressures by 16% and 36%, respectively as compared to that at which no EGR is utilised. Peak temperature decreases by 173 K when the EGR rate is 5% and undergoes a further reduction of 374 K when the EGR rate reaches 10%. The peak temperature is effectively reduced by 24% going from EGR-0 to EGR-10. Moreover, the delay in the occurrence of peak temperature as EGR rate is increased indicates lower rate of combustion as highlighted previously in Figure 7-28.

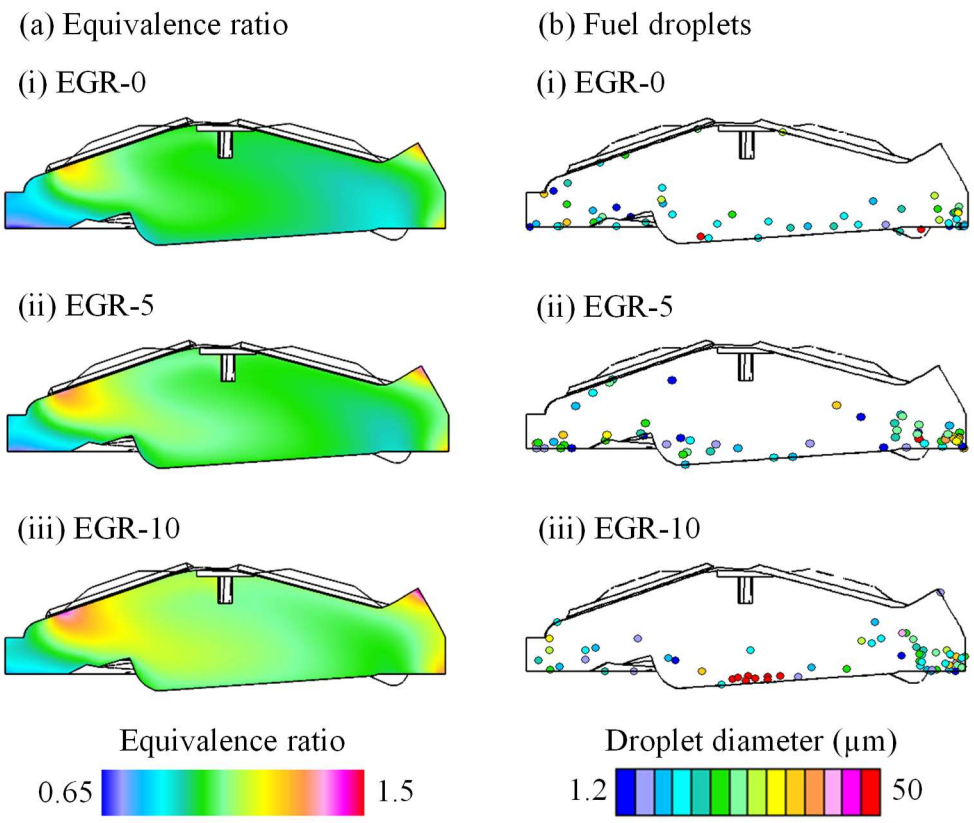


Figure 7-30 In-cylinder distributions of (a) equivalence ratio and (b) fuel droplets coloured by their diameters at SI timing for EGR rates at (i) 0%, (ii) 5% and (iii) 10%.

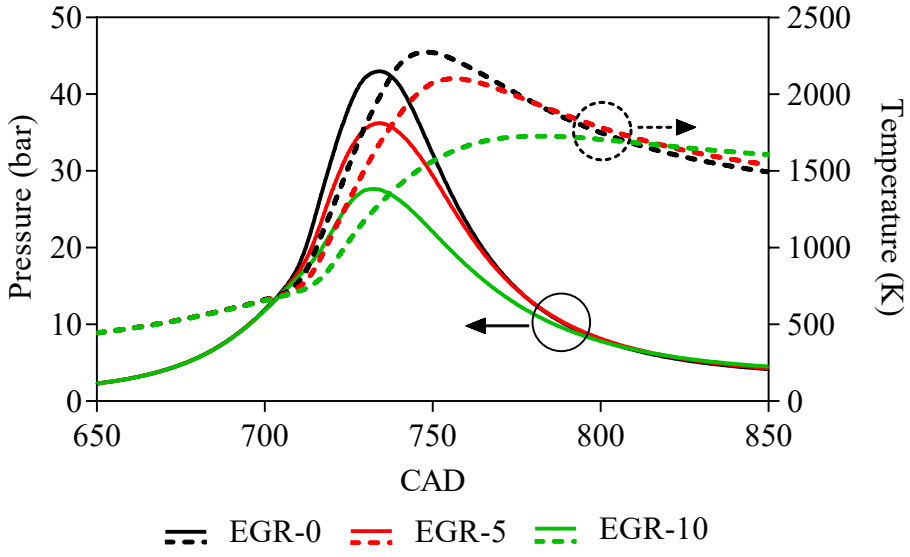


Figure 7-31 In-cylinder pressures and temperatures for different EGR rates.

Varying EGR rate has a profound influence on speciation profiles of C_2H_2 and A4 as displayed in Figure 7-32. Initial production rates of both species across all the EGR

rates are similar up to their respective peak values. When EGR is utilised, peak mass of C_2H_2 and A4 increases with a remarkably higher degree of increment observed for C_2H_2. Moving from EGR-0 to EGR-10, the maximum mass of C_2H_2 achieved is larger by a factor of 1.6 while that of A4 increases by a factor of 1.1. The continual increase in species mass at higher EGR rates leading to larger peak values reflects diminished species consumption rate. Slow depletion of both C_2H_2 and A4 eventually results in higher amount of residue at the instance of EVO. For the EGR rate at 10%, about 47% of the peak mass of C_2H_2 and 27% of the peak mass of A4 remain unconsumed by the EVO timing.

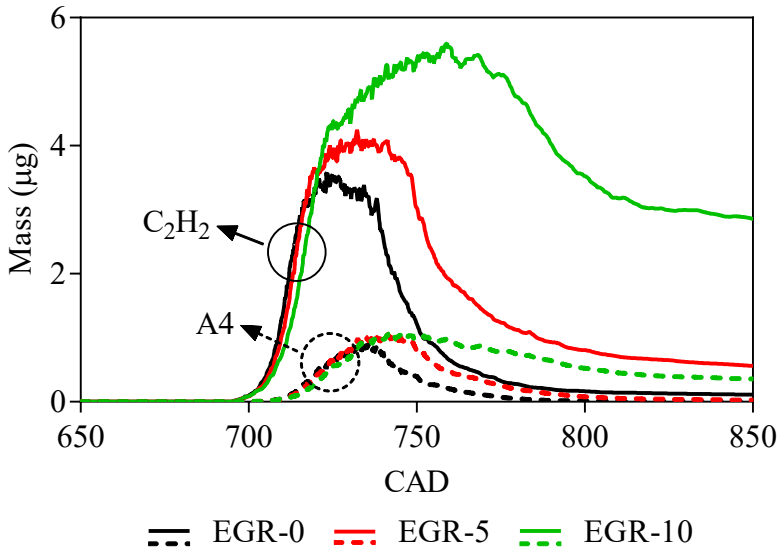


Figure 7-32 In-cylinder mass of C_2H_2 and A4 as a function of CAD for different EGR rates.

The effect of applying EGR on number density and mass density of soot is represented graphically in Figure 7-33, along with the respective normalised values based on the reference case. Reduction in particle number of soot becomes effective when EGR is introduced at a rate of 10% whereby number density decreases by 24%. Lower EGR rate of 5% scales up number density by approximately 20%. This is mainly associated with the peak combustion temperatures as plotted in Figure 7-31. The significantly lowered in-cylinder temperatures for EGR-10 are unfavourable for soot formation despite the higher equivalence ratios observed. Furthermore, soot oxidation by OH

radicals is enhanced for EGR-10 as the exhaust temperature is higher by 99 K and 144 K than those for EGR-5 and EGR-0, respectively.

Likewise, mass density increases when the rate of EGR is first applied at 5% and then decreases when it is amplified to 10%. However, it is noted that at both EGR rates, mass density spikes up by a factor of nearly two as compared to that when no EGR is utilised. The increase in soot mass under EGR conditions can be largely related to the abundance of C_2H_2 displayed in Figure 7-32 which facilitates surface growth of the particles. Discordant trends in number density and mass density due to the presence of EGR may imply higher contribution of C_2H_2 and A4 towards surface growth and PAH condensation instead of particle inception. Consequently, there is an increase in mass density for EGR-10 despite the apparent decline in number density.

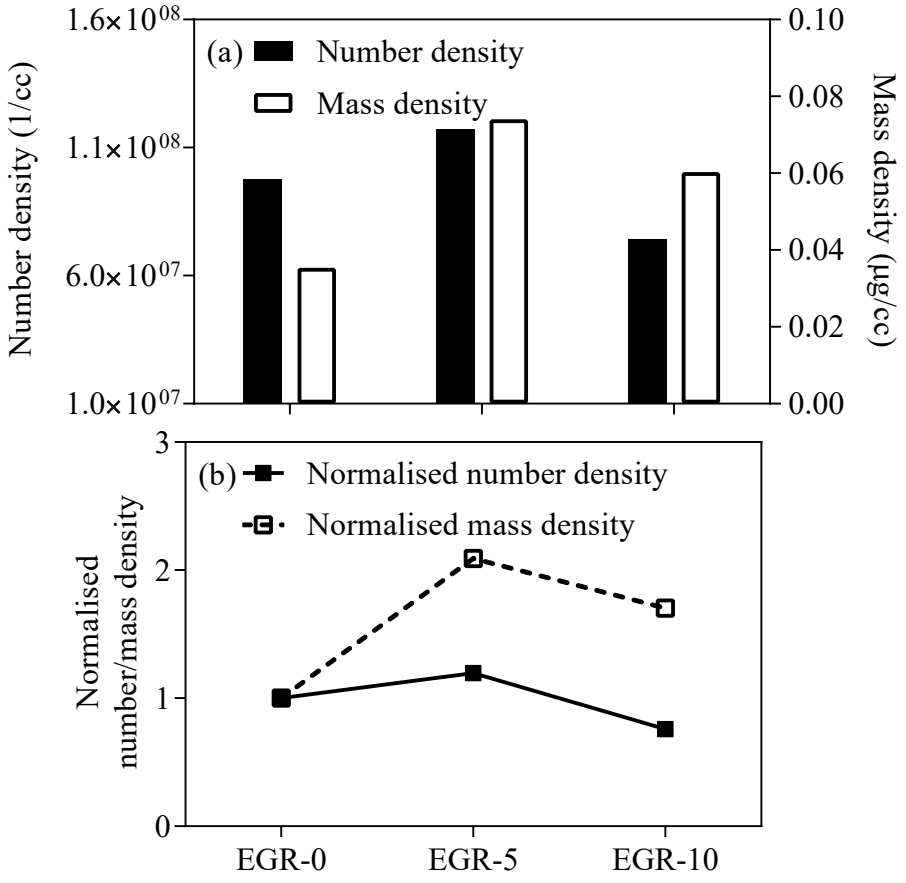


Figure 7-33 (a) Number density and mass density of soot at EVO timing and (b) their normalised values based on the reference case for different EGR rates.

In essence, EGR induces higher equivalence ratio within the cylinder as a result of lowered oxygen intake. The connection of fuel-rich condition to elevated level of soot formation is, however, overridden by low combustion temperature provided by EGR. Lower in-cylinder temperature effectively restrains generation of soot particles from precursor species, thus leading to reduced number density when the EGR rate is 10%. In contrast, low temperature towards the end of power stroke deteriorates the post-flame oxidation. Thus, along with the high availability of surface growth species, the competition between particle growth and oxidation is likely to benefit the former as the cycle approaches EVO. This is manifested in the rise in mass density when EGR is introduced to the combustion system.

Contrasting effects of EGR on PM emissions are reported in numerous experimental studies on GDI engines [249,260,270–272]. The observed increase in number density with increasing EGR rates [260,271] is attributed to reduced exhaust temperature which is detrimental to post-flame oxidation. On the other hand, lower combustion temperature at higher EGR rate is postulated to cause decreased number density [270] and mass density [249,270]. Li et al. [272] demonstrated that EGR rates influence the number density distinctly at different SOI timings and linked the variations to gas temperature. The role of in-cylinder temperature at varied EGR rates is affirmed in the present study. Hence, to reduce PM emissions with EGR, the temperature needs to be low enough to suppress particle inception, but high enough to support particle oxidation.

7.6 Concluding Remarks

The conceptual model describing the ultra-fine PM processes in the wall-guided GDI engine is proposed based on the integrated CFD-chemical kinetic modelling approach. Two major sources of PM formation are identified as the presence of fuel-rich regions and the remaining liquid fuel droplets which are not volatilised. Imperfect mixture preparation can be traced back to fuel impingement on dome, piston and wall which forms liquid fuel film. Film stripping and continuous fuel evaporation then create fuel-rich pockets in the cylinder. As a result of counter-clockwise tumble flow, in-cylinder equivalence ratio distribution at SI timing features an increasing contour from bottom right to upper left of the cylinder, along with the residual fuel droplets.

Due to the mixture inhomogeneity, combustion mode in the GDI engine is more accurately termed theoretically homogenous combustion. Flame propagation from the central point of ignition is characterised by high-temperature core (up to 2800 K) and high concentration of OH radicals. Meanwhile, C_2H_2, C_2H_4 and PAH (A1–A4) are distributed around the high-temperature core. Soot clouds become visible at 19 CAD after SI at the left and bottom portions of cylinder. Nucleation from A4 and particle growth through HACA mechanism and PAH condensation proceed with simultaneous oxidation by oxygen and OH radicals. Eventually, post-flame oxidation of particles dominates under high-temperature conditions with abundant OH radicals up to EVO.

Based on the conceptual model, the effects of SOI timing, SI timing and EGR rate on PM emissions are examined. Varying SOI timing entails the compromise between longer mixing time and lower fuel impingement. Sufficient mixing time turns out to be very crucial to improve mixture homogeneity and reduce amount of PM emitted. Delaying the optimal SOI timing by 20 CAD results in a 78% increase in number density and a threefold increase in mass density. PM control strategy can benefit from retarding SI timing as it prolongs the mixing time and shortens the soot residence time. A delay of 10 CAD from the SI timing at 25 CAD BTDC reduces number density and mass density by 65% and 57%, respectively.

EGR suppresses combustion temperature, thus rendering the in-cylinder condition unfavourable for PM formation despite the overall increase in equivalence ratio. For the EGR rate at 10%, a drop of 547 K in peak temperature decreases number density by 24%. However, mass density increases by a factor of 1.7 due to the high availability of particle growth species. The effects of operating parameters on number density and mass density are represented in Figure 7-34 which ranks their sensitivities on PM emissions in the following descending order: SOI timing, SI timing and EGR rate. Key changes in in-cylinder conditions contributing to PM emissions with respect to the variations in operating parameters are also summarised in Table 7-4.

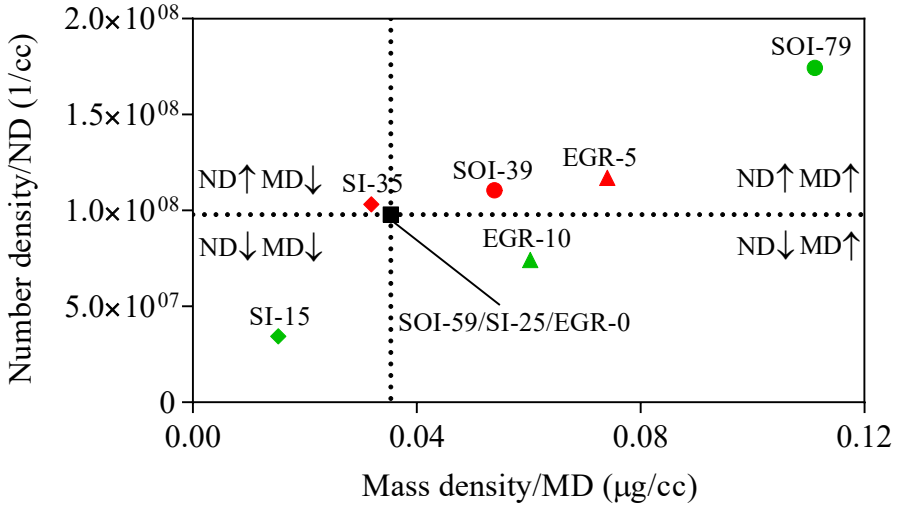


Figure 7-34 Effects of operating parameters on number density and mass density of soot segregated into four zones based on an increase or a decrease.

Table 7-4 Summary of key changes in in-cylinder conditions contributing to PM emissions with respect to the variations in operating parameters.

Operating parameter	SOI timing		SI timing		EGR rate
Variation	←	→	←	→	↑
Mixing time	↑	↓	↓	↑	—
Mixture homogeneity at SI	↑	↓	↓	↑	↓
Fuel droplets at SI	↓	↑	↑	↓	—
Peak temperature	↑	—	↑	↓	↓
Soot residence time	—	—	↑	↓	—
Soot number density	↑	↑	↑	↓	↓
Soot mass density	↑	↑	↓	↓	↑

CHAPTER 8
CONCLUSIONS AND FUTURE WORK

8.1 Conclusions

In the present work reported, a fundamental conceptual model detailing the ultra-fine PM processes within the GDI engine operating under the homogenous stoichiometric mode is developed through CFD modelling with direct integration of fuel chemical kinetics. Within this context, reduced TRF mechanisms serving as gasoline surrogates are evaluated thoroughly under pre-established validation criteria and operating conditions pertinent to GDI engines. To model various in-cylinder events, a complete set of CFD sub-models is formulated with the focus on the Detailed Chemistry model and the sectional method. Engine modelling is then validated against the experimental measurements of in-cylinder pressure curve, number density and mass density of PM. In addition, fidelity of the numerical approach is retained across varied engine speeds and loads. Based on the insights derived from the conceptual model, effects of the engine operating parameters on PM emissions are investigated numerically.

8.1.1 Evaluation of TRF Mechanisms for Application in GDI Engines

Given the nature of spark-ignited engines, high-temperature chemistry (> 900 K) is of paramount importance to describe both SI and combustion processes. During the high-temperature combustion, in-cylinder pressures of the wall-guided engine range from 30 bar to 50 bar. The homogenous stoichiometric combustion indicates that the main equivalence ratio of interest is unity. However, fuel-rich conditions with equivalence ratios reaching up to two are taken into account for the relevance in soot formation. These operating conditions act as the validation criteria to evaluate the applicability of reduced TRF mechanisms in the GDI engine.

The validation targets are ID, laminar flame speed and speciation profiles measured across ST, flame configurations and JSR, prioritising those involving real fuels and multi-component surrogates. While all the mechanisms generally exhibit reasonable agreement in ID predictions, significant quantitative deviations in computations of flame speed and speciation are seen for some. The rationale behind the discrepancies

among the mechanisms is exemplified through the chemical kinetic analyses carried out at critical operating points in which the main findings are summarised as follows.

i. Fuel ignition is initiated and sustained by chain branching of H_2O_2 and H-abstractions from fuel species and alkyl radicals. Reactions opposing the system reactivity consist of chain terminations of HO_2 and alkyl radicals. The under-prediction of 31% in ID time of RD387 by Wang-TRF at 55 bar and 1000 K is potentially attributed to the overestimation in toluene reactivity. It is evidenced by the positive contributions from formation of alkoxy benzyl radicals which are not captured by the other mechanisms.
ii. Flame speed is determined as the outcome of competing reactions which either generate H (higher speed) or consume H (lower speed). The reactions showing high sensitivity primarily involve the chemistry of H, OH radicals and small hydrocarbon species. Particularly, neglecting some of the inhibiting reaction pathways in Jiao-TRF over-predicts the stoichiometric flame speed of CR-87 at 353 K and 500 K by 32% and 25%, respectively.
iii. In the rich premixed n-heptane flame, the net production of A1 depends on the rates of reversible conversion between A1 and A1- through free active radicals of H, CH_3, OH and O. The magnitude of ROP of A1 for Jiao-TRF directly explains the under-prediction in A1 mole fraction up to 83%. Conversely, the A1-promoting reactions related to toluene are likely the cause of higher A1 concentrations computed by Wang-TRF at HAB larger than 0.4 cm. So, the role of aromatic-specific reactions in Wang-TRF may be over-emphasised in the flame of the non-aromatic fuel.

8.1.2 Integrated CFD-Chemical Kinetic Modelling of GDI Engines

The whole panoply of in-cylinder events of turbulence, spray, fuel impingement, liquid film formation, SI, combustion, flame propagation and PM emissions are modelled numerically by a complete set of CFD sub-models. Under spray condition within the static vessel, the KH-RT model reproduces the spray tip penetration length accurately within a margin of error of 1 mm. Importance of the multi-component TRF surrogate to emulate the gasoline fuel is highlighted as using neat isooctane lowers computed soot number density and mass density by five orders of magnitude due to the absence of aromatics. Through the Detailed Chemistry model, chemical kinetics

from An-TRF is incorporated to describe combustion and flame propagation. Under the DMZ partitioning method, flow variables proposed to segregate the cell groups are temperature, mixture fraction, enthalpy and mass fraction of H. Formation, growth and oxidation of soot particles are computed by the sectional method through both collisional and chemical source terms.

The modelling approach is implemented and validated across the operations map in which the engine speed changes from 1600 rpm to 3000 rpm while the torque is varied from 60 N m to 120 N m. At different speed-load points, in-cylinder pressures are replicated with the highest deviation of 1.5% in their peak values. Computed number density and mass density of soot particles stay within the same order of magnitude as the experimental tailpipe measurements. In addition, number-weighted PSDF derived captures the experimental trend of decreasing particle number when the diameter is increased from 10 nm to 100 nm. However, the lower peak of accumulation mode is not reproduced and the normalised PSDF are not sensitive towards speed or load. Key observations made as a result of varying speed and load are:

i. Engine speed essentially controls in-cylinder flow field and time available for mixture preparation. When speed increases, higher flow velocity and stronger mixing intensity promote droplet breakup and vaporisation. The maximum turbulence kinetic energy after fuel injection becomes higher by a factor of 2.4–3.9 at 2300–3000 rpm as compared to that at 1600 rpm. The level of mixture homogeneity at SI timing improves at higher speed with reduced fuel-rich pockets. Consequently, number density of soot at 3000 rpm is lowered by an order of magnitude and mass density decreases by a factor of six from those recorded at lower speeds.
ii. Increasing engine load dictates larger amount of fuel to be injected at higher injection pressure, accompanied by increased pressure at the intake manifold. Collectively, these lead to enhanced spray characteristics of fuel droplets as corroborated by the 33% increase in the maximum turbulence kinetic energy when the torque is raised from 60 N m to 120 N m. By SI timing, fuel-rich regions are located further away from the spark plug as the load increases. Also, the amount of liquid droplets remained clearly decreases. Thus, a drop of an order of magnitude in number density of soot and a 78% decrease in mass density are seen as the load is increased from 60–90 N m to 120 N m.

8.1.3 Conceptual Model for Ultra-Fine PM Processes in GDI Engines

The conceptual model detailing the ultra-fine PM processes within the wall-guided GDI engine is developed under the homogenous stoichiometric mode. It is extracted from the reference case of 2300-90 due to its largest mass density and comparatively high number density of PM. Sequence of the in-cylinder engine phenomena building up to PM emissions is outlined as follows.

i. At the onset of SOI of fuel, intense spray impingement results in formation of liquid film on combustion dome, piston crown and cylinder wall. Piston and wall surfaces are more susceptible to fuel deposition in which piston and wall wetting account for 76% and 20% of the maximum mass of total liquid film formed, respectively.
ii. After EOI, film stripping and evaporation give rise to emergence and growth of fuel-rich regions (equivalence ratios up to 5–6) located close to piston and wall surfaces. Through continuous mixing, there is an apparent reduction in number of fuel droplets and local equivalence ratios.
iii. Given the nature of tumble flow in counter-clockwise direction within the cylinder, the fuel-rich pockets are transported upwards towards the spark plug when the cycle approaches the end of compression stroke.
iv. At SI timing, spatial distribution of the leaner bottom right piston region to the richer upper left exhaust port region (equivalence ratio range of 0.65–1.25) is indicative of the mixture inhomogeneity. On top of that, fuel droplets with diameters ranging from 4 μm to 60 μm surviving up to the event of SI are scattered around the piston crown.
v. These represent the two prime contributors to soot formation in the GDI engine. When soot formation becomes noticeable at 19 CAD after SI, spatial distribution of soot clouds on the left side and near the piston conforms to the locations of fuel-rich regions and liquid fuel droplets at SI timing.
vi. Flame propagation is visualised through development of contours of high-temperature core with accelerated concentration of OH radicals. At the same time, species related to surface growth (C_2H_2) and precursors of soot (A1–A4) are distributed around the high-temperature core at about 1000–2000 K.
vii. Speciation profiles of C_2H_2 and A4 in mass exhibit coherent agreement with the temporal development in mass and particle number of soot, respectively.

Thus, the role of C_2H_2 in increasing soot mass and that of A4 as the soot precursor are further reassured.

viii. Conversely, in order to reduce soot particles, post-flame oxidation takes place effectively under the critical in-cylinder conditions of high temperature and large concentration of OH radicals.

8.1.4 Numerical Study on PM Emissions from GDI Engines

Based on the critical operating point for 2300-90, effects of fuel injection timing (SOI timing), ignition timing (SI timing) and level of EGR (EGR rate) on PM emissions are numerically investigated. Benchmarked against experimental measurements from GDI test engines, trends in number emissions of PM are captured qualitatively. The operating parameters are ranked as EGR rate, SI timing and SOI timing according to their increasing sensitivities to PM emissions. Principal results from varying each operating parameter are summarised as follows.

i. Earlier SOI is associated with stronger fuel impingement and increased mass of liquid film formed while later SOI drastically cuts down the mixing time available before SI. These manifest the existence of an optimised range of SOI timings for minimised PM formation. It is found that the role of mixing time is more dominant in supporting homogeneous combustion. Advancing and retarding the optimised SOI timing at 59 CAD ATDC, each by 20 CAD, cause respective increases of 13% and 78% in soot number density.

ii. Selection of SI timing affects in-cylinder mixture preparation mainly through the length of mixing time. Delaying SI timing promotes mixture homogeneity as evidenced by lower local equivalence ratios at SI timing. In addition, soot residence time is shortened to hinder potential nucleation and surface growth. Therefore, retarding the SI timing at 25 CAD BTDC by 10 CAD decreases the soot number density by 65%.

iii. Acting as a diluent, EGR lowers oxygen intake and suppresses in-cylinder combustion temperature. Despite the increase in local equivalence ratios with higher EGR rate, lower peak combustion temperature limits nucleation of soot particles from precursor species. Higher exhaust temperature also aids in soot oxidation by OH radicals. When EGR is applied at the rate of 10%, a reduction

of 24% is observed in number density of soot. This is primarily attributed to the similar 24% decline in peak temperature.

8.2 Future Work

Fuel components from naphthenes, olefins and oxygenates are currently incorporated in reaction mechanisms of gasoline. Applicability of the complex mechanisms in GDI engines should be evaluated, subject to availability of related fundamental combustion experiments. In the present study, the sectional method employed for soot modelling reveals the limitation in capturing the number of particles from accumulation mode in the PSDF across the speed-load domain. This issue, along with the underestimation in mass density, needs to be addressed through potential inclusion of agglomeration and aggregation modelling with increasing details of the soot model.

The integrated CFD-chemical kinetic modelling approach can be further extended to stratified charge operations in GDI engines which involve late fuel injection during the compression stroke. This way, distinct differences in PM formation mechanisms between homogenous and stratified modes can be pinpointed. Also, the formulated numerical approach can be implemented to computationally study the effects of intrinsic and extrinsic engine variables such as fuel type, fuel-air ratio, injector type, spray pattern and valve timing on PM emissions. The knowledge acquired will be beneficial in strategy optimisation for PM mitigation.

REFERENCES

[1] Brehob DD, Fleming JE, Haghgooie M, Stein RA. Stratified-Charge Engine Fuel Economy and Emission Characteristics. SAE Tech Pap 1998. doi:10.4271/982704.

[2] Ganesan V. Internal Combustion Engines. 4th ed. New Delhi: Tata McGraw-Hill; 2012.

[3] Zhao F, Lai M-C, Harrington D. Automotive spark-ignited direct-injection gasoline engines. Prog Energy Combust Sci 1999;25:437–562. doi:10.1016/S0360-1285(99)00004-0.

[4] Hentschel W. Optical diagnostics for combustion process development of direct-injection gasoline engines. Proc Combust Inst 2000;28:1119–35. doi:10.1016/S0082-0784(00)80322-7.

[5] Küsell M, Moser W, Philipp M. Motronic MED7 for Gasoline Direct Injection Engines: Engine Management System and Calibration Procedures. SAE Tech Pap 1999. doi:10.4271/1999-01-1284.

[6] Andersson J, Giechaskiel B, Muñoz-Bueno R, Sandbach E, Dilara P. Particle Measurement Programme (PMP) Light-duty Inter-laboratory Correlation Exercise (ILCE_LD) Final Report. 2007.

[7] Braisher M, Stone R, Price P. Particle Number Emissions from a Range of European Vehicles. SAE Tech Pap 2010. doi:10.4271/2010-01-0786.

[8] Raza M, Chen L, Leach F, Ding S, Raza M, Chen L, et al. A Review of Particulate Number (PN) Emissions from Gasoline Direct Injection (GDI) Engines and Their Control Techniques. Energies 2018;11:1417. doi:10.3390/en11061417.

[9] Maricq MM, Szente JJ, Jahr K. The Impact of Ethanol Fuel Blends on PM Emissions from a Light-Duty GDI Vehicle. Aerosol Sci Technol 2012;46:576–83. doi:10.1080/02786826.2011.648780.

[10] Fushimi A, Kondo Y, Kobayashi S, Fujitani Y, Saitoh K, Takami A, et al. Chemical composition and source of fine and nanoparticles from recent direct injection gasoline passenger cars: Effects of fuel and ambient temperature. Atmos Environ 2016;124:77–84. doi:10.1016/J.ATMOSENV.2015.11.017.

[11] Heyder J. Deposition of Inhaled Particles in the Human Respiratory Tract and Consequences for Regional Targeting in Respiratory Drug Delivery. Proc. Am. Thorac. Soc., vol. 1, American Thoracic Society; 2004, p. 315–20.

[12] Peters A, Veronesi B, Calderón-Garcidueñas L, Gehr P, Chen LC, Geiser M, et al. Translocation and potential neurological effects of fine and ultrafine particles a critical update. Part Fibre Toxicol 2006;3:13. doi:10.1186/1743-8977-3-13.

[13] Brugge D, Durant JL, Rioux C. Near-highway pollutants in motor vehicle exhaust: a review of epidemiologic evidence of cardiac and pulmonary health risks. Environ Health 2007;6:23. doi:10.1186/1476-069X-6-23.

[14] Demuynck J, Favre C, Bosteels D, Hamje H, Andersson J. Real-World Emissions Measurements of a Gasoline Direct Injection Vehicle without and with a Gasoline Particulate Filter, 2017. doi:10.4271/2017-01-0985.

[15] Sementa P, Maria Vaglieco B, Catapano F. Thermodynamic and optical characterizations of a high performance GDI engine operating in homogeneous and stratified charge mixture conditions fueled with gasoline and bio-ethanol. Fuel 2012;96:204–19. doi:10.1016/J.FUEL.2011.12.068.

[16] Geiler JN, Grzeszik R, Quaing S, Manz A, Kaiser SA. Development of laser-induced fluorescence to quantify in-cylinder fuel wall films. Int J Engine Res 2018;19:134–47. doi:10.1177/1468087417733865.

[17] Velji A, Yeom K, Wagner U, Spicher U, Rossbach M, Suntz R, et al. Investigations of the Formation and Oxidation of Soot Inside a Direct Injection Spark Ignition Engine Using Advanced Laser-Techniques. SAE Tech Pap 2010. doi:10.4271/2010-01-0352.

[18] Maricq MM, Podsiadlik DH, Brehob DD, Haghgooie M. Particulate Emissions from a Direct-Injection Spark-Ignition (DISI) Engine. SAE Tech Pap 1999. doi:10.4271/1999-01-1530.

[19] Choi K, Kim J, Myung C-L, Lee M, Kwon S, Lee Y, et al. Effect of the mixture preparation on the nanoparticle characteristics of gasoline direct-injection vehicles. Proc Inst Mech Eng Part D J Automob Eng 2012;226:1514–24. doi:10.1177/0954407012445534.

[20] Barone TL, Storey JME, Youngquist AD, Szybist JP. An analysis of direct-injection spark-ignition (DISI) soot morphology. Atmos Environ 2012;49:268–74. doi:10.1016/j.atmosenv.2011.11.047.

[21] La Rocca A, Bonatesta F, Fay MW, Campanella F. Characterisation of soot in oil from a gasoline direct injection engine using Transmission Electron Microscopy. Tribol Int 2015;86:77–84. doi:10.1016/j.triboint.2015.01.025.

[22] Karjalainen P, Pirjola L, Heikkilä J, Lähde T, Tzamkiozis T, Ntziachristos L, et al. Exhaust particles of modern gasoline vehicles: A laboratory and an on-road study. Atmos Environ 2014;97:262–70. doi:10.1016/j.atmosenv.2014.08.025.

[23] Netzell K, Lehtiniemi H, Mauss F. Calculating the soot particle size distribution function in turbulent diffusion flames using a sectional method. Proc Combust Inst 2007;31:667–74. doi:10.1016/j.proci.2006.08.081.

[24] Aubagnac-Karkar D, El Bakali A, Desgroux P. Soot particles inception and PAH condensation modelling applied in a soot model utilizing a sectional method. Combust Flame 2018;189:190–206. doi:10.1016/J.COMBUSTFLAME.2017.10.027.

[25] Aubagnac-Karkar D, Michel J-B, Colin O, Vervisch-Kljakic PE, Darabiha N. Sectional soot model coupled to tabulated chemistry for Diesel RANS simulations. Combust Flame 2015;162:3081–99. doi:10.1016/J.COMBUSTFLAME.2015.03.005.

[26] Pitz WJ, Cernansky NP, Dryer FL, Egolfopoulos FN, Farrell JT, Friend DG, et al. Development of an Experimental Database and Chemical Kinetic Models for Surrogate Gasoline Fuels. SAE Tech Pap 2007. doi:10.4271/2007-01-0175.

[27] Machado GB, Barros JEM, Braga SL, Braga CVM, de Oliveira EJ, da Silva AHM da FT, et al. Investigations on surrogate fuels for high-octane oxygenated gasolines. Fuel 2011;90:640–6. doi:10.1016/j.fuel.2010.10.024.

[28] Cai L, Pitsch H. Optimized chemical mechanism for combustion of gasoline surrogate fuels. Combust Flame 2015;162:1623–37. doi:10.1016/j.combustflame.2014.11.018.

[29] Mehl M, Chen JY, Pitz WJ, Sarathy SM, Westbrook CK. An approach for formulating surrogates for gasoline with application toward a reduced surrogate mechanism for CFD engine modeling. Energy and Fuels 2011;25:5215–23. doi:10.1021/ef201099y.

[30] Galmiche B, Halter F, Foucher F. Effects of high pressure, high temperature and dilution on laminar burning velocities and Markstein lengths of iso-octane/air mixtures. Combust Flame 2012;159:3286–99. doi:10.1016/j.combustflame.2012.06.008.

[31] Lucchini T, D'Errico G, Onorati A, Bonandrini G, Venturoli L, Di Gioia R. Development and application of a computational fluid dynamics methodology to predict fuel-air mixing and sources of soot formation in gasoline direct injection engines. Int J Engine Res 2013;15:581–96. doi:10.1177/1468087413500297.

[32] Bonatesta F, La Rocca S, Hopkins E, Bell D. Application of Computational Fluid Dynamics to Explore the Sources of Soot Formation in a Gasoline Direct Injection Engine. SAE Tech Pap 2014. doi:10.4271/2014-01-2569.

[33] Kalghatgi GT, Nakata K, Mogi K. Octane Appetite Studies in Direct Injection Spark Ignition (DISI) Engines. SAE Tech Pap 2005. doi:10.4271/2005-01-0244.

[34] Kalghatgi GT. Auto-Ignition Quality of Practical Fuels and Implications for Fuel Requirements of Future SI and HCCI Engines. SAE Tech Pap 2005. doi:10.4271/2005-01-0239.

[35] Edgar G. Measurement of Knock Characteristics of Gasoline in Terms of a Standard Fuel. Ind Eng Chem 1927;19:145–6. doi:10.1021/ie50205a049.

[36] Morgan N, Smallbone A, Bhave A, Kraft M, Cracknell R, Kalghatgi G. Mapping surrogate gasoline compositions into RON/MON space. Combust Flame 2010;157:1122–31. doi:10.1016/j.combustflame.2010.02.003.

[37] Standard Test Method for Research Octane Number of Spark-Ignition Engine Fuel. West Conshohocken: 2013.

[38] Standard Test Method for Motor Octane Number of Spark-Ignition Engine Fuel. West Conshohocken: 2014.

[39] Bradley D, Head RA. Engine autoignition: The relationship between octane numbers and autoignition delay times. Combust Flame 2006;147:171–84. doi:10.1016/j.combustflame.2006.09.001.

[40] Yan S, Jiang Y-J, Marsh ND, Eddings EG, Sarofim AF, Pugmire RJ. Study of the Evolution of Soot from Various Fuels. Energy & Fuels 2005;19:1804–11. doi:10.1021/ef049742u.

[41] Yang Y, Boehman AL, Santoro RJ. A study of jet fuel sooting tendency using the threshold sooting index (TSI) model. Combust Flame 2007;149:191–205. doi:10.1016/j.combustflame.2006.11.007.

[42] Mcenally C, Pfefferle L. Improved sooting tendency measurements for aromatic hydrocarbons and their implications for naphthalene formation pathways. Combust Flame 2007;148:210–22. doi:10.1016/j.combustflame.2006.11.003.

[43] Lu T, Law CK. Toward accommodating realistic fuel chemistry in large-scale computations. Prog Energy Combust Sci 2009;35:192–215. doi:10.1016/j.pecs.2008.10.002.

[44] Wang H, Frenklach M. Detailed reduction of reaction mechanisms for flame modeling. Combust Flame 1991;87:365–70. doi:10.1016/0010-2180(91)90120-Z.

[45] Lu T, Law CK. A directed relation graph method for mechanism reduction. Proc Combust Inst 2005;30:1333–41. doi:10.1016/j.proci.2004.08.145.

[46] Patel A, Kong S-C, Reitz RD. Development and Validation of a Reduced Reaction Mechanism for HCCI Engine Simulations. SAE Tech Pap 2004. doi:10.4271/2004-01-0558.

[47] Nagy T, Turányi T. Reduction of very large reaction mechanisms using methods based on simulation error minimization. Combust Flame 2009;156:417–28. doi:10.1016/j.combustflame.2008.11.001.

[48] Nakano M, Mandokoro Y, Kubo S, Yamazaki S. Effects of exhaust gas recirculation in homogeneous charge compression ignition engines. Int J Engine Res 2000;1:269–79. doi:10.1243/1468087001545173.

[49] Ogink R, Golovitchev V. Gasoline HCCI Modeling: An Engine Cycle Simulation Code with a Multi-Zone Combustion Model. SAE Tech Pap 2002. doi:10.4271/2002-01-1745.

[50] Andrae JCG, Björnbom P, Cracknell RF, Kalghatgi GT. Autoignition of toluene reference fuels at high pressures modeled with detailed chemical kinetics. Combust Flame 2007;149:2–24. doi:10.1016/j.combustflame.2006.12.014.

[51] Chaos M, Zhao Z, Kazakov A, Gokulakrishnan P, Angioletti M, Dryer FL. A PRF+Toluene Surrogate Fuel Model for Simulating Gasoline Kinetics. 5th US Combust. Meet., San Diego:

2007.

[52] Andrae JCG, Brinck T, Kalghatgi GT. HCCI experiments with toluene reference fuels modeled by a semidetailed chemical kinetic model. Combust Flame 2008;155:696–712. doi:10.1016/j.combustflame.2008.05.010.

[53] Anderlohr J, Bounaceur R, da Cruz AP, Battin-Leclerc F. Modeling of autoignition and NO sensitization for the oxidation of IC engine surrogate fuels. Combust Flame 2009;156:505–21. doi:10.1016/j.combustflame.2008.09.009.

[54] Cancino LR, Fikri M, Oliveira AAM, Schulz C. Autoignition of gasoline surrogate mixtures at intermediate temperatures and high pressures: Experimental and numerical approaches. Proc Combust Inst 2009;32:501–8. doi:10.1016/j.proci.2008.06.180.

[55] Sakai Y, Miyoshi A, Koshi M, Pitz WJ. A kinetic modeling study on the oxidation of primary reference fuel–toluene mixtures including cross reactions between aromatics and aliphatics. Proc Combust Inst 2009;32:411–8. doi:10.1016/j.proci.2008.06.154.

[56] Machrafi H, Cavadias S, Amouroux J. The development and experimental validation of a reduced ternary kinetic mechanism for the auto-ignition at HCCI conditions, proposing a global reaction path for ternary gasoline surrogates. Fuel Process Technol 2009;90:247–63. doi:10.1016/j.fuproc.2008.08.015.

[57] Lee K, Kim Y, Min K. Development of a reduced chemical kinetic mechanism for a gasoline surrogate for gasoline HCCI combustion. Combust Theory Model 2010;15:107–24. doi:10.1080/13647830.2010.528037.

[58] Zhang QF, Zheng ZL, He ZW, Wang Y. Reduced Chemical Kinetic Model of Toluene Reference Fuels for HCCI Combustion. Acta Physico-Chimica Sin 2011;27:530–8. doi:10.3866/PKU.WHXB20110334.

[59] Raj A, Prada IDC, Amer AA, Chung SH. A reaction mechanism for gasoline surrogate fuels for large polycyclic aromatic hydrocarbons. Combust Flame 2012;159:500–15. doi:10.1016/j.combustflame.2011.08.011.

[60] Liu Y-D, Jia M, Xie M-Z, Pang B. Development of a New Skeletal Chemical Kinetic Model of Toluene Reference Fuel with Application to Gasoline Surrogate Fuels for Computational Fluid Dynamics Engine Simulation. Energy & Fuels 2013;27:4899–909. doi:10.1021/ef4009955.

[61] Ranzi E, Frassoldati A, Stagni A, Pelucchi M, Cuoci A, Faravelli T. Reduced Kinetic Schemes of Complex Reaction Systems: Fossil and Biomass-Derived Transportation Fuels. Int J Chem Kinet 2014;46:512–42. doi:10.1002/kin.20867.

[62] Niemeyer KE, Sung C-J. Mechanism reduction for multicomponent surrogates: A case study using toluene reference fuels. Combust Flame 2014;161:2752–64. doi:10.1016/j.combustflame.2014.05.001.

[63] Jiao Q, Reitz RD. Modeling soot emissions from wall films in a direct-injection spark-ignition engine. Int J Engine Res 2014;16:994–1013. doi:10.1177/1468087414562008.

[64] Zheng Z, Lv Z. A new skeletal chemical kinetic model of gasoline surrogate fuel with nitric oxide in HCCI combustion. Appl Energy 2015;147:59–66. doi:10.1016/j.apenergy.2015.01.062.

[65] Wang H, Yao M, Yue Z, Jia M, Reitz RD. A reduced toluene reference fuel chemical kinetic mechanism for combustion and polycyclic-aromatic hydrocarbon predictions. Combust Flame 2015;162:2390–404. doi:10.1016/j.combustflame.2015.02.005.

[66] An Y, Pei Y, Qin J, Zhao H, Li X. Kinetic modeling of polycyclic aromatic hydrocarbons formation process for gasoline surrogate fuels. Energy Convers Manag 2015;100:249–61. doi:10.1016/j.enconman.2015.05.013.

[67] An Y, Pei Y, Qin J, Zhao H, Teng S, Li B, et al. Development of a PAH (polycyclic aromatic hydrocarbon) formation model for gasoline surrogates and its application for GDI (gasoline direct injection) engine CFD (computational fluid dynamics) simulation. Energy 2016;94:367–79. doi:10.1016/J.ENERGY.2015.11.014.

[68] Sivaramakrishnan R, Tranter RS, Brezinsky K. A high pressure model for the oxidation of toluene. Proc Combust Inst 2005;30:1165–73. doi:10.1016/j.proci.2004.08.128.

[69] Curran H, Gaffuri P, Pitz WJ, Westbrook CK. A comprehensive modeling study of iso-octane oxidation. Combust Flame 2002;129:253–80. doi:10.1016/S0010-2180(01)00373-X.

[70] Sakai Y, Ozawa H, Ogura T, Miyoshi A, Koshi M, Pitz WJ. Effects of Toluene Addition to Primary Reference Fuel at High Temperature. SAE Tech Pap 2007. doi:10.4271/2007-01-4104.

[71] Schuetz CA, Frenklach M. Nucleation of soot: Molecular dynamics simulations of pyrene dimerization. Proc Combust Inst 2002;29:2307–14. doi:10.1016/S1540-7489(02)80281-4.

[72] Richter H, Howard J. Formation of polycyclic aromatic hydrocarbons and their growth to soot—a review of chemical reaction pathways. Prog Energy Combust Sci 2000;26:565–608. doi:10.1016/S0360-1285(00)00009-5.

[73] Blanquart G, Pepiot-Desjardins P, Pitsch H. Chemical mechanism for high temperature combustion of engine relevant fuels with emphasis on soot precursors. Combust Flame 2009;156:588–607. doi:10.1016/j.combustflame.2008.12.007.

[74] Marchal C, Delfau J-L, Vovelle C, Moréac G, Mounaı¨m-Rousselle C, Mauss F. Modelling of aromatics and soot formation from large fuel molecules. Proc Combust Inst 2009;32:753–9. doi:10.1016/j.proci.2008.06.115.

[75] Liang L, Reitz RD. Spark Ignition Engine Combustion Modeling Using a Level Set Method with Detailed Chemistry. SAE Tech Pap 2006. doi:10.4271/2006-01-0243.

[76] Bieleveld T, Frassoldati A, Cuoci A, Faravelli T, Ranzi E, Niemann U, et al. Experimental and kinetic modeling study of combustion of gasoline, its surrogates and components in laminar non-premixed flows. Proc Combust Inst 2009;32:493–500. doi:10.1016/j.proci.2008.06.214.

[77] Golovitchev VI, Rinaldini CA, Cantore G. Development and Application of Gasoline/EtOH Combustion Mechanism : Modeling of Direct Injection Ethanol Boosted Gasoline Engine(SI: Spark-Ignition Engine Combustion,General Session Papers). Int Symp Diagnostics Model Combust Intern Combust Engines 2008;2008:251–7.

[78] Shi Y, Ge H-W, Reitz RD. Computational Optimization of Internal Combustion Engines. London: Springer London; 2011. doi:10.1007/978-0-85729-619-1.

[79] Haworth DC. A Review of Turbulent Combustion Modeling for Multidimensional In-Cylinder CFD. SAE Tech Pap 2005. doi:10.4271/2005-01-0993.

[80] Drake MC, Haworth DC. Advanced gasoline engine development using optical diagnostics and numerical modeling. Proc Combust Inst 2007;31:99–124. doi:10.1016/j.proci.2006.08.120.

[81] Li H. CFD modelling study of sprays and combustion of gasoline and DMF in direct injection gasoline engines. The University of Birmingham, 2013.

[82] Gill A, Gutheil E, Warnatz J. Numerical Investigation of the Combustion Process in a Direct-Injection Stratified Charge Engine. Combust Sci Technol 1996;115:317–33. doi:10.1080/00102209608935534.

[83] Kech J, Reissing J, Gindele J, Spicher U. Analyses of the Combustion Process in a Direct Injection Gasoline Engine. Fourth Int. Symp. COMODIA 98, Institut Fur Kolbenmaschinen Universitat Karlsruhe: 1998, p. 287–92.

[84] Duclos J, Zolver M. 3D Modeling of Intake, Injection and Combustion in a DI-SI Engine under Homogeneous and Stratified Operating Conditions. Fourth Int. Symp. COMODIA 98, Institut Francais Du Petrole: 1998, p. 335–40.

[85] Tatschl R, Riediger H. PDF Modelling of Stratified Charge SI Engine Combustion. SAE Tech Pap 1998. doi:10.4271/981464.

[86] Henriot S, Chaouche A, Cheve E, Duclos JM. CFD Aided Development of a Si-Di Engine. Oil Gas Sci Technol 1999;54:279–86. doi:10.2516/ogst:1999026.

[87] Duclos JP, Zolver M, Baritaud T. 3D Modeling of Combustion for DI-SI Engines. Oil Gas Sci Technol 1999;54:259–64. doi:10.2516/ogst:1999023.

[88] Fan L, Li G, Han Z, Reitz RD. Modeling Fuel Preparation and Stratified Combustion in a Gasoline Direct Injection Engine. SAE Tech Pap 1999. doi:10.4271/1999-01-0175.

[89] Georjon T, Bourguignon E, Duverger T, Delhaye B, Voisard P. Characteristics of Mixture Formation and Combustion in a Spray-Guided Concept Gasoline Direct Injection Engine: An Experimental and Numerical Approach. SAE Tech Pap 2000. doi:10.4271/2000-01-0534.

[90] Tatschl R, Riediger H, Künsberg Sarre C v., Putz N, Kickinger F. Rapid Meshing and Advanced Physical Modeling for Gasoline DI Engine Application. Int. Multidimens. Model. User's Gr. Meet. SAE Congr., Detroit: 2000.

[91] Hélie J, Duclos J-M, Baritaud T, Poinsot T, Trouvé A. Influence of Mixture Fluctuations on Combustion in Direct Injection Spark Ignition Engines Simulations. SAE Tech Pap 2001. doi:10.4271/2001-01-1226.

[92] Nomura Y, Miyagawa H, Fujikawa T, Tomoda T, Kubota M, Abe S. Numerical Study of Mixture Formation and Combustion Processes in a Direct Injection Gasoline Engine with Fan-Shaped Spray. SAE Tech Pap 2001. doi:10.4271/2001-01-0738.

[93] Wallesten J, Lipatnikov A, Chomiak J. Modeling of stratified combustion in a direct-ignition, spark-ignition engine accounting for complex chemistry. Proc Combust Inst 2002;29:703–9. doi:10.1016/S1540-7489(02)80090-6.

[94] Castagné M, Dumas JP, Henriot S, Pierre P. Use of Advanced Tools for the Analysis of Gasoline Direct Injection Engines. Oil Gas Sci Technol 2003;58:79–100. doi:10.2516/ogst:2003006.

[95] Colin O, Benkenida A, Angelberger C. 3D Modeling of Mixing, Ignition and Combustion Phenomena in Highly Stratified Gasoline Engines. Oil Gas Sci Technol 2003;58:47–62. doi:10.2516/ogst:2003004.

[96] Wakisaka T, Esumi T. CFD Simulation of Mixture Formation and Combustion Processes in a Direct-Injection Gasoline Engine Using a GTT Code. SAE Tech Pap 2003. doi:10.4271/2003-01-1842.

[97] Tan Z, Kong S-C, Reitz RD. Modeling Premixed and Direct Injection SI Engine Combustion Using the G-Equation Model. SAE Tech Pap 2003. doi:10.4271/2003-01-1843.

[98] Vanzieleghem BP, Sick V, Im HG, Assanis DN. Modeling of Gasoline Direct Injection Mixture Formation with KIVA-3V and Validation with Optical Engine Planar Laser Induced Fluorescence Measurements : Development of an Extended Coherent Flamelet Model (S.I. Engines, G.D.I. Modelling). Int Symp Diagnostics Model Combust Intern Combust Engines 2004;2004:537–44.

[99] Drake MC, Fansler TD, Lippert AM. Stratified-charge combustion: modeling and imaging of a spray-guided direct-injection spark-ignition engine. Proc Combust Inst 2005;30:2683–91. doi:10.1016/j.proci.2004.07.028.

[100] Gao J, Jiang DM, Huang ZH, Wang X Bin. Numerical study on spray and mixture stratified

combustion in a direct injection gasoline engine. Neiranji Xuebao/Transactions CSICE (Chinese Soc Intern Combust Engines) 2005;23:297–306.

[101] Olmo L, Thornton J. CFD Analysis of Mixture Formation and Combustion Process for High Performance DI Gasoline Engine. SAE Tech Pap 2005. doi:10.4271/2005-01-0214.

[102] Liu J, Gong J, Cai L, Tan L, Ni X, Gao W. Multi-dimensional Simulation of Air/Fuel Premixing and Stratified Combustion in a Gasoline Direct Injection Engine with Combustion Chamber Bowl Offset, 2006. doi:10.4271/2006-32-0006.

[103] Rotondi R. Modeling Mixture Formation in a Gasoline Direct Injection Engine. J Appl Mech 2006;73:931. doi:10.1115/1.2173284.

[104] Bohbot J, Chryssakis C, Miche M. Simulation of a 4-Cylinder Turbocharged Gasoline Direct Injection Engine Using a Direct Temporal Coupling Between a 1D Simulation Software and a 3D Combustion Code. SAE Tech Pap 2006. doi:10.4271/2006-01-3263.

[105] Kim S-J, Kim Y-N, Lee J-H. Analysis of the In-Cylinder Flow, Mixture Formation and Combustion Processes in a Spray-Guided GDI Engine. SAE Tech Pap 2008. doi:10.4271/2008-01-0142.

[106] Yang S, Reitz RD. Integration of a Continuous Multi-Component Fuel Evaporation Model with an Improved G-Equation Combustion and Detailed Chemical Kinetics Model with Application to GDI Engines. SAE Tech Pap 2009. doi:10.4271/2009-01-0722.

[107] Dahms R, Fansler TD, Drake MC, Kuo T-W, Lippert AM, Peters N. Modeling ignition phenomena in spray-guided spark-ignited engines. Proc Combust Inst 2009;32:2743–50. doi:10.1016/j.proci.2008.05.052.

[108] Bai Y, Wang Z, Shuai S, Wang J. Three-Dimensional Numerical Simulation of Spray, Mixed Gas Formation and Combustion Process for Gasoline Direct Injection Engine. J Combust Sci Technol 2010;16.

[109] Dahms RN, Drake MC, Grover RO, Solomon AS, Fansler TD. Detailed Simulations of Stratified Ignition and Combustion Processes in a Spray-Guided Gasoline Engine using the SparkCIMM/G-Equation Modeling Framework. SAE Int J Engines 2012;5:141–61. doi:10.4271/2012-01-0132.

[110] Yang X, Solomon A, Kuo T-W. Ignition and Combustion Simulations of Spray-Guided SIDI Engine using Arrhenius Combustion with Spark-Energy Deposition Model. SAE Tech Pap 2012. doi:10.4271/2012-01-0147.

[111] Givler SD, Raju M, Pomraning E, Senecal PK, Salman N, Reese R. Gasoline Combustion Modeling of Direct and Port-Fuel Injected Engines using a Reduced Chemical Mechanism. SAE Tech Pap 2013. doi:10.4271/2013-01-1098.

[112] Costa M, Marchitto L, Merola SS, Sorge U. Study of mixture formation and early flame development in a research GDI (gasoline direct injection) engine through numerical simulation and UV-digital imaging. Energy 2014;77:88–96. doi:10.1016/j.energy.2014.04.114.

[113] Costa M, Sorge U, Sementa P, Vaglieco BM. CFD Modeling of a Mixed Mode Boosted GDI Engine and Performance Optimization for the Avoidance of Knocking. In: Obaidat MS, Ören T, Kacprzyk J, Filipe J, editors. Simul. Model. Methodol. Technol. Appl., Springer, Cham; 2015, p. 195–215. doi:10.1007/978-3-319-26470-7_10.

[114] Kim T, Song J, Park S. Effects of turbulence enhancement on combustion process using a double injection strategy in direct-injection spark-ignition (DISI) gasoline engines. Int J Heat Fluid Flow 2015;56:124–36. doi:10.1016/j.ijheatfluidflow.2015.07.013.

[115] Qian Y, Gong Z, Zhuang Y, Wang C, Zhao P. Mechanism study of scavenging process and its effect on combustion characteristics in a boosted GDI engine. Energy 2018;165:246–66. doi:10.1016/J.ENERGY.2018.09.077.

[116] Qian Y, Gong Z, Shao X, Tao C, Zhuang Y. Numerical study of the effect of combustion chamber structure on scavenging process in a boosted GDI engine. Energy 2019;168:9–29. doi:10.1016/J.ENERGY.2018.11.080.

[117] Yakhot V, Smith LM. The renormalization group, the ε-expansion and derivation of turbulence models. J Sci Comput 1992;7:35–61. doi:10.1007/BF01060210.

[118] Rodi W. Influence of buoyancy and rotation on equations for the turbulent length scale. Symp. Turbul. Shear Flows, London: 1979, p. 10.37-10.42.

[119] Westbrook CK, Mizobuchi Y, Poinsot TJ, Smith PJ, Warnatz J. Computational combustion. Proc Combust Inst 2005;30:125–57. doi:10.1016/j.proci.2004.08.275.

[120] Faeth G., Hsiang L-P, Wu P-K. Structure and breakup properties of sprays. Int J Multiph Flow 1995;21:99–127. doi:10.1016/0301-9322(95)00059-7.

[121] Hirt C., Nichols B. Volume of fluid (VOF) method for the dynamics of free boundaries. J Comput Phys 1981;39:201–25. doi:10.1016/0021-9991(81)90145-5.

[122] Sanjosé M, Senoner JM, Jaegle F, Cuenot B, Moreau S, Poinsot T. Fuel injection model for Euler–Euler and Euler–Lagrange large-eddy simulations of an evaporating spray inside an aeronautical combustor. Int J Multiph Flow 2011;37:514–29. doi:10.1016/j.ijmultiphaseflow.2011.01.008.

[123] Beck JC, Watkins AP. The droplet number moments approach to spray modelling: The development of heat and mass transfer sub-models. Int J Heat Fluid Flow 2003;24:242–59. doi:10.1016/S0142-727X(02)00242-4.

[124] Faeth GM. Spray combustion phenomena. Symp Combust 1996;26:1593–612. doi:10.1016/S0082-0784(96)80383-3.

[125] Jenny P, Roekaerts D, Beishuizen N. Modeling of turbulent dilute spray combustion. Prog Energy Combust Sci 2012;38:846–87. doi:10.1016/j.pecs.2012.07.001.

[126] Godsave G. Studies of the Combustion of Drops in a Fuel Spray—The Burning of Single Drops of Fuel. Fourth Symp. Combust., Williams and Wilkins, Baltimore: 1953, p. 818–30.

[127] Spalding D. The Combustion of Liquid Fuels. Fourth Symp. Combust., Williams and Wilkins, Baltimore: 1953, p. 847–64.

[128] Lindgren R, Denbratt I. Modeling Gasoline Spray-Wall Interactions and Comparison to Experimental Data. SAE Tech Pap 2004. doi:10.4271/2004-01-3003.

[129] Cossali GE, Coghe A, Marengo M. The impact of a single drop on a wetted solid surface. Exp Fluids 1997;22:463–72. doi:10.1007/s003480050073.

[130] Reitz RD, Diwakar R. Effect of Drop Breakup on Fuel Sprays. SAE Tech Pap 1986. doi:10.4271/860469.

[131] Reitz RD, Diwakar R. Structure of High-Pressure Fuel Sprays. SAE Tech Pap 1987. doi:10.4271/870598.

[132] Huang C, Lipatnikov A. Modelling of Gasoline and Ethanol Hollow-Cone Sprays Using OpenFOAM. SAE Tech Pap 2011. doi:10.4271/2011-01-1896.

[133] Yi Y, DeMinco CM. Numerical Investigation of Mixture Preparation in a GDI Engine. SAE Tech Pap 2006. doi:10.4271/2006-01-3375.

[134] Çelik MB, Ozdalyan B. Gasoline Direct Injection. In: Siano D, editor. Fuel Inject., Sciyo; 2010.

[135] Dec JE. A Conceptual Model of DI Diesel Combustion Based on Laser-Sheet Imaging*, 1997. doi:10.4271/970873.

[136] Meisam Ahmadi Ghadikolaei. Study of Combustion Characteristics of Spray for Gasoline Direct Injection (GDI) Hot Surface Ignition Heavy Duty Engine. Int J Appl or Innov Eng Manag 2015;4.

[137] Wang B, Mosbach S, Schmutzhard S, Shuai S, Huang Y, Kraft M. Modelling soot formation from wall films in a gasoline direct injection engine using a detailed population balance model. Appl Energy 2016;163:154–66. doi:10.1016/j.apenergy.2015.11.011.

[138] Bonatesta F, Chiappetta E, La Rocca A. Part-load particulate matter from a GDI engine and the connection with combustion characteristics. Appl Energy 2014;124:366–76. doi:10.1016/j.apenergy.2014.03.030.

[139] Spalding DB. Mixing and chemical reaction in steady confined turbulent flames. Symp Combust 1971;13:649–57. doi:10.1016/S0082-0784(71)80067-X.

[140] Abraham J, Bracco FV, Reitz RD. Comparisons of computed and measured premixed charge engine combustion. Combust Flame 1985;60:309–22. doi:10.1016/0010-2180(85)90036-7.

[141] Bray KNC. Turbulent flows with premixed reactants. In: Libby P, Williams F, editors. Turbul. React. Flows, Berlin: Springer-Verlag; 1980, p. 115–83.

[142] Marble FE, Broadwell JE. The Coherent Flame Model for Turbulent Chemical Reactions. 1977.

[143] Peters N. Turbulent Combustion. Cambridge: Cambridge University Press; 2000. doi:10.1017/CBO9780511612701.

[144] Lipatnikov AN, Chomiak J. Turbulent flame speed and thickness: phenomenology, evaluation, and application in multi-dimensional simulations. Prog Energy Combust Sci 2002;28:1–74. doi:10.1016/S0360-1285(01)00007-7.

[145] Dold JW. Flame propagation in a nonuniform mixture: Analysis of a slowly varying Triple Flame. Combust Flame 1989;76:71–88. doi:10.1016/0010-2180(89)90079-5.

[146] Koch T, Schänzlin K, Boulouchos K. Characterization and Phenomenological Modeling of Mixture Formation and Combustion in a Direct Injection Spark Ignition Engine. SAE Tech Pap 2002. doi:10.4271/2002-01-1138.

[147] Reitz R, Sun Y. Advanced computational fluid dynamics modeling of direct injection engines. In: Zhao H, editor. Adv. Direct Inject. Combust. Engine Technol. Dev., Cambridge: Woodhead Publishing Limited; 2010, p. 676–707.

[148] Andersson J, Keenan M, Åkerman K. GDI Particles – Legislation, Current Levels And Control. Cambridge Part. Meet., 2009.

[149] Ericsson P, Samson A. Characterization of Particulate Emissions Propagating in the Exhaust Line for Spark Ignited Engines. SAE Tech Pap 2009. doi:10.4271/2009-01-2654.

[150] Ntziachristos L, Mamakos A, Samaras Z, Mathis U, Mohr M, Thompson N, et al. Overview of the European "Particulates" Project on the Characterization of Exhaust Particulate Emissions From Road Vehicles: Results for Light-Duty Vehicles. SAE Tech Pap 2004. doi:10.4271/2004-01-1985.

[151] Tree DR, Svensson KI. Soot processes in compression ignition engines. Prog Energy Combust Sci 2007;33:272–309. doi:10.1016/j.pecs.2006.03.002.

[152] Dobbins RA, Subramaniasivam H. Soot Precursor Particles in Flames. In: Bockhorn H, editor. Soot Form. Combust., Berlin: Springer Berlin Heidelberg; 1994, p. 290–301.

[153] L.Walker P, Austin LG, Nandi. SP. Chemistry and Physics of Carbon. 2nd ed. New York: Marcel Dekker; 1966.

[154] Glassman I. Soot formation in combustion processes. Symp Combust 1989;22:295–311.

doi:10.1016/S0082-0784(89)80036-0.

[155] Stanmore B., Brilhac J., Gilot P. The oxidation of soot: a review of experiments, mechanisms and models. Carbon N Y 2001;39:2247–68. doi:10.1016/S0008-6223(01)00109-9.

[156] Frenklach M. Reaction mechanism of soot formation in flames. Phys Chem Chem Phys 2002;4:2028–37. doi:10.1039/b110045a.

[157] Glassman I. Combustion. 3rd ed. San Diego, CA: Academic Press; 1996.

[158] Xi J, Zhong B-J. Soot in Diesel Combustion Systems. Chem Eng Technol 2006;29:665–73. doi:10.1002/ceat.200600016.

[159] Mosbach S, Celnik MS, Raj A, Kraft M, Zhang HR, Kubo S, et al. Towards a detailed soot model for internal combustion engines. Combust Flame 2009;156:1156–65. doi:10.1016/j.combustflame.2009.01.003.

[160] Frenklach M, Wang H. Detailed Mechanism and Modeling of Soot Particle Formation. In: Bockhorn H, editor. Soot Form. Combust., vol. 59, Berlin, Heidelberg: Springer Berlin Heidelberg; 1994. doi:10.1007/978-3-642-85167-4.

[161] Bartok W, Sarofim AF, editors. Fossil Fuel Combustion: A Source Book. California: Wiley-Interscience; 1991.

[162] Kellerer H, Koch R, Wittig S. Measurements of the growth and coagulation of soot particles in a high-pressure shock tube. Combust Flame 2000;120:188–99. doi:10.1016/S0010-2180(99)00067-X.

[163] Kennedy IM. Models of soot formation and oxidation. Prog Energy Combust Sci 1997;23:95–132. doi:10.1016/S0360-1285(97)00007-5.

[164] Stevens E, Steeper R. Piston Wetting in an Optical DISI Engine: Fuel Films, Pool Fires, and Soot Generation. SAE Tech Pap 2001. doi:10.4271/2001-01-1203.

[165] Stojkovic BD, Fansler TD, Drake MC, Sick V. High-speed imaging of OH* and soot temperature and concentration in a stratified-charge direct-injection gasoline engine. Proc Combust Inst 2005;30:2657–65. doi:10.1016/j.proci.2004.08.021.

[166] Drake MC, Fansler TD, Solomon AS, Szekely GA. Piston Fuel Films as a Source of Smoke and Hydrocarbon Emissions from a Wall-Controlled Spark-Ignited Direct-Injection Engine. SAE Tech Pap 2003. doi:10.4271/2003-01-0547.

[167] Fujimoto H. Study on the oil dilution of a DI gasoline engine - 1st report: dilution on the cylinder wall. Proc. JSAE Spring Conv., 1999.

[168] Appel J, Bockhorn H, Frenklach M. Kinetic modeling of soot formation with detailed chemistry and physics: laminar premixed flames of C2 hydrocarbons. Combust Flame 2000;121:122–36. doi:10.1016/S0010-2180(99)00135-2.

[169] Mueller ME, Blanquart G, Pitsch H. A joint volume-surface model of soot aggregation with the method of moments. Proc Combust Inst 2009;32:785–92. doi:10.1016/j.proci.2008.06.207.

[170] Balthasar M, Kraft M. A stochastic approach to calculate the particle size distribution function of soot particles in laminar premixed flames. Combust Flame 2003;133:289–98. doi:10.1016/S0010-2180(03)00003-8.

[171] Gelbard F, Seinfeld JH. Simulation of multicomponent aerosol dynamics. J Colloid Interface Sci 1980;78:485–501. doi:10.1016/0021-9797(80)90587-1.

[172] Frenklach M, Harris SJ. Aerosol dynamics modeling using the method of moments. J Colloid Interface Sci 1987;118:252–61. doi:10.1016/0021-9797(87)90454-1.

[173] Wallesten J, Lipatnikov A, Chomiak J. Simulations of Fuel/Air Mixing, Combustion, and

Pollutant Formation in a Direct Injection Gasoline Engine. SAE Tech Pap 2002. doi:10.4271/2002-01-0835.

[174] Etheridge J, Mosbach S, Kraft M, Wu H, Collings N. Modelling soot formation in a DISI engine. Proc Combust Inst 2011;33:3159–67. doi:10.1016/j.proci.2010.07.039.

[175] Kwon H, Choi H, Kim J, Min K. Combustion and emission modelling of a direct-injection spark-ignition engine by combining flamelet models for premixed and diffusion flames. Combust Theory Model 2012;16:1089–108. doi:10.1080/13647830.2012.708056.

[176] Kim J, Kim G, Lee H, Min K. Numerical Analysis of Pollutant Formation in Direct-Injection Spark-Ignition Engines by Incorporating the G- Equation with a Flamelet Library. SAE Tech Pap 2014. doi:10.4271/2014-01-1145.

[177] Naik C V., Liang L, Puduppakkam K, Meeks E. Simulation and Analysis of In-Cylinder Soot Formation in a Gasoline Direct-Injection Engine Using a Detailed Reaction Mechanism. SAE Tech Pap 2014. doi:10.4271/2014-01-1135.

[178] Liang L, Naik C V., Puduppakkam K V., Modak AU, Meeks E. Application of Detailed Soot-Particle Model to Simulations of Fundamental Spray Experiments and GDI Engine. Int. Multidimens. Engine Model. User's Gr. Meet., Detroit, Michigan: 2014.

[179] An Y, Li X, Teng S, Wang K, Pei Y, Qin J, et al. Development of a soot particle model with PAHs as precursors through simulations and experiments. Fuel 2016;179:246–57. doi:10.1016/J.FUEL.2016.03.100.

[180] Kim J, Kim N, Min K. Numerical Investigation of Soot Emission in Direct-Injection Spark-Ignition Engines Using a Detailed Soot Model Framework, 2016. doi:10.4271/2016-01-0580.

[181] Dong Z, Shuai S, Wang Z, Zhao H. CFD Modeling of Mixture Preparation and Soot Formation in a Downsized Gasoline Direct Injection Engine. SAE Tech Pap 2016. doi:10.4271/2016-01-0586.

[182] Costa M, Catapano F, Sementa P, Sorge U, Vaglieco BM. Mixture preparation and combustion in a GDI engine under stoichiometric or lean charge: an experimental and numerical study on an optically accessible engine. Appl Energy 2016;180:86–103. doi:10.1016/J.APENERGY.2016.07.089.

[183] Gong Z, Feng L, Wang Z. Experimental and numerical study of the effect of injection strategy and intake valve lift on super-knock and engine performance in a boosted GDI engine. Fuel 2019;249:309–25. doi:10.1016/J.FUEL.2019.03.005.

[184] Fusco A, Knox-Kelecy A, Foster D. Application of a phenomenological soot model to diesel engine combustion. Int Symp COMODIA 1994.

[185] El-Asrag H, Lu T, Law C, Menon S. Simulation of soot formation in turbulent premixed flames. Combust Flame 2007;150:108–26. doi:10.1016/j.combustflame.2007.01.005.

[186] Puduppakkam K V., Modak AU, Naik C V., Camacho J, Wang H, Meeks E. A Soot Chemistry Model That Captures Fuel Effects. ASME Turbo Expo 2014 Turbine Tech. Conf. Expo., Düsseldorf, Germany: ASME; 2014. doi:10.1115/GT2014-27123.

[187] Puduppakkam K, Modak A, Naik C. Progress in Predicting Soot Particle Numbers in CFD Simulations of GDI and Diesel Engines. Int. Multidimens. Engine Model. User's Gr. Meet., Detroit, Michigan: 2015.

[188] Vishwanathan G, Reitz RD. Development of a Practical Soot Modeling Approach and Its Application to Low-Temperature Diesel Combustion. Combust Sci Technol 2010;182:1050–82. doi:10.1080/00102200903548124.

[189] Jiao Q, Reitz RD. Modeling of Equivalence Ratio Effects on Particulate Formation in a Spark-Ignition Engine under Premixed Conditions. SAE Tech Pap 2014. doi:10.4271/2014-01-1607.

[190] Jiao Q, Reitz RD. The Effect of Operating Parameters on Soot Emissions in GDI Engines. SAE Int J Engines 2015;8:2015-01-1071. doi:10.4271/2015-01-1071.

[191] Nikolaou N, Papadopoulos CE, Gaglias IA, Pitarakis KG. A new non-linear calculation method of isomerisation gasoline research octane number based on gas chromatographic data. Fuel 2004;83:517–23. doi:10.1016/J.FUEL.2003.09.011.

[192] Knop V, Loos M, Pera C, Jeuland N. A linear-by-mole blending rule for octane numbers of n-heptane/iso-octane/toluene mixtures. Fuel 2014;115:666–73. doi:10.1016/J.FUEL.2013.07.093.

[193] Badra JA, Bokhumseen N, Mulla N, Sarathy SM, Farooq A, Kalghatgi G, et al. A methodology to relate octane numbers of binary and ternary n-heptane, iso-octane and toluene mixtures with simulated ignition delay times. Fuel 2015;160:458–69. doi:10.1016/J.FUEL.2015.08.007.

[194] Westbrook CK, Sjöberg M, Cernansky NP. A new chemical kinetic method of determining RON and MON values for single component and multicomponent mixtures of engine fuels. Combust Flame 2018;195:50–62. doi:10.1016/J.COMBUSTFLAME.2018.03.038.

[195] Burcat A. Thermochemical Data for Combustion Calculations. Combust. Chem., New York: Springer US; 1984, p. 455–73. doi:10.1007/978-1-4684-0186-8_8.

[196] Yakhot V, Orszag SA, Thangam S, Gatski TB, Speziale CG. Development of turbulence models for shear flows by a double expansion technique. Phys Fluids A Fluid Dyn 1992;4:1510–20. doi:10.1063/1.858424.

[197] Patterson MA, Reitz RD. Modeling the Effects of Fuel Spray Characteristics on Diesel Engine Combustion and Emission 1998. doi:10.4271/980131.

[198] Bai C, Gosman AD. Development of Methodology for Spray Impingement Simulation 1995. doi:10.4271/950283.

[199] Rosa NG, Villedieu P, Dewitte J, Lavergne G. A new droplet-wall interaction model. 10th Int. Conf. Liq. At. Spray Syst., Kyoto: 2006.

[200] Westbrook CK, Mehl M, Pitz WJ, Sjöberg M. Chemical kinetics of octane sensitivity in a spark-ignition engine. Combust Flame 2017;175:2–15. doi:10.1016/J.COMBUSTFLAME.2016.05.022.

[201] Szybist JP, Splitter DA. Pressure and temperature effects on fuels with varying octane sensitivity at high load in SI engines. Combust Flame 2017;177:49–66. doi:10.1016/J.COMBUSTFLAME.2016.12.002.

[202] Sarathy SM, Farooq A, Kalghatgi GT. Recent progress in gasoline surrogate fuels. Prog Energy Combust Sci 2018;65:67–108. doi:10.1016/j.pecs.2017.09.004.

[203] Lee C, Ahmed A, Nasir EF, Badra J, Kalghatgi G, Sarathy SM, et al. Autoignition characteristics of oxygenated gasolines. Combust Flame 2017;186:114–28. doi:10.1016/J.COMBUSTFLAME.2017.07.034.

[204] AlAbbad M, Javed T, Khaled F, Badra J, Farooq A. Ignition delay time measurements of primary reference fuel blends. Combust Flame 2017;178:205–16. doi:10.1016/J.COMBUSTFLAME.2016.12.027.

[205] Gauthier BM, Davidson DF, Hanson RK. Shock tube determination of ignition delay times in full-blend and surrogate fuel mixtures. Combust Flame 2004;139:300–11. doi:10.1016/j.combustflame.2004.08.015.

[206] Fieweger K, Blumenthal R, Adomeit G. Self-ignition of S.I. engine model fuels: A shock tube investigation at high pressure. Combust Flame 1997;109:599–619. doi:10.1016/S0010-2180(97)00049-7.

[207] Ciezki HK, Adomeit G. Shock-tube investigation of self-ignition of n-heptane-air mixtures under engine relevant conditions. Combust Flame 1993;93:421–33. doi:10.1016/0010-2180(93)90142-P.

[208] Shen H-PS, Vanderover J, Oehlschlaeger MA. A shock tube study of the auto-ignition of toluene/air mixtures at high pressures. Proc Combust Inst 2009;32:165–72. doi:10.1016/j.proci.2008.05.004.

[209] Davidson DF, Gauthier BM, Hanson RK. Shock tube ignition measurements of iso-octane/air and toluene/air at high pressures. Proc Combust Inst 2005;30:1175–82. doi:10.1016/j.proci.2004.08.004.

[210] Dec JE, Yang Y. Boosted HCCI for High Power without Engine Knock and with Ultra-Low NOx Emissions - using Conventional Gasoline. vol. 3. 2010. doi:10.4271/2010-01-1086.

[211] Davis SG, Law CK. Laminar flame speeds and oxidation kinetics of iso-octane-air and n-heptane-air flames. Symp Combust 1998;27:521–7. doi:10.1016/S0082-0784(98)80442-6.

[212] Tian G, Daniel R, Li H, Xu H, Shuai S, Richards P. Laminar Burning Velocities of 2,5-Dimethylfuran Compared with Ethanol and Gasoline. Energy & Fuels 2010;24:3898–905. doi:10.1021/ef100452c.

[213] Zhao Z, Conley JP, Kazakov A, Dryer FL. Burning Velocities of Real Gasoline Fuel at 353 K and 500 K, 2003. doi:10.4271/2003-01-3265.

[214] Dirrenberger P, Glaude PA, Bounaceur R, Le Gall H, da Cruz AP, Konnov AA, et al. Laminar burning velocity of gasolines with addition of ethanol. Fuel 2014;115:162–9. doi:10.1016/j.fuel.2013.07.015.

[215] Huang Y, Sung C, Eng J. Laminar flame speeds of primary reference fuels and reformer gas mixtures. Combust Flame 2004;139:239–51. doi:10.1016/j.combustflame.2004.08.011.

[216] Jerzembeck S, Peters N, Pepiotdesjardins P, Pitsch H. Laminar burning velocities at high pressure for primary reference fuels and gasoline: Experimental and numerical investigation. Combust Flame 2009;156:292–301. doi:10.1016/j.combustflame.2008.11.009.

[217] Sileghem L, Alekseev VA, Vancoillie J, Van Geem KM, Nilsson EJK, Verhelst S, et al. Laminar burning velocity of gasoline and the gasoline surrogate components iso-octane, n-heptane and toluene. Fuel 2013;112:355–65. doi:10.1016/j.fuel.2013.05.049.

[218] Zhong B-J, Zheng D. A chemical mechanism for ignition and oxidation of multi-component gasoline surrogate fuels. Fuel 2014;128:458–66. doi:10.1016/j.fuel.2014.03.044.

[219] Bakali AE, Delfau J-L, Vovelle C. Experimental Study of 1 Atmosphere, Rich, Premixed n -heptane and iso-octane Flames. Combust Sci Technol 1998;140:69–91. doi:10.1080/00102209808915768.

[220] Inal F, Senkan SM. Effects of equivalence ratio on species and soot concentrations in premixed n-heptane flames. Combust Flame 2002;131:16–28. doi:10.1016/S0010-2180(02)00388-7.

[221] Dagaut P, Reuillon M, Cathonnet M. High Pressure Oxidation of Liquid Fuels From Low to High Temperature. 1. n-Heptane and iso-Octane. Combust Sci Technol 1993;95:233–60. doi:10.1080/00102209408935336.

[222] Dagaut P, Reuillon M, Cathonnet M. High Pressure Oxidation of Liquid Fuels from Low to High Temperature. 2. Mixtures of n-Heptane and iso-Octane. Combust Sci Technol 1994;103:315–36. doi:10.1080/00102209408907701.

[223] Somers KP, Simmie JM, Gillespie F, Conroy C, Black G, Metcalfe WK, et al. A comprehensive experimental and detailed chemical kinetic modelling study of 2,5-dimethylfuran pyrolysis and oxidation. Combust Flame 2013;160:2291–318. doi:10.1016/J.COMBUSTFLAME.2013.06.007.

[224] Zhong B-J, Peng H-S. Measurement of Laminar Flame Speed and Chemical Kinetic Model of 1-Pentene/Air Mixtures. Combust Sci Technol 2017;189:1698–712. doi:10.1080/00102202.2017.1320551.

[225] Babushok VI, Tsang W. Kinetic Modeling of Heptane Combustion and PAH Formation. J Propuls Power 2004;20:403–14. doi:10.2514/1.2323.

[226] Wang H, Frenklach M. Calculations of Rate Coefficients for the Chemically Activated Reactions of Acetylene with Vinylic and Aromatic Radicals. J Phys Chem 1994;98:11465–89. doi:10.1021/j100095a033.

[227] Miller JA, Klippenstein SJ. The Recombination of Propargyl Radicals and Other Reactions on a C6H6 Potential 2003. doi:10.1021/JP030375H.

[228] Sciortino D, Bonatesta F, Hopkins E, Yang C, Morrey D, Sciortino DD, et al. A Combined Experimental and Computational Fluid Dynamics Investigation of Particulate Matter Emissions from a Wall-Guided Gasoline Direct Injection Engine. Energies 2017;10:1408. doi:10.3390/en10091408.

[229] Montanaro A, Malaguti S, Alfuso S. Wall Impingement Process of a Multi-Hole GDI Spray: Experimental and Numerical Investigation. SAE Tech Pap 2012. doi:10.4271/2012-01-1266.

[230] Angelberger C, Poinsot T, Delhay B. Improving Near-Wall Combustion and Wall Heat Transfer Modeling in SI Engine Computations. SAE Tech Pap 1997. doi:10.4271/972881.

[231] Montanaro A, Allocca L, Ettorre D, Lucchini T, Brusiani F, Cazzoli G. Experimental Characterization of High-Pressure Impinging Sprays for CFD Modeling of GDI Engines. SAE Int J Engines 2011;4:747–63. doi:10.4271/2011-01-0685.

[232] Rotondi R, Bella G. Gasoline direct injection spray simulation. Int J Therm Sci 2006;45:168–79. doi:10.1016/j.ijthermalsci.2005.06.001.

[233] Imren A, Haworth DC. On the merits of extrapolation-based stiff ODE solvers for combustion CFD. Combust Flame 2016;174:1–15. doi:10.1016/J.COMBUSTFLAME.2016.09.018.

[234] Liang L, Stevens JG, Farrell JT. A Dynamic Multi-Zone Partitioning Scheme for Solving Detailed Chemical Kinetics in Reactive Flow Computations. Combust Sci Technol 2009;181:1345–71. doi:10.1080/00102200903190836.

[235] Liang L, Naik C V., Puduppakkam K, Wang C, Modak A, Meeks E, et al. Efficient Simulation of Diesel Engine Combustion Using Realistic Chemical Kinetics in CFD. SAE Tech Pap 2010. doi:10.4271/2010-01-0178.

[236] Yang J, Johansson M, Naik C, Puduppakkam K, Golovitchev V, Meeks E. 3D CFD Modeling of a Biodiesel-Fueled Diesel Engine Based on a Detailed Chemical Mechanism. SAE Tech Pap 2012. doi:10.4271/2012-01-0151.

[237] Wen JZ, Thomson MJ, Lightstne MF, Park SH, Rogak SN. An improved moving sectional aerosol model of soot formation in a plug flow reactor. Combust Sci Technol 2006;178:921–51. doi:10.1080/00102200500270007.

[238] Zhao B, Yang Z, Li Z, Johnston M V., Wang H. Particle size distribution function of incipient soot in laminar premixed ethylene flames: effect of flame temperature. Proc Combust Inst 2005;30:1441–8. doi:10.1016/J.PROCI.2004.08.104.

[239] Seo J, Lee JS, Choi KH, Kim HY, Yoon SS. Numerical investigation of the combustion characteristics and wall impingement with dependence on split-injection strategies from a gasoline direct-injection spark ignition engine. Proc Inst Mech Eng Part D J Automob Eng 2013;227:1518–35. doi:10.1177/0954407013491216.

[240] Hepkaya E, Karaaslan S, Uslu S, Dinler N, Yucel N. A Case Study of Combustion Modeling in a Spark Ignition Engine Using Coherent Flame Model. J Therm Sci Technol 2014;34:111–

21.

[241] Whelan I. A study of particulate matter emissions from gasoline direct injection engines. University College Dublin, 2013.

[242] Hoffmann G, Befrui B, Berndorfer A, Piock WF, Varble DL. Fuel System Pressure Increase for Enhanced Performance of GDi Multi-Hole Injection Systems. SAE Int J Engines 2014;7:2014-01-1209. doi:10.4271/2014-01-1209.

[243] Mao Q, van Duin ACT, Luo KH. Formation of incipient soot particles from polycyclic aromatic hydrocarbons: A ReaxFF molecular dynamics study. Carbon N Y 2017;121:380–8. doi:10.1016/J.CARBON.2017.06.009.

[244] Zhao B, Yang Z, Johnston M V., Wang H, Wexler AS, Balthasar M, et al. Measurement and numerical simulation of soot particle size distribution functions in a laminar premixed ethylene-oxygen-argon flame. Combust Flame 2003;133:173–88. doi:10.1016/S0010-2180(02)00574-6.

[245] Pang KM, Jangi M, Bai X-S, Schramm J. Evaluation and optimisation of phenomenological multi-step soot model for spray combustion under diesel engine-like operating conditions. Combust Theory Model 2015;19:279–308. doi:10.1080/13647830.2015.1019929.

[246] Mauss F, Schäfer T, Bockhorn H. Inception and growth of soot particles in dependence on the surrounding gas phase. Combust Flame 1994;99:697–705. doi:10.1016/0010-2180(94)90064-7.

[247] Frenklach M, Wang H. Detailed modeling of soot particle nucleation and growth. Symp Combust 1991;23:1559–66. doi:10.1016/S0082-0784(06)80426-1.

[248] Addepalli SK, Mallikarjuna JM. Parametric analysis of a 4-stroke GDI engine using CFD. Alexandria Eng J 2018;57:23–34. doi:10.1016/J.AEJ.2016.10.007.

[249] An Y, Teng S, Pei Y, Qin J, Li X, Zhao H. An experimental study of polycyclic aromatic hydrocarbons and soot emissions from a GDI engine fueled with commercial gasoline. Fuel 2016;164:160–71. doi:10.1016/J.FUEL.2015.10.007.

[250] Kim T, Song J, Park J, Park S. Numerical and experimental study on effects of fuel injection timings on combustion and emission characteristics of a direct-injection spark-ignition gasoline engine with a 50 MPa fuel injection system. Appl Therm Eng 2018;144:890–900. doi:10.1016/J.APPLTHERMALENG.2018.09.007.

[251] Wang C, Xu H, Herreros JM, Wang J, Cracknell R. Impact of fuel and injection system on particle emissions from a GDI engine. Appl Energy 2014;132:178–91. doi:10.1016/j.apenergy.2014.06.012.

[252] Abas MA, Salim O, Martinez-Botas R, Rajoo S. Efforts to Establish Malaysian Urban Drive-Cycle for Fuel Economy Analysis. SAE Tech Pap 2014. doi:10.4271/2014-01-1159.

[253] Eastwood P. Particulate Emissions from Vehicles. Chichester, UK: John Wiley & Sons, Ltd; 2007. doi:10.1002/9780470986516.

[254] Lumley JL. Engines: An Introduction. Cambridge University Press; 1999.

[255] Hentschel W, Block B, Hovestadt T, Meyer H, Ohmstede G, Richter V, et al. Optical Diagnostics and CFD-Simulations to Support the Combustion Process Development of the Volkswagen FSI® Direct-Injection Gasoline Engine, 2001. doi:10.4271/2001-01-3648.

[256] Kuwahara K, Ando H. Diagnostics of in-cylinder flow, mixing and combustion in gasoline engines. Meas Sci Technol 2000;11:R95–111. doi:10.1088/0957-0233/11/6/202.

[257] An Y, Teng S, Li X, Qin J, Zhao H, Zhan ZS, et al. Study of Polycyclic Aromatic Hydrocarbons Evolution Processing in GDI Engines Using TRF-PAH Chemical Kinetic Mechanism, 2016.

doi:10.4271/2016-01-0690.

[258] He X, Ratcliff MA, Zigler BT. Effects of Gasoline Direct Injection Engine Operating Parameters on Particle Number Emissions. Energy & Fuels 2012;26:2014–27. doi:10.1021/ef201917p.

[259] Szybist JP, Youngquist AD, Barone TL, Storey JM, Moore WR, Foster M, et al. Ethanol Blends and Engine Operating Strategy Effects on Light-Duty Spark-Ignition Engine Particle Emissions. Energy & Fuels 2011;25:4977–85. doi:10.1021/ef201127y.

[260] Sabathil D, Koenigstein A, Schaffner P, Fritzsche J, Doehler A. The Influence of DISI Engine Operating Parameters on Particle Number Emissions. SAE Tech Pap 2011. doi:10.4271/2011-01-0143.

[261] Qin J, Li X, Pei Y. Effects of Combustion Parameters and Lubricating Oil on Particulate Matter Emissions from a Turbo-Charged GDI Engine Fueled with Methanol/Gasoline Blends. SAE Tech Pap 2014. doi:10.4271/2014-01-2841.

[262] Cho J, Si W, Jang W, Jin D, Myung C-L, Park S. Impact of intermediate ethanol blends on particulate matter emission from a spark ignition direct injection (SIDI) engine. Appl Energy 2015;160:592–602. doi:10.1016/J.APENERGY.2015.08.010.

[263] Rodriguez JF, Cheng WK. Effect of Operation Strategy on First Cycle CO, HC, and PM/PN Emissions in a GDI Engine. SAE Int J Engines 2015;8:2015-01–0887. doi:10.4271/2015-01-0887.

[264] Price P, Twiney B, Stone R, Kar K, Walmsley H. Particulate and Hydrocarbon Emissions from a Spray Guided Direct Injection Spark Ignition Engine with Oxygenate Fuel Blends. SAE Tech Pap 2007. doi:10.4271/2007-01-0472.

[265] Heywood J. Internal Combustion Engine Fundamentals. New York: McGraw-Hill Education; 1988.

[266] Cairns A, Blaxill H, Irlam G. Exhaust Gas Recirculation for Improved Part and Full Load Fuel Economy in a Turbocharged Gasoline Engine. SAE Tech Pap 2006. doi:10.4271/2006-01-0047.

[267] Alger T, Chauvet T, Dimitrova Z. Synergies between High EGR Operation and GDI Systems. SAE Int J Engines 2008;1:2008-01–0134. doi:10.4271/2008-01-0134.

[268] Han D, Ickes AM, Bohac S V., Huang Z, Assanis DN. HC and CO emissions of premixed low-temperature combustion fueled by blends of diesel and gasoline. Fuel 2012;99:13–9. doi:10.1016/J.FUEL.2012.04.010.

[269] Gupta SB, Bihari B, Biruduganti M, Sekar R. In-Cylinder Equivalence Ratio Measurements in an EGR Equipped Engine. J Eng Gas Turbines Power 2011;133:114504. doi:10.1115/1.4003789.

[270] Hedge M, Weber P, Gingrich J, Alger T, Khalek IA. Effect of EGR on Particle Emissions from a GDI Engine. SAE Int J Engines 2011;4:2011-01–0636. doi:10.4271/2011-01-0636.

[271] Leach F, Stone R, Richardson D, Lewis A, Akehurst S, Turner J, et al. Particulate emissions from a highly boosted gasoline direct injection engine. Int J Engine Res 2018;19:347–59. doi:10.1177/1468087417710583.

[272] Li L, Wang T, Duan J, Sun K. Impact of butanol isomers and EGR on the combustion characteristics and emissions of a SIDI engine at various injection timings. Appl Therm Eng 2019;151:417–30. doi:10.1016/J.APPLTHERMALENG.2019.01.082.

APPENDICES

Appendix A Chemical Kinetic Validation Results for Neat Hydrocarbons

ID Time

While it is important to retain the predictive ability of multi-component reaction mechanisms for their respective neat components, one should bear in mind that their simplified chemistry is expected to compromise the accuracy of chemical kinetics for pure fuel components to a certain extent. Thus, the performance of mechanisms in replicating the ID times is appraised for each individual constituent making up the TRF, namely isooctane, n-heptane and toluene.

Fieweger et al. [206] also studied the auto-ignition of stoichiometric mixtures of isooctane and air under varying pressures of 13 bar, 34 bar and 45 bar. The predicted ID times of isooctane are compared against the experimental measurements in Figure A-1 in which good agreement is displayed by all the mechanisms for the high-temperature region. The effect of pressures on ID times is also successfully captured by the mechanisms. On the other hand, the ignition characteristics of n-heptane under stoichiometric conditions were examined by Ciezki and Adomeit [207] in a ST from 660 K to 1350 K. The measured and computed ID times of n-heptane at initial pressures of 13.5 bar, 30 bar and 42 bar are illustrated in Figure A-2. Although high-temperature chemistry of n-heptane is adequately described in all the mechanisms, only An-TRF manages to capture the apparent NTC behaviour of n-heptane accurately, particularly at high pressures. Both Jiao-TRF and Wang-TRF predict shorter ID times at the NTC regions with the largest deviations at 42 bar.

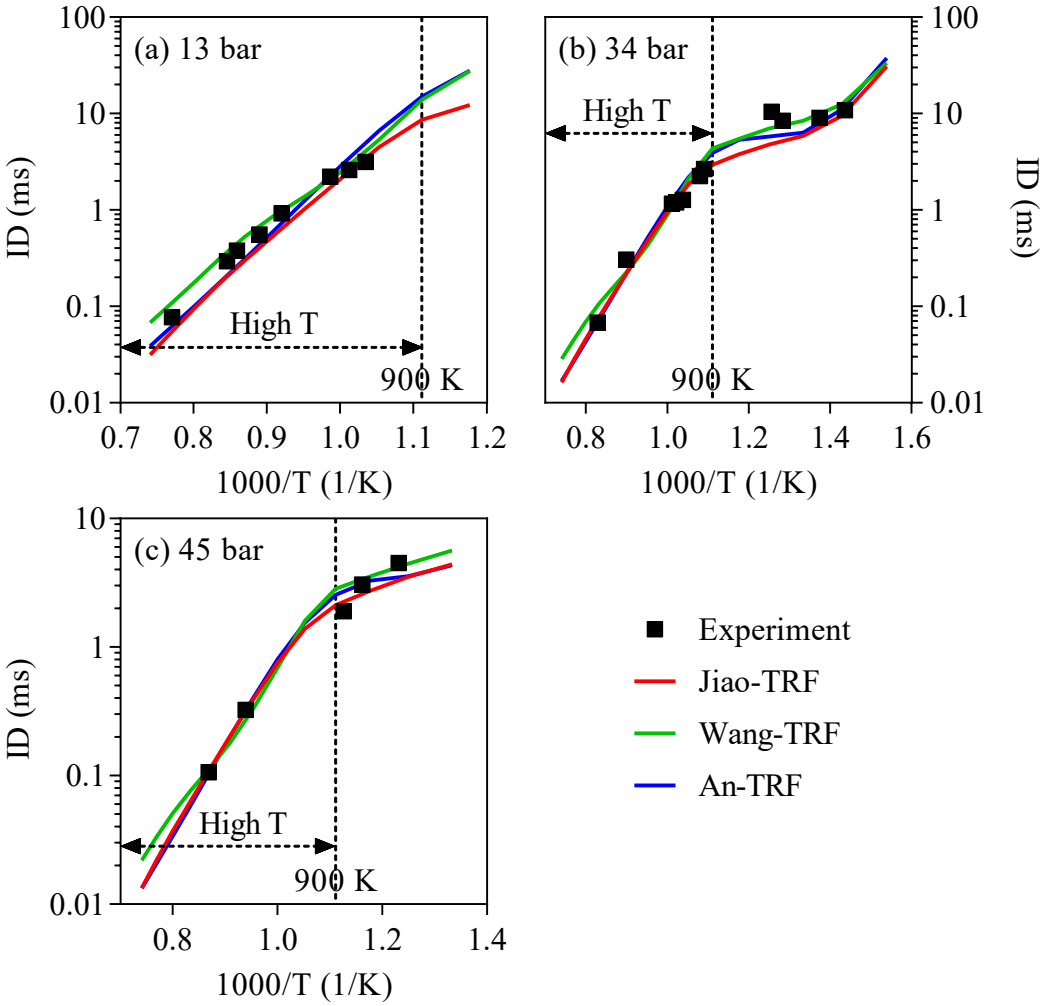


Figure A-1 Measured [206] and computed ID times of isooctane at pressures of (a) 13 bar, (b) 34 bar and (c) 45 bar with the equivalence ratio of 1.

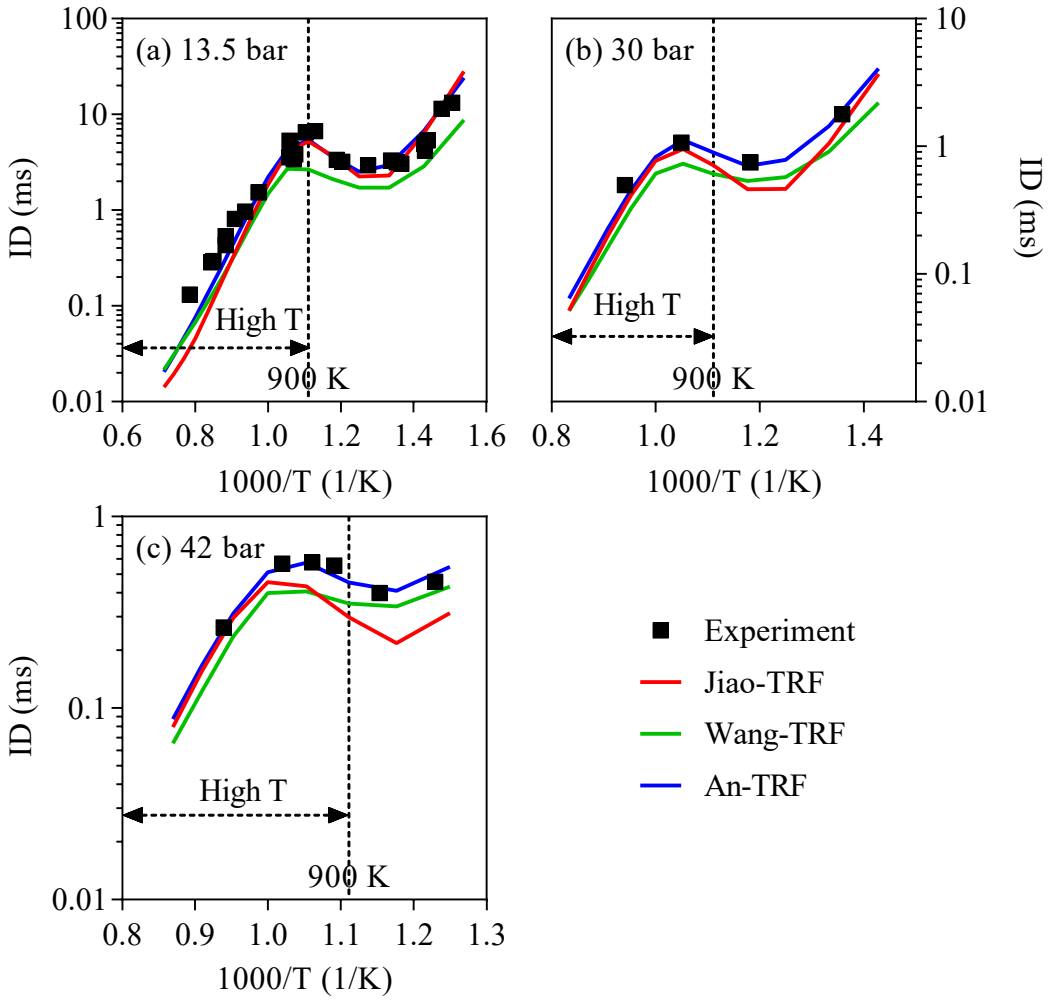


Figure A-2 Measured [207] and computed ID times of n-heptane at pressures of (a) 13.5 bar, (b) 30 bar and (c) 42 bar with the equivalence ratio of 1.

Unlike n- and isoparaffins, initiating the oxidation of aromatics is hindered by the high bond dissociation energies required to break the bonds between hydrogen atoms and the aromatic ring [202]. To understand the combustion kinetics of toluene, Shen et al. [208] measured the ID times of its stoichiometric mixtures in a ST and scaled them to 12 bar and 50 bar. Figure A-3 shows the experimental data and predicted ID times of toluene from 855 K to 1400 K. Additionally, the measurements of ID times at 50 bar by Davidson et al. [209] are included in Figure A-3(b). Among the mechanisms, only Wang-TRF reproduces the ID times of toluene correctly across the pressures. An-TRF consistently computes higher ID times while Jiao-TRF under-predicts the ID times at 20 bar and over-predicts them at 50 bar. The deficiency of toluene kinetics in An-TRF and Jiao-TRF is likely a compromising consequence from their simplified chemistry to emulate the ID times of RD387 and TRF surrogates. Pitz et al. [26] highlighted that

basic mechanistic issues remain unresolved for toluene and its reaction pathways are still not well understood, specifically at higher pressures. The ability of Wang-TRF to properly characterise the low reactivity of toluene partly explains the under-prediction of ID times of RD387 as shown in Figure 4-3(a)(ii) and (b)(ii).

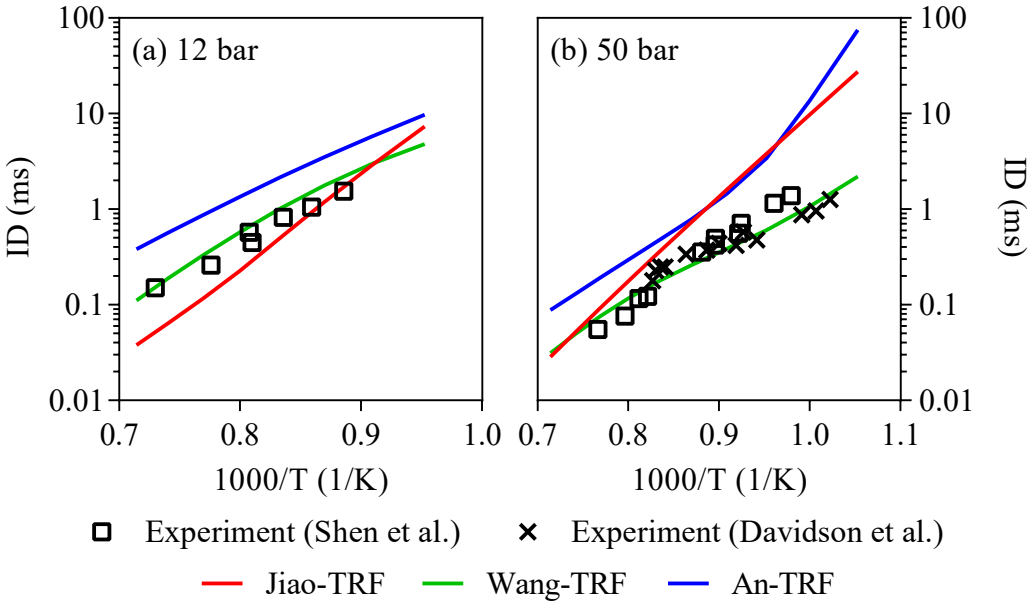


Figure A-3 Measured [208,209] and computed ID times of toluene at pressures of (a) 12 bar and (b) 50 bar with the equivalence ratio of 1.

Flame Speed

For validations involving neat components of TRF, experimental measurements of flame speed of isooctane, n-heptane and toluene on a flat flame burner carried out by Sileghem et al. [217] at atmospheric pressure is incorporated. The measured and computed values of flame speeds of isooctane, n-heptane and toluene are compared in Figure A-4, Figure A-5 and Figure A-6, respectively for initial temperatures of 298 K and 358 K. Only Wang-TRF retains the accurate predictions of flame speeds of all the individual components. The consistent over-predictions in flame speeds by Jiao-TRF is also evident for the neat components. While An-TRF exhibits reasonable agreement with the experimental data of n-heptane, significant deviations from the measured values are seen for both isooctane and toluene. It is noteworthy to highlight that all TRF mechanisms capture the experimental variations of flame speeds with respect to equivalence ratios qualitatively for isooctane and n-heptane. However, the simulated trends of flame speeds with changes of equivalence ratios for toluene appear

to be slightly skewed from the experimental one, thus reflecting the current lack of understanding in toluene chemistry.

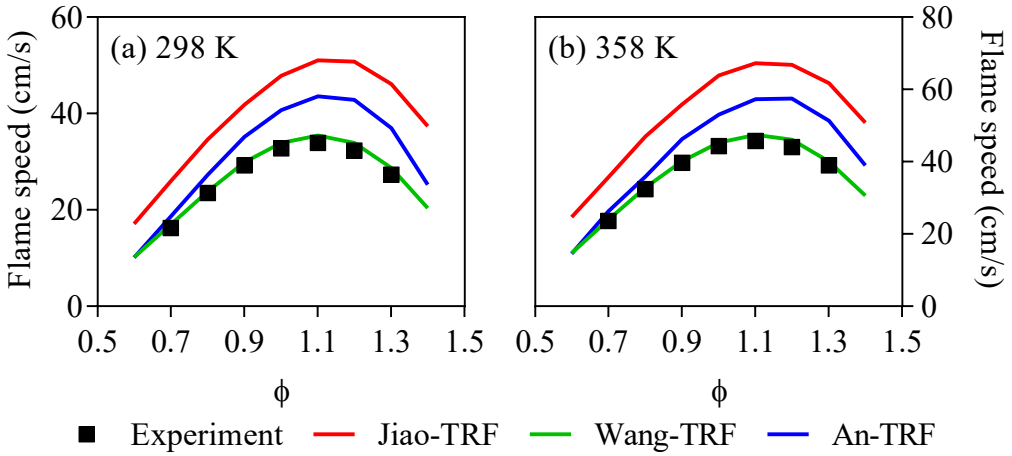


Figure A-4 Measured [217] and computed flame speeds of isooctane at the pressure of 1 bar and initial temperatures of (a) 298 K and (b) 358 K.

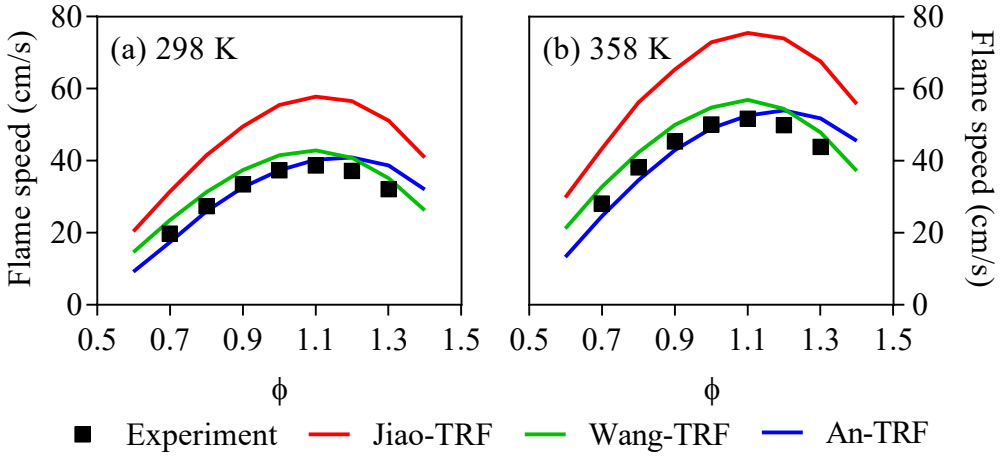


Figure A-5 Measured [217] and computed flame speeds of n-heptane at the pressure of 1 bar and initial temperatures of (a) 298 K and (b) 358 K.

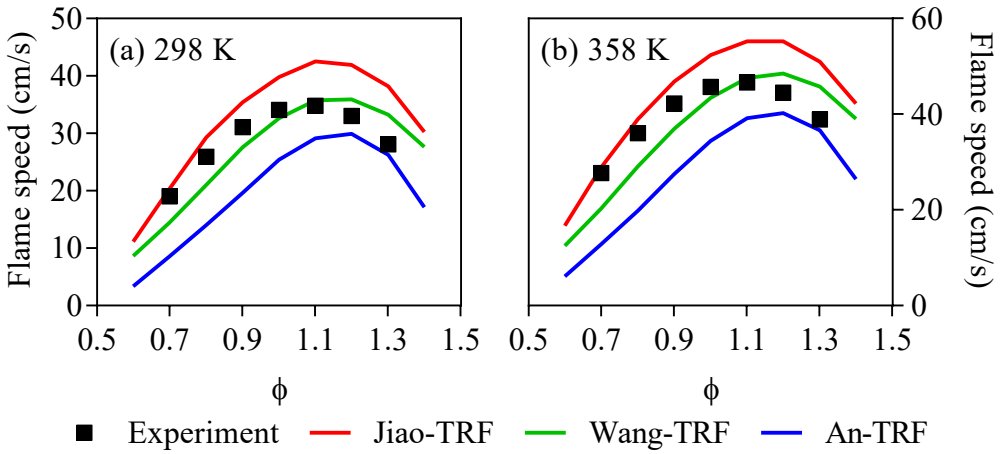


Figure A-6 Measured [217] and computed flame speeds of toluene at the pressure of 1 bar and initial temperatures of (a) 298 K and (b) 358 K.

Speciation Profile from JSR

The oxidation of neat fuels of isooctane and n-heptane in the JSR was also investigated by Dagaut et al. [221] at low- and high-temperature conditions with the pressure of 10 bar. The measured and resulting computed speciation profiles of isooctane and n-heptane are illustrated in Figure A-7 and Figure A-8, respectively. In general, acceptable agreement between the computed mole fractions and the experimental measurements is noted for consumption of fuel and O_2 as well as production of CO and CO_2. For C_2H_2, the experimental trends of increased concentrations from 800 K and reduced production beyond 1000 K of both neat fuels are reproduced by An-TRF, albeit with higher peaks. Jiao-TRF and Wang-TRF predict continuously increasing concentrations of C_2H_2 with increasing temperatures. Similar to PRF 90, reasonable agreement with the experiment speciation data of A1 for isooctane fuel is only seen for An-TRF.

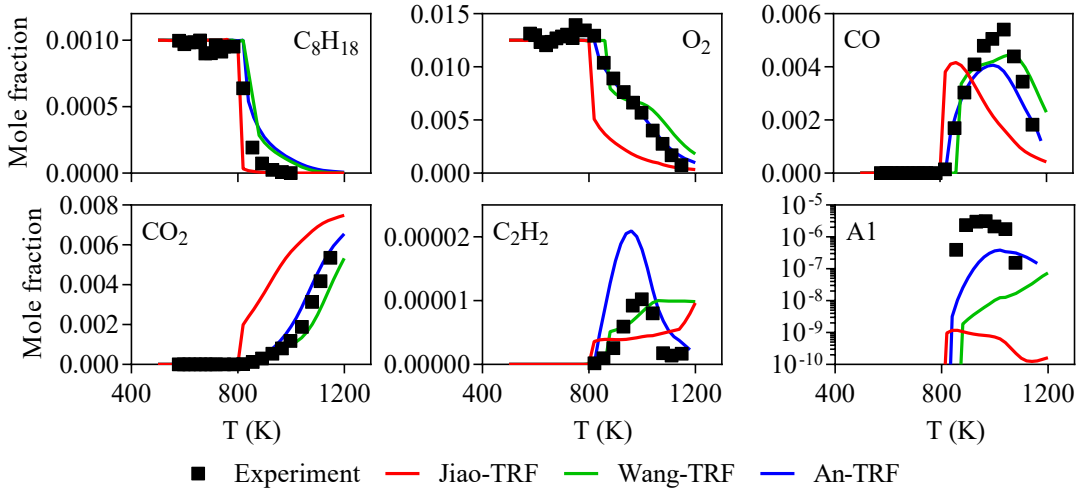


Figure A-7 Measured and computed speciation profiles of isooctane in the JSR at the pressure of 10 bar, mean residence time of 1 s and equivalence ratio of 1.

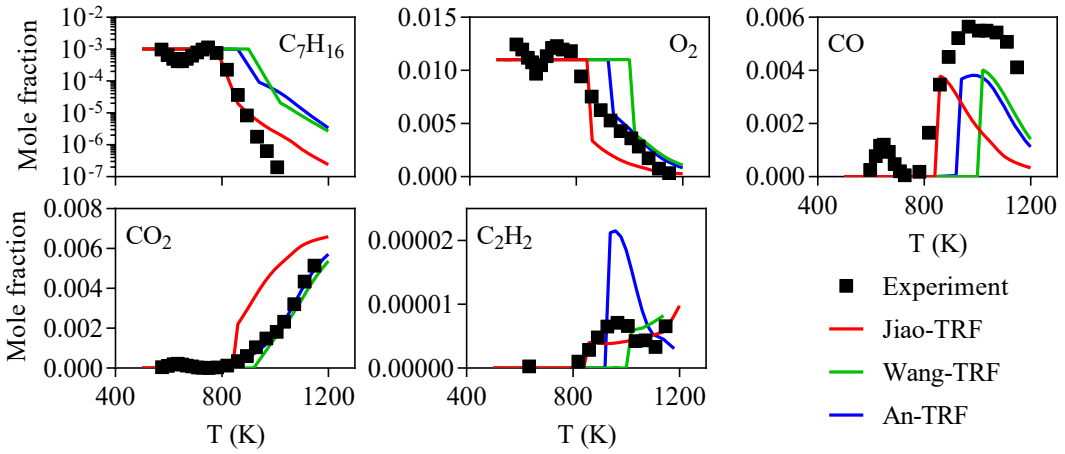


Figure A-8 Measured and computed speciation profiles of n-heptane in the JSR at the pressure of 10 bar, mean residence time of 1 s and equivalence ratio of 1.

Appendix B Chemical Reactions under An-TRF

Table B-1 Chemical reactions of the reduced TRF mechanism by An et al. [67] with 85 species and 232 reactions.

No.	Reaction	A (cm^3/mol/s)	n	E_a (cal/mol)
1	C7H16+O2=C7H15+HO2	1.00E+16	0	46000
	Reverse Arrhenius coefficients:	1.00E+12	0	0
2	C7H15+O2=C7H15O2	3.00E+12	0	0
	Reverse Arrhenius coefficients:	2.51E+13	0	27400
3	C7H15O2=C7H14OOH	1.51E+11	0	19000
	Reverse Arrhenius coefficients:	1.00E+11	0	11000
4	C7H14OOH+O2=O2C7H14OOH	6.16E+10	0	0
	Reverse Arrhenius coefficients:	2.51E+13	0	27400
5	O2C7H14OOH=>C7KET+OH	8.91E+10	0	17000
6	C7KET=>C5H11CO+CH2O+OH	3.98E+15	0	43000
7	C5H11CO+O2=>C3H7+C2H3+CO+HO2	3.16E+13	0	10000
8	C7H16+OH=>C7H15+H2O	5.00E+13	0	3000
9	C7H15+O2=C7H14+HO2	3.16E+11	0	6000
	Reverse Arrhenius coefficients:	3.16E+11	0	19500
10	C7H14+O2=>C3H6+C2H5+CH2O+HCO	3.16E+13	0	10000
11	C7H16+HO2=>C7H15+H2O2	1.00E+13	0	16950
12	C7H15=>C3H6+C2H5+C2H4	6.50E+12	0	28810
13	C8H18+O2=C8H17+HO2	6.00E+15	0	46000
	Reverse Arrhenius coefficients:	1.00E+12	0	0
14	C8H17+O2=C8H17O2	1.00E+12	0	0
	Reverse Arrhenius coefficients:	2.51E+13	0	27400
15	C8H17O2=C8H16OOH	1.51E+11	0	21800
	Reverse Arrhenius coefficients:	1.00E+11	0	11000
16	C8H16OOH+O2=O2C8H16OOH	1.16E+11	0	0
	Reverse Arrhenius coefficients:	2.51E+13	0	27400
17	O2C8H16OOH=>C8KET+OH	8.91E+10	0	17000
18	C8KET=>C6H13CO+CH2O+OH	3.98E+15	0	43000
19	C6H13CO+O2=>C3H7+C3H5+CO+HO2	3.16E+13	0	10000
20	C8H18+OH=>C8H17+H2O	2.00E+13	0	3000
21	C8H17+O2=C8H16+HO2	3.16E+11	0	6000
	Reverse Arrhenius coefficients:	3.16E+11	0	19500
22	C8H16+O2=>C3H7+C3H6+CH2O+HCO	3.16E+13	0	10000
23	C8H18+HO2=>C8H17+H2O2	1.00E+13	0	16950
24	C8H17=>C3H7+C3H6+C2H4	1.12E+17	-1.3	29700
25	C6H5CH3=C6H5CH2+H	2.09E+15	0	87463.4
26	C6H5CH3=>A1-+CH3	8.66E+15	0	97830.4
27	C6H5CH3+H=C6H5CH2+H2	6.47E+00	4	3394
28	C6H5CH3+O2=C6H5CH2+HO2	1.50E+14	0	41400
29	C6H5CH3+H=A1+CH3	1.20E+13	0	5100

No.	Reaction	A (cm^3/mol/s)	n	E_a (cal/mol)
30	C6H5CH3+OH=C6H5CH2+H2O	3.00E+12	0	1700
31	C6H5CH2+O=C6H5CHO+H	2.11E+14	0	0
32	C6H5CH2+O=A1-+CH2O	1.19E+14	0	0
33	C6H5CH2+HO2=>C6H5CHO+H+OH	5.00E+14	0	0
34	C6H5CHO+OH=H2O+C6H5CO	3.44E+09	1.2	-447
35	C6H5CHO+H=H2+C6H5CO	2.28E+10	1.1	3279
36	C6H5CO=A1-+CO	3.00E+12	0	34860
37	C6H5O=C5H5+CO	7.40E+11	0	43900
38	C6H5O+H=C6H5OH	2.50E+14	0	0
39	C6H5OH+O2=C6H5O+HO2	1.00E+13	0	38000
40	C6H5OH+H=C6H5O+H2	1.20E+14	0	12400
41	C6H5OH+O=C6H5O+OH	1.30E+13	0	2900
42	C6H5OH+OH=C6H5O+H2O	3.00E+06	2	-1310
43	C6H5OH+HO2=C6H5O+H2O2	1.00E+12	0	1000
44	C5H5+O=C4H5+CO	3.20E+13	-0.2	440
45	C5H5+OH=C5H4OH+H	3.50E+57	-12.2	48350
46	C5H4OH=C5H4O+H	2.10E+13	0	54000
47	C5H4O=>C2H2+C2H2+CO (duplicate)	5.70E+32	-6.8	68500
48	C5H4O=>C2H2+C2H2+CO (duplicate)	6.20E+41	-7.9	98700
49	C4H5=C2H2+C2H3	1.00E+14	0	43890
50	C2H2+C2H=C4H2+H	9.03E+13	0	0
51	C4H4+C2H=C4H2+C2H3	1.00E+13	0	0
52	C4H2+O=C3H2+CO	7.89E+12	0	1348
53	C4H2+OH=C3H2+HCO	6.68E+12	0	-408.7
54	2C2H2=C4H2+H2	1.51E+13	0	42420
55	C4H2+H2=C4H4	4.00E+14	0	53250
56	2C2H3<=>C4H5+H	4.00E+13	0	0
57	C4H5+C2H<=>2C3H3	4.00E+12	0	0
58	C4H5(+M)<=>C4H4+H(+M)	1.00E+14	0	49680
	Low pressure limit: 0.20000E+16 0.00000E+00 0.41730E5			
59	C4H5+O2<=>C4H4+HO2	1.00E+12	0	2980
60	C4H5+H<=>C4H4+H2	1.00E+14	0	0
61	C4H5+OH<=>C4H4+H2O	2.00E+07	2	999.1
62	C3H7=C2H4+CH3	9.60E+13	0	30950
63	C3H7=C3H6+H	1.25E+14	0	36900
64	C3H6=C2H3+CH3	3.15E+15	0	85500
65	C3H6+CH3=C3H5+CH4	9.00E+12	0	8480
66	C3H5+O2=C3H4+HO2	6.00E+11	0	10000
67	C3H4+OH=C2H3+CH2O	1.00E+12	0	0
68	C3H4+OH=C2H4+HCO	1.00E+12	0	0
69	C2H5+O2=C2H4+HO2	2.00E+10	0	-2200
70	C2H4+OH=CH2O+CH3	6.00E+13	0	960
71	C2H4+OH=C2H3+H2O	8.02E+13	0	5955
72	C2H3+O2=CH2O+HCO	4.00E+12	0	-250
73	C2H3+HCO=C2H4+CO	6.03E+13	0	0

No.	Reaction	A (cm^3/mol/s)	n	E_a (cal/mol)
74	C3H2+OH=C2H2+CO+H	5.00E+13	0	0
75	C3H2+O=C2H+H+CO	6.80E+13	0	0
76	C3H5=C2H2+CH3	2.40E+48	-9.9	82080
	Reverse Arrhenius coefficients:	2.61E+46	-9.8	36950
77	C2H4(+M)=C2H2+H2(+M)	1.80E+13	0	76000
	Low pressure limit: 0.15000E+16 0.00000E+00 0.55440E5			
78	C2H3+O2=C2H2+HO2	2.12E-06	6	9484
	Reverse Arrhenius coefficients:	1.11E-07	6.3	17570
79	C2H3+H=C2H2+H2	2.00E+13	0	2500
	Reverse Arrhenius coefficients:	1.33E+13	0	68080
80	C2H2+H(+M)=C2H3(+M)	3.11E+11	0.6	2589
	Low pressure limit: 0.22540E+41 -0.72690E+01 0.65770E4			
	TROE centering: 0.10000E+01 0.10000E-14 0.67500E+03 0.10000E+16			
	H2 Enhanced by 2; H2O Enhanced by 5; CO Enhanced by 2; CO2 Enhanced by 3			
81	C2H2+O2=HCCO+OH	2.00E+08	1.5	30100
	Reverse Arrhenius coefficients:	2.23E+05	1.5	25400
82	C2H2+O=HCCO+H	1.43E+07	2	1900
	Reverse Arrhenius coefficients:	2.02E+05	2	13310
83	C2H2+OH=CH2CO+H	2.19E-04	4.5	-1000
	Reverse Arrhenius coefficients:	2.16E-03	4.5	19660
84	CH2CO+H=CH3+CO	1.10E+13	0	3400
	Reverse Arrhenius coefficients:	2.40E+12	0	40200
85	CH2CO+O=HCCO+OH	1.00E+13	0	8000
	Reverse Arrhenius coefficients:	1.43E+10	0	-1255
86	CH2CO+OH=HCCO+H2O	1.00E+13	0	2000
	Reverse Arrhenius coefficients:	1.41E+11	0	9995
87	CH2CO+H=HCCO+H2	2.00E+14	0	8000
	Reverse Arrhenius coefficients:	6.52E+11	0	840
88	HCCO+OH=HCO+HCO	1.00E+13	0	0
	Reverse Arrhenius coefficients:	2.41E+14	0	40360
89	HCCO+O=H+CO+CO	8.00E+13	0	0
90	HCCO+O2=CO2+HCO	2.40E+11	0	-854
	Reverse Arrhenius coefficients:	1.47E+14	0	133600
91	H+O2=O+OH	3.55E+15	-0.4	16599
92	O+H2=H+OH	5.08E+04	2.7	6290
93	H2+OH=H2O+H	2.16E+08	1.5	3430
94	O+H2O=OH+OH	2.97E+06	2	13400
95	H2+M=H+H+M	4.58E+19	-1.4	104380
	H2 Enhanced by 2.5; H2O Enhanced by 12; CO Enhanced by 1.9; CO2 Enhanced by 3.8			
96	O+O+M=O2+M	6.16E+15	-0.5	0
	H2 Enhanced by 2.5; H2O Enhanced by 12; CO Enhanced by 1.9; CO2 Enhanced by 3.8			
97	O+H+M=OH+M	4.71E+18	-1	0
	H2 Enhanced by 2.5; H2O Enhanced by 12; CO Enhanced by 1.9; CO2 Enhanced by 3.8			
98	H+OH+M=H2O+M	3.80E+22	-2	0
	H2 Enhanced by 2.5; H2O Enhanced by 12; CO Enhanced by 1.9; CO2 Enhanced by 3.8			

No.	Reaction	A (cm^3/mol/s)	n	E_a (cal/mol)
99	H+O2(+M)=HO2(+M)	1.48E+12	0.6	0
	Low pressure limit: 0.63660E+21 -0.17200E+01 0.52480E3			
	TROE centering: 0.80000E+00 0.10000E-29 0.10000E31			
	Enhanced by H2: 2; H2O: 11; O2: 0.78; CO: 1.9; CO2: 3.8			
100	HO2+H=H2+O2	1.66E+13	0	823
101	HO2+H=OH+OH	7.08E+13	0	295
102	HO2+O=O2+OH	3.25E+13	0	0
103	HO2+OH=H2O+O2	2.89E+13	0	-497
104	HO2+HO2=H2O2+O2 (duplicate)	4.20E+14	0	11982
105	HO2+HO2=H2O2+O2 (duplicate)	1.30E+11	0	-1629.3
106	H2O2(+M)=OH+OH(+M)	2.95E+14	0	48430
	Low pressure limit: 0.12020E+18 0.00000E+00 0.45500E5			
	TROE centering: 0.50000E+00 0.10000E-29 0.10000E31			
	H2 Enhanced by 2.5; H2O Enhanced by 12; CO Enhanced by 1.9; CO2 Enhanced by 3.8			
107	H2O2+H=H2O+OH	2.41E+13	0	3970
108	H2O2+H=HO2+H2	4.82E+13	0	7950
109	H2O2+O=OH+HO2	9.55E+06	2	3970
110	H2O2+OH=HO2+H2O (duplicate)	1.00E+12	0	0
111	H2O2+OH=HO2+H2O (duplicate)	5.80E+14	0	9557
112	CO+O(+M)=CO2(+M)	1.80E+10	0	2384
	Low pressure limit: 0.15500E+25 -0.27900E+01 0.41910E4			
	H2 Enhanced by 2.5; H2O Enhanced by 12; CO Enhanced by 1.9; CO2 Enhanced by 3.8			
113	CO+O2=CO2+O	2.53E+12	0	47700
114	CO+HO2=CO2+OH	3.01E+13	0	23000
115	CO+OH=CO2+H	2.23E+05	1.9	-1158.7
116	HCO+M=H+CO+M	4.75E+11	0.7	14874
	H2 Enhanced by 2.5; H2O Enhanced by 12; CO Enhanced by 1.9; CO2 Enhanced by 3.8			
117	HCO+O2=CO+HO2	7.58E+12	0	410
118	HCO+H=CO+H2	7.23E+13	0	0
119	HCO+O=CO+OH	3.02E+13	0	0
120	HCO+OH=CO+H2O	3.02E+13	0	0
121	HCO+O=CO2+H	3.00E+13	0	0
122	HCO+HO2=CO2+OH+H	3.00E+13	0	0
123	HCO+CH3=CO+CH4	1.20E+14	0	0
124	HCO+HCO=H2+CO+CO	3.00E+12	0	0
125	HCO+HCO=CH2O+CO	3.00E+13	0	0
126	CH2O+M=HCO+H+M	3.30E+39	-6.3	99900
	H2 Enhanced by 2.5; H2O Enhanced by 12; CO Enhanced by 1.9; CO2 Enhanced by 3.8			
127	CH2O+M=CO+H2+M	3.10E+45	-8	97510
	H2 Enhanced by 2.5; H2O Enhanced by 12; CO Enhanced by 1.9; CO2 Enhanced by 3.8			
128	CH2O+H=HCO+H2	5.74E+07	1.9	2748.6
129	CH2O+O=HCO+OH	1.81E+13	0	3080
130	CH2O+OH=HCO+H2O	3.43E+09	1.2	-447
131	CH2O+O2=HCO+HO2	1.23E+06	3	52000
132	CH2O+HO2=HCO+H2O2	4.11E+04	2.5	10210

No.	Reaction	A (cm^3/mol/s)	n	E_a (cal/mol)
133	CH2O+CH3=HCO+CH4	3.64E-06	5.4	998
134	CH3+O=CH2O+H	8.43E+13	0	0
135	CH3+O2=CH3O+O	1.99E+18	-1.6	29230
136	CH3+O2=CH2O+OH	3.74E+11	0	14640
137	CH3+HO2=CH3O+OH	2.41E+10	0.8	-2325
138	CH3+H(+M)=CH4(+M)	1.27E+16	-0.6	383
	Low pressure limit: 0.24770E+34 -0.47600E+01 0.24400E4			
	TROE centering: 0.78300E+00 0.74000E+02 0.29410E+04 0.69640E+04			
	Enhanced by H2: 2; H2O: 6; CH4: 2; CO: 1.5; CO2: 2			
139	CH4+H=CH3+H2	5.47E+07	2	11210
140	CH4+O=CH3+OH	3.15E+12	0.5	10290
141	CH4+OH=CH3+H2O	5.72E+06	2	2639
142	CH3+HO2=CH4+O2	3.16E+12	0	0
143	CH4+HO2=CH3+H2O2	1.81E+11	0	18580
144	CH2OH+M=CH2O+H+M	1.00E+14	0	25100
145	CH2OH+H=CH2O+H2	6.00E+12	0	0
146	CH2OH+H=CH3+OH	9.64E+13	0	0
147	CH2OH+O=CH2O+OH	4.20E+13	0	0
148	CH2OH+OH=CH2O+H2O	2.40E+13	0	0
149	CH2OH+O2=CH2O+HO2 (duplicate)	2.41E+14	0	5017
150	CH2OH+O2=CH2O+HO2 (duplicate)	1.51E+15	-1	0
151	CH2OH+HO2=CH2O+H2O2	1.20E+13	0	0
152	CH2OH+HCO=CH3OH+CO	1.00E+13	0	0
153	CH2OH+HCO=CH2O+CH2O	1.50E+13	0	0
154	2CH2OH=CH3OH+CH2O	3.00E+12	0	0
155	CH2OH+CH3O=CH3OH+CH2O	2.40E+13	0	0
156	CH3O+M=CH2O+H+M	8.30E+17	-1.2	15500
157	CH3O+H=CH3+OH	3.20E+13	0	0
158	CH3O+O=CH2O+OH	6.00E+12	0	0
159	CH3O+OH=CH2O+H2O	1.80E+13	0	0
160	CH3O+O2=CH2O+HO2 (duplicate)	9.03E+13	0	11980
161	CH3O+O2=CH2O+HO2 (duplicate)	2.20E+10	0	1748
162	CH3O+HO2=CH2O+H2O2	3.00E+11	0	0
163	CH3O+CO=CH3+CO2	1.60E+13	0	11800
164	CH3O+HCO=CH3OH+CO	9.00E+13	0	0
165	2CH3O=CH3OH+CH2O	6.00E+13	0	0
166	OH+CH3(+M)<=>CH3OH(+M)	2.79E+18	-1.4	1330
	Low pressure limit: 0.40000E+37 -0.59200E+01 0.31400E4			
	TROE centering: 0.41200E+00 0.19500E+03 0.59000E+04 0.63940E+04			
	Enhanced by H2: 2; H2O: 6; CH4: 2; CO: 1.5; CO2: 2			
167	H+CH2OH(+M)<=>CH3OH(+M)	1.06E+12	0.5	86
	Low pressure limit: 0.43600E+32 -0.46500E+01 0.50800E4			
	TROE centering: 0.60000E+00 0.10000E+03 0.90000E+05 0.10000E+05			
	Enhanced by H2: 2; H2O: 6; CH4: 2; CO: 1.5; CO2: 2			
168	H+CH3O(+M)<=>CH3OH(+M)	2.43E+12	0.5	50

No.	Reaction	A (cm^3/mol/s)	n	E_a (cal/mol)
	Low pressure limit: 0.46600E+42 -0.74400E+01 0.14080E5			
	TROE centering: 0.70000E+00 0.10000E+03 0.90000E+05 0.10000E+05			
	Enhanced by H2: 2; H2O: 6; CH4: 2; CO: 1.5; CO2: 2			
169	CH3OH+H=CH2OH+H2	3.20E+13	0	6095
170	CH3OH+H=CH3O+H2	8.00E+12	0	6095
171	CH3OH+O=CH2OH+OH	3.88E+05	2.5	3080
172	CH3OH+OH=CH3O+H2O	1.00E+06	2.1	496.7
173	CH3OH+OH=CH2OH+H2O	7.10E+06	1.8	-596
174	CH3OH+O2=CH2OH+HO2	2.05E+13	0	44900
175	CH3OH+HCO=CH2OH+CH2O	9.64E+03	2.9	13110
176	CH3OH+HO2=CH2OH+H2O2	3.98E+13	0	19400
177	CH3OH+CH3=CH2OH+CH4	3.19E+01	3.2	7172
178	CH3OH+CH3O=CH3OH+CH2OH	3.00E+11	0	4060
179	C8H18=C5H11+C3H7	2.00E+12	0	77990.4
180	C7H16=C7H15+H	3.97E+10	-0.9	103200
181	C6H5CH2=C5H5+C2H2	1.00E+06	0	34879.4
182	C6H5CH2=C4H4+C3H3	2.00E+04	0	83376.1
183	CH2+CH2=C2H2+H2	1.20E+13	0	800
184	CH2+CH2=C2H2+H+H	1.20E+14	0	800
185	C2H2+O=CH2+CO	8.05E+05	2	1900
186	C2H2+O=C2H+OH	4.60E+19	-1.4	28950
	Reverse Arrhenius coefficients:	3.02E+15	-0.6	-1782
187	CH2+C2H2=C3H3+H	2.40E+13	0	6620
188	C2H2+CH3=C3H4+H	2.72E+18	-2	20200
189	C3H4+H=C3H3+H2	1.15E+08	1.9	7530
190	C3H3+OH=C2H3+HCO	2.00E+13	0	0
191	C3H3+O2=CH2CO+HCO	3.00E+10	0	2878
192	C2H2+C2H3=C4H4+H	4.90E+16	-1.1	11800
193	C3H3+C2H2=C5H5	6.35E+10	0	9995.2
194	C3H3+C3H3=A1	5.56E+20	-2.5	1692
195	C3H4+C3H3=A1+H	4.40E+08	0	2000
196	C4H5+C2H2=A1+H	1.60E+15	-1.3	5365
197	A1=A1-+H	1.29E+62	-12.5	148085.6
198	A1+H=A1-+H2	2.50E+14	0	16000
199	A1+CH3=>A1-+CH4	4.42E+01	3.9	11463
200	A1+C3H3=C9H8+H	6.26E+09	2.6	56500
201	A1+O=C6H5O+H	2.20E+13	0	4530
202	A1+OH=C6H5OH+H	1.30E+13	0	10600
203	A1-+C4H4=A2+H	2.50E+29	-4.4	26400
204	2C5H5=A2+2H	5.30E+12	0	4888.3
205	C4H5+C4H2=A1C2H+H	3.16E+11	0	1788
206	A1-+C2H2=A1C2H+H	2.50E+29	-4.4	26400
207	A1C2H+H=A1C2H*+H2	2.50E+14	0	16000
208	A1C2H+OH=A1C2H*+H2O	1.60E+08	1.4	1450
209	A2+H=>A2-1+H2	2.20E+07	1.9	9829.5

No.	Reaction	A (cm^3/mol/s)	n	E_a (cal/mol)
210	A1C2H-+C4H4=A2R5+H	1.60E+16	-1.3	6557
211	A2-1+C2H2=A2R5+H	1.90E+31	-5.3	20860
212	A2R5=A1C2H+C4H2	2.00E+17	0	115200
213	A2R5+OH=A2-1+CH2CO	1.00E+11	0	9935
214	A2R5+C2H2=A3	2.76E+04	2.5	29080
215	A2R5+C4H2=A4	2.41E+02	2.2	-1131
216	A2CH3+H=A2+CH3	3.85E+06	2.2	4163.5
217	C6H5CH2+C3H3=C10H10	1.51E+75	-17.9	39600
218	C10H10+H=C10H9+H2	1.00E+13	0	0
219	C10H9+H=A2+H2	1.00E+14	0	0
220	A2-1+C4H4=A3+H	2.50E+26	-4.4	26400
221	A1+A1-=P2+H	1.10E+23	-2.9	15890
222	P2+H=P2-+H2	2.50E+14	0	16000
223	P2-+C2H2=A3+H	4.60E+06	2	7300
224	A1C2H*+A1=A3+H	1.10E+24	-2.9	15890
225	A1-+A1C2H=A3+H	1.10E+24	-2.9	15890
226	A3+H=>A3-4+H2	5.00E+08	1.9	9829.5
227	C9H8=C9H7+H	1.73E+68	-15.2	116371.9
228	C9H7+C5H5=>A3+2H	6.39E+29	-4	35205.5
229	A3-4+C2H2=A4+H	1.40E+29	-3.4	17800
230	C9H7+C9H7=>A4+C2H2+H2	6.39E+29	-4	35205.5
231	A4+CH3=>A4-1+CH4	5.40E+00	3.9	11771
232	C6H5CH2+C9H7=A4+H2+H2	2.00E+13	0	2000

Appendix C Computational Mesh of the GDI Engine

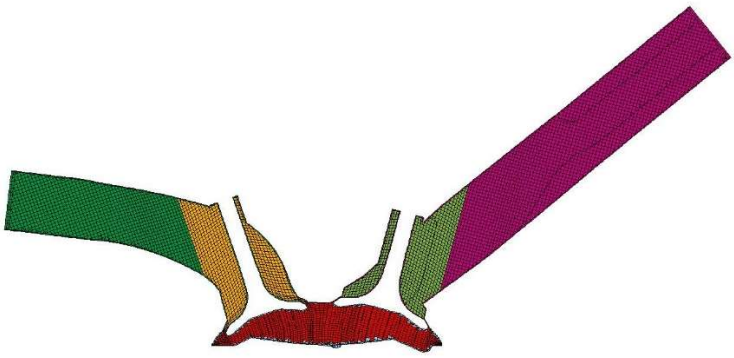


Figure C-1 Cross section of the computational mesh when the piston is at TDC.

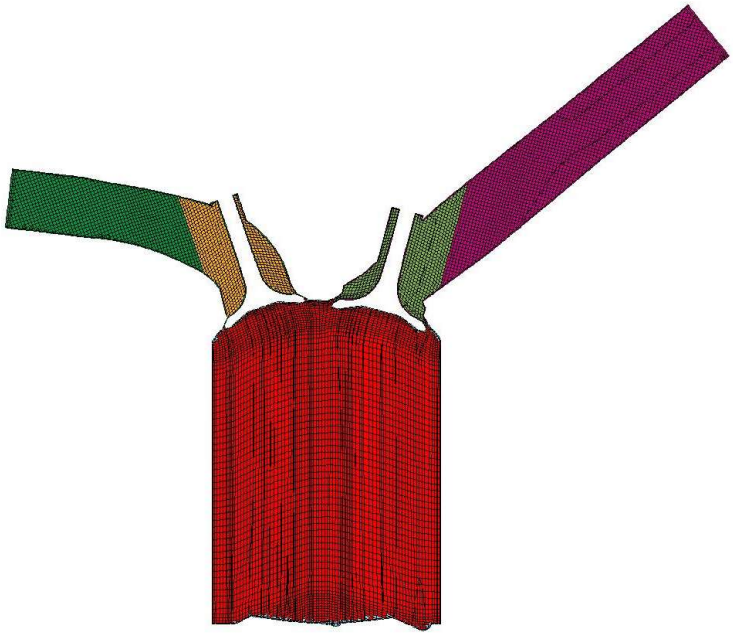


Figure C-2 Cross section of the computational mesh when the piston is at BDC.